Measurement of the Weak Boson Production Cross Section in the Events with Muons in Proton-Proton Collisions at $\sqrt{s} = 7$ TeV with the ATLAS Detector

Takashi Kubota

A dissertation submitted to the Department of Physics
for the degree of Doctor of Philosophy

The University of Tokyo

February 2011

Abstract

The Large Hadron Collider (LHC) – a proton-proton collider with the highest center-of-mass energy which surpasses the previous energy frontier – was built at CERN to investigate the TeV energy region where the existence of undiscovered physics such as the origin of the electroweak symmetry breaking and the Supersymmetry is expected. The LHC started operation on 30 March, 2010, then has been delivering proton-proton collision events.

The ATLAS (A Toroidal LHC ApparatuS) experiment is held using one of the two general purpose detectors placed at the LHC. The detector is designed to exploit the full physics potential of the LHC.

In this thesis, a measurement of the W and Z-boson production cross sections in proton-proton collisions at $\sqrt{s} = 7$ TeV are presented in the $W \rightarrow \mu\nu$ and $Z \rightarrow \mu\mu$ processes using the data collected with the ATLAS detector. The integrated luminosity used in the $W \rightarrow \mu\nu$ analysis is 310 nb^{-1} and in the $Z \rightarrow \mu\mu$ analysis is 331 nb^{-1}.

This production cross sections measurement is particularly significant in two aspects. One is to provide the first test of QCD prediction on the distribution of partons in proton-proton collisions at $\sqrt{s} = 7$ TeV. This will constitute a solid basis for every physics analysis performed in the ATLAS experiment. The other is to establish an event selection criterion for $Z \rightarrow \mu\mu$ process. This process plays a central role in the precise calibrations of detectors and algorithms for its ease of identification and the precise knowledge of the Z-boson mass and width.

The muon detection efficiency of the ATLAS detector is estimated using experimental data. The muon trigger efficiency is estimated by counting the number of muon trigger signatures on the path of a given reconstructed muon track. The data taken by triggers based on the calorimeter information are used to avoid trigger biases. The muon reconstruction efficiency is estimated with respect to a track reconstructed in the inner tracking detector. In the estimation, about half the number of the layers in the muon spectrometer are required to be fired on the extrapolated path of a given inner detector track to reject non-muon backgrounds.

The results of both efficiency estimations are confirmed by other independent estimation using muons in $Z \rightarrow \mu\mu$ process. This estimation provides the first trial of the detector performance measurement utilizing $Z \rightarrow \mu\mu$ process in the ATLAS experiment.

The results of the cross sections measurement are as follows.

$$
\begin{aligned}
\sigma_W \times BR\,(W \rightarrow \mu\nu) &= 9.57 \pm 0.31 \text{ (stat)} \pm 1.15 \text{ (syst) nb.} \\
\sigma_{W^+} \times BR\,(W^+ \rightarrow \mu^+\nu) &= 5.69 \pm 0.23 \text{ (stat)} \pm 0.69 \text{ (syst) nb.} \\
\sigma_{W^-} \times BR\,(W^- \rightarrow \mu^-\nu) &= 3.87 \pm 0.20 \text{ (stat)} \pm 0.47 \text{ (syst) nb.} \\
\sigma_Z \times BR(Z \rightarrow \mu\mu) &= 0.87 \pm 0.08 \text{ (stat)} \pm 0.12 \text{ (syst) nb.}
\end{aligned}
$$

1181 W-bosons and 109 Z-bosons are observed in data. The $\sigma_W \times BR\,(W \rightarrow \mu\nu)$ is measured with a transverse mass cut of $M_\mathrm{T} > 40$ GeV and $\sigma_Z \times BR\,(Z \rightarrow \mu\mu)$ is measured within an invariant mass window of $66 < m_{\mu\mu} < 116$ GeV. All the results are in agreements with the theoretical prediction including next-to-next-to leading order QCD corrections.

This measurement is the W and Z-boson production cross sections measurement performed at the highest center-of-mass energy ever.

Contents

List of Figures

List of Tables

Chapter 1

Introduction

On the ground of relativistic quantum field theory, the Standard Model (SM) of the elementary particle physics has been developed so far. This model incorporates Glashow-Weinberg-Saslam (GWS) theory [3, 4] of the electroweak interaction and the Quantum Chromo Dynamics (QCD) of strong interaction, and both have shown excellent agreements with results of experiments ever done. In both theories, there arise corresponding force mediators, called gauge bosons.

In the GWS theory, electromagnetism is mediated by a massless gauge boson, photon, and the weak interaction is mediated by massive Z and $W^{\pm}$-bosons. The GWS theory requires gauge bosons to be intrinsically massless whereas nonzero masses of Z and $W^{\pm}$-bosons are well established experimentally. This contradiction can be solved by introducing a scalar doublet into the GSW theory. This mechanism is called the Higgs mechanism [5, 6], and the spin 0 quantum of the scalar doublet is called Higgs boson which is widely considered as the last undiscovered the elementary particle in the SM.

Discovery of the Higgs boson has been regarded as one of the most important goals in the elementary particle physics. The presence of the Higgs boson with a mass below 114.4 GeV [7] and between 158 and 175 GeV [8] has been already excluded with 95 % C.L. (Confidence Level) by the experiments at the LEP and the Tevatron colliders. Figure **1.1** shows the observed and expected exclusion limits for the Higgs boson at the 95 % C.L. for the combined CDF and D0 experiments results at the Tevatron as well as the indication of the excluded mass region.

The QCD has a massless gauge boson, gluon, which interacts with quarks via exchanges of an additional quantum number, color. The concept of the color was introduced to explain the fact that baryons like Δ^{++} (u ↑ u ↑ u ↑) or Ω^{-} (s ↑ s ↑ s ↑) behave as fermions. The color charge has three degrees of freedom which are labeled as R (Red), G (Green) and B (Blue) (the name came from an analogy to the color of light). The hypothesis of the existence of color charge is supported by experimental results like the observed R value of $e^{+}e^{-} \rightarrow$ hadrons, the decay rate of $\pi^{0} \rightarrow \gamma\gamma$, the study of Drell-Yann process and decay width of the W and Z-bosons. Furthermore, the three-jet events from $e^{+}e^{-}$ annihilations observed in PETRA experiments provided the direct evidence of gluons [9–12].

One of the most important application of the QCD is the concept of the parton distribution functions (PDFs) inside hadrons. The concept of partons, free point-like constituents of hadrons, have been established through a series of experiments like e-p deep-inelastic scatter-
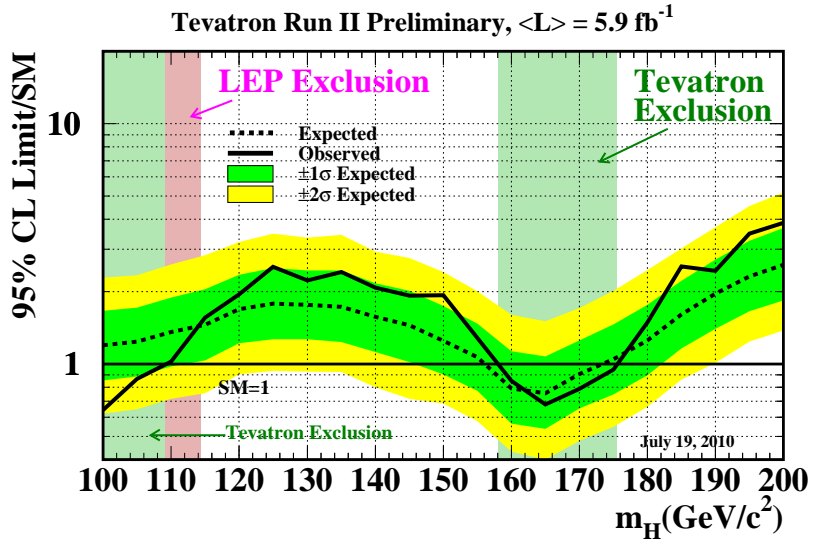
Figure 1.1: Observed and expected exclusion limits for the SM Higgs boson at the 95 % C.L. for the combined CDF and D0 experiments at the Tevatron [8].

ing experiments at SLAC [13, 14], and neutrino-nucleon scattering experiment performed at CERN [15]. Theoretical supports were also given by Bjorken [16] and Feynmann [17]. Now, partons are understood as gluons and quarks in hadrons.

PDFs evolve depending on the energy scale due to the running of the coupling constant of strong interaction, α_S. However, once PDFs are measured at a certain energy scale, the evolution of PDFs can be theoretically predicted by the DGLAP (Dokshitzer-Gribov-Lipatov-Altarelli-Parisi) evolution function [18–20]. For this reason, a measurement of the PDFs at the higher energy provides a good test of the QCD.

Despite all the excellent agreements with experiments, the SM has some difficulties to overcome. One such difficulty is the instability of the Higgs boson mass against radiative correction which needs 10^{26} orders of fine tuning to be prevented. As a candidate of possible new extension to the SM, the theories including the Supersymmetry (SUSY), which is a symmetry between bosons and fermions, have been developed. SUSY predicts the existence of new particles, all of which have a SM counterpart. SUSY particles contribute to the radiative corrections on the Higgs boson mass with opposite direction to the contribution of their SM partners, thus canceling the instability of the Higgs boson mass.

Precise measurements of the electroweak properties such as W-boson mass can provide an indirect constraint on the SM Higgs boson mass and properties of SUSY particles. Figure **1.2** shows the predicted mass of W-boson as a function of the top quark mass indicating the allowed region for SM Higgs boson mass and mass scale of the SUSY particles in the Minimally Super-

symmetric Standard Model (MSSM) [21–23].
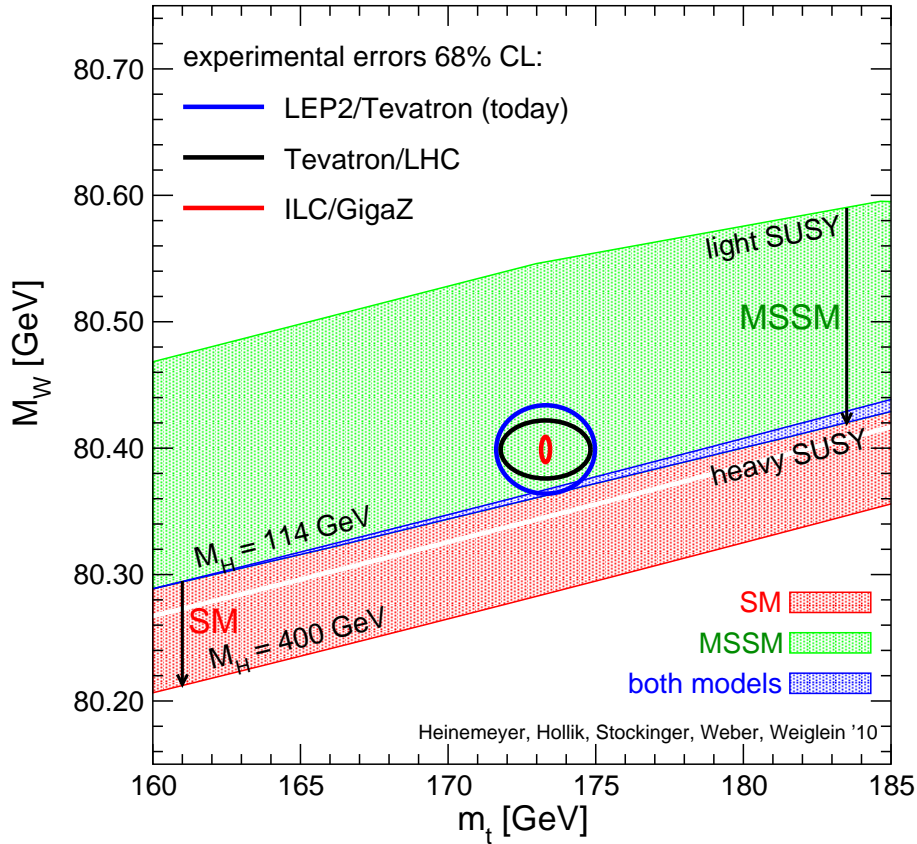
Figure 1.2: Prediction for the *W*-boson mass in the MSSM and the SM as a function of the top quark mass [21–23].

In the situation described above, the Large Hadron Collider – a proton-proton collider with the highest center-of-mass energy which surpasses the previous energy frontier – was constructed at the European Organization of Nuclear Research (CERN), Geneva. Along with the unprecedented design luminosity of 10^{34} cm^{-2}s^{-1}, the LHC is expected to bring new knowledge which enlarge the current understandings of the elementary particle physics. The LHC started proton-proton collisions with a center-of-mass energy of $\sqrt{s} = 7$ TeV on 30 March, 2010.

The ATLAS (A Toroidal LHC ApparatuS) experiments is held using one of the two general purpose detectors placed at the LHC. The detector is designed to exploit the full physics potential of the LHC such as the discovery of the Higgs boson and the SUSY, precise measurement of the electroweak and top quark physics and stringent test of the QCD. The ATLAS detector mainly consists of an inner tracking detector with a homogeneous solenoidal magnetic field of 2 T, electromagnetic and hadronic calorimeters, and a muon spectrometer with a dedicated toroidal magnet system. These detectors have been commissioned during 2008 and 2009 using cosmic ray and single beam data. Still, further understanding of the detectors is one of the most urgent tasks to be done using collision data.
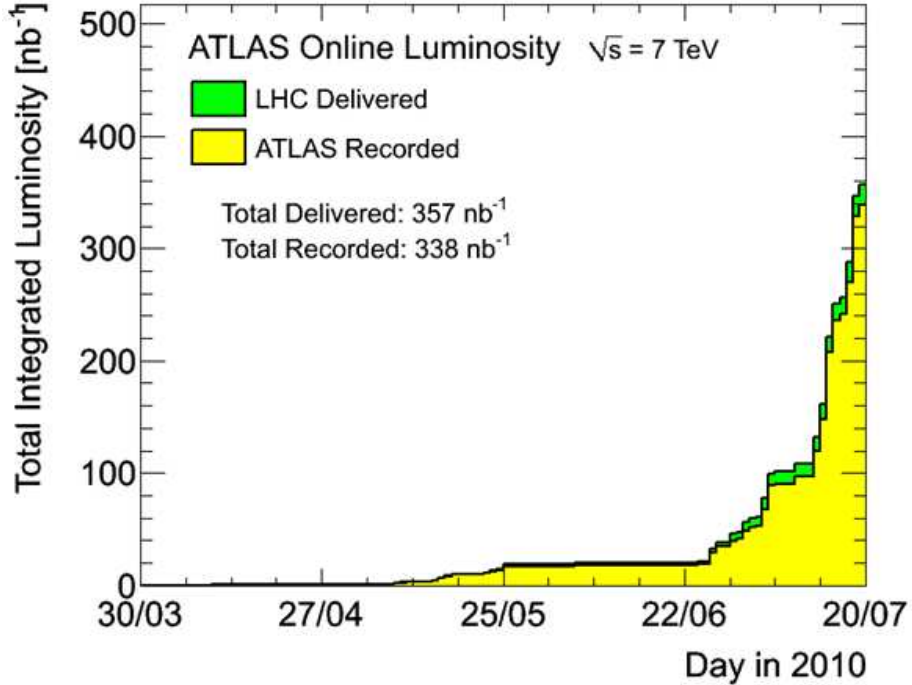
Figure 1.3: Cumulative luminosity in the ATLAS experiment versus day.

In this thesis, a measurement of the *W* and *Z*-boson production cross sections in proton-proton collisions at $\sqrt{s}$ = 7 TeV are presented in the $W \rightarrow \mu\nu$ and $Z \rightarrow \mu\mu$ processes using the data collected with the ATLAS detector from April to July, 2010. The integrated luminosity used in the $W \rightarrow \mu\nu$ analysis is 310 nb^{-1} and in the $Z \rightarrow \mu\mu$ analysis is 331 nb^{-1}. Shown in Figure **1.3** is the accumulated integrated luminosity in the ATLAS experiment versus day. The LHC has been steadily delivering proton-proton collisions and ATLAS recorded the event data with a high efficiency of approximately 95 %.

This production cross sections measurement is particularly significant in two aspects. One is to perform the first test of the QCD prediction on the distribution of partons in proton-proton collisions at $\sqrt{s}$ = 7 TeV. Especially, the sensitivity for the PDFs of sea quarks in low-*x* region surpasses the previous limitation set by the measurement at the Tevatron collider. The precise knowledge on the PDFs are indispensable for every physics analysis which will be performed at the LHC.

The other is to establish an event selection criterion for the $Z \rightarrow \mu\mu$ process. This process plays a central role in the precise calibrations of the detectors, algorithms and Monte Calro simulations for its ease of identification and the precise knowledge of the mass and width of *Z*-boson. This leads to a series of the precise electroweak measurements which aims to obtain, for example, new knowledge of the Higgs boson mass and the properties of the SUSY particles.

Muon is the most important physics object in this measurement. Especially, a precise knowledge on the muon identification efficiency is crucial. Hence the muon identification efficiency

is estimated using the experimental data.

The muon trigger efficiency is estimated with respect to a reconstructed muon track because one muon track with high transverse momentum is required in both the $W \to \mu\nu$ and the $Z \to \mu\mu$ candidate event selections. The efficiency is deduced by counting the number of muon trigger signatures on the path of a given track. The estimation is done using data taken by triggers which are based on the calorimeter information to avoid trigger biases.

The muon reconstruction efficiency is measured with respect to a reconstructed track in the inner detector. The efficiency is deduced by counting the number of tracks in the muon spectrometer which has consistent track parameters with a given muons track's reconstructed in the inner detector. In the estimation, about half the number of the layers in the muon spectrometer are required to be fired on the extrapolated path of a given inner detector track to reject non-muon backgrounds.

The results of both efficiency estimations are checked with other independent estimation using muons in $Z \to \mu\mu$ events which are selected thorough the selection criteria established in this study. This is the first trial of detector performance measurement using $Z \to \mu\mu$ process in the ATLAS experiment.

The Organization of the Thesis

The first part of this thesis is on a introductory purpose. In Chapter 2, a short description about the theoretical framework of some parts of the SM and expected precise electro-weak measurement at the LHC is given to illustrate the motivation and significance of the study. Chapter 3 and 4 are devoted to give an overview of the LHC and the accelerator complex as well as the ATLAS detector and its target performance. Muon is the most important physics object in the analysis, thus Chapter 5 and 6 are devoted to explain the muon trigger and reconstruction scheme in the ATLAS experiment in some detail.

The second part presents the results of the analysis. In Chapter 7 a brief description of the actual experimental condition and the dataset used in the analysis are given. Chapter 9 and 10 show the methods and results for the muon efficiency measurement for trigger and reconstruction. Chapter 11 and 12 present the results of W / Z-boson production cross sections measurement using $Z \to \mu\mu$ and $W \to \mu\nu$ processes. The closing chapter gives a discussion on the results and overviews the thesis, then presents conclusions.

Chapter 2

Physics Background

This thesis describes measurement of the production cross sections of W and Z-bosons through the $Z \rightarrow \mu\mu$ and $W \rightarrow \mu\nu$ processes in proton-proton collisions at $\sqrt{s} = 7$ TeV. This measurement is the $W \rightarrow \mu\nu$ and $Z \rightarrow \mu\mu$ production cross section measurement performed at the highest center-of-mass energy ever.

To illustrate the current situation of the elementary particle physics and the objective of the measurement concretely, the following items are described in this section.

- An overview of the SM which makes a solid basis of our understanding for nature of elementary particles and their interactions

- A description of the precise electroweak measurement at the LHC

- The motivation and significance of the production cross section measurement of W and Z-bosons at the LHC

2.1 The Standard Model of the Elementary Particle Physics

Elementary particles are classified into two categories according to its spin. The particles with half-integer spin are called fermions, which are considered as the fundamental building blocks of the matter around us. Fermions are further classified as quarks and leptons. The list of quarks and leptons are summarized in Table **2.1**. Quarks and leptons make up three left-handed isospin doublet (denoted as $_L$) and three (lepton) or six (quark) right-handed singlets (denoted as $_R$). The fermions in one column in Table **2.1** form one *generation*. Both quarks and leptons have three generation structure. The non-existence of 4th generation with neutrino with relevantly light mass ($< m_Z/2 \sim 45$ GeV) was proved by the LEP experiments [24–27]. A lepton doublet consists of one neutrino and one charged lepton, namely e, μ and τ. Bottom part of quark doublets is marked by dash. This indicates the quarks in eigenstates of the weak interactions, not of mass. The transformation between mass and weak eigenstate is described by the Cabbibo-Kobayashi-Maskawa (CKM) Matrix [28]. Q, T_3, Y and C in Table **2.1** are *charges* for each interaction. The details are described in the following sections.

The particles with integer spin are called bosons. Especially gauge bosons, which theoretically arise from invariance against arbitrary quantum phase transformations in space-time

coordinates, play a role of force mediator between fermions. This invariance is called gauge invariance or gauge symmetry [29]. The explanation of the gauge symmetry is given in sub-section 2.1.1 taking the Quantum Electrodynamics (QED [30–35]), which describes the electro magnetic interaction, as an example.

The Grashow-Weinberg-Salam (GSW) theory [3, 4] is the theory of $SU(2)_L \times U(1)_Y$ gauge symmetry. This theory describes weak interactions as well as electro magnetic interactions in which W and Z-bosons mediate interactions. Further description of the GSW theory is given in sub-section 2.1.2.

W and Z-bosons are generated in proton-proton collisions at the LHC. Protons are composite particles made of quarks and gluons which are coupled each other by strong interaction described by Quantum Chromodynamics (QCD), a theory of the SU(3) gauge symmetry. In sub-section 2.1.3, the description of QCD is given as well as the concept of partons, which is highly important to describe interactions at the LHC.

Fermions			Quantum Numbers			
			Q	T_3	Y	C
Leptons						
$\begin{pmatrix} \nu_e \\ e^- \end{pmatrix}_L$ $\begin{pmatrix} \nu_\mu \\ \mu^- \end{pmatrix}_L$ $\begin{pmatrix} \nu_\tau \\ \tau^- \end{pmatrix}_L$			$\begin{matrix} 0 \\ -1 \end{matrix}$	$\begin{matrix} +\frac{1}{2} \\ -\frac{1}{2} \end{matrix}$	-1	0
e_R	μ_R	τ_R	-1	0	-2	0
Quarks						
$\begin{pmatrix} u \\ d' \end{pmatrix}_L$ $\begin{pmatrix} c \\ s' \end{pmatrix}_L$ $\begin{pmatrix} t \\ b' \end{pmatrix}_L$			$\begin{matrix} +\frac{2}{3} \\ -\frac{1}{3} \end{matrix}$	$\begin{matrix} +\frac{1}{2} \\ -\frac{1}{2} \end{matrix}$	$+\frac{1}{3}$	(R, G, B)
u_R	c_R	t_R	$+\frac{2}{3}$	0	$+\frac{4}{3}$	(R, G, B)
d'_R	s'_R	b'_R	$-\frac{1}{3}$	0	$-\frac{2}{3}$	(R, G, B)

Table 2.1: Fermion constituents in the standard model.

2.1.1   The Quantum Electrodynamics

Regarding $\psi(x)$ as a Dirac field at x in space-time coordinate, U(1) gauge transformation in QED is written as

$$\psi(x) \rightarrow e^{iQ\theta(x)}\psi(x). \tag{2.1}$$

Q is the generator of the gauge transformation physically corresponding to electric charge of the field $\psi(x)$. $\theta(x)$ is the magnitude of the transformation which depends on space and time in a completely arbitrary way. The U(1) gauge symmetry which takes Q as a generator is called $U(1)_{EM}$ symmetry.

Lagrangean density $\mathcal{L}$ (hereafter denoted as Lagrangean) for the free Dirac field is written as

$$\mathcal{L} = \overline{\psi}(i\gamma^\mu \partial_\mu - m)\psi. \tag{2.2}$$

However, the first term of this $\mathcal{L}$ is not invariant under the $U(1)_{EM}$ transformation. To restoring the gauge symmetry, covariant derivative D_μ is defined as

$$D_\mu = \partial_\mu - ieA_\mu. \tag{2.3}$$

A_μ is the $U(1)_{EM}$ gauge field, its transformation is defined as

$$A_\mu \rightarrow A_\mu + \frac{1}{e}\partial_\mu \alpha. \tag{2.4}$$

This transformation keeps the equations of Maxwell unchanged. Here we define field strength

$$F_{\mu\nu} = \partial_\mu A_\nu - \partial_\nu A_\mu, \tag{2.5}$$

to introduce a gauge invariant kinematic term of the gauge field into the Lagrangean. Then we obtained the $U(1)_{EM}$ invariant QED Lagrangean

$$\mathcal{L} = \overline{\psi}(i\gamma^\mu D_\mu - m)\psi - \frac{1}{4}F_{\mu\nu}F^{\mu\nu}. \tag{2.6}$$

The first term represents the kinetic energy of the Dirac field and interaction with the gauge field, the second is the mass term of the Dirac field and the last is the kinetic term of the gauge field. As mentioned above, a requirement of gauge invariance introduces a gauge field and defines its kinematics and interactions. From the first term, one can see the interaction between a Dirac and gauge field has the form

$$Q\overline{\psi}\gamma^\mu A_\mu \psi \equiv iQj_\mu^{em}A^\mu, \tag{2.7}$$

j_μ^{em} is called electro magnetic current. One significant feature of gauge theory is the fact that interaction occurs as coupling between vector current of fermion and gauge field. In QED, gauge field A_μ is identified as photon and couples with the electro magnetic current with the strength proportional to electric charge.

Note that gauge boson mass term $mA_\mu A^\mu$ is prohibited by the gauge symmetry and consequently, in this case, photon is massless.

2.1.2   The Grashow-Weinberg-Salam Theory

Interaction of Gauge Bosons with Fermions

The GSW theory is the theory of $SU(2)_L \times U(1)_Y$ symmetry which describes the electro magnetic interaction and weak interaction as a whole. The $_L$ attached on SU(2) indicates that SU(2) symmetry is imposed only on the left-handed particles, in other words, particle with the third-component of the *weak isospin* $T_3 = \pm 1/2$. Isospin is an internal degree of freedom which plays a role of the charge for weak interactions. Y is called *weak hypercharge* which was introduced to explain the origin of the right handed component in neutral current of weak interaction. The relation between electric charge Q and T_3, Y is written as

$$Q = T_3 + \frac{Y}{2}, \tag{2.8}$$

Q, T_3 and Y for each fermion are summarized in Table **2.1**.

Here we define weak isospin current $\boldsymbol{J}_\mu$ and weak hypercharge current j^Y which couple to isotriplet of the vector fields W_μ^i and single vector field B_μ respectively.

$$J_\mu^i(x) = \overline{\chi}_L \gamma_\mu \frac{1}{2} \tau^i \chi_L \quad \text{with i } = 1, 2, 3, \tag{2.9}$$

$$j^Y = 2(J_\mu^3 - j_\mu^{em}), \tag{2.10}$$

where χ_L represents a left-handed isospin doublet and τ_i is the i-th Pauli spin matrix. The currents and vector fields are assumed to couple each other with the coupling constant of g (weak isospin) and g' (weak hypercharge). Then the electroweak Lagrangean has a form

$$\mathcal{L} = g \boldsymbol{J}_\mu \cdot \boldsymbol{W}_\mu + g' j_\mu^Y B^\mu. \tag{2.11}$$

The physical bosons consist of the charged and neutral weak gauge boson $W_\mu^\pm$, Z_μ and photon A_μ. Define the relations between physical gauge bosons and W_μ^i, B_μ as

$$W_\mu^\pm = \frac{1}{\sqrt{2}}(W_\mu^1 \mp W_\mu^2), \tag{2.12}$$

$$Z_\mu = \frac{-g' B_\mu + g W_\mu^3}{\sqrt{g^2 + g'^2}}, \tag{2.13}$$

$$A_\mu = \frac{g B_\mu + g' W_\mu^3}{\sqrt{g^2 + g'^2}}. \tag{2.14}$$

The interaction Lagrangean in Eq (2.11) can be transformed as

$$\begin{aligned}
\mathcal{L} = {} & \frac{g}{\sqrt{2}} \left(J_\mu^- W_\mu^+ + J_\mu^+ W_\mu^- \right) \ (CC) \\
& + \frac{g}{\cos\theta_W} (J_\mu^3 - \sin^2\theta_W j_\mu^{em}) Z_\mu \ (NC) \\
& + g \sin\theta_W j_\mu^{em} A_\mu \ (EM),
\end{aligned} \tag{2.15}$$

where $J_\mu^\pm$, θ_W are defined as $J_\mu^\pm = J_\mu^1 \pm iJ_\mu^2$ and $g'/g = \tan\theta_W$. CC, NC and EM represents the charged current, neutral current of weak interaction and electro magnetic current respectively. θ_W is called Weinberg-angle which determines the ratio of the coupling constants of electro magnetic and weak interactions. From the third term of Eq (2.15), one can see the relation of

$$e = g'\sin\theta_W, \tag{2.16}$$

where e is the unit electric charge.

Eq (2.15) is well summarizing the interaction of the gauge bosons in the GSW theory. First, three types of gauge bosons, namely $W_\mu^\pm$, Z_μ and A_μ exist. A_μ is photon, the identical gauge field arises in the QED couples to electro magnetic current j_μ^{em} with the magnitude proportional to the electric charge. $W_\mu^\pm$ is called W-boson which couples to charged current with the magnitude of g. W-bosons interact only with left-handed fermions since charged current is made of purely weak isospin components. Z_μ is called Z-boson which couples to neutral current with the magnitude of $g/\cos\theta_W$. W and Z-bosons are called weak bosons as a whole. Unlike charged current, neutral current is made of both weak isospin and hypercharge components. Hypercharges for right-handed fermion are non-zero, thus Z-boson couples to right-handed fermions. The form of neutral current in Eq.(2.15) can be transformed as

$$
\begin{aligned}
J_\mu^{NC} &= J_\mu^3 - \sin^2\theta_W j_\mu^{em} \\
&= \frac{1}{2}\bar{\psi}\gamma^\mu(v_f - a_f\gamma^5)\psi,
\end{aligned}
\tag{2.17}
$$

where

$$
\begin{aligned}
v_f &= T_3 - 2Q\sin^2\theta_W, \\
a_f &= T_3.
\end{aligned}
\tag{2.18}
$$

v_f and a_f are the coupling strengths of the vector and axial vector components in the neutral current to the Z-boson.

The Mass of Weak Bosons

As mentioned above, mass terms of gauge bosons are prohibited by the gauge symmetry. However, actual W and Z-boson have mass [36].

$$
\begin{aligned}
m_W &= 80.399 \pm 0.023\text{GeV}, \tag{2.19}\\
m_Z &= 91.1876 \pm 0.0021\text{GeV}. \tag{2.20}
\end{aligned}
$$

This contradiction is solved by the introduction of a complex scalar (spin-0) isospin doublet called Higgs doublet ϕ. Defining weak hypercharge of the Higgs doublet as 1, ϕ is written as

$$\phi \equiv \sqrt{\frac{1}{2}}\begin{pmatrix}\phi^+ \\ \phi^0\end{pmatrix}, \tag{2.21}$$

where $+$, 0 represent the electric charge of each complex component.

Then define a Lagrangean which is invariant under $SU(2)_L \times U(1)_Y$ transformation as

$$\mathcal{L}_{scalar} = |D_\mu \phi|^2 - \left(|\phi|^2 - \frac{\mu^2}{2\lambda}\right)^2 \quad \lambda > 0, \tag{2.22}$$

$$D_\mu = \partial_\mu + igW_\mu \cdot \frac{\tau}{2} + ig'B_\mu \cdot \frac{Y}{2}, \tag{2.23}$$

At high energy, μ^2 is considered to be positive. When temperature decreases μ^2 become negative, this lead to the existence of an infinite set of degenerate vacuum state. Define vacuum expected value of ϕ as

$$\langle \phi \rangle = \sqrt{\frac{1}{2}} \begin{pmatrix} \langle \phi^+ \rangle \\ \langle \phi^0 \rangle \end{pmatrix}, \tag{2.24}$$

where

$$\langle \phi^+ \rangle^2 + \langle \phi^0 \rangle^2 = \frac{-\mu^2}{2\lambda}. \tag{2.25}$$

A choice of the the actual vacuum state among them violates the $SU(2)_L \times U(1)_Y$ symmetry. This is called spontaneous symmetry breaking. However, $U(1)_{EM}$ symmetry still remains after the spontaneous symmetry breaking. Thus the vacuum state is required to be invariant under $U(1)_{EM}$ transformation

$$\langle e^{iQ\theta(x)}\phi \rangle = \langle \phi \rangle. \tag{2.26}$$

This means the operator Q annihilates the vacuum as

$$Q\langle \phi \rangle = \left(T_3 + \frac{Y}{2}\right)\langle \phi \rangle = \begin{pmatrix} 1 & 0 \\ 0 & 0 \end{pmatrix} \sqrt{\frac{1}{2}} \begin{pmatrix} \langle \phi^+ \rangle \\ \langle \phi^0 \rangle \end{pmatrix} = \langle \phi^+ \rangle = 0. \tag{2.27}$$

Hence the vacuum state is selected as

$$\langle \phi \rangle = \phi = \sqrt{\frac{1}{2}} \begin{pmatrix} 0 \\ v \end{pmatrix}, \tag{2.28}$$

where

$$\langle \phi \rangle = \frac{v}{\sqrt{2}}, \quad v = \sqrt{-\frac{\mu^2}{\lambda}}. \tag{2.29}$$

The Higgs doublet can be written using v as

$$\phi = e^{i\tau_i\theta^i(x)/v} \sqrt{\frac{1}{2}} \begin{pmatrix} 0 \\ v + h(x) \end{pmatrix}. \tag{2.30}$$

The three fields $\theta_i(x)$ (i = 1, 2, 3) are interpreted as massless Nambu-Goldstone bosons. Because of the existence of the $SU(2)_L$ invariance, these Nambu-Goldstone bosons disappear after fixing the gauge as

$$\phi' = e^{-i\tau_i\theta^i(x)/v}\phi = \sqrt{\frac{1}{2}} \begin{pmatrix} 0 \\ v + h(x) \end{pmatrix}, \tag{2.31}$$

$h(x)$ corresponds to a physical particle with spin = 0. This particle is called SM Higgs boson.

Then the $\mathcal{L}_{scalar}$ becomes

$$
\begin{aligned}
\mathcal{L}_{scalar} &= \frac{1}{2}\partial_\mu h\partial^\mu h + \mu^2 h^2 + \\
&\quad \frac{g^2 v^2}{4}W^+W^- + \frac{\sqrt{g^2+g'^2}}{8}v^2 Z_\mu Z^\mu + \\
&\quad \frac{g^2 vh}{4}W^+W^- + \frac{\sqrt{g^2+g'^2}}{8}vh Z_\mu Z^\mu + O(h^2).
\end{aligned}
\tag{2.32}
$$

The first term is the kinetic term of the SM Higgs, the term from second to fourth are the mass terms of Higgs (m_H), W (m_W) and Z (m_Z) bosons, respectively

$$
\begin{aligned}
m_H &= \sqrt{-2\mu^2}. \tag{2.33}\\
m_W &= gv/2. \tag{2.34}\\
m_Z &= \sqrt{g^2+g'^2}v/2. \tag{2.35}
\end{aligned}
$$

The vacuum expectation value is calculated as $v = (\sqrt{2}G_F)^{1/2} \sim 246$ GeV. All the vacuum expectation value, masses of Higgs, W and Z-bosons exist at the energy scale of order of $O(100)$ GeV. This energy scale is called the electroweak (EW) energy scale.

The fifth and sixth terms in Eq.(2.32) are the interaction between Higgs and W, Z-bosons.

Decay of the Weak Bosons

W-boson   W-bosons are generated and decay only through the interaction with two fermions which make up a left-hand isospin doublet. The coupling of the W-boson to the left-handed doublet is expressed in the first term in Eq (2.15). The tree level Feynman diagram of the $W \to ff$ (f : fermion) vertex is depicted in Figure **2.1**.

(a)
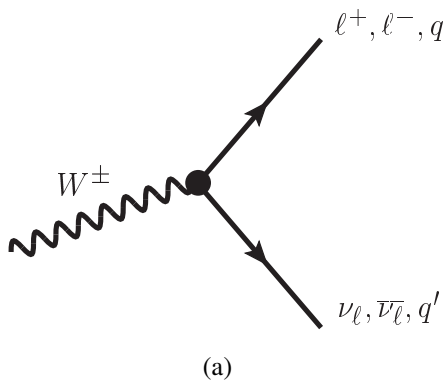
Figure 2.1: Tree level Feynmann diagram of the $W \to ff$ vertex.

Actual possible pairs to which W-bosons can decay are listed in Table **2.2** [37] as well as calculated partial decay widths and branching ratios assuming $\alpha_S(m_Z) = 0.1200$. Top quark is heavier than W-boson, so decay to a state with top quark is prohibited. Decays to quark states

which contains quarks in different generations like (u, s) is realized through an off-diagonal element of the CKM Matrix.

The decay width of the W-boson to leptons is written in Eq (2.36) where the assumption that lepton mass is negligible is made.

$$
\begin{aligned}
\Gamma(W^\pm \to l^\pm \nu) &= \frac{g^2 m_W}{48\pi} \\
&= \frac{G_F m_W^3}{6\sqrt{2}\pi} \\
&\sim 226.31 \pm 0.07 \text{ MeV.}
\end{aligned} \tag{2.36}
$$

Also the decay width to quarks can be written as

$$
\begin{aligned}
\Gamma(W^\pm \to q_i \bar{q}_j) &= N_c |V_{ij}|^2 \Gamma_l \\
&= C \frac{G_F m_W^3}{2\sqrt{2}\pi} |V_{ij}|^2 \\
&\sim (706.18 \pm 0.22) |V_{ij}| \text{ MeV,}
\end{aligned} \tag{2.37}
$$

where N_c (=3) is the color factor and V_{ij} is the corresponding CKM-Matrix element. C is a correction for QCD effect which is written as

$$
\begin{aligned}
C &= 1 + \frac{\alpha_S(m_W)}{\pi} + 1.409 \left(\frac{\alpha_S(m_W)}{\pi}\right)^2 - 12.77 \left(\frac{\alpha_S(m_W)}{\pi}\right)^3 - 80.0 \left(\frac{\alpha_S(m_W)}{\pi}\right)^4 \\
&\sim 1.0394 \pm 0.0005.
\end{aligned} \tag{2.38}
$$
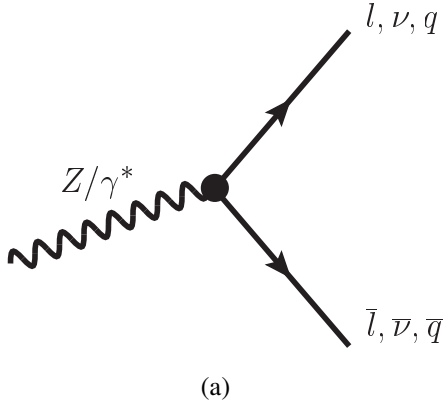
The branching ratio of $W \to \mu\nu$ channel is of the most interest in this study. The current world average of measured value is [36]

$$
BR(W \to \mu\nu) = 10.57 \pm 0.15\%. \tag{2.39}
$$

Decay mode	Partial width (MeV)	Branching ratio (%)
$e\bar{\nu}_e$	226.3 ± 0.1	10.82 ± 0.00
$\mu\bar{\nu}_\mu$	226.3 ± 0.1	10.82 ± 0.00
$\tau\bar{\nu}_\tau$	226.3 ± 0.1	10.82 ± 0.00
$\bar{u}d$	670.3 ± 0.3	32.06 ± 0.00
$\bar{c}s$	669.2 ± 0.3	32.00 ± 0.00
$\bar{u}s$	35.8 ± 0.1	1.71 ± 0.02
$\bar{c}d$	35.8 ± 0.1	1.71 ± 0.02
$\bar{c}b$	1.2 ± 0.0	0.06 ± 0.02
$\bar{u}b$	0.0	0.00
$\Gamma_W = \mathbf{2091 \pm 1}$ **MeV**		

Table 2.2: Calculated decay width and branching ratio of W-boson ($\alpha_S(m_Z) = 0.1200$) [36].

***Z*-boson**   *Z*-boson can couple to both left-handed and right-handed fermions thus the possible decay modes are different from those of *W*-boson. Most significantly, *Z*-boson can decay into oppositely charged lepton pairs such as $Z \rightarrow \mu\mu$. Due to the large mass of *Z*-boson, the leptons have high transverse momenta which result in a clear experimental signal. The tree level Feynman diagram of the $Z \rightarrow ff$ vertex is depicted in Figure **2.2**.

(a)

Figure 2.2: Tree level Feynmann diagram of the $Z \rightarrow \mu\mu$ vertex.

Actual possible pairs to which *Z*-bosons can decay are listed in Table **2.3** as well as calculated partial decay width and branching ratio assuming $\alpha_S(m_Z) = 0.1200$. Top quark is heavier than *Z*-boson, so decay to a top pair is prohibited.

The decay width of $Z \rightarrow ff$ channel is written as

$$\begin{aligned}
\Gamma(Z \rightarrow \overline{f}f) &= \frac{N_{cf} g_z^2 m_z}{48\pi}(1 - 4x)^{\frac{1}{2}}[v_f^2(1 + 2x) + a_f^2(1 - 4x)] \\
&= \frac{N_{cf} G_N m_z^3}{6\sqrt{2}\pi}(1 - 4x)^{\frac{1}{2}}[v_f^2(1 + 2x) + a_f^2(1 - 4x)].
\end{aligned} \tag{2.40}$$

where $x = m^2/m_Z^2$ (m is fermion mass). N_{cf} accounts for the QCD corrections such as in Eq.(2.38) as well as QED corrections [36].

Here, ignoring mass of quarks and leptons, one obtains

$$\begin{aligned}
\Gamma(Z \rightarrow \overline{f}f) &= 2(v_f^2 + a_f^2)N_{cf}\Gamma_\nu, \\
\Gamma_\nu &= \frac{G_N m_Z^3}{12\sqrt{2}\pi}.
\end{aligned} \tag{2.41}$$

Γ_ν is a decay width for a certain type of a neutrino pair. The branching ratio of $Z \rightarrow \mu\mu$ channel is of the most interest in this study. The current world average of measured value is [36],

$$BR(Z \rightarrow \mu\mu) = 3.366 \pm 0.007\%. \tag{2.42}$$

Decay mode	v_f	a_f	Γ_f/Γ_v	Part. width (MeV)	BR (%)
v	$\dfrac{1}{2}$	$\dfrac{1}{2}$	1	167.21 ± 0.02	6.700 ± 0.001
e, μ, τ	$-\dfrac{1}{2} + 2x_W$	$-\dfrac{1}{2}$	$\dfrac{1}{2}[1 + (1 - 4x_W)^2]$	83.99 ± 0.01	3.365 ± 0.001
u, c	$\dfrac{1}{2} - \dfrac{4}{3}x_W$	$\dfrac{1}{2}$	$\dfrac{N_{cf}}{2}[1 + (1 - \dfrac{8}{3}x_W)^2]$	300.20 ± 0.06	12.029 ± 0.003
d, s	$-\dfrac{1}{2} + \dfrac{2}{3}x_W$	$-\dfrac{1}{2}$	$\dfrac{N_{cf}}{2}[1 + (1 - \dfrac{4}{3}x_W)^2]$	382.98 ± 0.06	15.346 ± 0.003
b	"	"	" + mass correction	375.94 ± 0.04	15.064 ± 0.002
			$\Gamma_Z = \mathbf{24957 \pm 0.3\ MeV}$		

Table 2.3: Calculated decay width and branching ratio of Z-boson after QCD and QED corrections assuming $\alpha_S(m_Z) = 0.1200$ [36]. x_W represents the $\sin^2\theta_W$.

2.1.3   The Quantum Chromodynamics and the Parton Model

Proton is not an elemental particle like electron and muon but a composite particle made of quarks and gluons, the gauge bosons of strong interaction. In proton, interactions like gluon radiation ($q \rightarrow qg$), gluon pair-production ($g \rightarrow gg$) and gluon splitting ($g \rightarrow q\bar{q}$) take place continuously. In this section, an overview of the QCD, which describes the interaction between quarks and gluons is given followed by a description of the parton model which is crucial to understand the weak boson production process in proton-proton collisions.

In QCD, quarks are treated as three dimensional base vector in color SU(3) (SU(3)$_C$) space. Gluons, which are belonging to one of the eight states which correspond to SU(3)$_C$ octet, intermediate strong interactions through exchanges of color charge. The QCD Lagrangean density is written as [38, 39]

$$\mathcal{L} = -\frac{1}{4}F^A_{\mu\nu}F^{A\mu\nu} + \Sigma_i(i\gamma^\mu D_\mu - m_i)q_i + L_{gauge-fixing}, \tag{2.43}$$

$$F_{A\mu\nu} = \partial_\mu A^A_\nu - \partial_\nu A^A_\mu - \alpha_S f^{ABC}A^B_\mu A^C_\nu, \tag{2.44}$$

$$D_\mu = \partial_\mu - i\alpha_S A^A_\mu T^A, \tag{2.45}$$

where A^A_μ is the gluon field (A, B, C passes $1 \sim 8$, these correspond to the degrees of freedom for gluons), α_S is the strong coupling constant and f^{ABC} is the structure constant of SU(3). T^A is the generator of SU(3), satisfying

$$[T^A, T^B] = if^{ABC}T^C. \tag{2.46}$$

Note that due to the non-Abelian nature of the SU(3) as shown in Eq (2.46), Eq (2.44) has the self-coupling term of the gluons.

Color Confinement

Despite the vast efforts, no experiments found any evidence for the existence of free quark. All the composite particles made of quarks such as meson ($q\bar{q}$) and baryon (qqq) belong to a color single state. This fact is understood by assuming the existence of a potential between non color singlet quarks which increases with the distance between them. Thus colored quark state can't exist alone. This phenomenon is called color confinement. The potential between quarks play a role of a string which ties two quarks. Pulling out this string, the stored energy eventually reaches the point where it is energetically more favorable to create a $q\bar{q}$ pair (meson) with two short strings rather than long one. Since the transverse momenta involved in creating mesons are of order of a few times mass of the meson only, one obtains two collimated jets of hadrons traveling in opposite directions following the momentum vectors of the original quarks. For the massless nature of the gluon, strong interaction intrinsically reaches over long distance. However the nature is hidden by the confinement.

Asymptotic Freedom

In the classical electromagnetism, it is known that electric fields in a matter is transformed due to di-electric polarization and eventually results in a change of substantive charge density of

$\rho \rightarrow \rho/\epsilon$ (ϵ: electric permittivity > 1). This effect is called shielding. Likewise, the vacuum is filled with charges due to the effect of pair-production and if there is an electric field, could be polarized. This means that the coupling constant of the interactions between two charges differs depending on the distance between them. In the electromagnetism, the coupling constant decreases as the distance between charges increases.

In QCD, since the field is non-Abelian, a gluon can also give rise to a gluon pair. Thus, opposite to the classical electromagnetism case, an anti-shielding effect is produced. The coupling constant of the QCD, $\alpha_S(q^2)$, hence has the form in Leading-Logarithm Approximation (LLA).

$$
\begin{aligned}
\alpha_S(q^2) &= \frac{\alpha_S(q_0^2)}{1 + B\alpha_S(q_0^2)\ln(q^2/q_0^2)} \\
&= \frac{1}{B\ln(q^2/\Lambda^2)},
\end{aligned}
\tag{2.47}
$$

where $B = (33 - 2f)/12\pi$. Such shifting of the coupling constant depending on q^2 is called running of the coupling constant. Provided the number of quark flavors $f \leq 16$, it follows that $\alpha_S(q^2)$ decreases as q^2 increases. This decrease of α_S at large q^2 was first discussed in detail by Gross and Wilczek [40] and Politzer [41]. Eq (2.47) shows that at asymptotically large q^2 we have $\alpha_S(q^2) \rightarrow 0$, that is, the quarks behave as if free. This phenomenon is called asymptotic freedom which guarantee the quasi-free behavior of strongly interacting particles expected in the parton model described in the next section.

The Parton Model

The invariant variables in deep inelastic lepton-nucleon scattering is defined as depicted in Figure **2.3**.
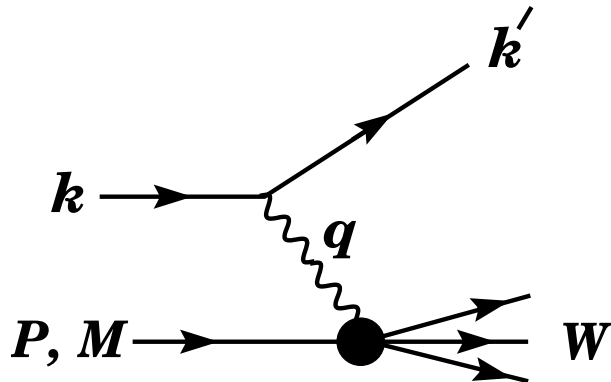
Figure 2.3: The kinematics in deep inelastic lepton-nucleon scattering.

$$
\nu = \frac{q \cdot P}{M} = E - E',
\tag{2.48}
$$

$$
Q^2 = -q^2 = 2(EE' - \mathbf{k} \cdot \mathbf{k}') - m_l^2 - m_{l'}^2,
\tag{2.49}
$$

$$x = \frac{Q^2}{2M\nu}. \tag{2.50}$$

Where E and E' represents the incident and emergent energy of the lepton in the rest frame of the nucleus. Thus ν means energy loss of the lepton. q is called momentum transfer written as $q = k - k'$. Q is the invariant mass or energy scale of the interaction and M is the mass of the nucleon. Ignoring the lepton mass, this can be written as

$$Q^2 \sim 4EE'\sin^2(\theta/2), \tag{2.51}$$

where θ is the scattering angle of the lepton against the beam axis in the rest frame of the nucleus.

If the scattering angle is small enough, Q^2 can be approximated as $Q^2 \sim (E\theta)^2 \sim (p_T)^2$, and invariant mass of the nucleus system scattered by the lepton is written as

$$W^2 = (P + q)^2 = M^2 + 2M\nu - Q^2. \tag{2.52}$$

Hence all the kinematics of the system can be described by $x(\nu)$ and Q^2. Figure **2.4** (a) shows a form factors measured by the ZEUS experiment [42] in e-p deep inelastic scattering. One can see the x and Q^2 dependence of the form factor is well described by the NLO theoretical calculation.

Figure **2.4** (b) shows the parton distribution functions (PDFs) of proton measured at ZEUS experiment ($Q^2 = 10\text{GeV}^2$). The horizontal axis is the x and the vertical axis is the form factor of partons. Valence u and d quarks have its peak at $x \sim 0.2$ and the ratio between peak height is $2:1$ which reflects the structure of proton. If partons were free point-like particle, the peak would be at $1/3$. This shift is due to the QCD effects. The half of the total momentum of proton is carried by the gluons.

Factorization and PDF Evolution

The cross section of partons in proton-proton collisions are expressed as in Eq (2.53).

$$\sigma(AB \to cX) = K \sum_{i,j} \int dx_a dx_b [f_i(x_a, Q^2) f_j(x_b, Q^2)] \widehat{\sigma_0}(ab \to cX), \tag{2.53}$$

where $f_i(x, Q^2)$ represents a PDF in a proton for a parton flavor i with energy fraction of x at interaction energy scale of Q^2. a, b are indices for partons and $\widehat{\sigma_0}(ab \to cX)$ is the production cross section of $c + X$ (anything) from parton a and b. The K factor is the higher order QCD correction which scales the cross section without changing shapes of PDFs.

Eq (2.53) means the cross section can be factorized into a soft part and a hard part. This is called factorization. The contributions on soft part are coming from exchanges of the soft gluons whereas hard part corresponds to the core parton interaction. Factorization is guaranteed by the fact that hard process undergo in a very short time compared to soft process. Hence PDFs do not change during the hard process. Consequently, all the contributions from soft processes are folded into PDFs. It is proved that factorization is possible in any order of the perturbation [43].
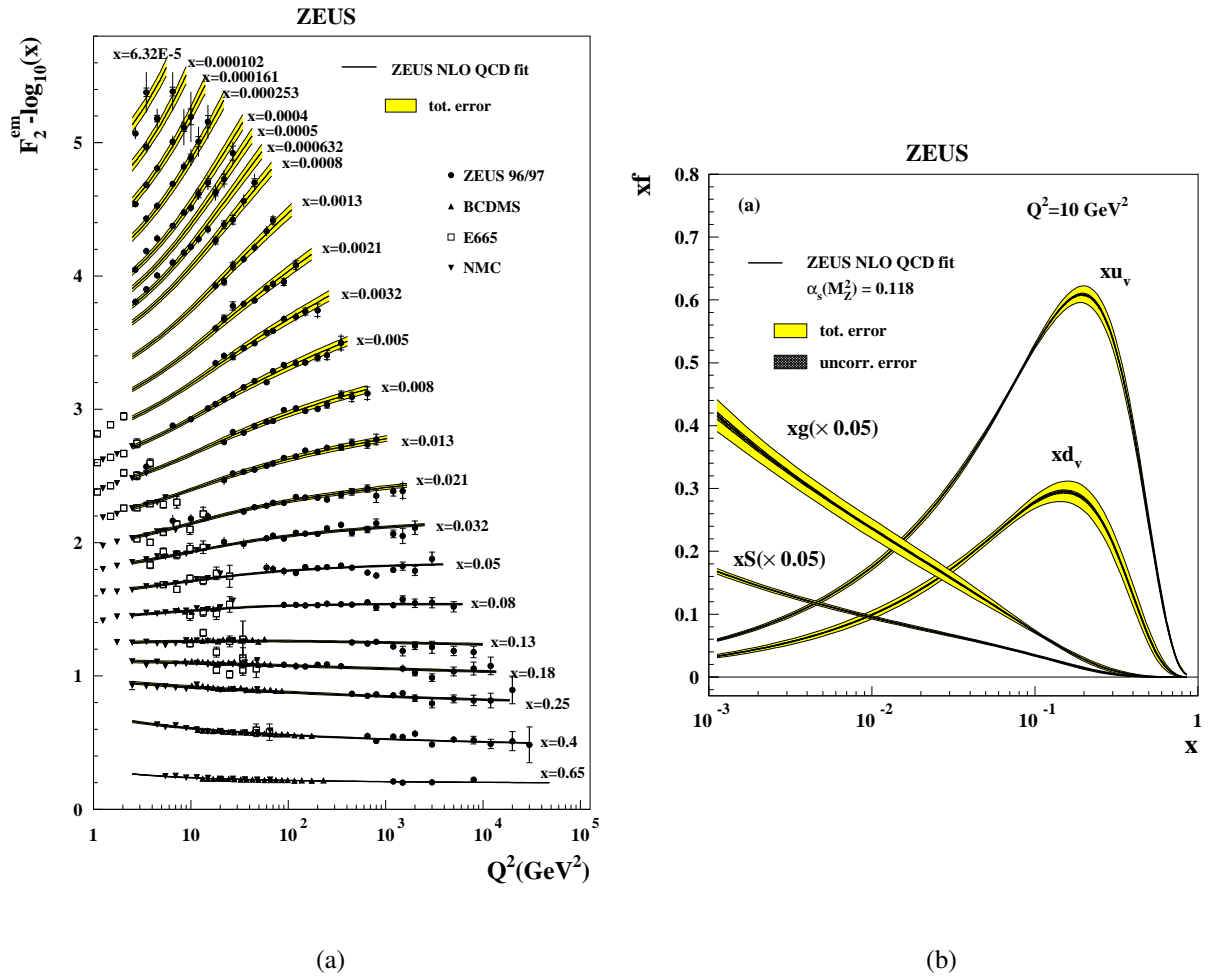
Figure 2.4: (a) The form factor measured by the ZEUS experiment at the HERA accelerator, DESY. (b) The parton distribution function measured at the ZEUS experiment ($Q^2 = 10\text{GeV}^2$) [42] .

Once a PDF is determined at certain $Q^2 = Q_0^2$, one can determine PDFs at any different Q^2 by the QCD calculation. The equation which describes the Q^2 evolution of PDFs is called DGLAP evolution function [18–20].

In the PDF evolution, x dependence is usually parametrized at a fixed scale Q_0^2 as

- valence quarks: $f(x, Q_0^2) \sim x^\lambda (1 - x)^\eta$

- sea quarks: $f(x, Q_0^2) \sim x^{-\lambda} (1 - x)^\eta$

Also different parametrization and number of free parameters are used in different studies. The prediction is not so accurate in terms of the x dependence of PDFs which has non-perturbative origin. Hence the in-situ constraint should be provided from experiments to improve the calculation which results in the reduction of the uncertainties on physics results.

2.2   Precise Electroweak Measurements at the LHC
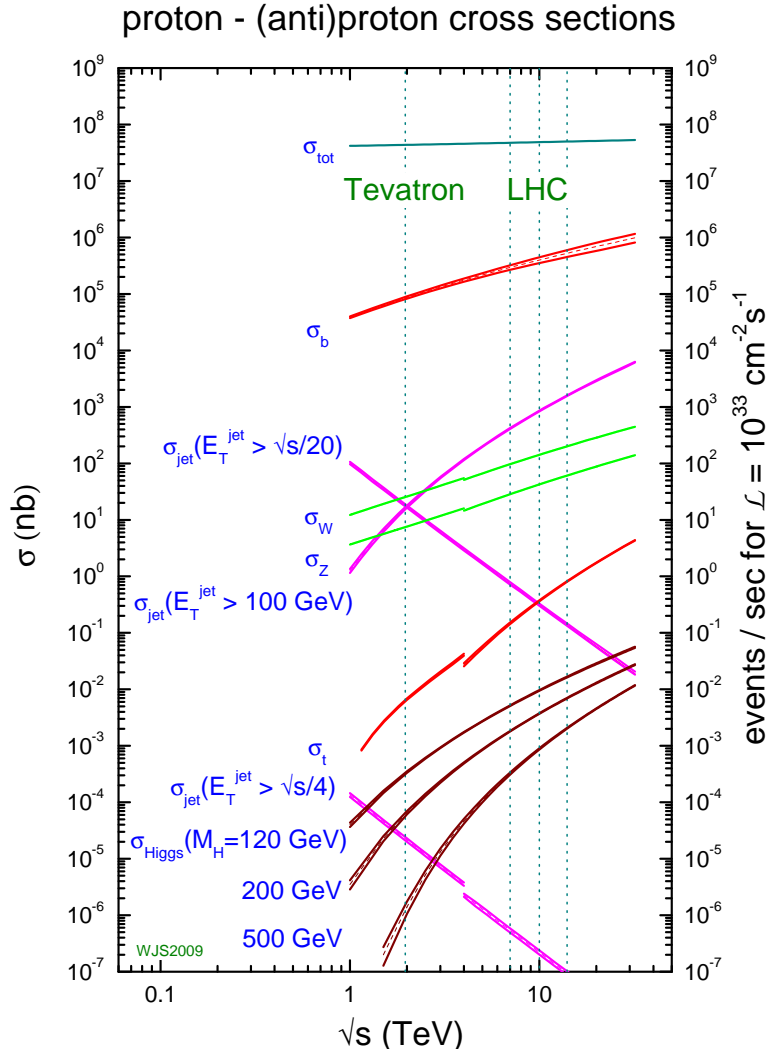
Figure 2.5: Cross sections for physics processes in proton-(anti)proton collisions calculated by MSTW team [44].

In the proton-proton collisions at the LHC, W and Z-bosons are abundantly produced. Figure **2.5** shows the calculated cross section of major physics processes. At the current operation with $\sqrt{s} = 7$ TeV, the cross section for W (Z) boson is about 100 (30) nb. Assuming an integrated luminosity of 10 fb^{-1}, the total number of generated bosons reaches 100 (30) $\times 10^6$.

For this plenty of weak bosons, precise measurement on electroweak properties make up one of the major objectives in the LHC physics program. A representative electroweak property is the mass of W-boson (m_W). As mentioned in chapter 1, along with precisely measured top quark mass, this leads to an indirect constraint on the lower limit for the SM Higgs mass, and properties of SUSY particles.

In the following subsections, first, experimental methods for m_W measurement is described. For the accurate m_W determination, following three items are essential,

1. detailed understanding and extensive calibration of the detector

2. accurate determination on the PDFs especially at EW energy scale

3. precise knowledge on the initial parton kinematics

All of them can be achieved through the measurement using $Z \rightarrow \ell\ell$ process as a control sample where complete kinematics in the final state can be reconstructed and clear experimental signal (two high-p_T leptons, see Figure **2.6**) lead to an easy event identification and background suppression. For the item 1, precisely measured Z-boson mass and width result in an in depth understanding of the detector performances such as detection efficiencies, momentum resolutions and scales. Actual measurements using $Z \rightarrow \mu\mu$ events are presented in chapter 9 and onwards. A measurement of Z-boson rapidity distribution put a constraint on the PDFs at EW energy scale. An overview of the measurement is presented in section 2.2.2. Also the measurement of Z-boson p_T distribution gives precise understanding of the initial parton kinematics. Section 2.2.3 is devoted for the description of the measurement.
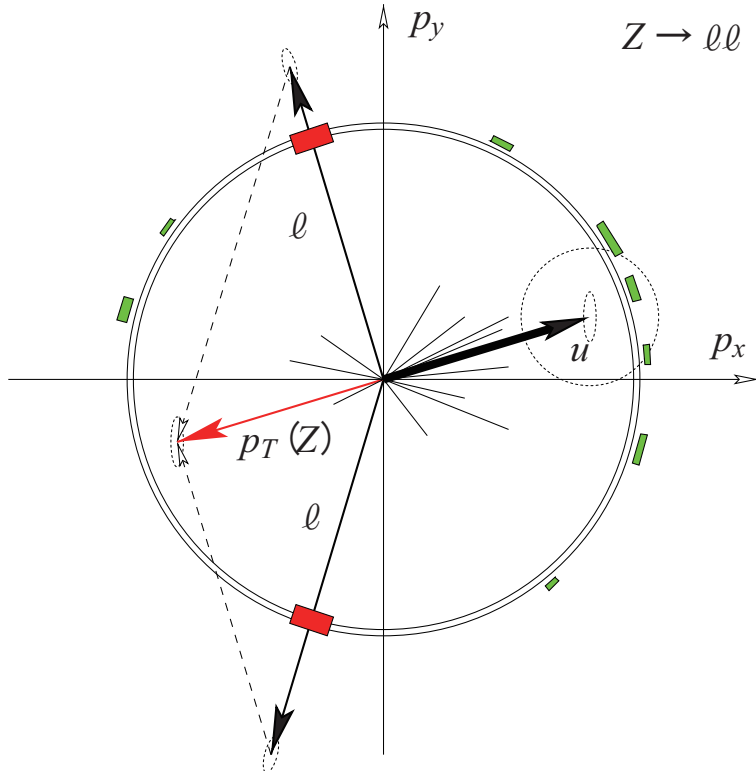
Figure 2.6: A transverse view of $Z \rightarrow \mu\mu$ event [45]. u represents the combined transverse momentum of the recoil.

2.2.1   *W*-boson Mass Measurement
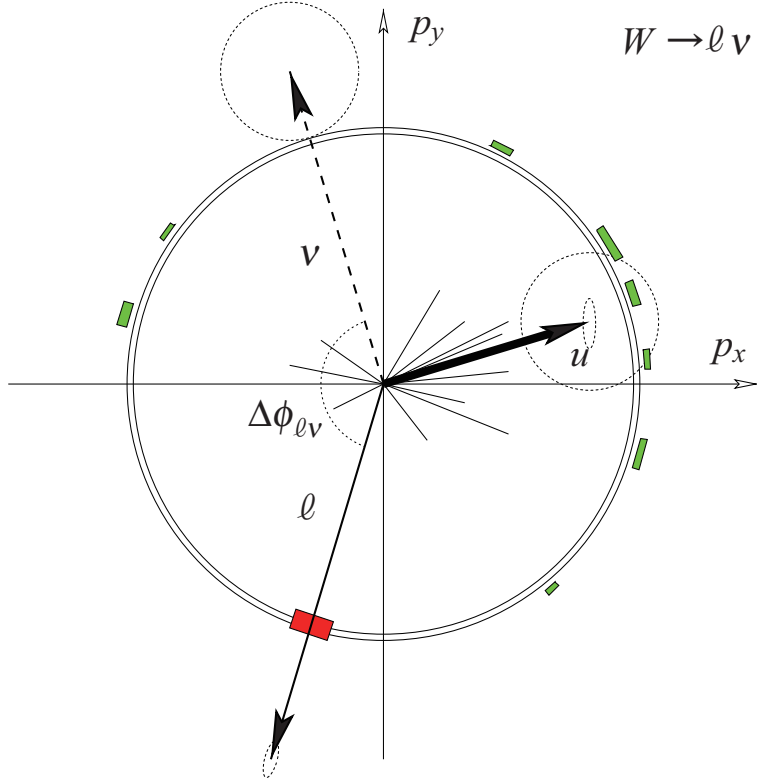
Figure 2.7: A transverse view of $W \rightarrow \mu\nu$ event [45]. u represents the combined transverse momentum of the recoil.

Figure **2.7** shows a scheme of $W \rightarrow \mu\nu$ event topology in $x - y$ plane (for the definition of the coordinates, see chapter 4). The presence of a neutrino is detected by a momentum imbalance in final states. However, due to the presence of the beam-pipe, detectors is not perfectly hermetic in the longitudinal direction. Hence only a momentum imbalance in the transverse direction (missing E_T: E_T^{miss}) is used for analyses. Consequently, the complete kinematics can not be reconstructed in final states. Hence the invariant mass can not be used to determine the m_W and one should use other variables sensitive to the m_W. In collider experiments, the m_W is determined thorough the following three variables.

- The transverse momentum of charged lepton: p_T^ℓ

- The transverse momentum of neutrino: $p_T^\nu = E_T^{\text{miss}}$

- The transverse mass of W: $M_T = \sqrt{2p_T^\ell p_T^\mu (1 - \cos(\phi^\ell - \phi^\nu))}$

The differential cross section of W-boson in terms of $p_T^{\ell(\nu)}$ and M_T is written as follows

$$\frac{d\sigma}{dp_T^{\ell(\nu)}} \propto \frac{\left(1 - 2p_T^{\ell(\nu)2}/\sqrt{\hat{s}}\right)}{\sqrt{1 - 4p_T^{\ell(\nu)2}/\sqrt{\hat{s}}}}, \tag{2.54}$$

$$\frac{d\sigma}{dM_T} \propto \frac{1}{(\widehat{s} - m_W^2)^2 + m_W^2 \Gamma_W^2} \frac{\left(2 - M_T^2/\sqrt{\widehat{s}}\right)}{\sqrt{1 - M_T^2/\sqrt{\widehat{s}}}}, \tag{2.55}$$

where $\sqrt{\widehat{s}}$ is the effective center-of-mass energy of the parton interaction for W-boson production. As one can see, $d\sigma/dp_T$ and $d\sigma/dM_T$ have a singularities at $p_T = \sqrt{\widehat{s}}/2$ and $M_T = \sqrt{\widehat{s}}$, respectively. The singularities arise as sharp peaks in the distribution of each differential cross section. This is called Jacobian peak, and m_W can be determined by fitting Jacobian peaks. Figure **2.8** shows calculation results of Eq.(2.54) and Eq.(2.55).

(a)   (b)
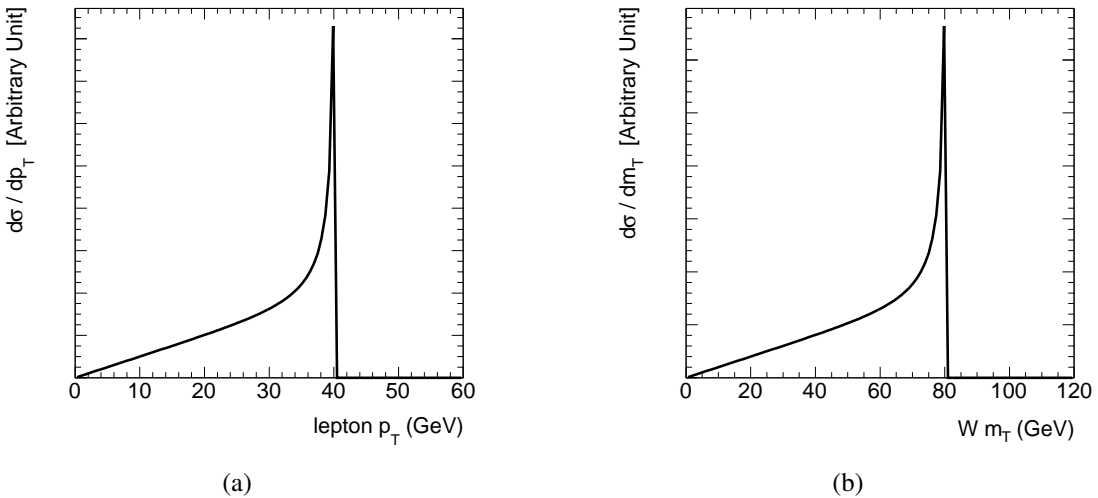
Figure 2.8: Calculated results of (a) $d\sigma/dp_T$ and (b) $d\sigma/dM_T$ showing sharp Jacobian peaks.

In actual experiments, Jacobian peaks are smeared by both detector resolution and W-boson p_T.

- p_T^l has a good detector resolution, but is affected by the limited knowledge of the initial p_T of W-boson

- E_T^{miss} has a bad detector resolution and also is affected by the limited knowledge of the initial p_T of W-boson

- M_T is robust against the limited knowledge of W-boson p_T but is affected by poorly reconstructed E_T^{miss}

Also momentum scale uncertainty, imperfect hadronic recoil modeling bring a large uncertainty. The LHC experiments are aiming at the m_W resolution of about 10 MeV [46]. In such a precision, the uncertainty on the PDFs also affects.

Figure **2.9** shows the combined W-boson mass results measured by the experiments at the LEP (ALEPH, DELPHI, L3, OPAL) [47] and the Tevatron (CDF, D0) [48] collider. Note that, in the LEP results, the measurement uses $WW \rightarrow l\nu qq$ and $WW \rightarrow qqqq$ events through cross section measurement just above the pair production threshold and direct invariant mass reconstruction. The current world average is $m_W = 80.399 \pm 0.023$ GeV [36], and the LHC experiments are aiming to surpass this accuracy.
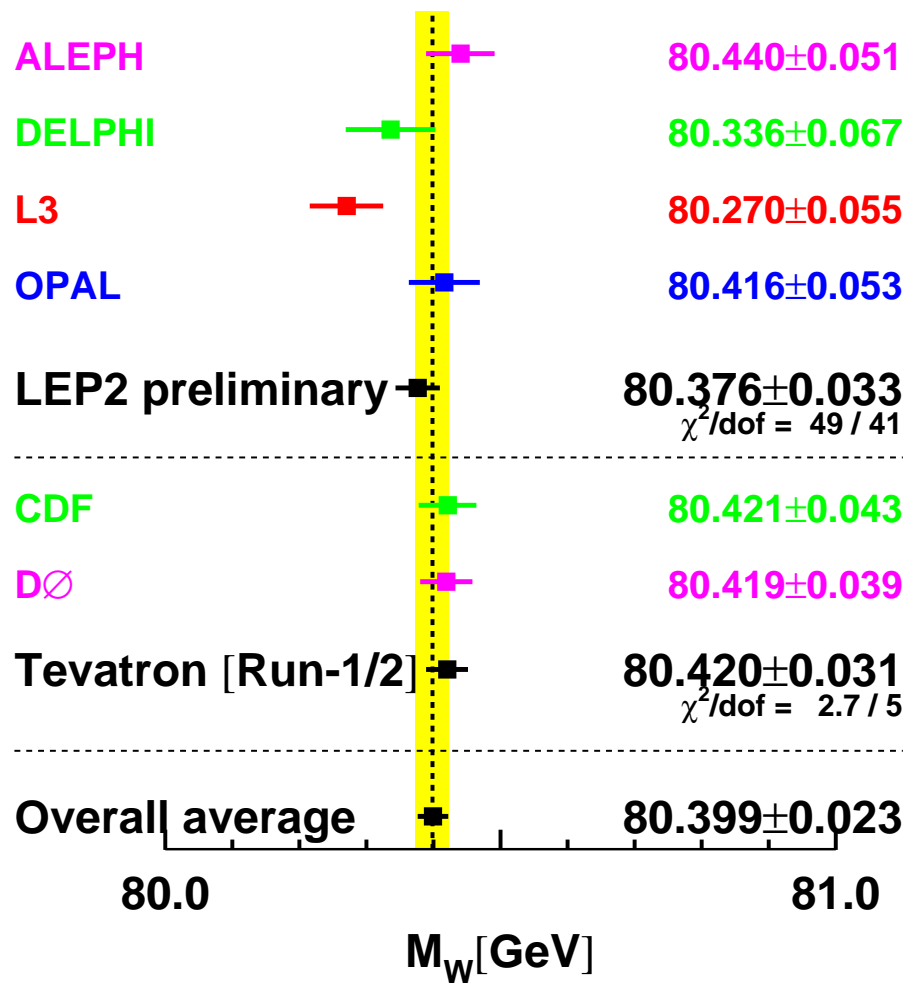
Figure 2.9: Measurement of the *W*-boson mass by the LEP and the Tevatron experiments [36].

2.2.2 Z-boson Rapidity Measurement
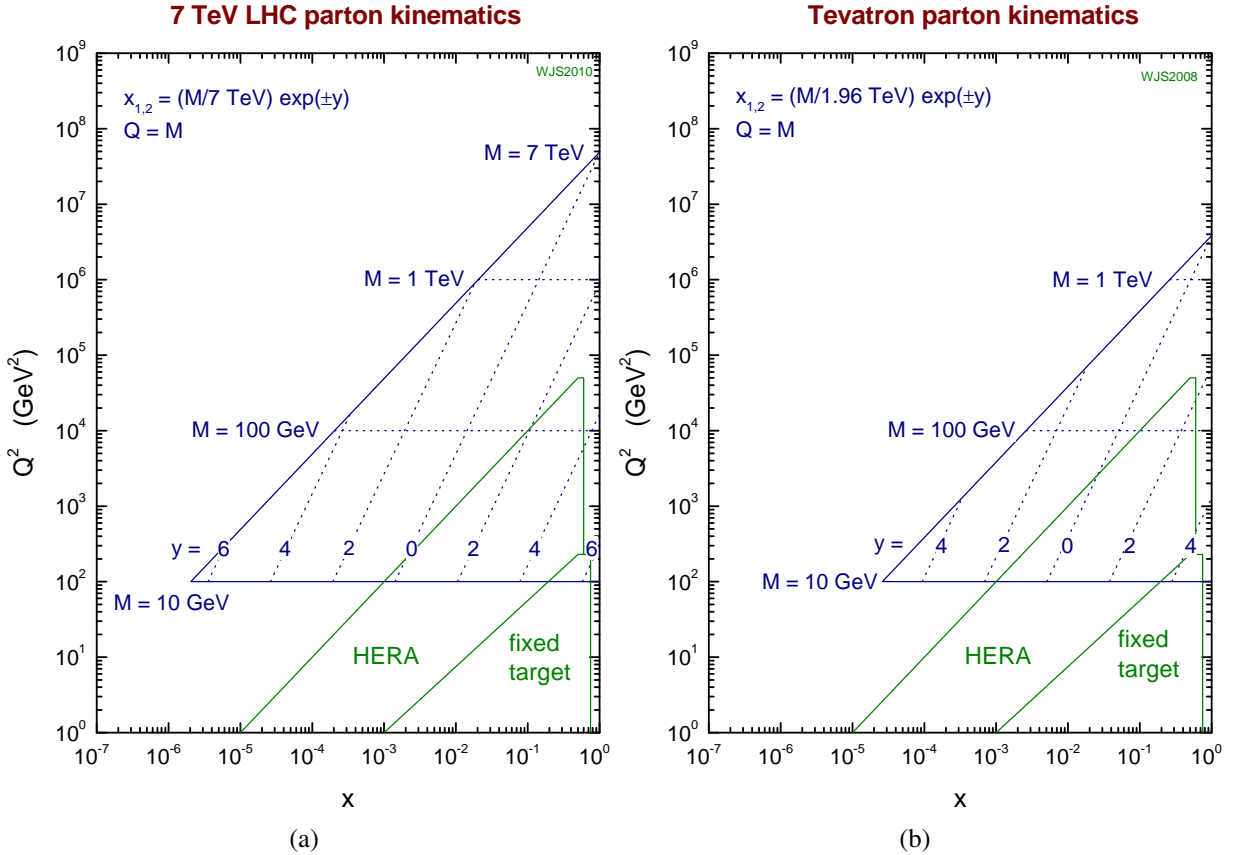
Figure 2.10: The allowed parton kinematic region for the LHC and the Tevatron [44].

Figure **2.10** shows a comparison of the allowed parton kinematic region between the LHC and the Tevatron. As one can see, the LHC has overwhelming reach in terms of measurable center-of-mass energy region of partons never achieved by any experiments. Hence the in-situ constraints on PDFs in such energy region is essential for all physics analysis performed in the region at the LHC.

A convenient variable to put a constraint on PDFs is rapidity (y) of heavy particles. For the W mass measurement, $Z \to \ell\ell$ is the most suitable. Assuming that a heavy particle is produced in proton-proton collisions with $\sqrt{s} = 2E$ from partons with energy fraction of x_1 and x_2 respectively. The kinematics for the two parton system is

$$
\begin{aligned}
\widehat{p_1} &= (x_1 E; 0, 0, x_1 E), \\
\widehat{p_2} &= (x_2 E; 0, 0, -x_2 E),
\end{aligned}
\tag{2.56}
$$

$$
\begin{aligned}
\widehat{E} &= (x_1 + x_2) E, \\
\widehat{p_z} &= (x_1 - x_2) E, \\
\widehat{s} &= \widehat{E}^2 - \widehat{p_z}^2 = x_1 x_2 s,
\end{aligned}
\tag{2.57}
$$

where $\widehat{p}_1$ and $\widehat{p}_2$ are four vectors of partons, $\widehat{E}$ is the effective interaction energy and $\widehat{p}_z$ is the momentum of the system in the z-direction. Then the rapidity of the heavy particle is expressed as

$$y = \frac{1}{2}\ln\frac{\widehat{E} + \widehat{p}_z}{\widehat{E} - \widehat{p}_z} = \frac{1}{2}\ln\frac{x_1}{x_2}. \tag{2.58}$$

If one can measure the rapidity distribution of a heavy particle with mass M, the PDF with x_1 and x_2 at $Q^2 = M^2$ is determined as

$$
\begin{aligned}
x_1 &= \frac{M}{\sqrt{s}}e^{+y}, \\
x_2 &= \frac{M}{\sqrt{s}}e^{-y}.
\end{aligned}
\tag{2.59}
$$

Assuming the y acceptance of the ATLAS detector in rapidity as $|y| < 2.5$, Figure **2.10** shows the fractional energy of partons at the EW scale ($\sim m_Z, m_W$) spans down to $x = 10^{-4}$. In this region, W/Z-bosons are produced from sea quarks and such sea quarks are produced from gluon splittings in higher energy region. Hence, one can conclude that the Z-boson rapidity measurement at the LHC is important for its sensitivity to,

- sea quark distribution in low-x region at EW energy scale

- gluon PDFs in higher energy region.

The experiments at the Tevatron have measured the distribution. However they are looking different energy fraction region of $0.05 < x < 0.3$ and the LHC explores five hundreds times smaller x region at the EW energy scale.

2.2.3 Z-boson Transverse Momentum Measurement

The primary objective for the Z-boson p_T measurement, in the context of the needed process for the precision W mass measurement, is the in-situ determination of the parton kinematics in the EW energy scale. This affects not only on the distribution shapes of M_T, p_T and E_T^{miss} but also on the production cross section itself through the acceptance calculation. Figure **2.6** and **2.7** show very similar topologies of $W \to \ell\nu$ and $Z \to \ell\ell$ boson events. Indeed, the p_T of W is very correlated that of Z-boson. Moreover, the hadronic recoil in $W \to \ell\nu$ events can be calibrated in $Z \to \mu\mu$ events.

Another important objective of the Z-boson p_T measurement is the test of non-perturbative QCD. As already implied in the Eq.(2.56), Z-bosons do not have initial p_T in leading order calculation. The non-zero p_T is theoretically only possible when the gluon radiation prior to the parton interaction into account.

At high p_T (> 30 GeV), the radiation of single (or double) parton dominates the cross section and fixed order perturbative QCD calculations should yield reliable results. At low p_T the emission of multiple soft gluons is important and calculations in fixed order perturbative QCD diverges. Formalisms are developed to predict the experimental Z-boson p_T distribution in the context of soft gluon emission resummation technique [49–51]. The shape of the distribution is predicted qualitatively but the full result depends on a limited number of free parameters which need to be extracted from measurement.

2.3   The Motivation and Significance of This Study

An Inclusive cross sections measurement of W and Z-boson is presented in this thesis. The motivation of this measurement is to perform the first test of the validity of our understanding on the production mechanism of W and Z-boson in proton-proton collisions at the center-of the energy of 7 TeV.

The production cross section of W and Z-boson at hadron colliders was measured previously by the UA1 [52] and UA2 [53] experiments at $\sqrt{s} = 0.63$ TeV at the CERN Sp$\bar{\text{p}}$S and by the CDF [54–56] and D0 [57, 58] experiments at the Fermilab Tevatron colliders. Both colliders utilizes proton-antiproton collisions. Most recently, the RHIC collider experiments [59, 60] have reported the first observation of W production in proton-proton collision at $\sqrt{s} = 0.5$ GeV.

The world highest energy of the LHC will result in an exploration in the new parton kinematic region at EW energy scale where low-x sea quarks driven by gluons through their splitting dominates. This lead to new constraints on the PDFs and stringent test of the QCD.

In this thesis, the total production cross sections measurement of W and Z-boson is performed in the $W \rightarrow \mu\nu$ and $Z \rightarrow \mu\mu$ processes. Through this measurement, selection criteria to extract W / Z events in each channel are established. Especially, the study on the $Z \rightarrow \mu\mu$ process leads to

- A detailed understanding of the detector performance with precise knowledge on the Z-boson mass and width

- In-situ determination of the PDF of 7 TeV protons through $d\sigma/dy^Z$ measurement

- A stringent test for the QCD predictions through $d\sigma/d\text{pt}^Z$ measurement

These constitute the first major step of the lasting program of the precise electroweak measurements, such as W-boson mass measurement, in the ATLAS. Furthermore, a precise understanding of PDF is essential in most of the measurement and searches which will be performed at the LHC.

Chapter 3

The Large Hadron Collider

The Large Hadron Collider (LHC), the proton-proton collider which achieved the highest center-of-mass energy ever, was built at the European Organization for Nuclear Research (CERN) in Geneva, Switzerland [61–65]. The LHC main ring is built in the tunnel with circumference of 26.7 km which was excavated at depth varying between 45 and 170 m [1]. The design center-of-mass energy is 14 TeV as well as the peak luminosity of 10^{34} cm^{-2}s^{-1}, both are the unprecedented performance never achieved by any other hadron colliders. The time spacing between proton bunches are designed to be 25 ns and about 23 events occur in a bunch crossing at the design peak luminosity.

The LHC has two general purpose experiments with high luminosity in proton-proton collisions, ATLAS [66] and CMS [67]. At the ±140 m away from the ATLAS interaction point (IP), the LHCf [68] is held to study forward production of neutral particles in proton-proton collisions at extremely low angles. There are also two low luminosity experiments namely LHCb [69] for B-physics aiming at peak luminosity of 10^{32} cm^{-2}s^{-1} and TOTEM [70] for the detection of protons from elastic scattering as small angles aiming at a peak luminosity of 2×10^{29} cm^{-2}s^{-1} with 156 bunches. The LHC is also capable to accelerate lead ion beams for heavy ion studies. There is one dedicated ion experiment, ALICE [71], aiming at a peak luminosity of 10^{27} cm^{-2}s^{-1} for nominal lead-lead ion operation.

The choice of the use of proton-proton collisions, not electron-positron or proton-anti-proton, was made for the following two advantages.

- To achieve a high center-of-mass energy: The accelerated particles lose their energy due to the synchrotron radiation as in the Eq (3.1),

$$\text{(energy loss)} = \frac{1}{6\pi\epsilon_0} \frac{e^2 c}{(mc^2)^4} \frac{E^4}{\rho^2}, \tag{3.1}$$

  where ϵ_0 is the permittivity of vacuum, e the electron charge, c the speed of light, m and E the mass and energy of the moving particle and ρ the bending radius. According to the equation, the energy loss heavily depends on the mass of the particle. Thus the LHC uses protons instead of electron-positron, and uses the world largest LEP tunnel which

---

[1]This tunnel was originally made for the Large Electron Position collider (LEP).

further suppresses the synchrotron radiation due to its large radius. The limitation on the acceleration for the LHC comes from the maximum magnetic field of the bending magnets. The field strength of the LHC dipole super-conducting magnet is 8.33 T.

- To achieve a high luminosity: Previous hadron colliders used proton-anti-proton collisions with a configuration which deploys a common vacuum and magnet system for both circulating beams. However, it is difficult to make anti-proton beam highly intense. Hence the LHC chose proton-proton collisions and developed a dedicated two-in-one design of dipole super-conducting magnets to deploy two separated beam pipes.

The LHC started proton-proton collisions on March 30, 2010 with the center-of-mass energy of 7 TeV and provided physics data until the end of October, 2010 then finished the scheduled operation of the year. The LHC achieved the peak luminosity of 10^{32} cm^{-2}s^{-1} which leads to sensitivities for many new physics in 2011.

3.1   The Injector Chain

The LHC injector chain consists of LINAC – Proton Synchrotron Booster (PSB) – Proton Synchrotron (PS) and Super Proton Synchrotron (SPS) as depicted in Figure **3.1** (PSB is indicated as BOOSTER in the figure).

At the beginning, hydrogen gas is injected into the duoplasmatron, a metal cylinder which dissociates hydrogen atoms and generates protons with kinetic energy of 90 keV. Then the protons are sent to a radio frequency quadrupole, QRF – an accelerating component that both speeds up and focuses the particles with RF field provided by four vanes. The spacing of the vanes bunches and accelerates the protons up to 750 keV. From the QRF, the particles are sent to the LINAC2 (a LINAC which is for the proton acceleration), a linear accelerator whose tank is a multi-chamber resonant cavity tuned to a specific frequency which creates potential differences in the cavities that accelerate the particle up to 50 MeV.

Protons cross the LINAC2 and reaches PSB, a circular accelerator with circumference of 157 m which consists of four identical rings mounted one above another. The beam line to the PSB from the LINAC2 is 80 m long. 20 quadrupole magnets focus the beam along the line and 2 bending and 8 steering magnets direct the beam. The PSB accelerates them to 1.4 GeV. Then protons are injected to the PS.

The PS is the circular accelerator with circumference of 628 m. Protons are accelerated to 25 GeV in it. The PS forms the 81 bunch packets of protons with 25 ns spacing for the LHC.

The SPS is the final link in the injector chain to the LHC with circumference of 7 km. Triplets of 81 bunches formed in the PS are injected to SPS. Three or four triplets are accelerated in the SPS to 450 GeV and finally transferred to the LHC.

Accelerator chain of CERN (operating or approved projects)
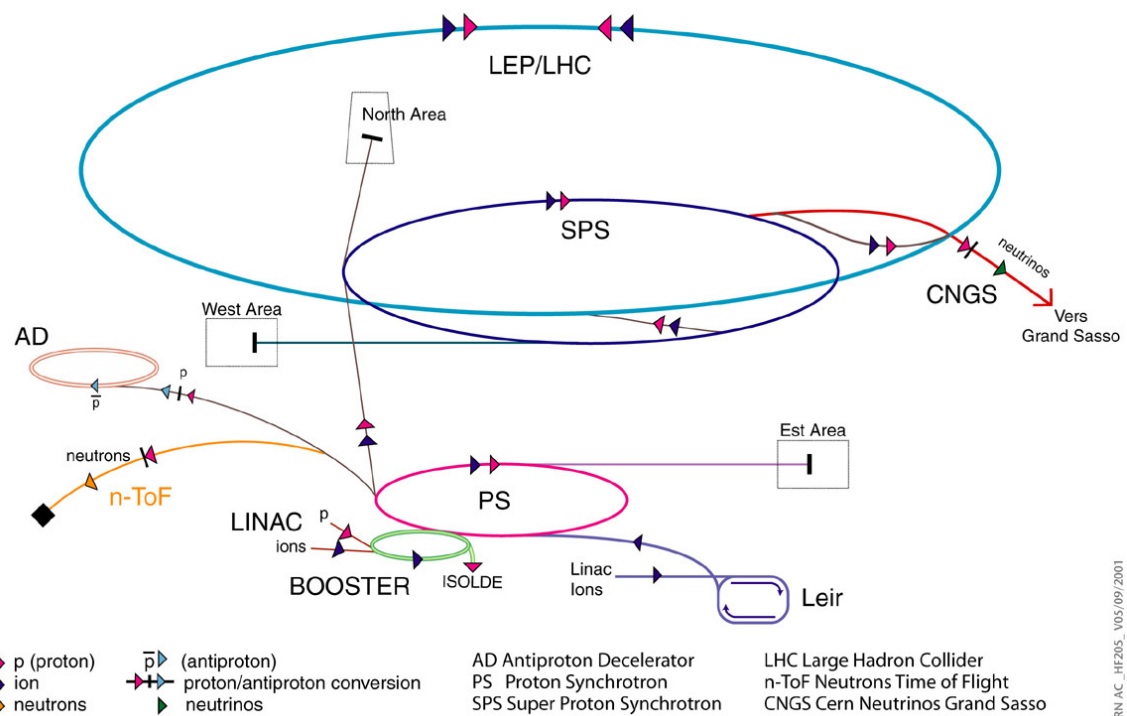
Figure 3.1: A schematic view of the LHC complex

3.2 The LHC Main Ring

The LHC main ring consists of eight arc sections and eight straight sections called insertions as depicted in Figure **3.2**. The length of each arc is 2.45 km and length of each insertion is 545 m.

Two proton beams are counter-rotate in separate beam pipes and collide at four out of eight insertions in which experiments are held at the IPs. The ATLAS detector is placed at point 1, CMS is at point 5. The ALICE and LHCb are located at point 2 and point 8 which also include the injection system for each beam. On upstream of each experiment, beam focusing systems which deploy three superconducting quadrupole magnets are located. Proton beams are designed to be focused into transverse radius of 16.7 μm at point 1 and 5, and 70.9 μm at point 2 and 8. At point 1 and 5, two proton beams collide vertically and at point 2 and 8, horizontally with the crossing angle of 142.5 μrad (point 1, 5), 150 μrad (point 2), 200 μrad (point 8), respectively.

The remaining insertions are equipped with a dedicated beam instrumentation each. Insertions at point 3 and point 7 have a collimation system to protect the LHC against unavoidable beam losses by performing beam cleaning. One of the most important facilities located in insertions is the RF cavities which are housed in point 4. The main role of the LHC cavities is to keep the 2808 proton bunches tightly bunched to ensure high luminosity at the IPs as well as delivering radio frequency power to the beams during acceleration. The LHC uses eight cavities per beam, each cavity is operated at 4.5 K of temperature and delivering 2 MV accelerating voltage at 400 MHz of frequency.

An arc is made of 23 arc cells. The configuration of a cell is illustrated in Figure **3.3**. Each cell is 106.9 m long and consists of two 53.45 m long half-cells each of which contains three 14.3 m long superconducting two-in-one dipole magnet. A schematic illustration of the standard cross section of dipole magnet is depicted in Figure **3.4**. Those dipoles produce magnetic fields of 8.33 T which bends the trajectory of protons to keep them along their orbit during acceleration. Besides dipoles, the LHC also deploys sextupole, octupole, and decapole magnets which are installed to correct for nonlinear movements due to magnetic field errors. The main LHC machine and proton beam parameters are summarized in Table.**3.1**.

The luminosity is describes by the machine parameters as

$$L = \frac{N^2 n_b f_r}{4\pi \sigma_x \sigma_y} F = \frac{N^2 n_b f_r \gamma}{4\pi \epsilon_n \beta^*} F, \tag{3.2}$$

where N is the number of protons in a bunch, n_b is the number of bunches stored in the Main Ring, f_r is the revolution frequency and $\sigma_{x,y}$ characterize the transverse beam profiles in the $x(y)$ direction. Also, ϵ_n is the normalized transverse beam emittance, the β^* is the beta function at the IP and the geometrical luminosity reduction factor F is expressed as

$$F = \frac{1}{\sqrt{1 + \frac{\theta_c^2 \sigma_z^2}{4\pi \sigma_x \sigma_y}}}, \tag{3.3}$$

with θ_c the full crossing angle at the IP and the σ_z the RMS bunch length.
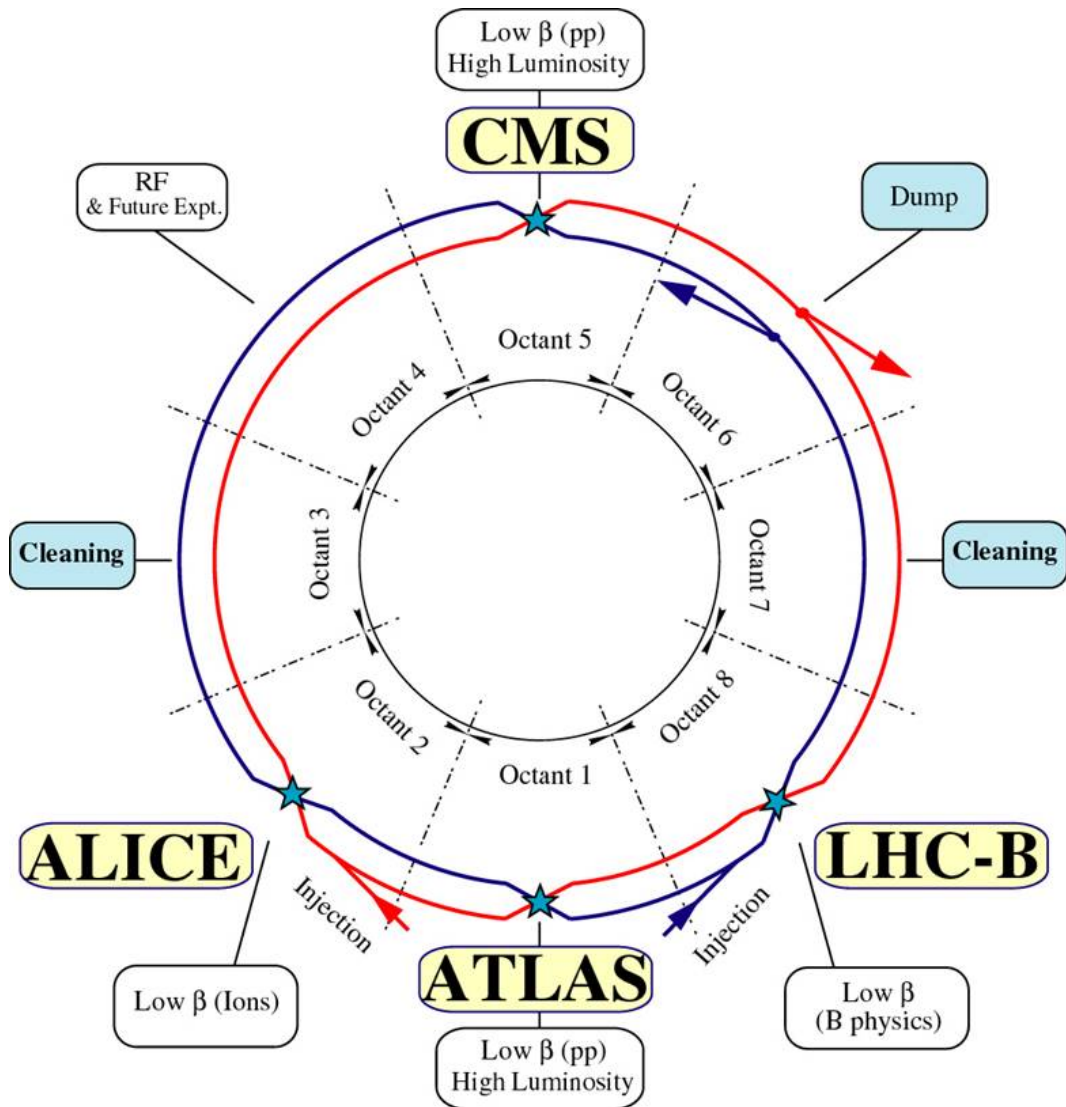
Figure 3.2: A schematic view of the LHC main ring.

MQT: trim quadrupole

MQS: skew trim quadrupole

MO: lattice octupole

MSCB: sextupole (skew sextupole) + orbit corrector

MCS: spool piece sextupole

MCDO: spool piece octupole + decapole
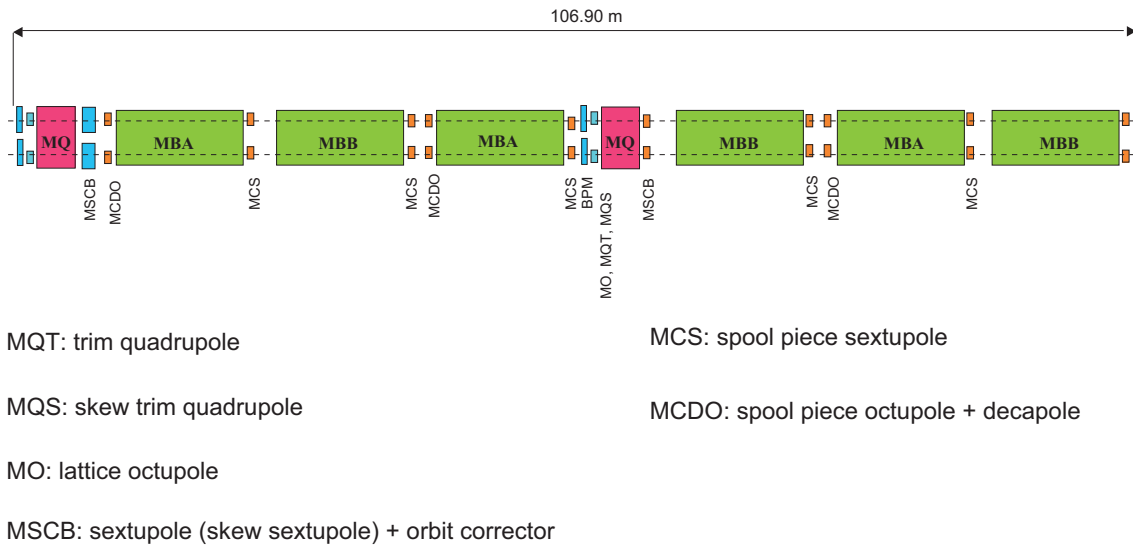
Figure 3.3: A schematic view of the LHC arc corrector magnets.
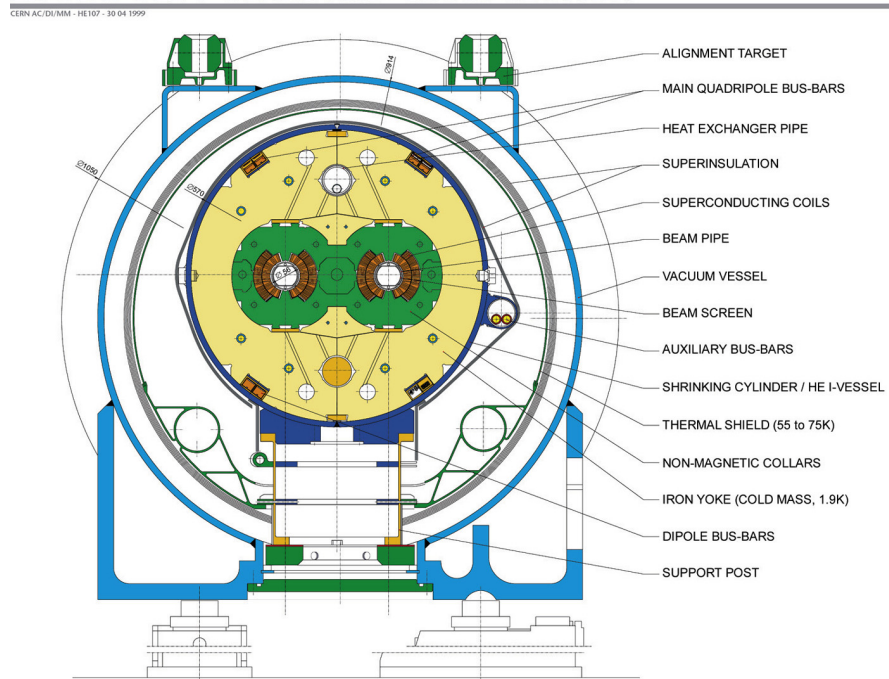
Figure 3.4: Standard cross section of the LHC two-in-one dipole magnet.

		Injection	Collision
Maximum proton energy	[GeV]	450	7000
Relativistic gamma		479.6	7461
Number of particles per bunch		1.15×10^{11}	
Number of bunches		2808	
Revolution frequency	Hz	11245.5	
Bunch spacing	ns	24.95	
Longitudinal emittance(4σ)		1.0	2.5
Transverse normalized emittance	μm rad	3.5	3.75
Circulating beam current	[A]	0.584	
Stored energy per beam	[MJ]	23.3	362
RMS bunch length	cm	11.24	7.55
RMS beam size at the IP1 and IP5	μm	375.2	16.7
RMS beam size at the IP2 and IP8	μm	279.6	70.9
Geometric luminosity reduction factor F		-	0.836
Peak luminosity in IP1 and IP5	cm^{-2}sec^{-1}	-	1.0×10^{34}
Peak luminosity per bunch crossing IP1 and IP5	cm^{-2}sec^{-1}	-	3.56×10^{30}
β^* at the IP1 and IP5	m	18	0.55
β^* at the IP2	m	10	0.5 for Pb / 10 for p
β^* at the IP8	m	10	$1.0 \leftrightarrow 50$
half crossing angle at the IP1 and IP5	μrad	± 160	± 142.5
half crossing angle at the IP2	μrad	± 240	± 150
half crossing angle at the IP8	μrad	± 300	± 200

Table 3.1: LHC design beam parameters [61].

Chapter 4

The ATLAS Detector
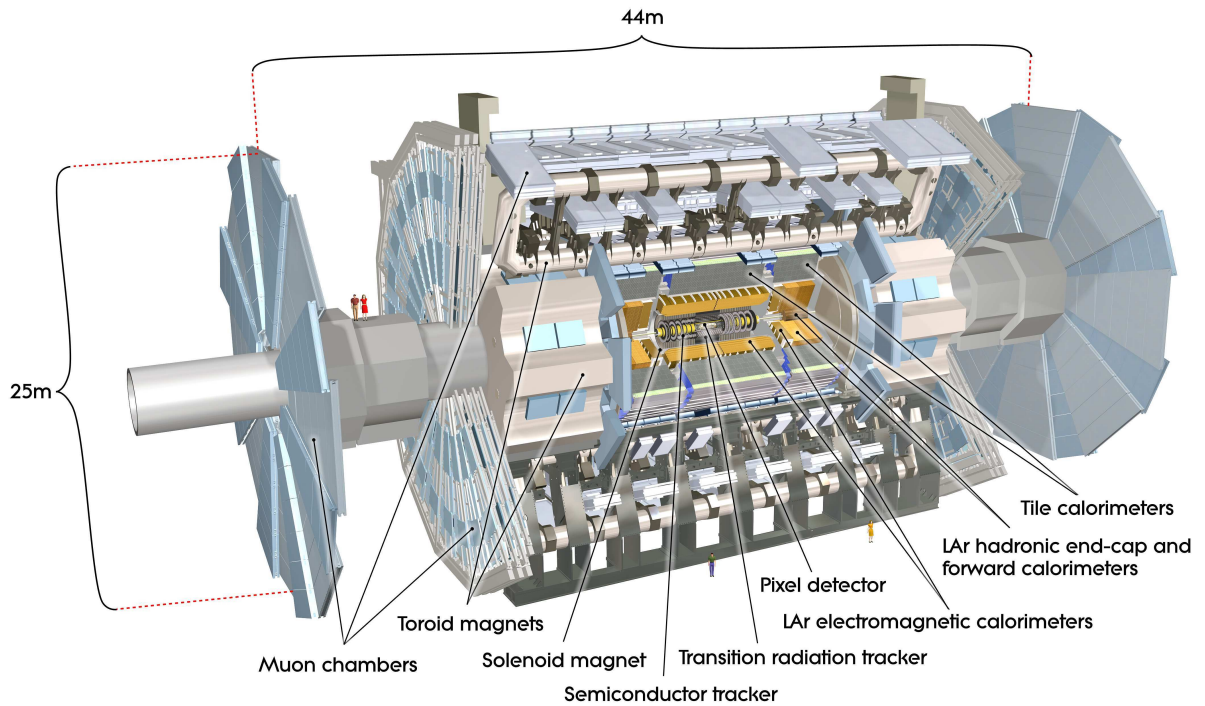
Figure 4.1: A cutaway view of the ATLAS detector.

The ATLAS detector [72], depicted in Figure **4.1**, is one of the two general purpose detectors placed at the LHC. The ATLAS detector is designed to exploit the full physics potential of the LHC such as the discovery of the Higgs boson and the SUSY, precise measurement of the electroweak and top quark physics and stringent test of QCD. The general requirements for the ATLAS detector performance are summarized as follows.

- Good muon identification and momentum measurement over a wide range of momenta with an accurate determination of the charge of high transverse momentum muons

- Good electromagnetic calorimetry with high resolutions on energy, position and direction of photon and electron within a wide geometric range

- Full coverage and good hermeticity of hadron calorimetry for accurate jet and missing transverse energy measurement

- Accurate tracking for charged particles with very good momentum resolution and tolerance against high radiation doses

- Robust and accurate vertex reconstruction

- Efficient triggering with as low as possible transverse momentum thresholds with sufficient background suppression to cover an acceptance for a wide range of the physics processes of interest

- Accurate luminosity determination

These performance will be accomplished by the detectors described in the following sections. The general concept of particle detections of the ATLAS detector is summarized in Figure **4.2**.
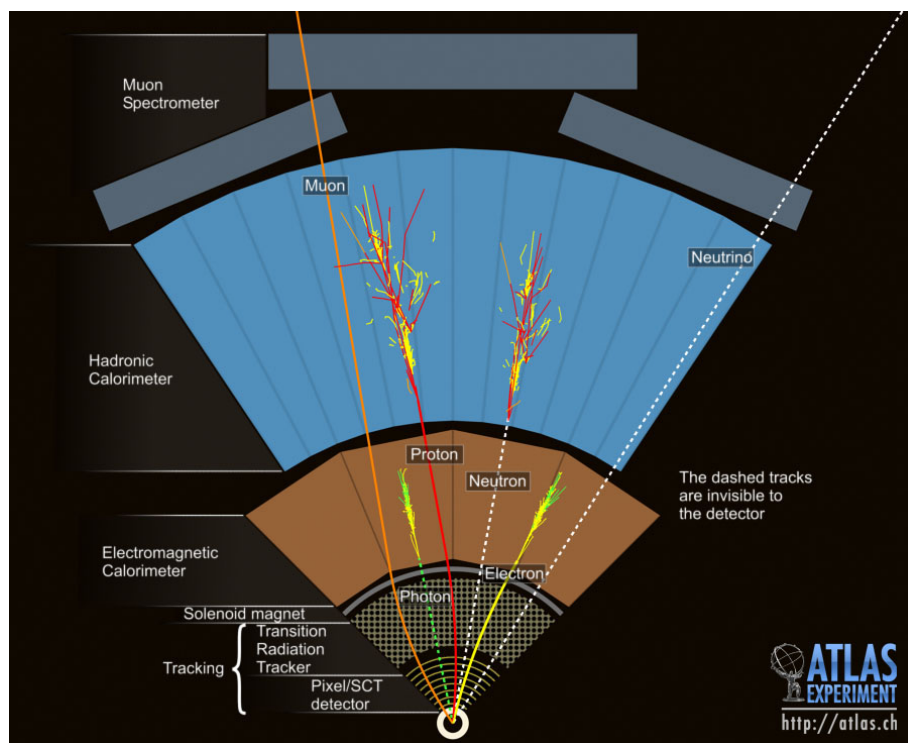
Figure 4.2: Particle detection in the ATLAS detector.

The ATLAS detector is designed in a mirror symmetric manner with respect to the interaction point. The dimensions of the detector are 25 m in height and 44 m in length. The overall weight of the detectors approximately 7000 tonnes.

The innermost layer is formed by several types of tracking detectors, which are referred to as the inner detector (ID). The ID is immersed in a 2 T homogeneous solenoidal field parallel to the beam axis. The measurements of charged particle momentum and interaction vertex reconstruction are performed. A more detailed description of the ID is given in section 4.2.

A liquid argon electromagnetic sampling calorimeters and scintillator-tile hadronic calorimeters are situated outside the solenoid. The calorimeters measure the energy deposits of neutral and charged particles. More details are described in section 4.3.

The outermost part is formed by the muon spectrometer with a dedicated air-core superconducting toroidal magnet system. A detailed description of the muon spectrometer is presented in section 4.4.

Additionally, several types of forward detectors are placed up-and-down stream of the ATLAS detector mainly to determine the luminosity. More details are explained in section 4.5.

The ATLAS Coordinate System

The origin of the ATLAS global Cartesian coordinate system is set as coincides with the nominal interaction point for the ATLAS experiment (IP). The z-axis is oriented parallel to the beam line in anti-clockwise direction looked from above, the x-axis is pointing in direction of the center of the LHC ring. The y-axis points upwards. The resulting coordinate system is right handed.

The side-A of the detector is defined as that with positive z and side-C is that with negative z. The azimuthal angle ϕ is the angle in the xy-plane originating from the x-axis and it increases clockwise if looking down the positive z-direction (side-A). The radial distance r in the transverse plane is defined as $\sqrt{x^2 + y^2}$. The polar angle θ is defined as the angle from the positive z-axis. The pseudo-rapidity is defined as $\eta = -\ln(\tan\theta/2)$. The transverse momentum is defined as the momentum in xy plane and denoted as p_T. Also, transverse energy is denoted as E_T and missing transverse energy is denoted as E_T^{miss}. The distance ΔR in the pseudorapidity-azimuthal angle space is defined as $\Delta R = \sqrt{\Delta\eta^2 + \Delta\phi^2}$. More details on the ATLAS coordinate system is presented in [73].

4.1   Magnet System
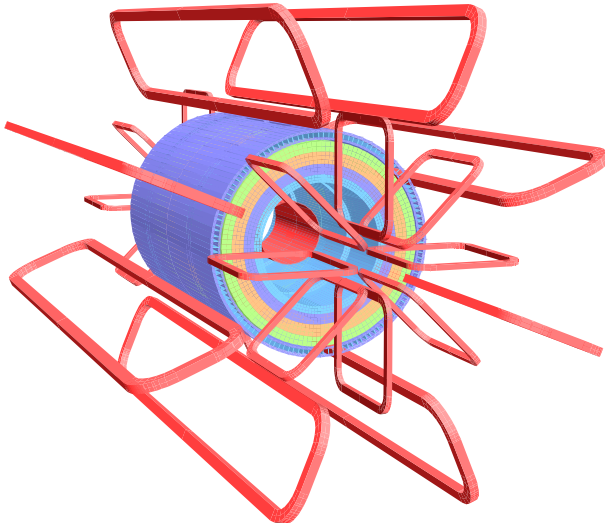
Figure 4.3: A cutaway view of the ATLAS superconducting magnetic system.

The ATLAS detector features a hybrid system of superconducting magnetic system with diameter of 22 m and length of 26 m with a stored energy of 1.6 GJ. The system consists of,

- A solenoid magnet for the p_T measurement in the inner detector

- Three toroid magnets for the p_T measurement in the muon spectrometer. One is placed in the barrel and the others are placed in each endcap region of the ATLAS detector

Figure **4.3** shows the general layout of the magnet system which provides the magnetic field over a volume of approximately 12,000 m^3. Eight barrel and two sets of eight endcap toroidal magnets are depicted as red windings. The cylinder with four layers indicate the hadronic calorimeter which plays a role of return york. The solenoid magnet is drawn as a red cylinder inside the hadronic calorimeter. Descriptions for each magnet system are described in the following subsections.

4.1.1   Solenoid Magnet

The solenoid magnet is situated between the inner detector and the calorimeter with inner and outer diameters of 2.46 m and 2.56 m and length of 5.8 m. The solenoid provides homogeneous axial magnetic field of 2 T at the nominal operation current of 7.730 kA and 4.5 K of temperature. To retain desired calorimeter performance, the material thickness in front of the calorimeter is reduced as low as possible. The solenoid assembly contribution is suppressed to about 0.66 radiation length at a nominal incidence. The single layer coil is wound with a high strength Al-stabilized NbTi conductor. The flux is returned by the steel of the ATLAS hadronic calorimeter and its girder structure.

4.1.2 Toroid Magnets

The barrel toroid provides the magnetic field in the cylindrical volume surrounding the calorimeters. It consists of eight coils. The overall size of the barrel toroid system is 25.3 m in length with inner and outer diameters of 9.4 m and 20.1 m. The field strength of the barrel toroid is about 0.5 T at the 20.5 kA operational current and 4.5 K temperature. The conductor and coil winding technology is based on winding a pure Al-stabilized Nb/Ti/Cu conductor into pancake-shape coils followed by vacuum impregnation.

The two endcap toroids form the magnetic field required in the endcap regions of the muon spectrometer. These magnets cover $1.65 < r < 10.7$ m with axial length of 5.0 m. The field strength of the endcap toroid is about 1.0 T in operation condition. The conductor and coil winding technology is basically the same as the one used for the barrel toroid.
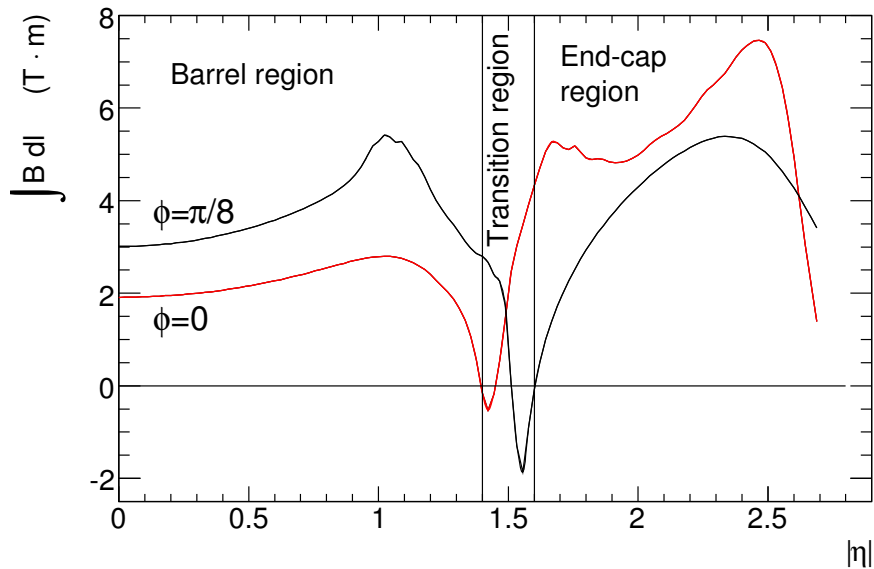
Figure 4.4: Bending power of the toroidal magnets in terms of η. The black and red lines show the bending power sliced at different ϕ positions in an octant.

Figure **4.4** shows computed toroidal field integrals as a function of $|\eta|$ from the innermost to the outermost muon spectrometer layer for infinite momentum tracks. The prediction at the barrel partially confirmed by the measurement within 0.2 % uncertainty. The field is not homogeneous especially in the barrel-endcap transition region of $1.3 < |\eta| < 1.65$. This inhomogeneities is caused by the superposition of the barrel and endcap fields.

4.2 Inner Detector
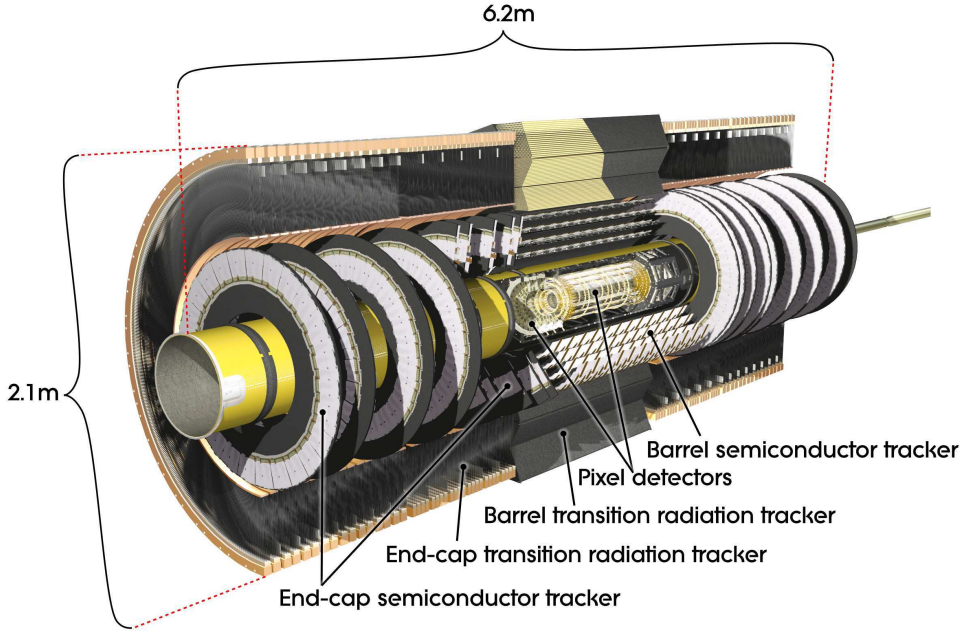
Figure 4.5: A cutaway view of the ATLAS Inner detector (ID).

The ATLAS inner detector [74], depicted in Figure **4.5**, consists of three detectors, namely Pixel Detector (PIXEL), Semiconductor Tracker (SCT) and Transition Radiation Tracker (TRT) from the closest to the beam pipe. The major performance requirements for the inner detector are as follows.

- A precise transverse momentum measurement for charged particles with

$$\frac{\sigma_{p_{\mathrm{T}}}}{p_{\mathrm{T}}} = 0.05 \times p_{\mathrm{T}} \text{ (GeV)} \ \oplus 1\% \ (|\eta| < 2.5). \tag{4.1}$$

- Vertex reconstruction capability which is accurate enough to observe secondary vertices (typically $\sigma = 15 \ \mu$m in the transverse plane).

As well as the electron identification over $|\eta| < 2.0$ within wide range of energies (from 0.5 GeV to 150 GeV).

The inner detector is situated as a cylindrical envelope of length ± 3512 mm and from the inner radius of 50.5 mm to outer radius of 1150 mm. The overall weight of the detectors approximately 4.5 tonnes. A detailed inner detector configuration is depicted in Figure **4.6**. Also the material distribution in the inner detector is summarized as a function of $|\eta|$ in Figure **4.7**.

All the three detectors are immersed in a 2 T solenoidal magnetic field. A particle originating from the interaction point crosses at least three PIXEL layers, four SCT layers and a
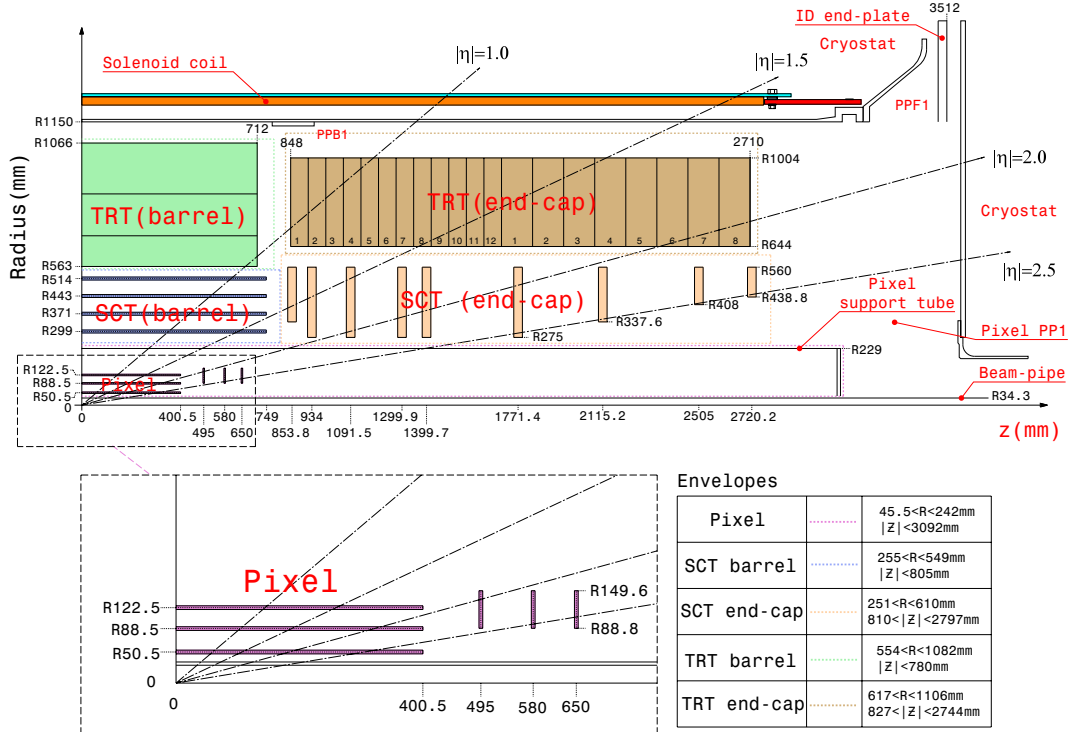
Figure 4.6: A detailed configuration of the ATLAS Inner Detectors.
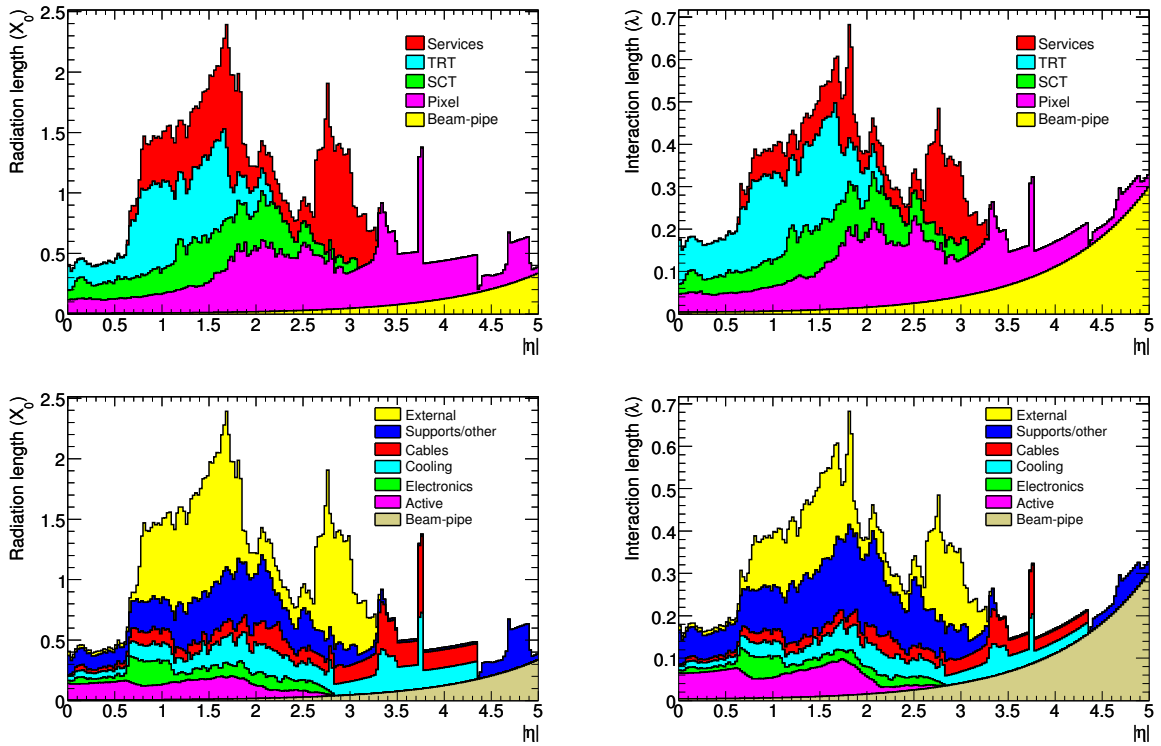
Figure 4.7: Material distribution in the inner detector as a function of $|\eta|$.

large number (typically 36) of TRT straws allowing a precise measurement of its momentum. To maintain an adequate noise performance after radiation damage, the PIXEL and the SCT is operated at low temperature of about $-10°C$. In contrast, the TRT is designed to operate at room temperature. Details of each detector are presented in the following subsections.

4.2.1 Pixel Detectors (PIXEL)
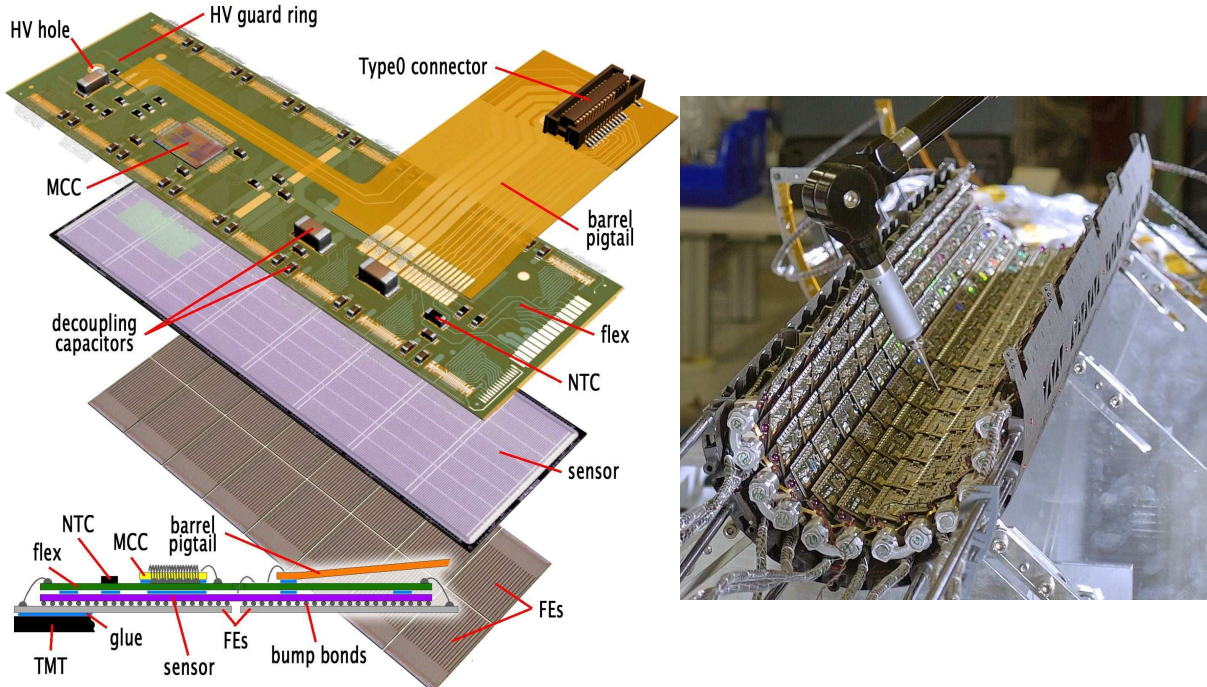
Figure 4.8: A schematic view and a picture of a PIXEL Modules.

The PIXEL is situated directly around the beam pipe which is inside the radius of 36 mm. The PIXEL has three layers and covers $|\eta| < 2.5$ as depicted in Figure **4.6**. The PIXEL deploys 1744 modules in total, in which 1456 modules are located in barrel and 288 are in endcap. A barrel stave is equipped with 13 PIXEL modules and staves are mounted on carbon-fiber structure as depicted in Figure **4.8**. An endcap sector is equipped with six PIXEL modules and eight sectors make up an endcap disk. Both two PIXEL endcaps consist of three identical disks.

The total system has 80 million pixel channels with 50 μm width in the $r - \phi$ direction and 400 μm length along the z-axis. Three measurements per track determine the impact parameter and are vital for the pattern recognition in the inner detector.

A schematic view and picture of a barrel PIXEL module is presented in Figure **4.8**. A PIXEL module consists the following components.

- 16 front-end electronics chips each has 2880 electronics channels

- the sensor tile of area 63.4×24.4 mm^2 and approximately 250 μm thick

- a flexible polyimide printed circuit board with module control chip

The channels and pixel sensor elements are connected with bump bonds (In or PbSn). A polyimide pig-tail with Cu lines and a connector (barrel) or a wire micro cable (endcap) are mounted on the top of them.

The typical resolution of a measurement of the PIXEL is 10 μm in the transverse plane and 115 μm in z (barrel) or R (endcap) direction.

4.2.2   Semiconductor Trackers (SCT)
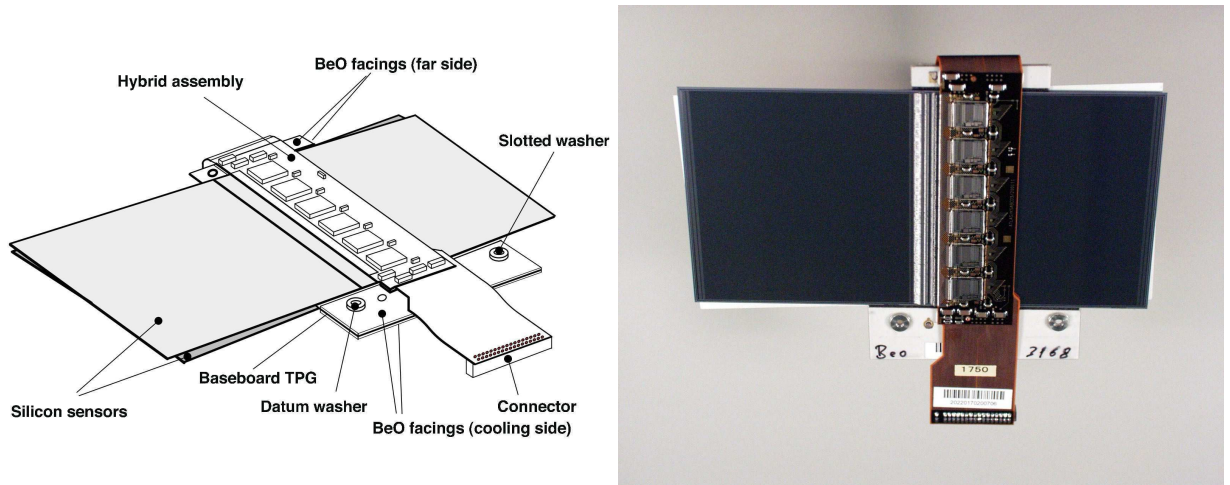
Figure 4.9: A schematic view and a picture of a SCT barrel modules.

The SCT consists of 4088 modules in total in which 2112 modules are forming four coaxial cylindrical layers. Remaining modules make up each endcap which contains nine disk layers as depicted in Figure **4.6**. The total coverage of the SCT is about 63 m^2 and this provides at least four precision position measurement over $|\eta| < 2.5$.

Figure **4.9** shows a schematic view and a picture of a barrel module. The specification of the endcap module is essentially similar to the barrel one. An SCT module consists of two layers of silicon strip sensors with a strip pitch of 80 μm providing accurate measurements in the $r - \phi$ plane. A layer consists of two sensors and a polyimide hybrid assembly with a carbon fiber substrate bridges these two sensors in a layer. The length of the layer is 128 mm (126 mm active with a 2 mm dead space) and contains 770 (768 active) channels. The two layers are rotated by ± 20 mrad each other. This stereo angle allows a modules to measure the position in z direction. Two layers are mounted on a 380 μm thick thermal pyrolitic graphite (TPG) based board which provides the thermal and mechanical structure.

The typical resolution of an SCT measurement is 17 μm in the transverse plane and 580 μm in z (barrel) and R (endcap) direction.

4.2.3   Transition Radiation Trackers (TRT)
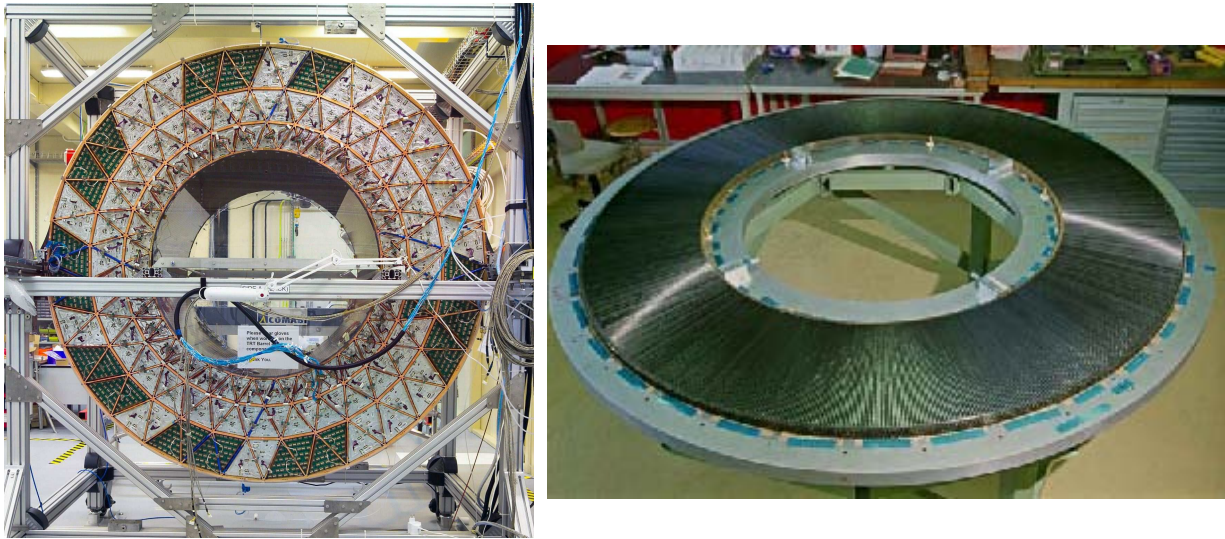
Figure 4.10: Pictures of the barrel and endcap TRT.

The TRT consists of a barrel ($|\eta| < 1.0$) and two endcaps ($1.0 < |\eta| < 2.0$) modules as depicted in Figure **4.6**. The barrel TRT contains up to 73 layers and straws are oriented parallel to the beam axis. The endcap TRT contains 160 layers and straws are pointing towards the beam axis. Any charged tracks with $p_T > 0.5$ GeV in the TRT fiducial volume transverse at least 36 straws except for the ones generated towards barrel-endcap transition region ($0.8 < |\eta| < 1.0$) where the number of straws decreases to a minimum of 22. Figure **4.10** shows pictures of a barrel and an endcap TRT module.

The basic element of the TRT is a polyimide straw tube with diameter of 4 mm, operating with a gas mixture of $Xe : CO_2 : O_2 = 70 : 27 : 3$ with $5 - 10$ mbar over pressure. The anode for TRT tube is 31 μm diameter gold plated tungsten (99.95 %). A gain of 2.5×10^4 is achieved at the operation voltage of -1530 V. The maximum electron collection time is about 48 ns under nominal operating condition. This leads to a typical p_T resolution per tube of 130 μm.

The Transition Radiation (TR) is used for the electron identification. In the TRT, 19 μm diameter polypropylene is used as the TR material. Since the TRT uses Xe based gas mixture, low energy TR photons are well absorbed and yield much larger signal than normal minimum ionizing charged particles. The distinction between TR and normal minimum ionizing signal is achieved on a straw-by-straw basis with separate double (low and high) thresholds scheme in the front-end electronics. Typically, seven to ten high-threshold TR hits are obtained for a electron with energy above 2.0 GeV.

4.3   Calorimetry
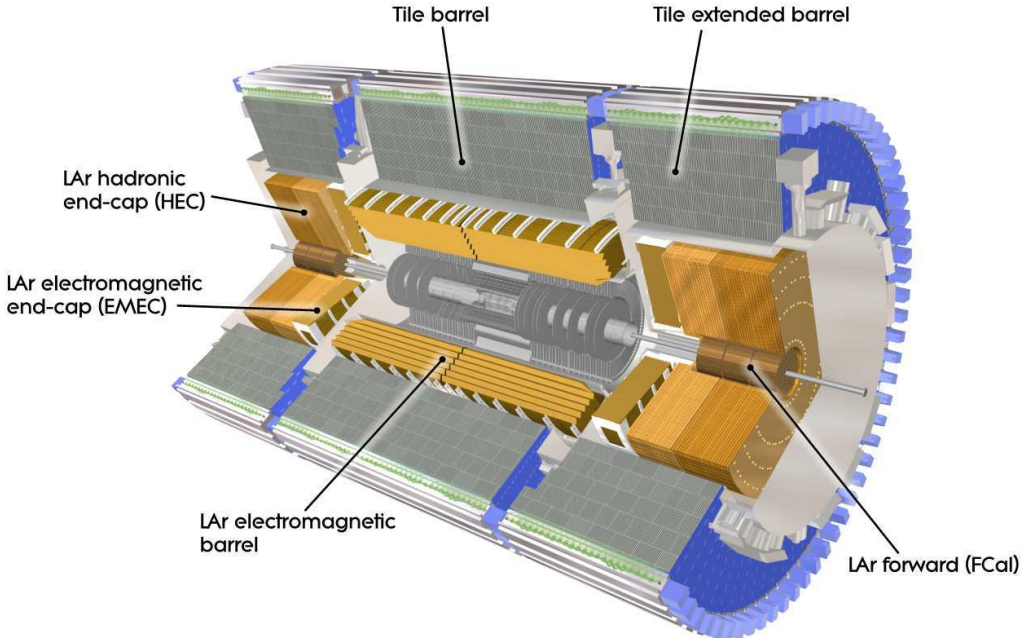
Figure 4.11: A cutaway view of the ATLAS Calorimeters.

The ATLAS calorimeter [75], depicted in Figure **4.11**, covers $|\eta| < 4.9$ and consists of electromagnetic (EM) and hadronic calorimeters. A summary of the coverage in $|\eta|$, granularity and segmentation in depth are given in Table **4.1**. The major performance requirements on the energy resolution for the calorimeters are as follows.

$$\bullet \quad \frac{\sigma_E}{E} \quad = \quad \frac{10}{\sqrt{E\,(\text{GeV})}} \oplus 0.7\% \quad (|\eta| < 3.2 \text{ for EM measurements})$$

$$\bullet \quad \frac{\sigma_E}{E} \quad = \quad \frac{50}{\sqrt{E\,(\text{GeV})}} \oplus 3\% \quad (|\eta| < 3.2 \text{ for hadronic measurements})$$

$$\bullet \quad \frac{\sigma_E}{E} \quad = \quad \frac{100}{\sqrt{E\,(\text{GeV})}} \oplus 10\% \quad (3.2 < |\eta| < 4.9 \text{ for hadronic measurements})$$

The ATLAS electromagnetic calorimeters are divided into two parts namely the barrel EM calorimeter ($|\eta| < 1.475$) and the Endcap ElectroMagnetic Calorimeter (EMEC) ($1.375 < |\eta| < 3.2$). Both deploy the same technology of liquid argon active material with accordion-shaped lead absorber. Over the fiducial coverage of the inner detector ($|\eta| < 2.5$), the EM calorimeters have finer granularity for precision measurements of electron and photon. The coarser granularity in the other region is sufficient for jet reconstruction and E_T^{miss} measurements.

In the region of $|\eta| < 1.8$, a presampler is deployed to correct for the energy deposit in the material upstream of the EM calorimeter. The presampler consists of an active liquid argon

layer with thickness of 1.1 cm (0.5 cm) in $|\eta| < 1.52$ ($1.52 < |\eta| < 1.8$).

The ATLAS hadronic calorimeter is divided into three parts namely scintillator tile calorimeter ($|\eta| < 1.7$), Hadronic Endcap Calorimeter (HEC) ($1.5 < |\eta| < 3.2$) and Forward Calorimeter (FCal) ($3.1 < |\eta| < 4.9$). The HEC and FCal deploys liquid argon technology with different absorbers.

The total radiation length (X_0) in the EM calorimeters is > 22 X_0 in the barrel and > 24 X_0 in the endcap. Also, the approximate total interaction length (λ) is about > 10 over the entire coverage. Figure **4.12**, **4.13** show the material distribution in front of and in the calorimeters in the unit of X_0 and λ. The blue histogram in Figure **4.13** shows the λ distribution in front of the first layer of the muon spectrometer. Details of each calorimeter are described in the following subsections.

(a)

(b)

(c)
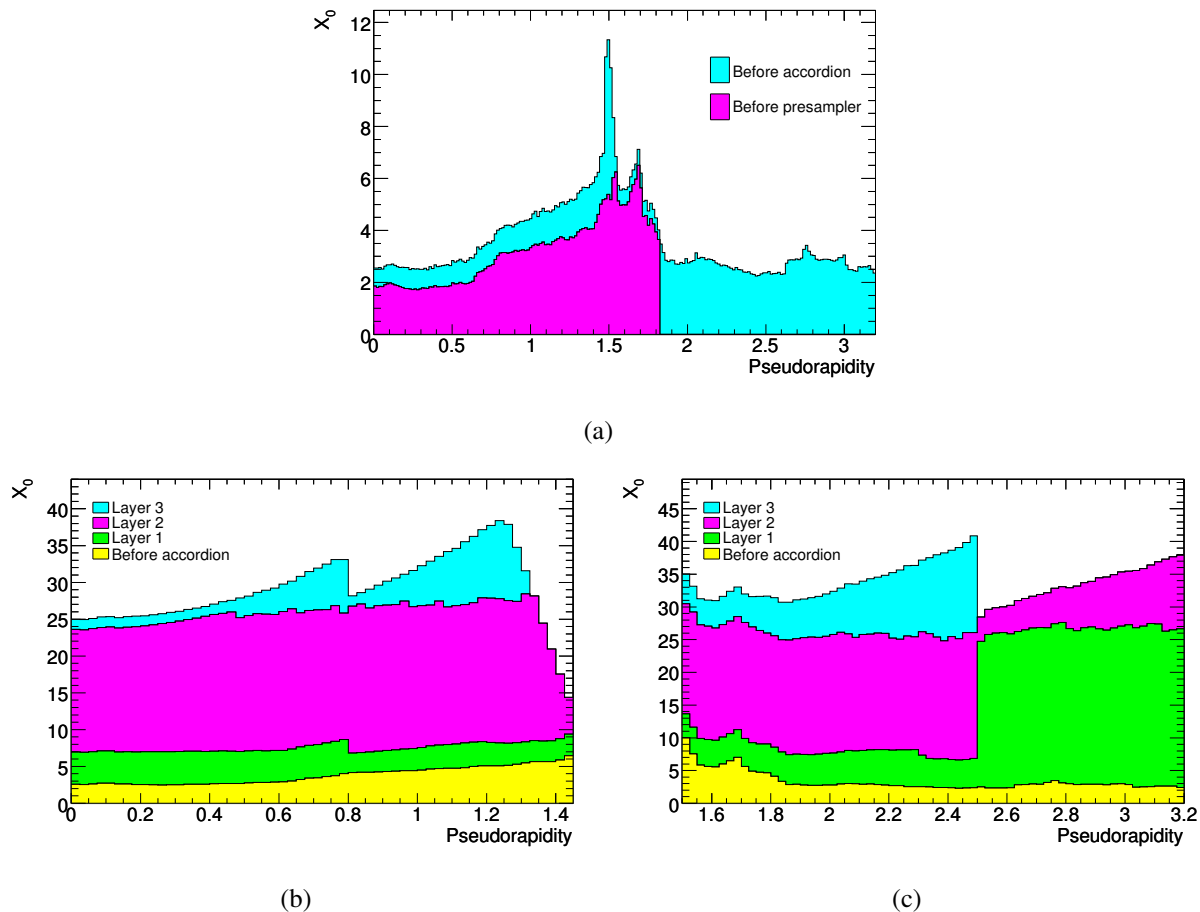
Figure 4.12: Cumulative amounts of material in units of X_0 (radiation length) and as a function of $|\eta|$ in front of and in the EM calorimeters. (a) The total amount of material in front of the presampler layer and in front of the first layer of the EM calorimeters over the full η range. (b) The thickness of each layer as well as the material in front of the first layer in the barrel. (c) The thickness of each layer as well as the material in front of the first layer in the endcap.

	Barrel	**Endcap**
EM Calorimeter		
number of layers and $\|\eta\|$ coverage		
Presampler	1 $\quad\quad\quad\quad\quad\quad \|\eta\| < 1.52$	1 $\quad\quad\quad\quad\quad\quad 1.5 < \|\eta\| < 1.8$
Calorimeter	3 $\quad\quad\quad\quad\quad\quad \|\eta\| < 1.35$ 2 $\quad\quad 1.35 < \|\eta\| < 1.475$	2 $\quad\quad\quad 1.375 < \|\eta\| < 1.5$ 3 $\quad\quad\quad\quad 1.5 < \|\eta\| < 2.5$ 2 $\quad\quad\quad\quad 2.5 < \|\eta\| < 3.2$
Granularity $\Delta\|\eta\| \times \Delta\phi$ vs $\|\eta\|$		
Presampler	$0.025 \times 0.1 \quad\quad\quad \|\eta\| < 1.52$	$0.025 \times 0.1 \quad\quad 1.5 < \|\eta\| < 1.8$
Calorimeter 1st layer	$0.025/8 \times 0.1 \quad\quad \|\eta\| < 1.40$ $0.025 \times 0.025 \quad 1.40 < \|\eta\| < 1.475$	$0.050 \times 0.1 \quad\quad 1.375 < \|\eta\| < 1.425$ $0.025 \times 0.1 \quad\quad 1.425 < \|\eta\| < 1.5$ $0.025/8 \times 0.1 \quad\quad 1.5 < \|\eta\| < 1.8$ $0.025/6 \times 0.1 \quad\quad 1.8 < \|\eta\| < 2.0$ $0.025/4 \times 0.1 \quad\quad 2.0 < \|\eta\| < 2.4$ $0.025 \times 0.1 \quad\quad 2.4 < \|\eta\| < 2.5$ $0.1 \times 0.1 \quad\quad 2.5 < \|\eta\| < 3.2$
Calorimeter 2nd layer	$0.025 \times 0.025 \quad\quad \|\eta\| < 1.40$ $0.075 \times 0.025 \quad 1.40 < \|\eta\| < 1.475$	$0.050 \times 0.025 \quad 1.375 < \|\eta\| < 1.425$ $0.025 \times 0.025 \quad 1.425 < \|\eta\| < 2.5$ $0.1 \times 0.1 \quad\quad 2.5 < \|\eta\| < 3.2$
Calorimeter 3rd layer	$0.050 \times 0.025 \quad\quad \|\eta\| < 1.35$	$0.050 \times 0.025 \quad\quad 1.5 < \|\eta\| < 2.5$
number of readout channels		
Presampler	7808	1536 (both sides)
Calorimeter	101760	62208 (both sides)
LAr hadronic endcap (HEC)		
$\|\eta\|$ coverage number of layers		$1.5 < \|\eta\| < 3.2$ 4
Granularity $\Delta\|\eta\| \times \Delta\phi$		$0.1 \times 0.1 \quad\quad 1.5 < \|\eta\| < 2.5$ $0.2 \times 0.2 \quad\quad 2.5 < \|\eta\| < 3.2$
number of readout channels		5632 (both sides)
LAr forward calorimeter (FCal)		
$\|\eta\|$ coverage number of layers		$3.1 < \|\eta\| < 4.9$ 3
Granularity $\Delta x \times \Delta y$ (cm)		FCal1: $3.0 \times 2.6 \quad\quad 3.15 < \|\eta\| < 4.30$ FCal1: $\sim$ 4 times finer $\quad 3.10 < \|\eta\| < 3.15$ $\quad\quad\quad\quad\quad\quad\quad\quad 4.30 < \|\eta\| < 4.83$ FCal2: $3.3 \times 4.2 \quad\quad 3.24 < \|\eta\| < 4.50$ FCal2: $\sim$ 4 times finer $\quad 3.20 < \|\eta\| < 3.24$ $\quad\quad\quad\quad\quad\quad\quad\quad 4.50 < \|\eta\| < 4.81$ FCal3: $5.4 \times 4.7 \quad\quad 3.32 < \|\eta\| < 4.60$ FCal3: $\sim$ 4 times finer $\quad 3.29 < \|\eta\| < 3.32$ $\quad\quad\quad\quad\quad\quad\quad\quad 4.60 < \|\eta\| < 4.75$
number of readout channels		3524 (both sides)
Scintillator tile calorimeter		
	Barrel	Extended barrel
$\|\eta\|$ coverage number of layers	$\|\eta\| < 1.0$ 3	$0.8 < \|\eta\| < 1.7$ 3
Granularity $\Delta\|\eta\| \times \Delta\phi$ for last layer	0.1×0.1 0.2×0.1	0.1×0.1 0.2×0.1
number of readout channels	5760	4092 (both sides)

Table 4.1: Coverage in η, granularity and segmentation in depth of the ATLAS calorimeters [72].
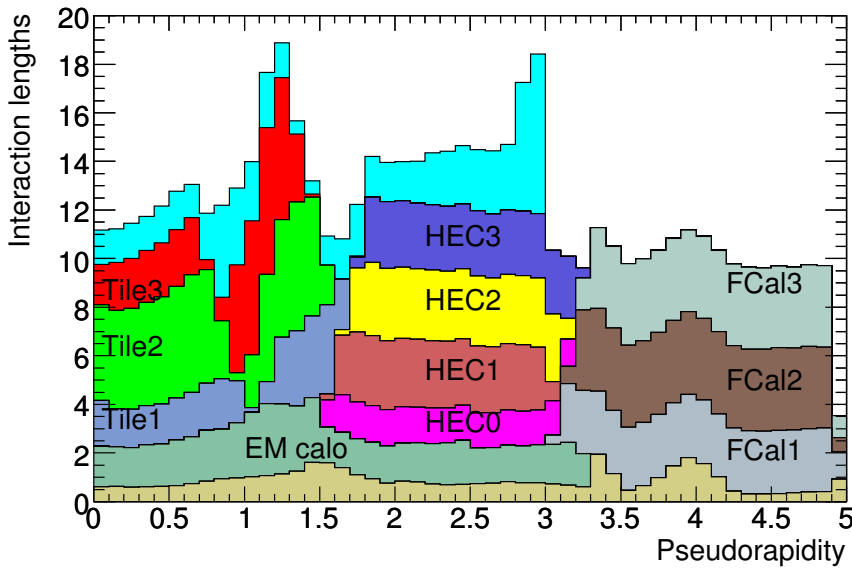
Figure 4.13: Cumulative amount of material in units of λ (interaction length) as a function of $|\eta|$ in front of and in the EM calorimeters, in each hadronic layer, the total amount at the end of the active calorimetry and the total amount of material in front of the first active layer of the muon spectrometer.

4.3.1   LAr Electromagnetic Calorimeter

The EM calorimeter is divided into a barrel part ($|\eta| < 1.475$) and two endcap parts ($1.375 < |\eta| < 3.2$) each is housed in its own cryostat. The barrel calorimeter consists of two identical half-barrels which are separated by a small gap (4 mm) at z = 0. Each endcap calorimeter consists of two coaxial wheels namely an outer wheel ($1.375 < |\eta| < 2.5$) and an inner wheel ($2.5 < \eta < 3.2$).

Both the barrel and the endcap calorimeters are sampling calorimeters which use accordion-shaped lead as absorber and liquid argon as active material. Its accordion geometry provides a complete ϕ coverage without azimuthal crack. The ionization charge is collected by copper clad kapton electrodes which also have accordion-shape. The lead plates in the barrel is 1.53 mm thick in $|\eta| < 0.8$ and 1.13 mm thick in $|\eta| > 0.8$. In the endcap calorimeters, the plates is 1.7 mm thick in $|\eta| < 2.5$ and of 2.2 mm thick in $|\eta| > 2.5$. These optimization are done to improve the performance in energy resolution.

Figure **4.14** shows a schematic of a barrel EM calorimeter module. A detailed summary of the granularity of the EM calorimeter is given in Table **4.1** and also in Figure **4.15**. Over the fiducial coverage of the inner detector ($|\eta| < 2.5$), which is used for precision measurements of electron and photon, the EM calorimeters are segmented into three sections in depth. As can be seen in Figure **4.14**, the first layer is finely segmented along η. This leads to a fine resolution on the polar direction of a EM shower of approximately $\Delta\theta = 50$ mrad/ $\sqrt{E\ (GeV)}$. The remaining region is segmented into two sections in depth and has a coarser lateral granularity.
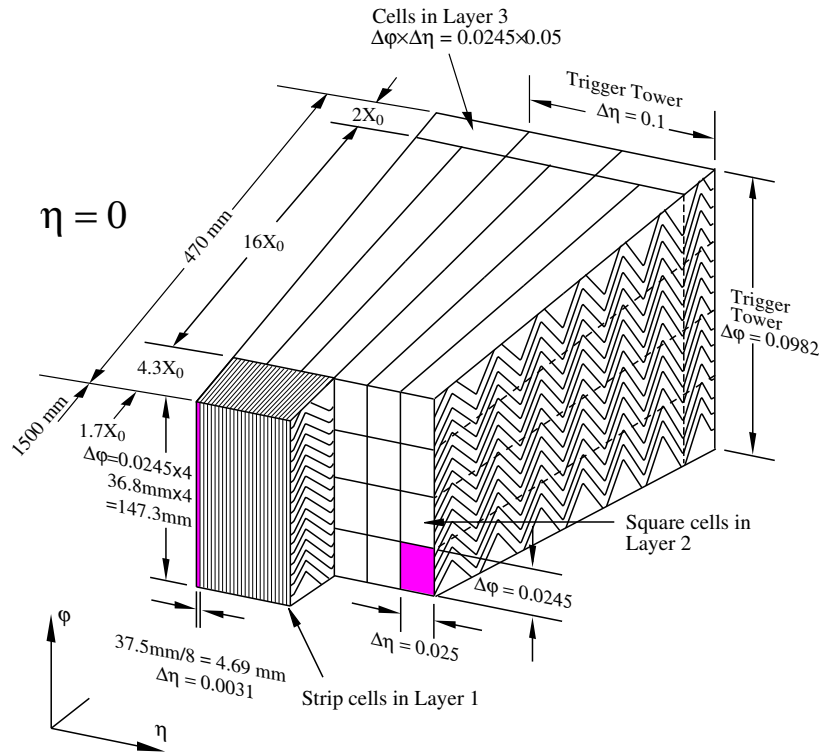
Figure 4.14: Sketch of a barrel LAr Calorimeter module.
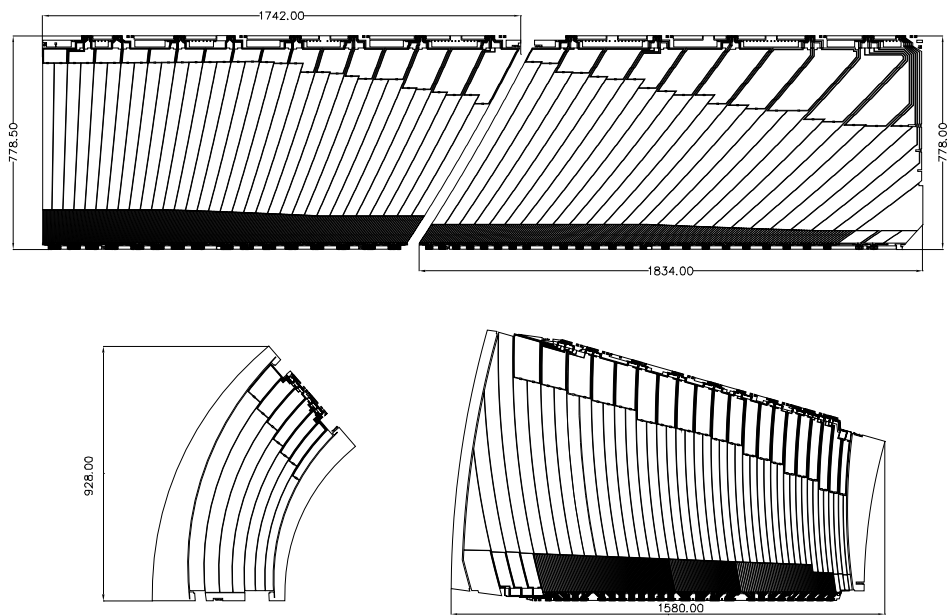
Figure 4.15: The layout of the signal layers in the EM calorimeters in $r - z$ plane. The figures on top are for the barrel and the extended endcap. The figure on bottom-left is for the endcap inner and bottom-right is for the endcap outer wheels.

4.3.2 Hadronic Calorimeters

Scintillator Tile Barrel Calorimeter

The hadronic calorimeter in the barrel region is placed directly outside the EM calorimeter envelope. The barrel hadronic calorimeter covers $|\eta| < 1.0$ and the extended barrel hadronic calorimeter covers $0.8 < |\eta| < 1.7$.

Figure **4.16** shows the coverage in η and radial segmentation of the barrel and extended barrel hadronic calorimeters which extends from an inner radius of 2280 mm to an outer radius of 3865 mm. Both calorimeters are segmented in depth into three layers, approximately 1.5, 4.1 and 1.8 interaction lengths (λ) thick for the barrel and 1.5, 2.6 and 3.3 λ thick for extended barrel. Azimuthally, both calorimeters are divided into 64 modules.
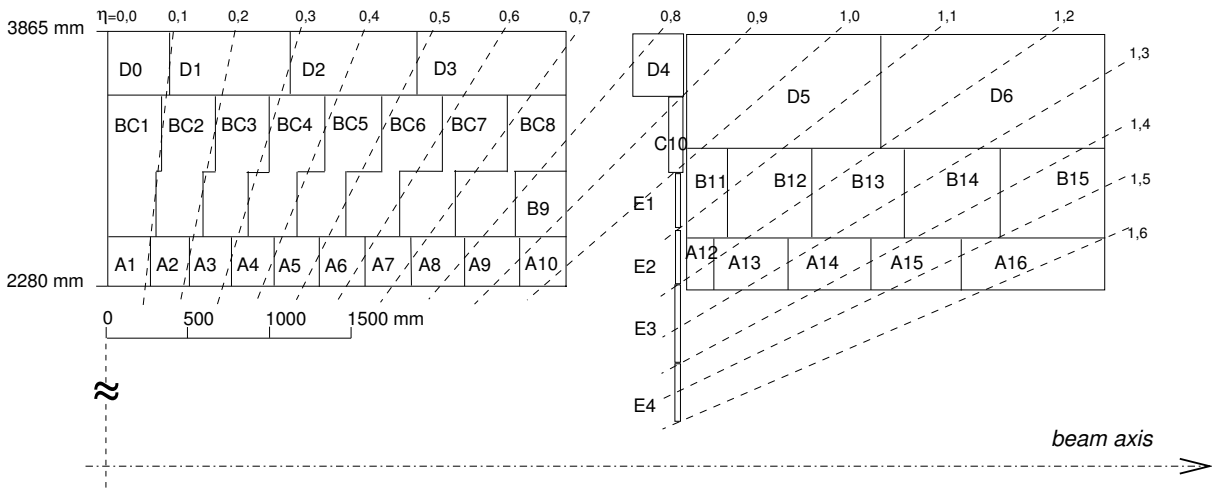
Figure 4.16: Scintillator tile calorimeter segmentation in the radial direction.

Figure **4.17** shows a schematic view of a scintillator tile calorimeter module. The basic components of the scintillator tile calorimeter are plastic scintillator tile with thickness of 3 mm and steel absorbers. The shape of each component varies depending on its location. The steel absorber structure is made of 5 mm thick master plates and 4 mm thick spacer plates. The spacer plates are glued on the master plate in a staggering fashion to form pockets for plastic scintillator tiles. The scintillation photons are collected by wave length shifting fiber then transported to and read out by photomultiplier tubes. The readout cells are built by grouping these fibers.
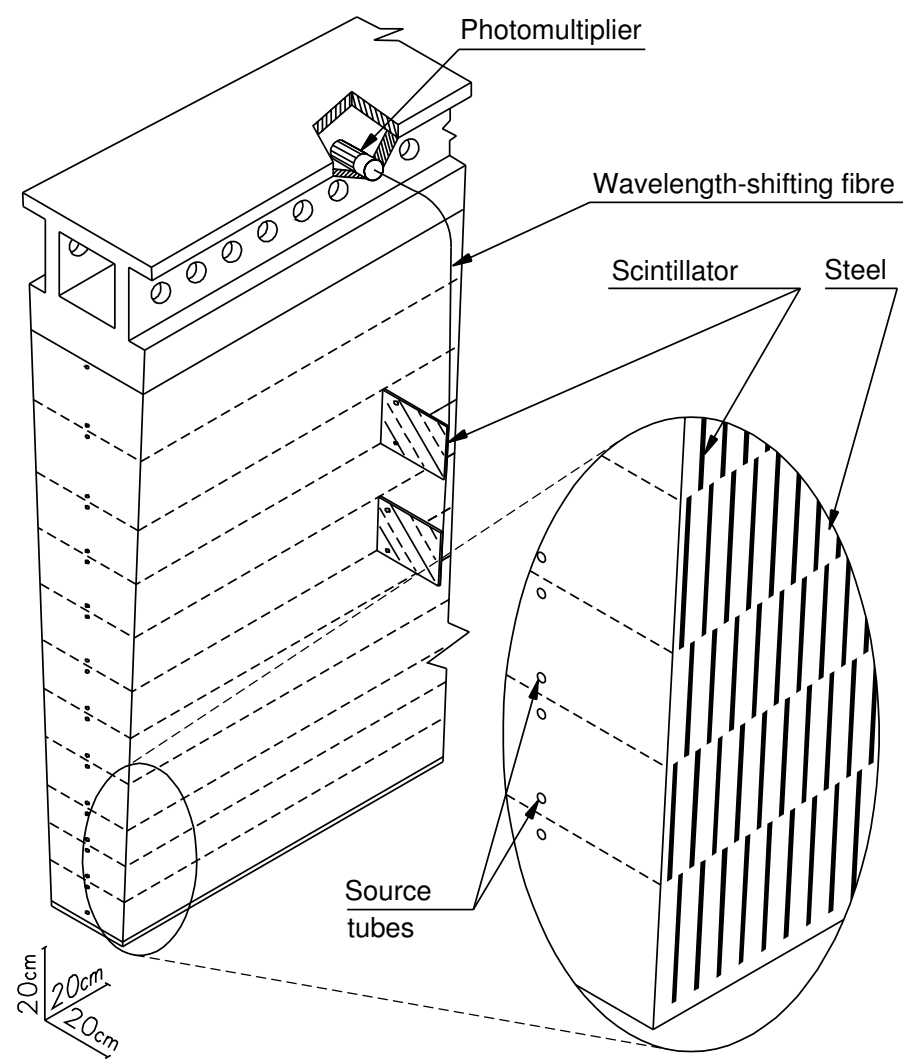
Figure 4.17: A schematic view of a scintillator tile calorimeter module.

LAr Hadronic Endcap Calorimeter (HEC)

The Hadronic Endcap Calorimeter (HEC) consists of two wheels on each endcap covering the $1.5 < |\eta| < 3.2$ region. The HEC is located directly behind the EMEC sharing the same cryostat. Figure **4.18** shows the layout of the calorimeters in the endcap and forward region. The figure also includes the FCals.
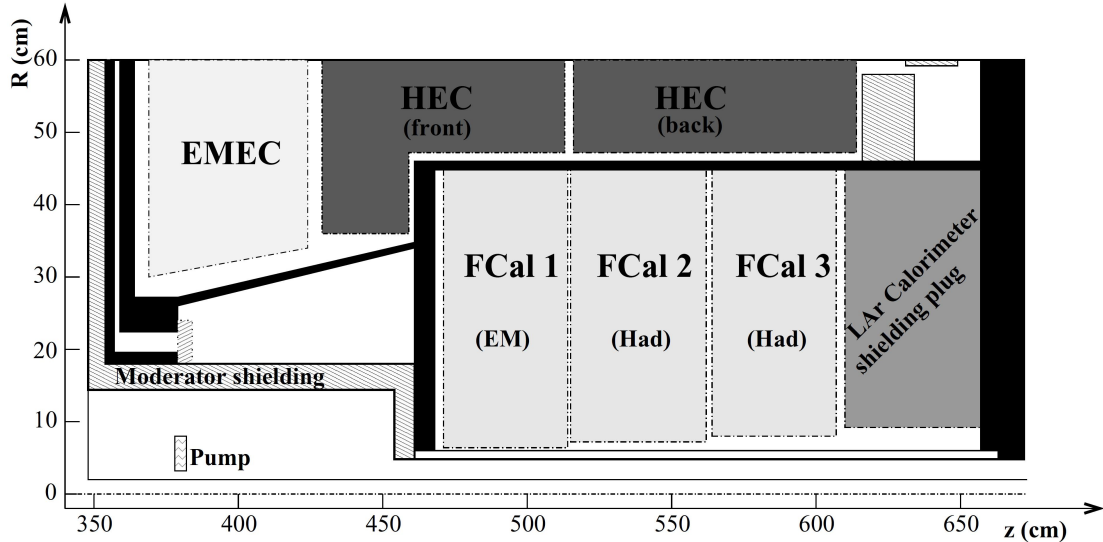
Figure 4.18: The layout of the calorimeters in the endcap and forward region. All the calorimeters are housed in the same cryostat.

Each HEC wheel is built from 32 identical wedge-shaped modules and each wheel is divided into two segments in depth (HEC1 and HEC2) as depicted in Figure **4.19**. The inner radius of HEC1 is 372 mm and of HEC2 is 475 mm.

The HEC is a copper - LAr sampling calorimeter with a flat-plate design. Figure **4.20** (a) shows a schematic view of a HEC1 module. The HEC1 (HEC2) consists of 24 (16) copper plates with thickness of 25 (50) mm. 8.5 mm thick readout gaps are located to house LAr as active material and electrodes between copper plates. Figure **4.20** (b) shows the structure of a HEC readout gap. The electrodes are made from carbon loaded kapton.
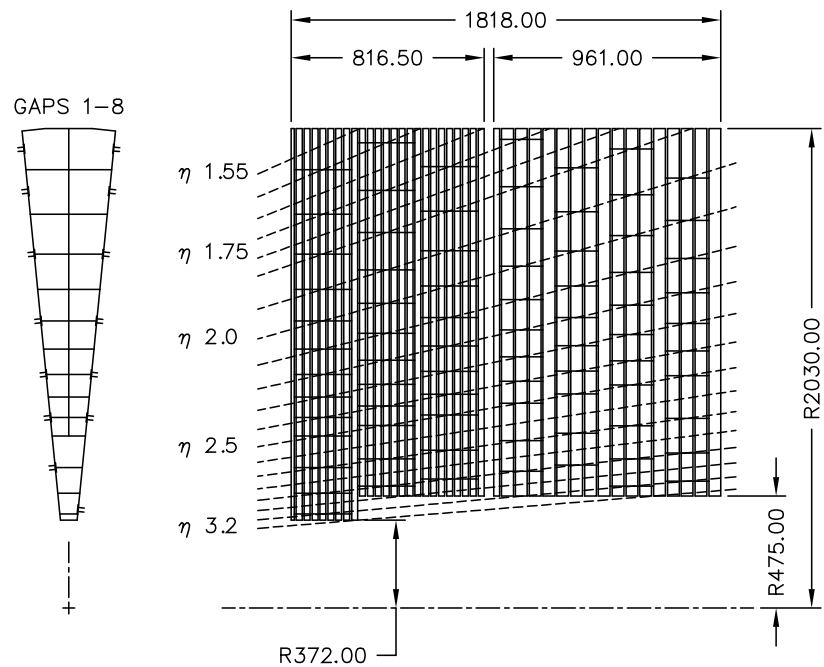
Figure 4.19: A schematic view of the HEC segmentation (Dimensions are in mm).
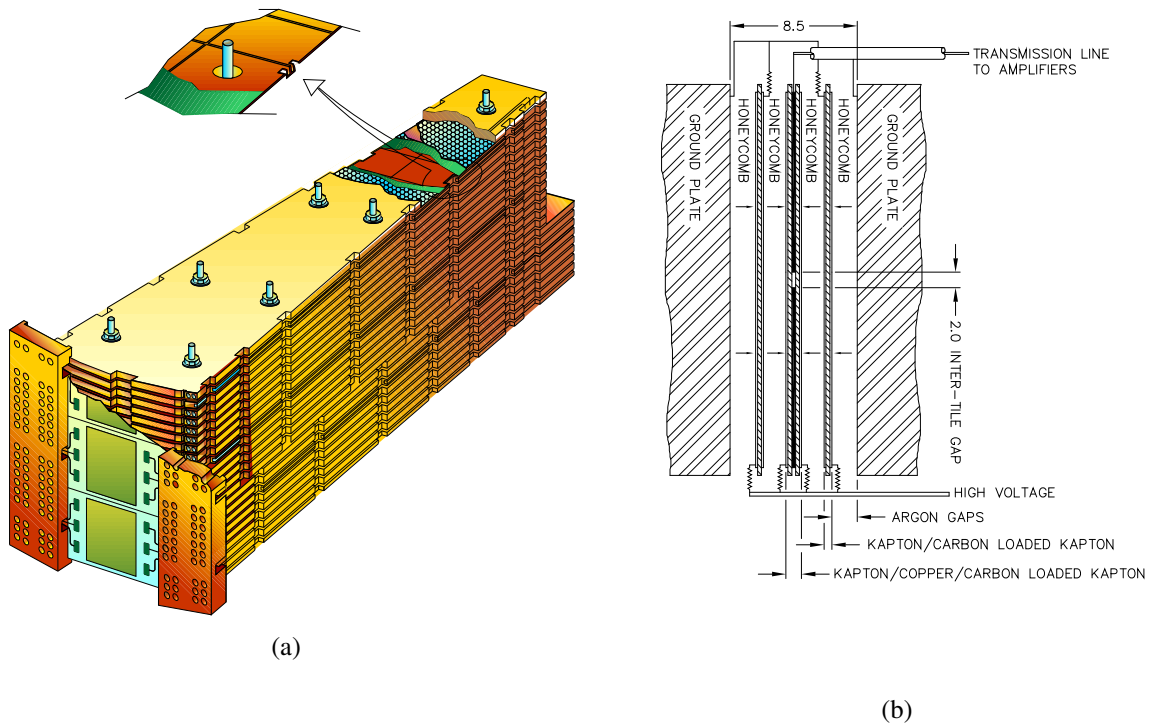
Figure 4.20: (a) A schematic view of a HEC1 module. (b) A schematic view of the arrangement of the HEC readout structure.

LAr Forward Calorimeter (FCal)

The Forward Calorimeter (FCal), which covers $3.1 < |\eta| < 4.9$, is integrated into the endcap cryostats to ensure uniformity of the calorimetric coverage as depicted in Figure **4.18**. The FCal on each side is divided into three 45 cm thick modules namely FCal1 for EM measurements and FCal2 and FCal3 for hadronic measurements.

To achieve a tolerance against the high radiation dose, the FCal deploys a design with very small LAr gaps which is obtained by using an electrode structure of small diameter rods centered in tubes which are oriented parallel to the beam direction. Figure **4.21** (a) shows a schematic view of an electrode of FCal1, which uses copper as the electrode material, in which a rad-hard plastic fiber aligned a rod at the center of the tube. Figure **4.21** (b) shows the layout of the electrodes of FCal1 in which many holes are drilled in copper plates.

FCal2 and FCal3 have the similar structure but tungsten is adopted as the materials for electrodes and main absorber material to provide containment and minimize the lateral spread of hadronic showers.
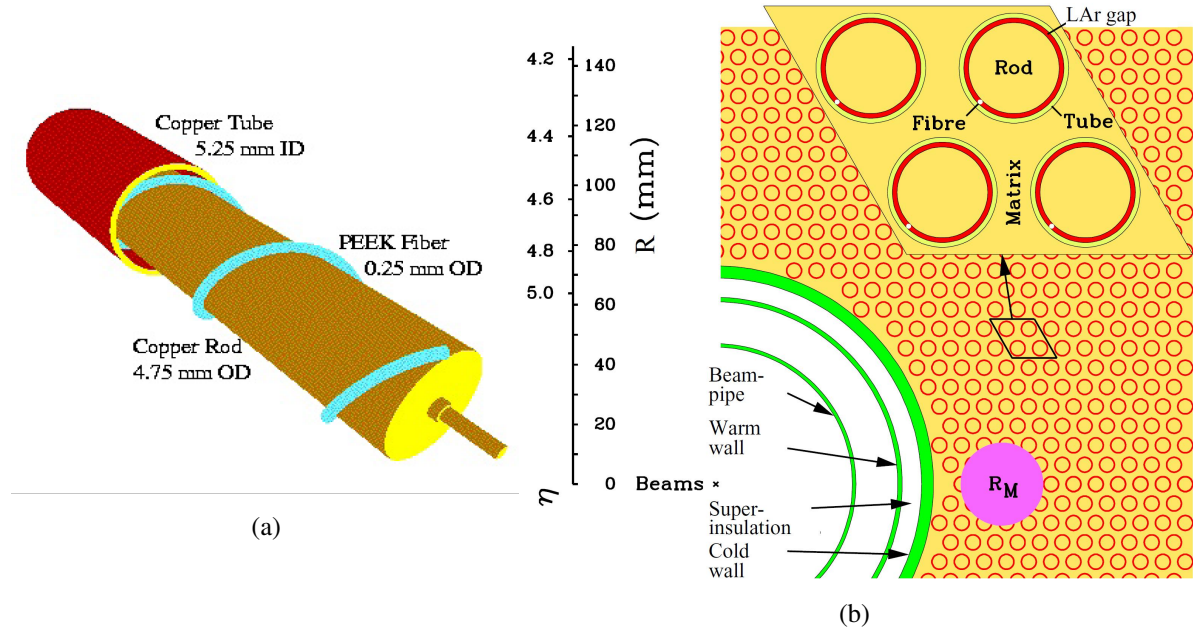
Figure 4.21: (a) A schematic view of a FCal1 copper electrode wound by a rad-hard plastic fiber. (b) The layout of the electrodes of FCal1. R_M represents the Moliere radius.

4.4 Muon Spectrometer
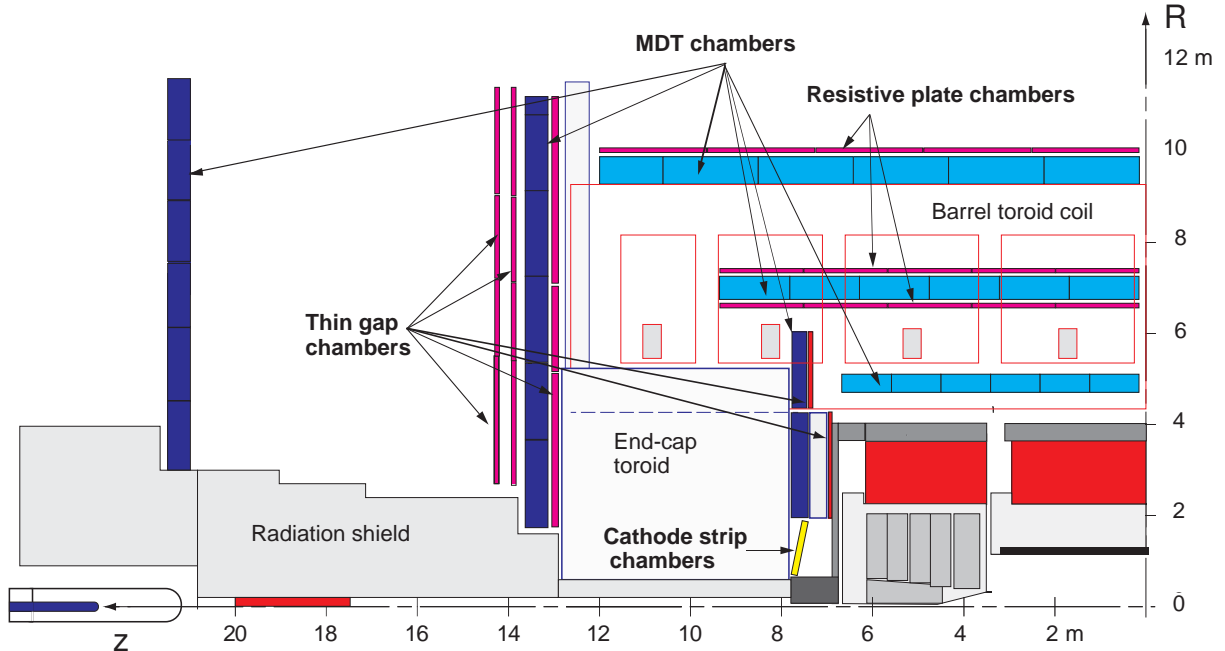
Figure 4.22: A schematic R-Z view of the ATLAS muon spectrometer.

The muon spectrometer [76] is situated at the outermost part of the ATLAS detector. Figure **4.22** shows the cross section in the R - Z plane. The muon spectrometer consists of following four independent detectors.

1. Monitored Drift Tubes (MDT: $|\eta| < 2.7$)

2. Cathode Strip Chambers (CSC: $2.0 < |\eta| < 2.7$, inner station only)

3. Thin Gap Chambers (TGC: $1.05 < |\eta| < 2.7$, $|\eta| < 2.4$ for triggering)

4. Resistive Plate Chambers (RPC: $|\eta| < 1.05$)

The MDT and the CSC reconstruct a trajectory of a muon for a precision transverse momentum measurement, whereas the TGC and RPC provide muon triggers with correct bunch crossing identification. Since precision tracking requires wide time window of about 700 μs, the independent trigger detectors are deployed. The major performance goals of the muon spectrometer are summarized as follows.

- To provide efficient muon identification and transverse momentum measurement for the muons with p_T of up to 1 TeV in $|\eta| < 2.7$ with a resolution of about up to 10 %.

- To provide muon trigger in $|\eta| < 2.4$ with correct bunch crossing identification.

The momentum measurement in the muon spectrometer is based on the detection of the deflection of muons in the magnetic field provided by the air-core toroid magnets. The bending power distribution of the magnets is shown in Figure **4.4**.

Figure **4.23** shows a breakdown of the contributions for the calculated muon p_T resolution as a function of p_T. At low momentum, resolutions are dominated by fluctuations in energy loss of muons in front of the muon spectrometer. Multiple coulomb scattering in the muon spectrometer plays an important role in the intermediate range. At p_T above 300 GeV, single hit resolution, insufficient alignment and calibration dominates the p_T resolution.
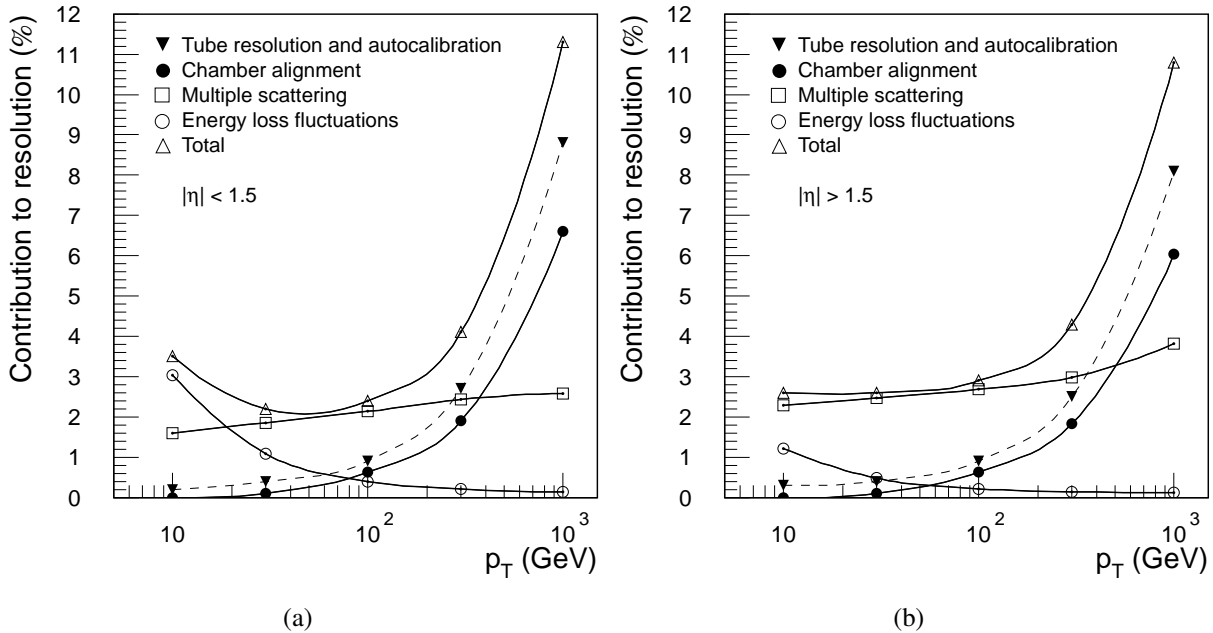
Figure 4.23: A calculated typical momentum resolution for muons reconstructed in the muon spectrometer. The alignment curve is for an uncertainty of 30 μm in the chamber positions. (a) is for $|\eta| < 1.5$ and (b) is for $|\eta| > 1.5$.

Trigger detectors are required to have timing accuracy better than 25 ns for the correct bunch crossing identification. Also the rough position resolution about 10 mm is required since tracking detectors are dedicated to the measurement in bending (η) coordinate and position in ϕ is provided by trigger detectors in the muon reconstruction algorithms.

The detailed descriptions about muon reconstruction and trigger are presented in the dedicated chapters. The overall layout of the muon spectrometer and the specifications for each detector technology are described in the remaining part of this section.

4.4.1   The Detector Layout

A 3-D view of the muon spectrometer is shown in Figure **4.24** as well as the toroid magnets and other detector structures. In the barrel, the muon chambers are arranged in three concentric cylinders around the beam axis. In the endcap, chambers form three disks on each side of the detector, concentric around the beam axis (see also Figure **4.22**). Each cylinder and disk is called inner, middle and outer station respectively from inside to outside.

The chambers are placed such that particles originate at the IP traverse three chamber stations. The position of these stations has been chosen to maximize the detector acceptance and to take optimum advantage of the magnetic field configuration.

Figure **4.25** shows the cross section in the R - ϕ plane. Both the barrel and the endcap toroid magnets have eight coils and are rotated in the azimuthal direction by 22.5° with respect to each other. There is a 16 fold segmented structure in azimuthal reflecting the magnet configuration. The muon chambers are arranged in large and small sectors. The large sectors cover the region between the barrel toroid coils whereas small sectors covers the azimuthal range of the barrel toroid coils. There are overlap regions at the boundaries between large and small sectors to maximize the acceptance.
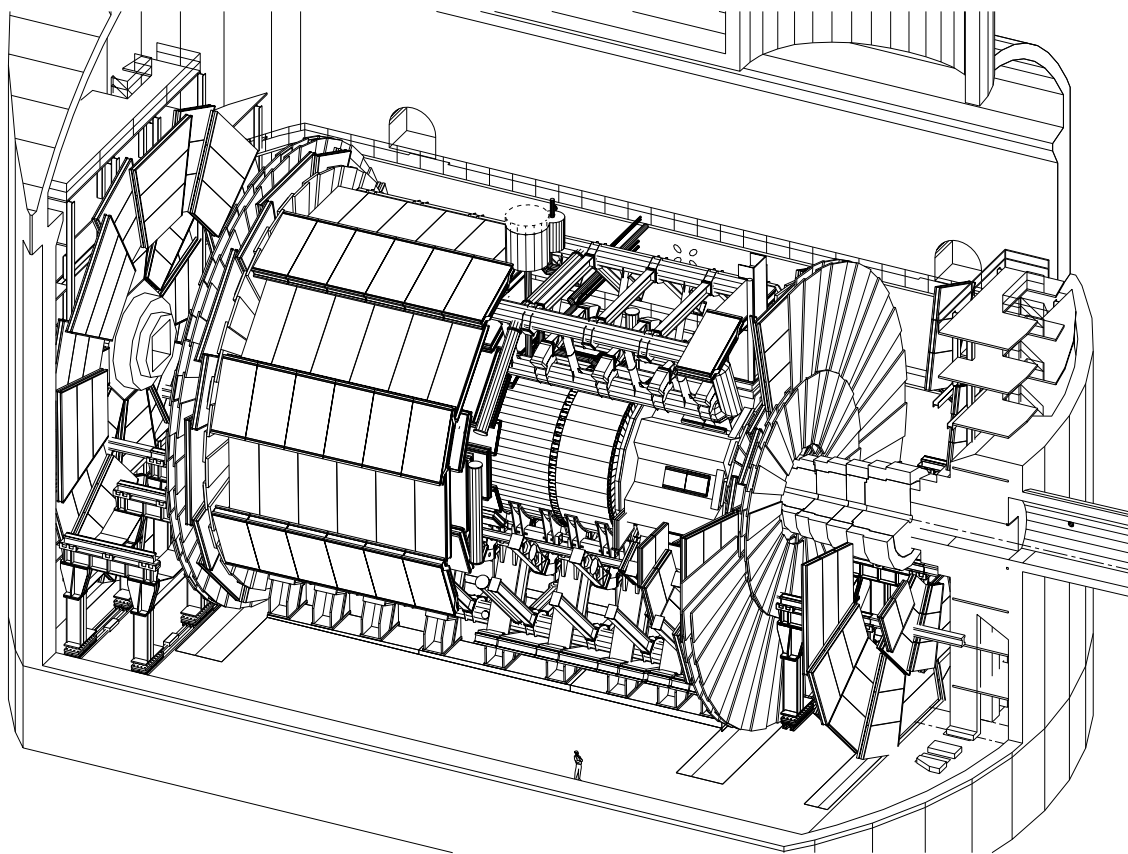
Figure 4.24: 3-D view of the ATLAS detector in the underground hall. The muon chambers (partly removed to show the inner structures) are arranged in three layers around the inner detector and the calorimeter in the space between 5 and 10 m in radius and 7 and 23 m distance from the interaction point.

Small Sector

Large Sector

MDT chambers

Resistive plate chambers

Barrel toroid coils

End-cap toroid

Inner detector

Calorimeters
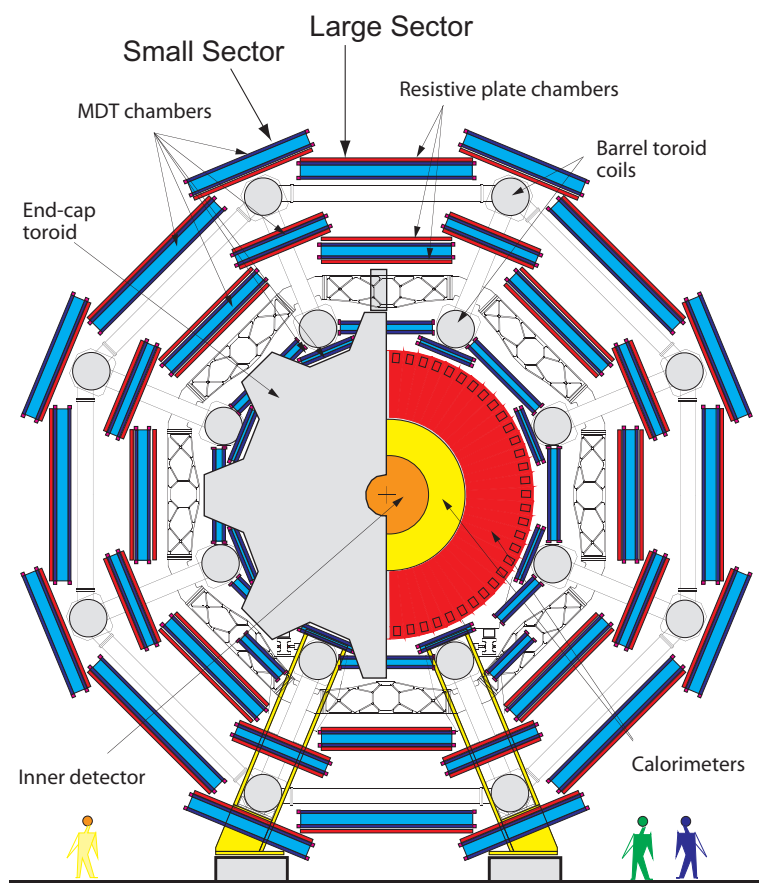
Figure 4.25: A schematic R - ϕ view of the ATLAS muon spectrometer.

4.4.2   Monitored Drift Tubes (MDT)

The MDT is the main detector in precision transverse momentum measurement of muons. The MDT covers the entire muon spectrometer acceptance except for the inner station in the forward region ($|\eta| > 2.0$).

The basic element of the MDT is a pressurized aluminium drift tube with a diameter of 29.970 mm, operating with Ar (97%) / CO_2 (3%) gas at 3 bar. The wall thickness of the tube is 0.4 mm. The electrons resulting from ionization are collected at the central tungsten-rhenium wire with a diameter of 50 μm at a potential of 3080 V. The achieved gas gain is about 2 $\times 10^4$. The wire is held in position at the tube ends by a cylindrical end-plug which guarantees the concentricity of the wire with respect to the tube with an accuracy of $\sigma < 10$ μm. The maximum drift time is about 700 ns and average spatial resolution per tube is about 80 μm. The main parameters of the MDT tube are summarized in Table **4.2**.

parameter	design
tube material	Al
outer tube diameter	29.970 mm
tube wall thickness	0.4 mm
wire material	gold-plated W / Re (97 / 3)
wire diameter	50 μm
gas mixture	Ar : CO_2 = 97 : 3
gas pressure	3.0 bar (absolute)
gas gain	2×10^4
operating voltage	3080 V
maximum drift time	~ 700 μm
average resolution per tube	~ 80 μm

Table 4.2: The MDT tube main parameters

The MDT tubes are packed together and form a chamber. All regular MDT chambers consist of two multi-layers which consists of three (middle, outer) or four (inner) tube layers. Figure **4.26** shows the structure of a barrel chamber. The shapes and dimensions of chambers were chosen to optimize solid angle coverage.

To achieve the required performance, the position and deformation of the chambers need to be known to a precision of 30 μm. The MDT deploys a system of optical alignment sensor, RASNIK [77], which consists of three active elements namely LED, lens and CCD camera. Its intrinsic precision is about 1 μm. Figure **4.27** shows an endcap MDT chamber equipped with the optical alignment system.
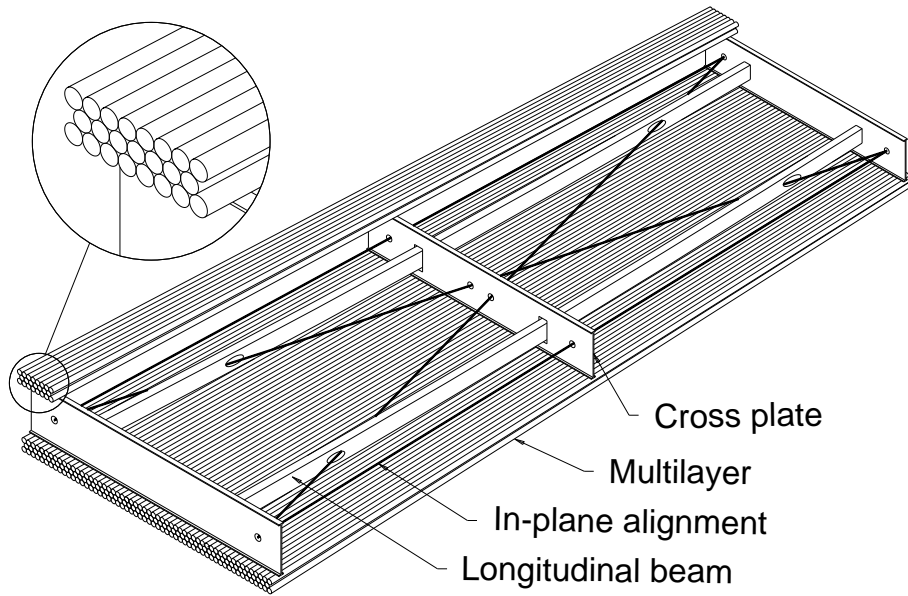
Figure 4.26: A schematic view of a barrel MDT chamber.
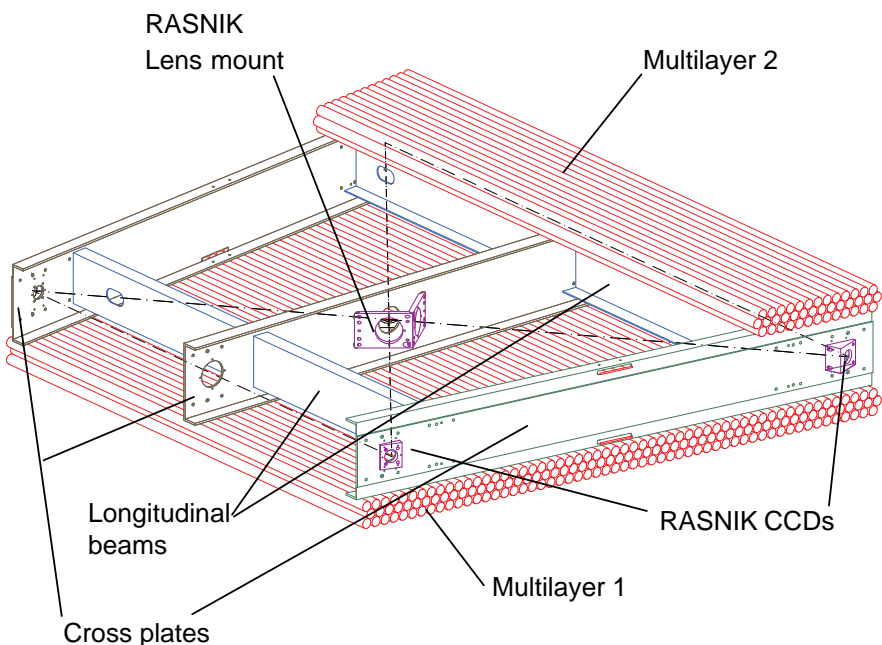
Figure 4.27: A schematic view of an endcap MDT chamber with the optical alignment system.

4.4.3   Cathode Strip Chambers (CSC)

In the region $|\eta| > 2.0$, the MDT inner station is replaced by the CSC which combines high spatial, time and double track resolution with high-rate capability and low neutron sensitivity. Due to the small electron drift time of less than 40 ns and the high spatial resolution, operation is considered safe up to counting rates of about 1k Hz/cm^2, which is sufficient for muon tracking in up to $|\eta| = 2.7$ at designed luminosity of the LHC. As in the case of the MDT, the CSC is segmented into large and small chambers in azimuthal. The whole CSC system consists of two disks with eight small chambers and eight large chambers. The CSC disks are installed with inclining angle of 11.59° (see Figure **4.28** (a)). Each chamber contains four cathode strip planes resulting in four independent $\eta - \phi$ measurements.

The CSC is multi-wire proportional chambers with the wires oriented in the radial direction. Figure **4.28** (b) shows a cutout view of a single CSC layer. Each chamber contains two orthogonal cathode planes one of which is perpendicular to the wires and the other parallel to the wires. The anode wire has a diameter of 30 μm and are made of gold-plated tungsten with 3% rhenium. Ar (80%) / CO_2 (20%) gas is used at the high voltage of 1900 V which leads to 6 $\times 10^4$ gain. The major CSC parameters are summarized in Table **4.3**.
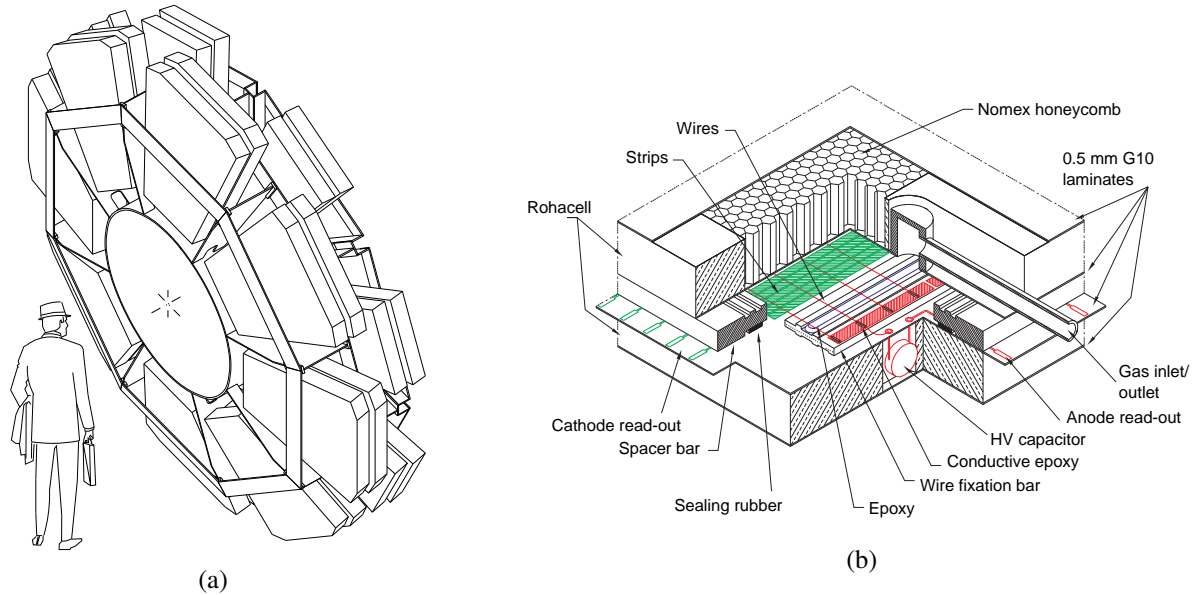
Figure 4.28: (a) The CSCs mounted on a rigid wheel inclined by 11.59°. (b) A cutout view of a single CSC layer.

The position of the track is obtained by interpolation between the charges induced on neighboring cathode strip. In the bending direction, with a readout pitch of 5.31 mm and 5.56 mm for the large and small chambers respectively, the CSC reaches a resolution of 60 μm per cathode plane. As described above, the CSC preforms measurement in ϕ-coordinate with resolution of about 5 mm as well.

parameter	design
wire material	gold-plated W / Re (97 / 3)
anode wire diameter	30 μm
gas mixture	Ar : CO_2 = 80 : 20
gas gain	6 ×10^4
operating voltage	1900 V
η resolution per cathode plane	~ 60 μm
ϕ resolution per cathode plane	~ 5 mm
total ionization for a nominal track	90 ion pairs

Table 4.3: The CSC chamber main parameters

4.4.4   Thin Gap Chambers (TGC)

The TGC provides muon triggers in the endcap region ($|\eta| > 1.05$) of the muon spectrometer.

The TGC is a multi-wire proportional chamber which is designed to operate in the saturated (limited proportional) mode. A schematic structure of a TGC chamber is shown in Figure **4.29** (a) with a typical size of 2×2 m^2. Actual shapes of TGCs depend on the geometry. The TGC deploys two dimensional readout which consists of wire groups (η - coordinate) and readout strips (ϕ - coordinate). The number of wires in a wire group varies from 4 to 20 (7.2 to 36 mm) and width of strip channels are about 30 to 50 mm.
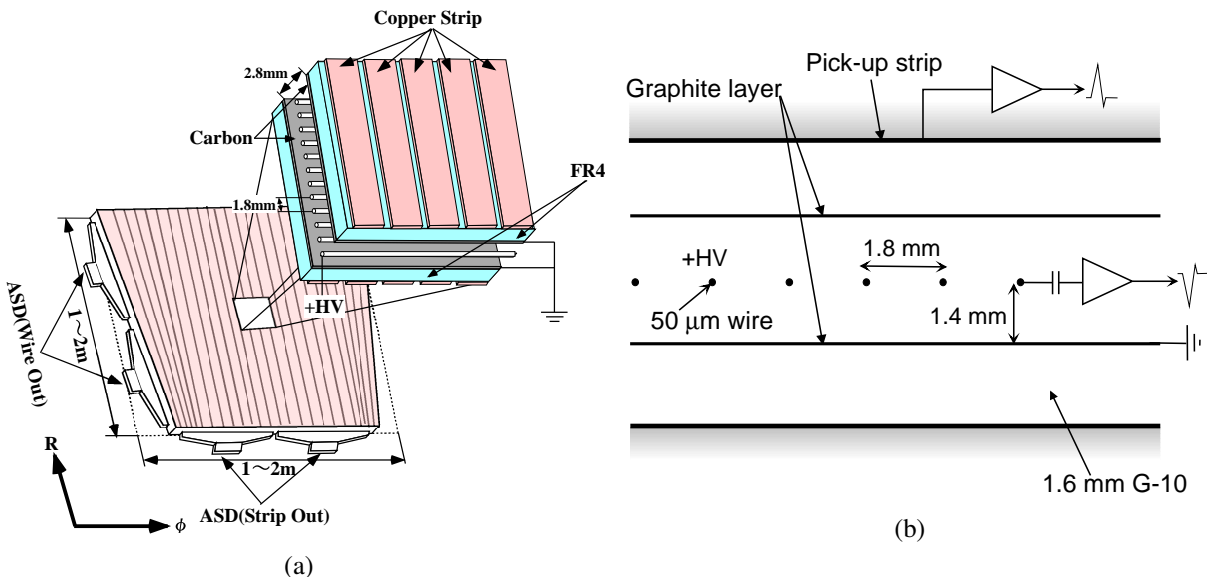
Figure 4.29: (a) A schematic illustration of a TGC chamber. (b) TGC structure showing anode wires, graphite cathodes, G-10 layers, and a read-out strip orthogonal to the wire.

The TGC uses a very strong quenching gas mixture of CO_2 (55 %) / n-C_5H_{12} (45 %) which allows a stable operation in the saturated mode. There are advantages operating in the saturated mode such as,

- high single hit efficiency

- small parallax – signals have rather small dependence of the incident angle of muons

Moreover, the highly quenching nature of the n-C_5H_{12} leads to a no streamer operation even in the case of the slow neutron interactions.

A significant feature of the TGC is its narrow anode-to-cathode distance (Figure **4.29** (b)). The anode-to-cathode distance is designed as 1.4 mm and anode-to-anode distance is 1.8 mm. Note that anode-to-anode distance is also short. This small distance between anodes and strong electric field reduce the drift component of ionization clusters hence leading to very good timing resolution required for the accurate bunch crossing identification. The major parameters of TGC are summarized in Table **4.4**.

parameter	design
gas gap	2.8 ± 0.1 mm
wire pitch	1.8 ± 0.05 mm
anode-to-cathode distance	1.4 ± 0.05 mm
wire material	gold - plated W / Re (97 / 3)
wire diameter	50 μm
gas mixture	CO_2 : n-C_5H_{12} = 55 : 45
gas gain	2×10^5
wire potential	2900 ± 100 V
intrinsic time jitter	4 ns
ϕ resolution per layer	3 – 7 mm

Table 4.4: The TGC chamber main parameters

As shown in Figure **4.22**, the TGC has no outer station and inner station is not used in the online-trigger, thus whole trigger functionalities are provided by the middle station. The TGC middle station consists of two doublet and one triplet chambers. A doublet chamber consists of two wire and two strip readout planes whereas a triplet chamber has three wire and only two strip readout planes. The cross section of the TGC triplet and doublet is shown in Figure **4.30**. Additional wire plane is to cope with false coincidences from background hits.

Figure **4.31** shows the measured time jitter of the TGC for the 3 GeV π^- beam under the several incident angle conditions. In the actual experiment, charged particle incident angle for TGC varies from 10° to 45°. Thus the intrinsic time resolution is accurate enough for the correct bunch crossing identification.
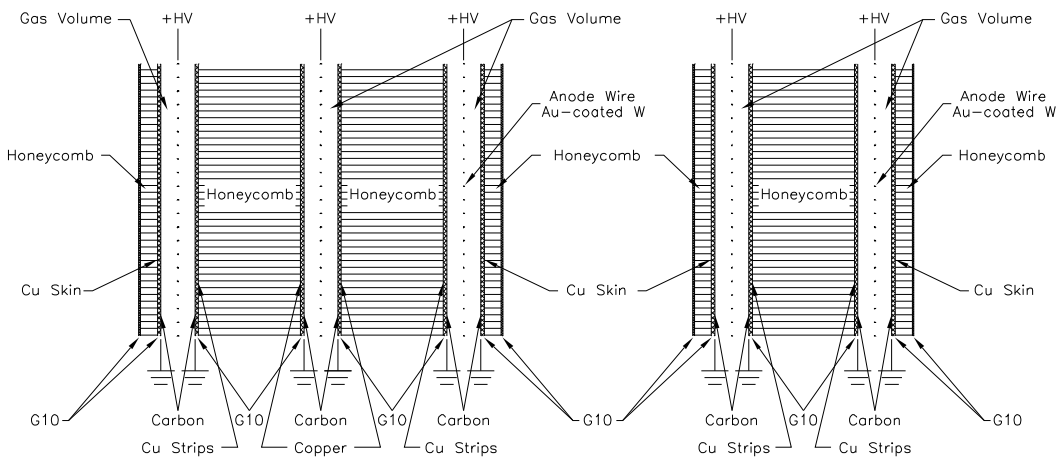
Figure 4.30: The cross section of five detector layers of the middle station of the TGC.
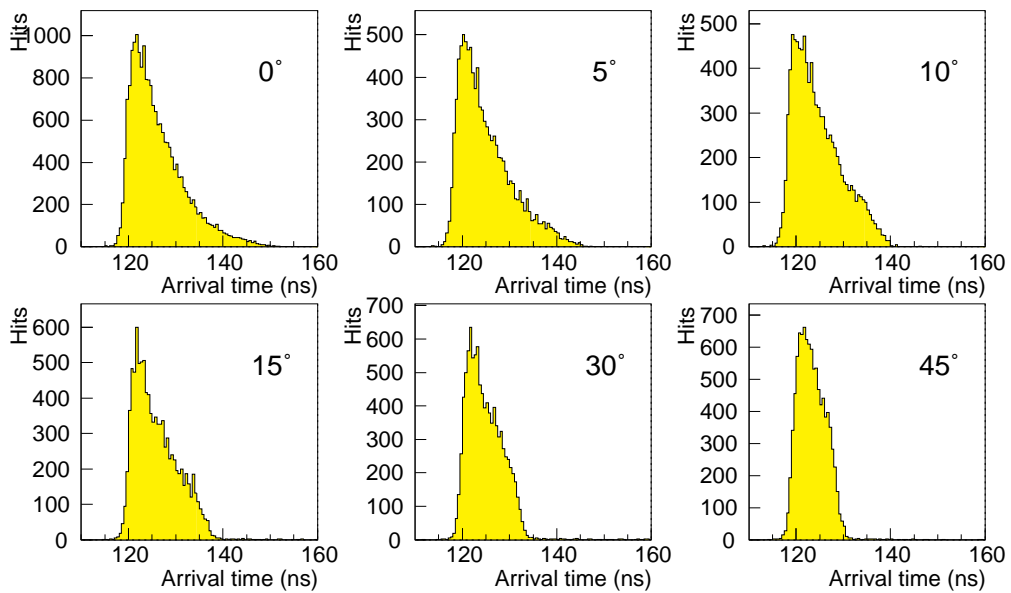
Figure 4.31: Time jitter of the TGC chamber for the various incident angles.

4.4.5   Resistive Plate Chambers (RPC)

The RPC provides muon triggers in the barrel region ($|\eta| < 1.05$) of the muon spectrometer.

The RPC is a gaseous parallel electrode-plate (i.e. no wire) detector. Two resistive plates, made of phenolic-melaminic plastic laminate, are kept parallel to each other at a distance of 2 mm by insulating spacers. The cross-section of an RPC is depicted in Figure **4.32**. The electric field between the plates of about 4.9 kV/mm allows avalanches to form along the ionizing tracks towards the anode. The signal is read out via capacitive coupling to metallic strips, which are mounted on the outer faces of the resistive plates. The gas used is a mixture of $C_2H_2F_4$ (94.7 %) / Iso-C_4H_{10} (5 %) / SF_6 (0.3 %). At the nominal operating voltage of 9.8 kV, a signal with a width of 5 ns is generated by the track with a streamer probability of less than 1 %. The position resolution in ϕ coordinate is about 10 mm, which is used in the muon reconstruction algorithm. The major parameters of the RPC are summarized in Table **4.5**.
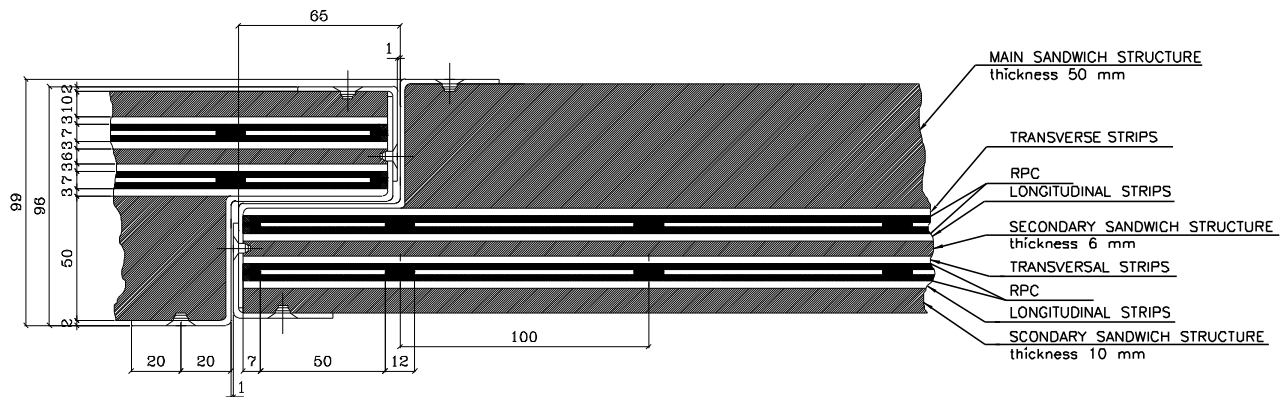
Figure 4.32: The cross section of a RPC chamber.

parameter	design
gas gap	2.00 ± 0.02 mm
gas mixture	$C_2H_2F_4$: Iso-C_4H_{10} : SF_6 = 94.7 : 5 : 0.3
operating voltage	9.80 ± 0.15 kV
Bakelite volume resistivity	$(1-5) \times 10^{10} \Omega$
intrinsic time jitter	< 1.5 ns
time jitter inclu. propagation time	< 10 ns
ϕ resolution per layer	10 mm

Table 4.5: The RPC chamber main parameters

4.5   Forward Detectors

Besides the main ATLAS detectors described in the previous sections, several detectors are placed in the very forward region. Among them, overviews of the Luminosity Measurement Using Cherenkov Integration Detector (LUCID), Absolute Luminosity For ATLAS (ALFA) and Minimum Bias Trigger Scintillator (MBTS) are presented in this section.

4.5.1   Luminosity Measurement Using Cherenkov Integrating Detector (LU-CID)

(a)   (b)
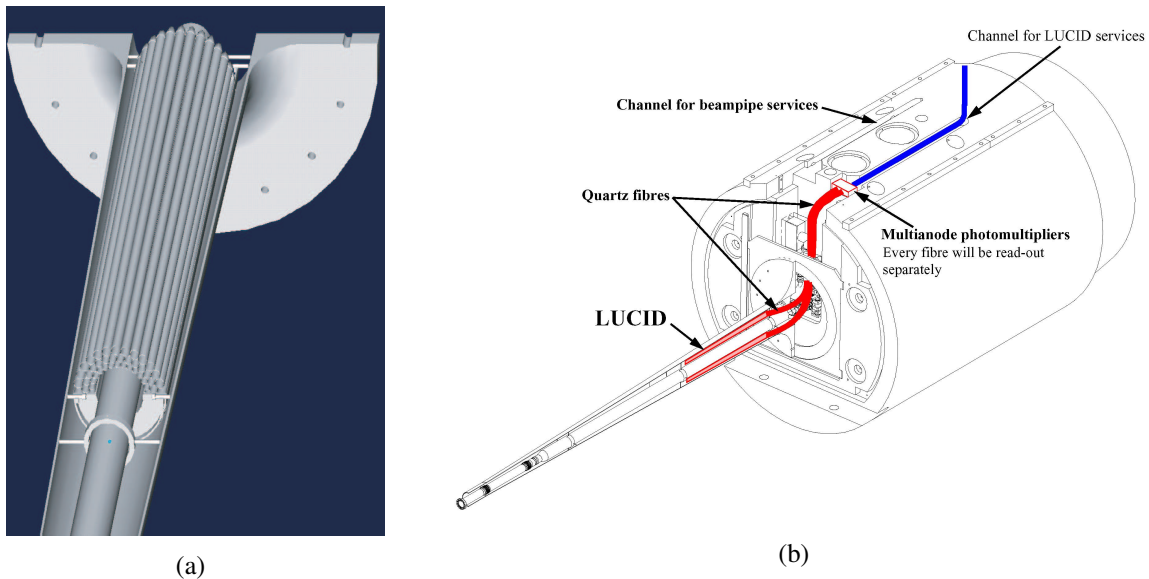
Figure 4.33: (a) The configuration of the LUCID in a side of the ATLAS detector around the beam-pipe. (b) A schematic view of a LUCID detector and its readout structure.

The main functionality of the LUCID is to detect inelastic pp scattering in order to both measure the integrated luminosity and to provide online monitoring of the instantaneous luminosity. In principle, the number of inelastic interactions is proportional to the number of particles detected in the LUCID. Thus the counting rate of the LUCID is used for luminosity determination once a scale factor which translates the counting rate to luminosity is obtained.

The two LUCID detectors are installed one in each side of the ATLAS at a distance of approximately ± 17 m from the IP. The LUCID is placed at a radial distance of approximately 10 cm from the beam-line ($|\eta| \sim 5.8$). A schematic view of the LUCID structure is depicted in Figure **4.33** (a). The LUCID consists of twenty aluminium tubes surrounding the beam-pipe. Each tube has 1.5 m length, 15 mm diameter and points towards the IP. The tubes are filled with C_4F_{10} gas at a constant pressure of 1.2 – 1.4 bar, providing a Cherenkov threshold of 2.8 GeV for pions and 10 MeV for electrons. The following advantages are obtained by counting Cherenkov photons by the LUCID.

- Since Cherenkov radiations have no decay time, the LUCID has enough time resolution for a bunch-by-bunch event counting

- Since there is no Landau tail in the Cherenkov photon measurement, it is possible to determine the number of particles entered a tube by pulse-height analyses

- Since the tubes are pointing to the IP, the background of low energy secondary particles can be rejected

The Cherenkov photons are readout by PMTs and FPGAs housed in the front-end electronics calculate the luminosity for each bunch crossing. Since the LUCID system is decoupled from the ATLAS trigger and DAQ system, it can provide independent LUCID trigger.

4.5.2 Absolute Luminosity For ATLAS (ALFA)
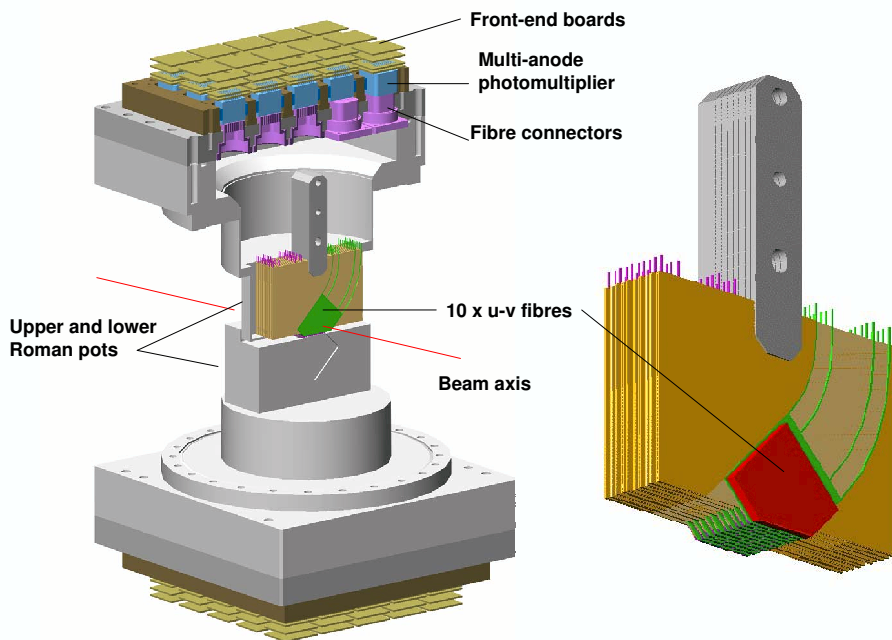
Figure 4.34: A schematic view of the ALFA detector in the Roman Pot.

The absolute luminosities at hadron colliders has been determined via elastic scattering at small angles. The optical theorem connects the elastic scattering amplitude in the forward direction to the total cross section. In the ATLAS experiment, the ALFA is used for absolute luminosity measurements. A schematic view of the ALFA in a Roman Pot is depicted in Figure **4.34**. The ALFA provides an absolute luminosity calibration through the measurement of elastic proton-proton scattering at in the Coulomb-Nuclear Interference (CNI) region as in Eq.(4.2).

$$\frac{dN}{dt} \approx L \cdot \left(\frac{4\pi\alpha^2}{|t|^2} - \frac{\alpha \cdot \rho \cdot \sigma_{tot} \cdot e^{\frac{-B \cdot |t|}{2}}}{|t|} + \frac{\sigma_{tot}^2 \cdot (1 + \rho^2) \cdot e^{-B \cdot |t|}}{16\pi} \right) \qquad (4.2)$$

where L is the absolute luminosity and ρ represents the ratio of real to imaginary part of the scattering amplitude, σ_{tot} is the total cross-section of $pp \rightarrow X$ and B is the nuclear slope. The parameters are extracted by a fit with these four free parameters. t is the momentum transfer defined as $-t = (p\sin\theta)^2 \sim (p\theta)^2$ with p the beam momentum and θ the scattering angle of a proton. A simulated dN/dt spectrum is shown in Figure **4.35** [78].
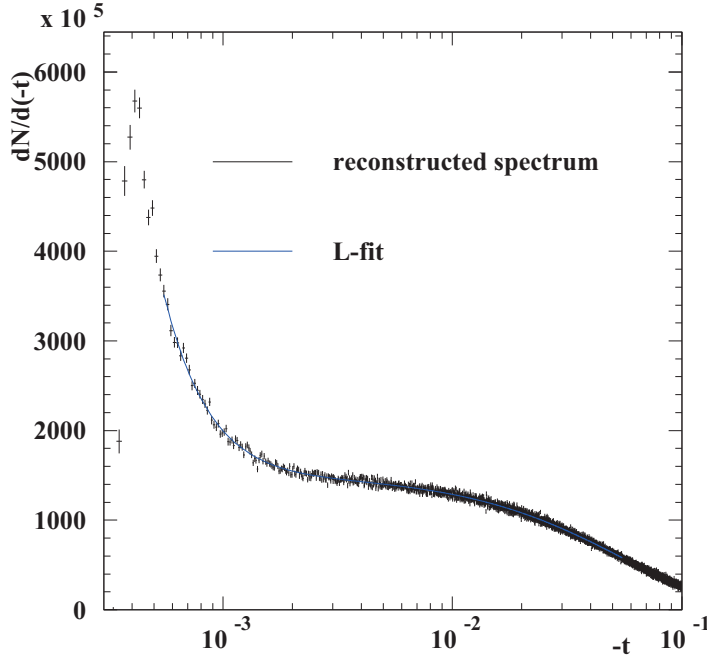
Figure 4.35: A simulated and fitted dN/dt spectrum by PYTHIA.

The ALFA detector is located in Roman Pots located at ±240 m from the interaction point. On each side there will be two Roman pot stations separated by 4 m. Since the minimum t value in interest is very small ($\sim 5 \times 10^{-4}$ GeV^2), The ALFA should be able to count the scattering rate at very small angle of about 3 μrad. Thus the ATLAS Roman pots have been designed to move the detectors as close as 1 mm to the beam from above and below.

The ALFA detector consists of ten double-sided scintillating fiber trackers each with 64 square fibers with width of 0.5 mm arranged in stereo u - v geometry on both sides. The staggered configuration of the ten trackers leads to a effective spacial resolution of 14.4 μm. The primary purpose of the ALFA is to measure the absolute luminosity to the precision of ~3 %.

Transportation of the Absolute Calibration to the Nominal Luminosity

Since the extremely small scattering angle is to be measured by the ALFA, the following special beam condition is needed for absolute luminosity calibrations [79].

- To minimize the beam divergence at the IP, the high beta optics is needed ($\beta^* = 2625$ m)

- To have zero beam crossing angle at the IP, the number of bunch should be small

These requirements lead the luminosity for the beam condition for the absolute calibration to about 10^{27}cm^{-2}s^{-1}. The luminosity monitor of the LUCID is also calibrated at this luminosity (by counting inelastic interactions) thus the calibration has to be carried over seven orders of magnitude to the nominal luminosity of 10^{34}cm^{-2}s^{-1}. This is done by simply assuming that the number of inelastic interactions is proportional to the number of particles detected in the LUCID at any luminosity value. This wide measurement range is achieved thanks to the good time resolution, particle counting capability and background rejection power of the LUCID .

4.5.3 Minimum Bias Trigger Scintillator (MBTS)

The main functionality of the MBTS is to provide the minimum bias trigger within $2.09 < |\eta| < 3.84$. The MBTS consists of two sets of scintillation counters located at $|z| = 3560$ mm and segmented into two sections in η (divided at $|\eta| = 2.82$) and eight sections in ϕ. Figure **4.36** is a picture of the MBTS mounted on the endcap calorimeter cryostat (The white disk surrounding the beam pipe is the MBTS).

The scintillation photons are read out by PMTs. The signals are sent to Central Trigger Processor (see section 4.6.1) after discriminated in the front-end electronics. The Central Trigger Processor calculates the multiplicity of hits then issues the MBTS trigger. The lowest threshold MBTS trigger requires only one hit in either side of the MBTS.
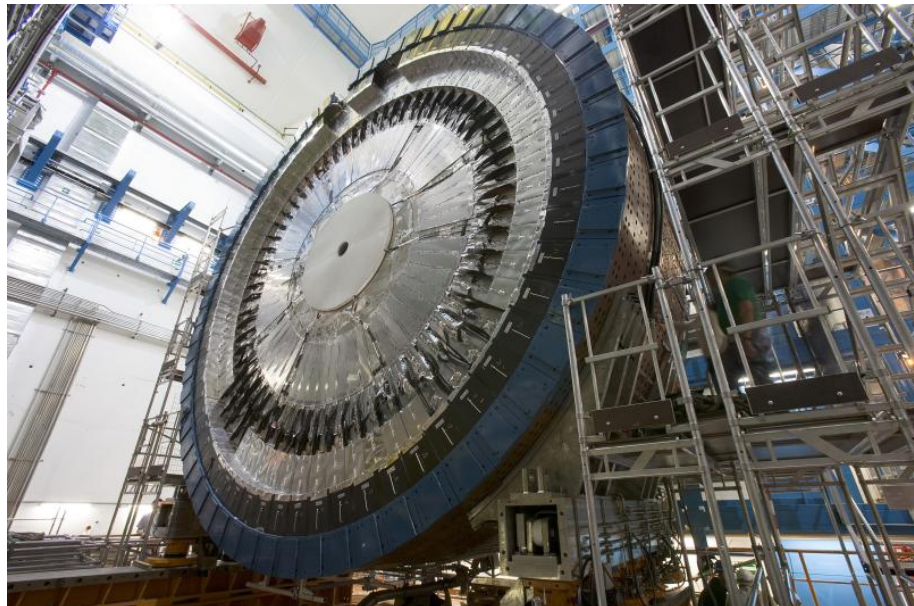
Figure 4.36: A picture of the MBTS mounted on endcap calorimeter cryostat.

4.6 Trigger System

The ATLAS trigger system consists of three levels of event selection, namely Level-1 (L1), Level-2 (L2) and Event Filter (EF) [80, 81]. The L2 – EF chain is also referred to as Higher Level Trigger (HLT) as a whole. L1 trigger decisions are made in the custom-made front-end electronics whereas HLT decisions are made in the dedicated computer farm. A schematic view of the ATLAS trigger system is depicted at Figure **4.37**.
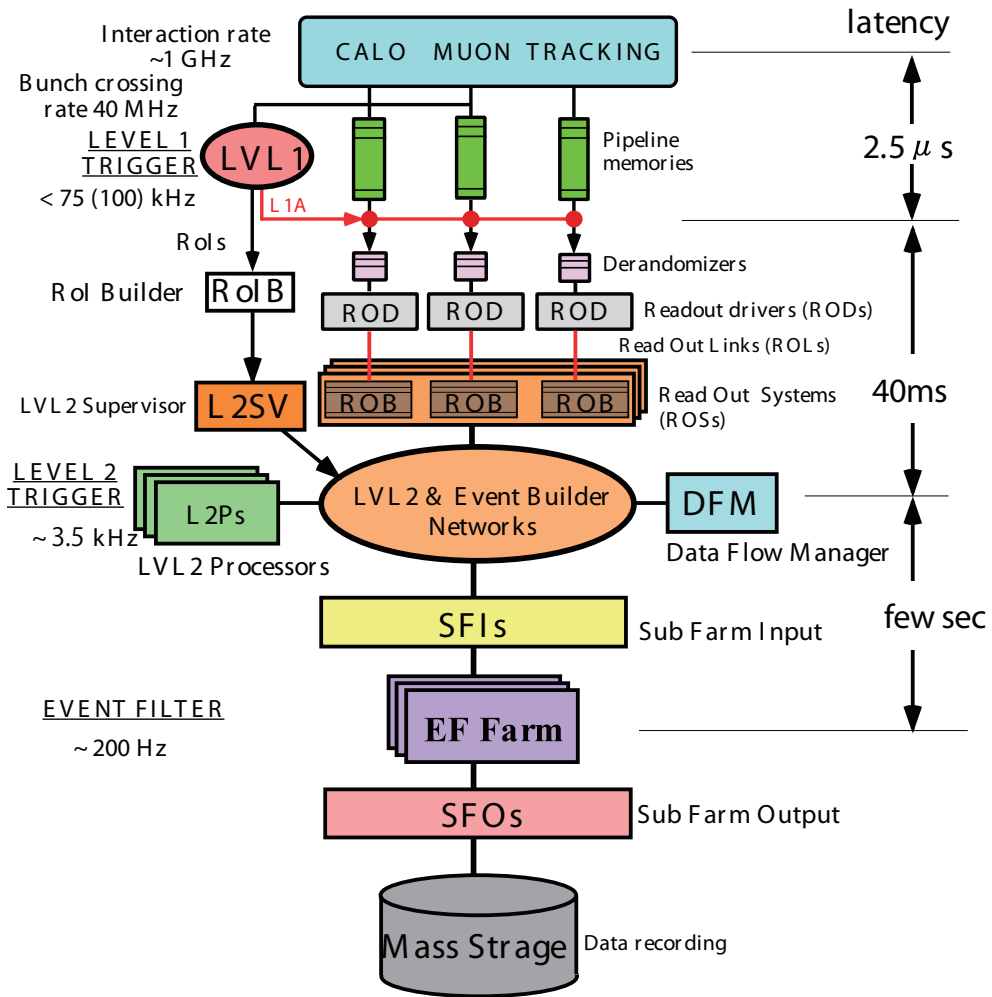
Figure 4.37: Schematic vies of the ATLAS TDAQ system.

The trigger system is responsible for reducing event rate from 1 GHz, which is expected at the design luminosity of the LHC, to recordable rate of about 200 Hz within allowed latency of few seconds.

The trigger system is designed to be sensitive for one or combinations of the following physics objects – muon, electron / photon, tau, jets (including b-tagged jets), missing E_T (E_T^{miss}) and E_T sums. The adequate thresholds are set for each object in terms of p_T and multiplicity.

4.6.1   Level-1 Trigger

The L1 trigger is performed based on the information of all calorimeter (LAr, Tile, HEC, FCal) and the muon spectrometer information. The overall L1 accept decision (L1A) is made by the Central Trigger Processor (CTP), which combined the information for different object types. Trigger menus can be programmed in CTP with up to 256 distinct items, each item being a combination of requirements on the input data. A diagram of the L1 trigger is shown in Figure **4.38**.
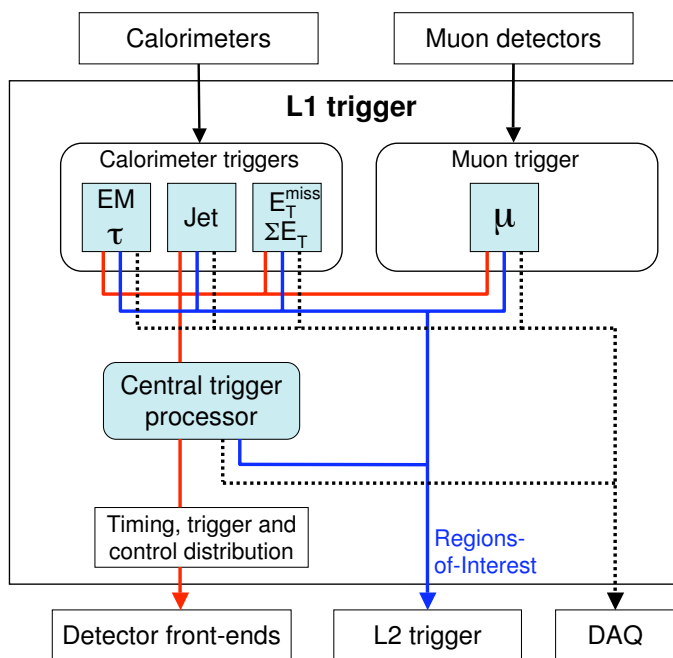
Figure 4.38: Block diagram of the L1 trigger.

The major steps included in the L1 trigger decision are summarized below.

- The number of objects which passed detector specific L1 trigger algorithms for all thresholds are passed from both the calorimeter and the muon spectrometer to the CTP.

- CTP integrates the information and check if any items in the trigger menu are satisfied or not. If one or more items are satisfied, the CTP provides L1A signal to all detectors.

- Upon receiving an L1A, all detectors send the information for all channels retained in their pipeline memories to the buffer storage for the HLT. The calorimeter and the muon spectrometer also send the information about $\eta - \phi$ locations of triggered objects, which is called Region of Interest (RoI). The RoI information is used as seeds in HLT algorithms.

The L1 trigger aims to identify high-p_T muons, electrons / photons, jets, and tau leptons decaying into hadrons, as well as events with large E_T^{miss}, large total transverse energy (E_T sum)

and scalar sum of jet transverse energy. An adequate trigger menu reflecting the situation of the experiments is used at the CTP stage.

At the L1 output, the 1 GHz event rate is reduced down to about 75 kHz within the L1 decision time of 2.5 μs with the unambiguous identification of the bunch crossing.

4.6.2   Level-2 Trigger

The L2 selection is seeded by the RoI information received from the L1 and provides a refined analysis of the L1 features based on the detector data with full granularity within RoIs. Also additional information, which is not available in L1, such as reconstructed track in the ID can be used in the L2 decision. The information from individual detectors can be matched to provide additional rejection and higher purity. For example, a muon reconstructed in the muon spectrometer can be matched with calorimeter information to utilize isolation information or with ID track information to reduce backgrounds.

The L2 trigger reduces the event rate below 3.5 kHz within an event processing time of approximately 40 ms in average.

4.6.3   Event Filter

The EF performs the final online selection on the events which passed L2 selections. As in the L2, the EF works in a seeded mode in nominal operation (for example, there is alternative mode in muon stream for trigger commissioning) with complete data for a given event. Unlike L2, the EF typically uses the algorithms based on the offline reconstruction.

The EF reduces the event rate down to about 200 Hz with an average processing time of order of few seconds.

4.7 Analysis Platform and Monte Carlo Samples

Most of the physics analyses in the ATLAS experiment are performed on the C++ based software framework called ATHENA [82]. In the ATHENA, both simulated and experimental data are processed through the same ATLAS event reconstruction packages to ensure the consistency between the Monte Carlo prediction and experimental results in the analyses. In this section, an overview of the ATHENA framework, with a special emphasis on its data preparation structure, is given.

4.7.1 The Data Preparation Chain in the ATHENA Framework

Shown in Figure **4.39** is a schema of the simulated and experimental data preparation in the ATHENA framework, which consists of following four major steps.

1. Event generation and immediate decays

2. Simulation of the detector and physics interactions

3. Digitization of the energy deposited in the detectors

4. Event reconstruction with dedicated algorithms to each physics object

Overviews for each step are given in the remaining part of this section.

Event Generation

The most of event generation process in the ATHENA framework is performed by external event generators such as PYTHIA [83] and POWHEG [84]. Also, the ATHENA uses the Les Houches Accord PDF Interface (LHAPDF [85]) library with CTEQ PDFs [86] as a default one. Particles with $c\tau < 10$ mm are decayed by the event generator and their interactions with material or curving in the magnetic field in the ATLAS detector are ignored. The resulted event information are stored in the format of HepMC event record [87].

Simulation

The standard simulation in the ATHENA relies on the GEANT4 [88] particle simulation kit which provides models for physics and infrastructure for particle transportation. The geometry description of the ATLAS detector is provided by the ATHENA side in the format which is dedicated for GEANT4. The energy deposited in the active volume of the detector are recorded for the digitization stage. The ATLAS detector geometry used in the simulation is designed to be built from databases containing the information of physical construction and experimental condition to fairly reflect the situation of the experiment. The same geometry description is also used in the digitization and event reconstruction stages.

Digitization

In the digitization stage, the information of the energy deposition is converted into the information of detector responses. The detector specific methods of conversion are deployed in this stage. Typically a digit is produced when the voltage or current on a readout channel crosses a certain threshold within a time window.

Event Reconstruction

The physics object specific reconstruction algorithms, such as for muon, electron and $E_\mathrm{T}^\mathrm{miss}$, are deployed in this stage. Both simulated and experimental data can be treated coherently onwards. The resulted physics object information, in two types of data format with different level of elaborations, each is called Event Summary Data (ESD) or Analysis Object Data (AOD) are used in the physics analyses.
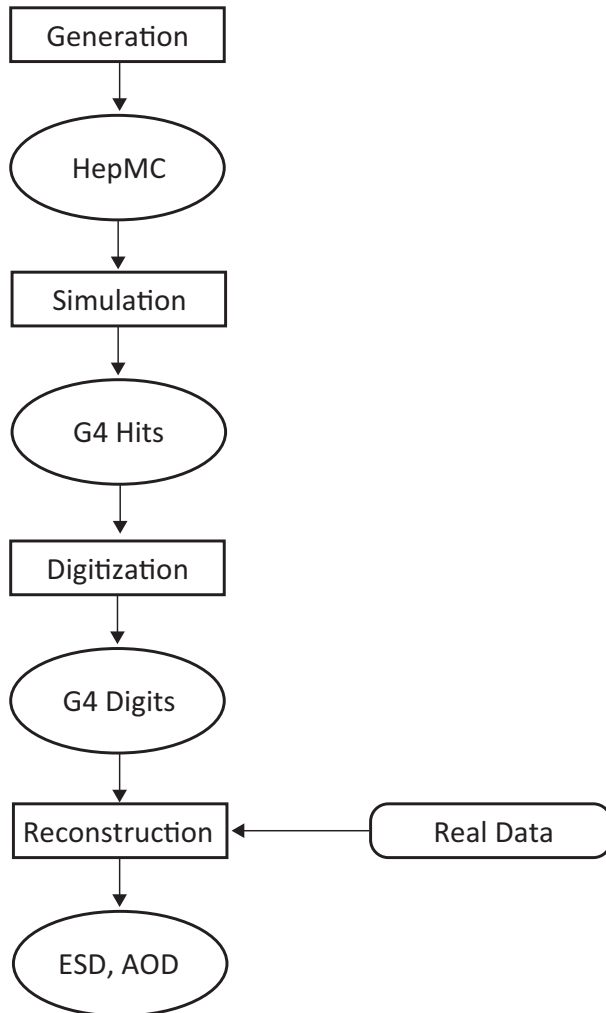
Figure 4.39: A schematic view of the data preparation chain in the ATHENA.

4.7.2 Monte Carlo Samples

Theoretical Prediction on the Cross Sections

The theoretical predictions on the W / Z-boson cross section is obtained from next-to-next-to leading order calculation provided by FEWZ [89, 90] with the MSTW 08 NNLO [91] structure function parametrization.

FEWZ calculates differential W / Z-boson cross sections. The spin correlation of leptons in the final states are considered. The calculations are done fully exclusively in each LO, NLO and NNLO level respectively. FEWZ supports variety of the PDF sets such as CTEQ and MSTW. In the calculation , the renormalization (μ_R) and factorization (μ_F) scales are set as $\mu_R = \mu_F = M_{W/Z}$, where $M_Z = 91.1876$ GeV and $M_W = 80.403$ GeV. The strong coupling constant $\alpha_S (M_Z)$ is dictated by the PDF set.

The MSTW PDF uses 2743 data sets obtained in the previous experiments. The x dependence of each flavor (quarks and gluon) is parametrized with 20 free parameters. Then the PDFs are evolved using the DGLAP evolution equations toward the energy scale (Q^2) in consideration. The resulted PDFs at $Q^2 = 10$ and 10^4 GeV^2 are shown in Figure **4.40** with 68 % C.L. errors from error eigenvectors. For the $t\bar{t}$ cross section, the top mass is assumed as $m_t = 172.5$ GeV and the corresponding cross section is taken from Ref.[92]. For the QCD process, cross sections are obtained by scaling a leading order Monte Carlo result with a data driven scale factor. All the cross section values (σ) used in this study are summarized in the third column in Table **4.6** multiplied by the branching ratio (BR) of the processes. The errors correspond to the systematic uncertainties described hereunder.
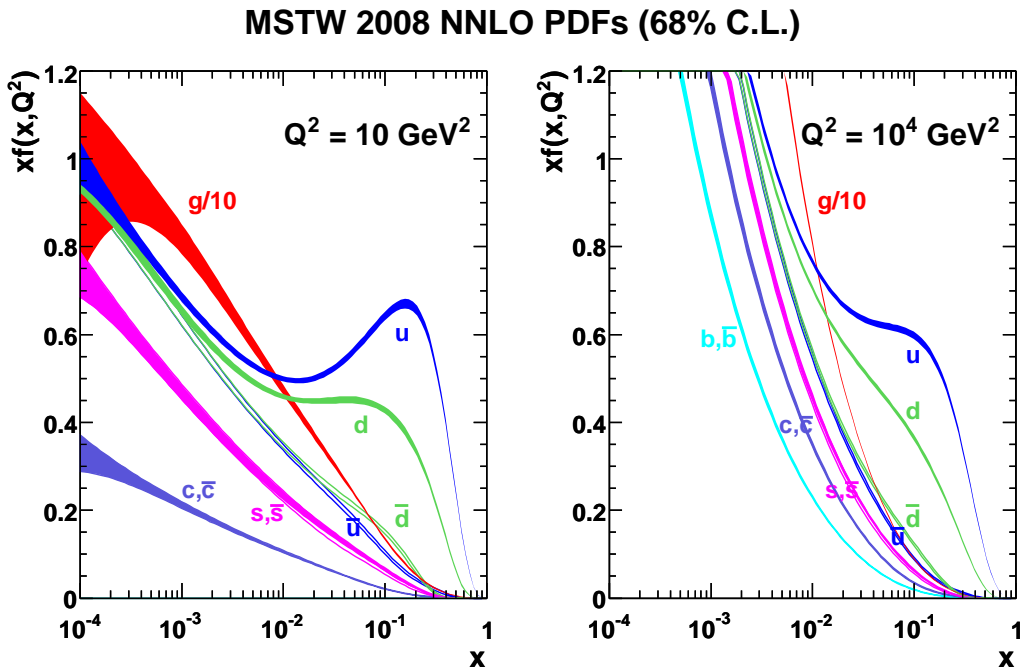
Figure 4.40: The MSTW 2008 NNLO PDFs (68 % C.L.).

For the $W\,/\,Z$ processes, the uncertainty of the next-to-next-to leading order calculation is estimated using the MSTW 08 NNLO PDF error eigenvectors at the 90 % C.L limit, variations of α_s in the range 0.1145 - 0.1176, and variations of the renormalization and factorization scales as $M_{W/Z}/2 < \mu_{R,F} < 2M_{W/Z}$ by factors. The estimated overall uncertainty for the $W\,/\,Z$ processes are 5 %. For the $t\bar{t}$ process, the uncertainty of 6 % is assumed. For the QCD scaling factor, the extraction method and uncertainties are described in section 11.4.1.

Monte Calro Sample Generation

Table **4.6** summarizes the generated data samples used in this study. These samples are used to calculate acceptances and to model the properties of signal and backgrounds. Events are generated using the PYTHIA (POWHEG only for $t\bar{t}$) generators with the MRST LO* [93] parton distribution function. All signal and background samples are generated at $\sqrt{s} = 7$ TeV and processed through the ATHENA data preparation chain described in section 4.7.1. The calculation in the PYTHIA is done in the leading order and the resulted cross section is not so reliable (The reason why PYTHIA is used is for statistics). Thus, in this study, the cross sections for the generated samples are normalized by the NNLO cross sections or a data driven scale factor, as mentioned above.

In the $W \to \mu\nu$, $Z \to \mu\mu$, and di-jet samples, the effect of multiple interactions per bunch crossing (pile-up) is modeled by overlaying simulated minimum bias events over the original hard-scattering event. However this pile-up modeling is not so accurately. Thus an event-by-event weighting of the number of reconstructed vertices is performed as described in section 8.3.3.

Process	Generator	$\sigma \times$ BR (nb)	Calculation order
$W \to \mu\nu$	PYTHIA	10.46 ± 0.52	NNLO
$\quad W^+ \to \mu^+\nu$		6.16 ± 0.31	
$\quad W^- \to \mu^-\nu$		4.30 ± 0.21	
$Z \to \mu\mu$ ($\sqrt{\hat{s}} > 60$ GeV)	PYTHIA	0.99 ± 0.05	NNLO
$W \to \tau\nu \to \mu\nu\nu$	PYTHIA	3.68 ± 0.18	NNLO
$Z \to \tau\tau$ ($\sqrt{\hat{s}} > 60$ GeV)	PYTHIA	0.99 ± 0.05	NNLO
$t\bar{t}$	POWHEG	0.16 ± 0.01	NNLO
		$\left(\epsilon_{1\,\mu} = 0.538 \right)$	
di-jet (8 GeV/c single muon filter)	PYTHIA	10.6×10^6	LO

Table 4.6: Summary of the Monte Calro samples used in this study. The cross-sections are the ones used to normalize number of events except for QCD di-jet samples. For QCD samples, a data driven scale factor is used for a normalization.

Chapter 5

The Muon Trigger at the ATLAS Experiment

In accordance with the ATLAS trigger scheme, the ATLAS muon trigger consists of following steps.

- The Level-1 muon trigger provided by the TGC and the RPC in $|\eta| < 2.4$

- The Level-2 and the Event Filter using other muon spectrometer (MDT and CSC) information as well as the inner detector and the calorimeter information as an auxiliary use

In each step, trigger scheme is designed and optimized to select high-p_T muons.

Description about general principle of the muon identification and transverse momentum measurement is given in section 5.1. Then the successive sections are devoted to describe each level of muon trigger – section 5.2 for the Level-1, section 5.3 for the Level-2 and section 5.4 for the Event Filter. Since only Level-1 trigger is used in the W / Z-boson cross sections measurement, a strong emphasis is placed on it.

5.1 Muon Identification and Transverse Momentum Measurement

Muon is only particle which can penetrate thick dense matters like calorimeter. Most of heavy particles decay even before they enter the calorimeter. The particles with long life time, such as electron and light hadrons (π / K) loose all of their energy in the calorimeter. Hence the assumption that a track reconstructed in the muon spectrometer represents a muon trajectory becomes true. In the first part of this section, a description about energy deposition of particles in matter is given to illustrate the muon identification principle.

The transverse momentum measurement in the muon spectrometer is based on the detection of the deflection of muons in a magnetic field. The second part of this section is devoted to describe this principle of transverse momentum measurement of muons.

5.1.1   Energy Loss of Charged Particles in Matter

Ionization Energy Loss

Moderately relativistic charged particles ($0.1 < \beta\gamma < 1000$) other than electrons lose their energy in matter primarily by ionization and atomic excitation. The mean rate of energy loss in the region is described by the Bethe-Bloch equation in Eq.(5.1).

Figure **5.1** shows the energy deposition of positive muons in copper. The unit of dE/dx is $\mathrm{MeVg^{-1}cm^2}$ hence this distribution is also true for other materials. The region where Bethe-Bloch approximation is valid is also indicated.

$$-\frac{dE}{dx} = Kz^2\frac{Z}{A}\frac{1}{\beta}\left[\frac{1}{2}\ln\frac{2m_ec^2\beta^2\gamma^2T_{\max}}{I^2} - \beta^2 - \frac{\delta(\beta\gamma)}{2}\right]. \tag{5.1}$$

$$K = 4\pi N_A r_e^2 m_e c^2$$

N_A :   Avogadro's number r_e : classical electron radius m_e : electron mass

Z :   atomic number of the matter A : atomic mass of the absorber

z :   electric charge of the incident particle I : mean excitation energy

$T_{\max}$:   the maximum kinetic energy imparted to a free electron in a single collision
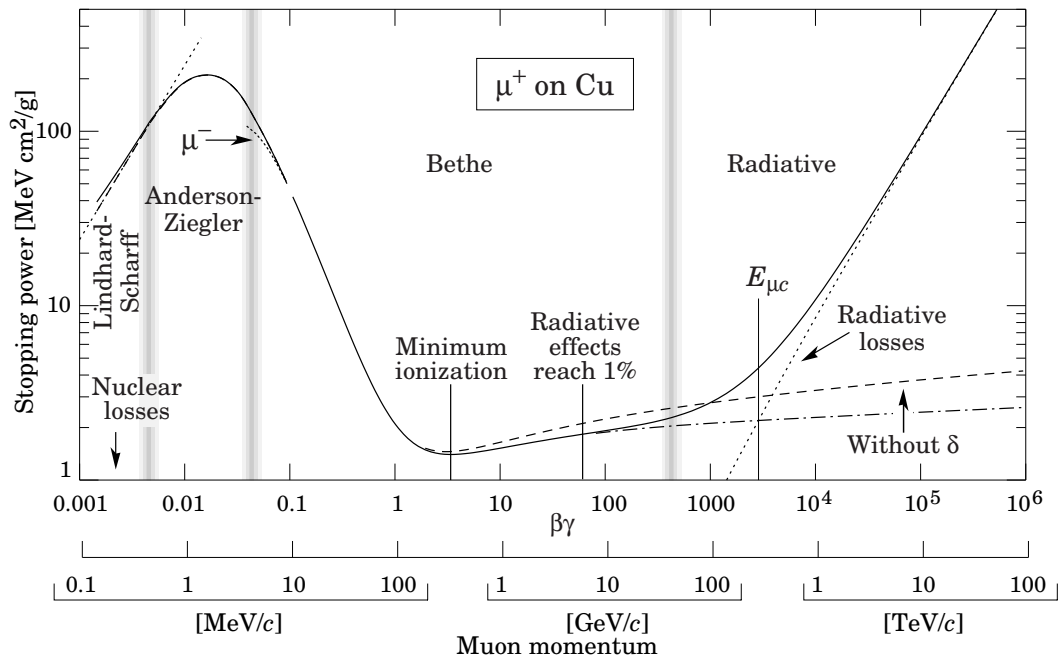
Figure 5.1: $-dE/dx$ for positive muons in copper as a function of $\beta\gamma$ (solid curve) [36].

The main features about $\beta\gamma$ dependence of mean rate of energy loss are as follows.

1. In the region of $0.1 < \beta\gamma < 1$, where classical electromagnetism is valid, the dE/dx is proportional to $1/\beta^2$.

2. Around $\beta\gamma = 3$, the energy deposition minimizes. In practical cases, most relativistic particles have mean energy deposition close to the minimum, and are said to be minimum ionizing particles (MIPs). Most of particles arise from proton-proton collisions at the LHC is MIPs.

3. In the region of $4 < \beta\gamma < 100$, the electric field formed by the incident particle flattens and extends due to the relativistic effect so that distant collision contribution increases as $\ln(\beta\gamma)$. This effect is called relativistic rise.

4. After relativistic rise reaches its maximum around $\beta\gamma = 100$, dE/dx becomes constant. This region is called Fermi Plateau.

The lower limit of the Bethe-Bloch region comes when the velocity of the incident particle becomes comparable to that of electrons in atoms. The higher limit is at several hundred GeV where muons become radiative and begin to lose its energy through bremsstrahlung.

As mentioned above, most of muons arising in the proton-proton collision in the LHC are MIPs. Concerning the thickness of the ATLAS calorimeter, muons with energy above 3 ~ 4 GeV can reach to the muon spectrometer.

The Energy Loss of High Energy Electrons – Electromagnetic Cascade
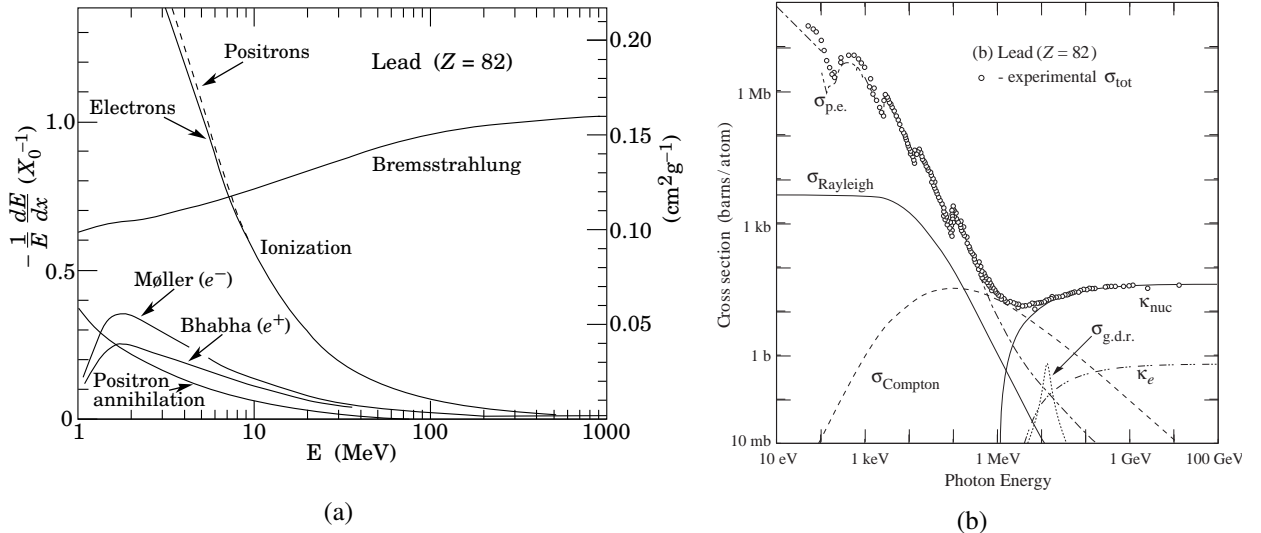
Figure 5.2: (a) Fractional energy loss per radiation length in lead as a function of electron or positron energy (b) Photon total cross section in lead as a function of energy

The radiation length (X_0) is defined as the average distance that an electron (positron) traverses in matter until it lost their energy down to $1/e$, can be expressed as a material dependent form

$$X_0 = \frac{716A}{Z(Z+1)\ln(287/\sqrt{Z})} \quad (\text{g/cm}^2). \tag{5.2}$$

Figure **5.2** (a) shows the fractional energy loss per X_0 for electron in lead. As in the figure, energy loss is dominated by the bremsstrahlung for incident energy above 10 MeV.

Figure **5.2** (b) shows the cross section of photons in lead. At the energy higher than 5 MeV, the energy deposition of the photon is dominated by the electron-position pair production due to nuclear or electron field (κ_{nuc} or κ_e). The average mean free path for a photon in terms of electron-positron pair production is called conversion length (X_p), which can be expressed as

$$X_p = \frac{9}{7}X_0.$$
(5.3)

When a high energy electron passes through the matter, it is very likely to create secondary photons by bremsstrahlung which also results third generation of an electron-position pair production. Third process continues until daughter particles do not have enough energy to create next particles. In this case, energy of final daughter particles only degraded through ionization. This phenomenon is called electromagnetic cascade.

The critical energy E_c is defined as the energy when the energy losses by ionization per radiation length equals to the traversing electron energy. Here, consider how many generations are created until the daughter particles energy become lower than E_c under the assumption that mean free path of bremsstrahlung and pair production is equals to X_0. Define N_{total} as the total number of produced electrons (+ positrons), t the length of cascade in the unit of X_0, $t_{\max}$ the t where final daughter particles are created, E_0 the initial energy of the incident electron

$$
\begin{aligned}
N_{\text{total}} &= \sum_{t=0}^{t_{\max}} 2^t \\
&= 2^{(t_{\max}+1)} - 1 \\
&\sim 2 \cdot 2^{t_{\max}} \\
&= 2\frac{E_0}{E_c},
\end{aligned}
$$
(5.4)

$$t_{\max} = \frac{\ln E_0/E_c}{\ln 2}.$$
(5.5)

The 95 % of the typical cascade length is expressed as

$$t_{95\%} = t_{\max} + 0.08Z + 9.6.$$
(5.6)

Taking lead ($E_c = 11.8$ MeV) as an example the $t_{95\%}$ is calculated as 23 (X_0). The thickness of the ATLAS EM calorimeter is about 25 X_0 hence most of electrons loose its energy through electromagnetic cascade and can not reach the muon spectrometer.

In addition, the critical energy for the muons can be expressed as

$$E_c^\mu = E_c^{elec} \left(\frac{m_\mu}{m_e}\right)^2.$$
(5.7)

Here $m_\mu/m_e \sim 200$, thus muons very unlikely to loose their energy through electromagnetic cascade.

The Energy Loss of High Energy Hadrons – Hadronic Cascade

High energy hadrons loose their energy through the sequential strong interactions, called Hadronic Cascade, as electrons lose their energy through electromagnetic cascade. Characteristic process in hadronic cascade is production of secondary hadrons by the strong interaction within a mean free path of λ, which is defined as the length through which hadrons lose their energy down to $1/e$. Figure **5.3** shows the longitudinal depth of hadrons in the unit of λ. The ATLAS hadronic calorimeter has the thickness of about 10 λ, hence most of hadrons are absorbed in the hadronic calorimeter and can not reach the muon spectrometer.
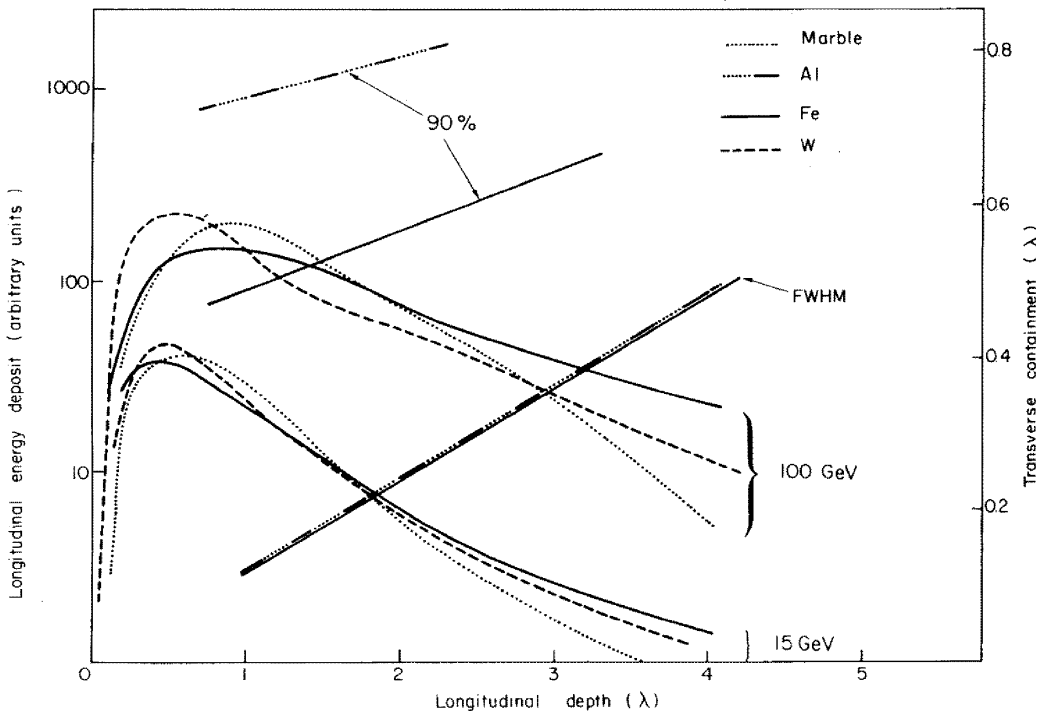
Figure 5.3: Energy deposition of hadrons in a matter [1].

$t_{\max}$ for hadrons can be expressed as

$$t_{\max}(\lambda) \sim 0.2\ln E \text{ (GeV)} + 0.7, \tag{5.8}$$

$$t_{95\%}(\lambda) \sim a\ln E + b, \tag{5.9}$$

where a and b are material dependent parameters. Taking irons as an example, $a = 9.4$ and $b = 39$ and $\lambda = 16.7$ cm. Then the $t_{95\%}$ for a hadron with energy of 100 GeV is calculated as 80 cm.

5.1.2   Muon Transverse Momentum Measurement

Figure **5.4** shows a drawing which illustrates the motion of a negative charged particle in a homogeneous magnetic field. As depicted in the figure, the trajectory behaves as a helix with a constant radius.
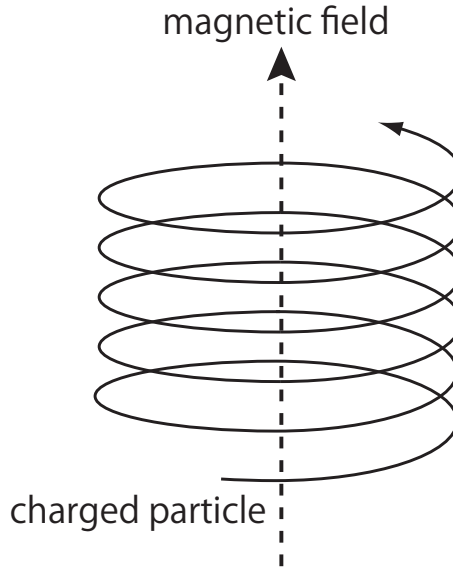
Figure 5.4: Motion of a negative charged particle in a homogeneous magnetic field.

A charged particle is subjected to Lorentz force in the magnetic field as

$$\vec{F} = q\left(\vec{v} \times \vec{B}\right), \tag{5.10}$$

where q is the electric charge of the particle, $\vec{v}$ the velocity, $\vec{B}$ the magnetic flux. Then the equation of motion is expressed as

$$\frac{mv^2}{\rho} = q\left(\vec{v} \times \vec{B}\right),$$
$$\rightarrow \quad p_\mathrm{T} = qB\rho, \tag{5.11}$$

where ρ is the radius of helix. Thus p_T of the particle with unit charge is

$$p_\mathrm{T}\,(\mathrm{GeV}) = 0.3B\rho\,(\mathrm{T} \cdot \mathrm{m}). \tag{5.12}$$

The equation means that one can calculate the p_T of a charged particles with the knowledge of the magnetic field and the curvature of the trajectory.

One of the straightforward approach to measure p_T is to fully reconstruct a trajectory with large number of precision position measurement. However there also exists useful and practical application for charged particle p_T determination, sagitta measurement. Figure **5.5** shows an overview of the sagitta measurement.
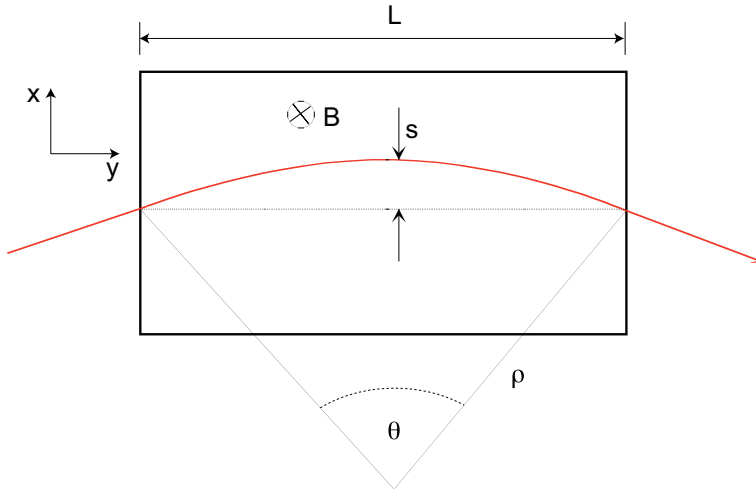
Figure 5.5: Sagitta measurement in a magnetic field.

Here transverse direction is defined as *x*-coordinate and longitudinal direction as *y*-coordinate. In the figure, *s* is a sagitta and *L* means the length in the longitudinal direction of the region where magnetic field exists. An assumption that $\rho \gg L$ is made in the discussion hereunder.

$$\frac{L}{2\rho} = \sin\theta/2 \ \sim \ \theta/2 \ \rightarrow \ \theta \sim \frac{0.3LB}{p_T}, \tag{5.13}$$

$$s = \rho\left(1 - \cos(\theta/2)\right) \ \sim \ \rho\frac{\theta^2}{8} \ \sim \ \frac{0.3}{8}\frac{L^2 B}{p_T}. \tag{5.14}$$

Here *s* the sagitta. As seen, sagitta *s* can be measured by the measurement of arbitrary three points in the magnetic field. Define each of the point as x_1, x_2 and x_3 with the error of $\sigma(x)$, then sagitta can be expressed as

$$s = x_x - \frac{1}{2}\left(x_2 + x_3\right), \tag{5.15}$$

here the resolution of p_T can be expressed as

$$\frac{\sigma(p_T)}{p_T}\Big|^{meas} = \frac{\sigma(s)}{s} = \frac{\sqrt{\frac{3}{2}}\sigma(x)}{s} = \frac{\sqrt{\frac{3}{2}}\sigma(x) \cdot 8p_T}{0.3 \cdot BL^2}. \tag{5.16}$$

As can be seen, the longer *L* is the more accurate $\sigma(p_T)/p_T$ becomes. This is why the ATLAS muon spectrometer deploys such a long lever-arm.

The ATLAS muon trigger system is based on the concept of the sagitta measurement thus they basically have three station structure. In barrel, all the RPC three layer immersed in the magnetic field, thus the detector actually measures sagitta. On the contrary in endcap, the detector configuration does not allow three points measurement in the magnetic field. Thus the IP is taken as an additional measurement and muons are assumed to be coming from the IP.

5.2   Level-1 Muon Trigger

The ATLAS L1 muon trigger consists of mainly the following three components.

- The TGC which consists of 144 trigger sectors ($1.05 < |\eta| < 2.4$)

- The RPC which consists of 64 trigger sectors ($|\eta| < 1.05$)

- The MUon to Central Trigger Processor Interface (MUCTPI)

A schematic drawing is shown in Figure **5.6** [94].
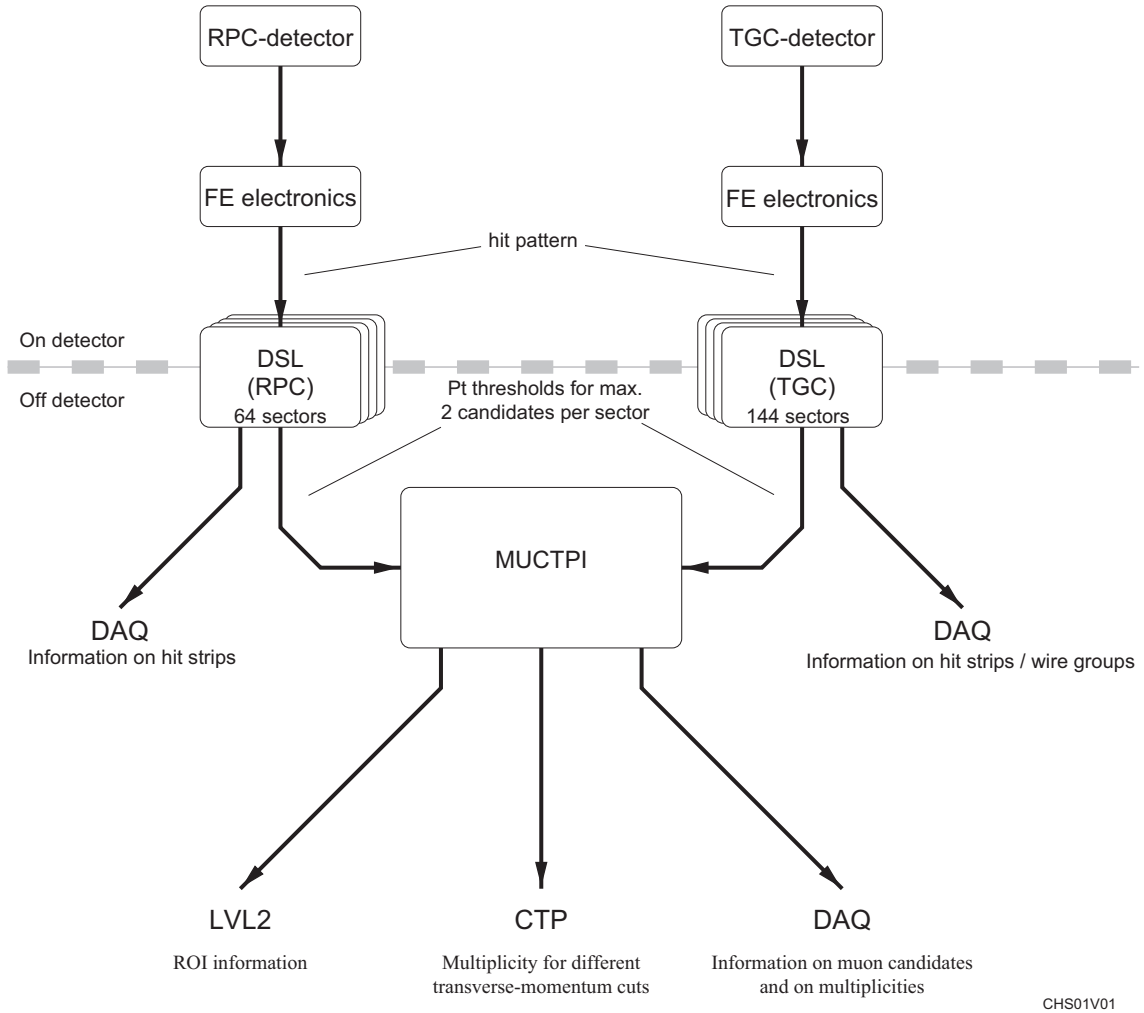
Figure 5.6: A schematic drawing of the ATLAS L1 muon trigger.

Both the TGC and the RPC can send up to two muon candidates per trigger sector to MUCTPI in an event with corresponding p_T threshold values. The MUCTPI calculates overall muon multiplicity for each of p_T threshold with correct overlap solving, After data processing and formatting, results are sent to the CTP, the L2 trigger and the DAQ. In this section, descriptions about each component are given.

5.2.1   Level-1 Endcap Muon Trigger

The endcap muon trigger is provided by the TGC placed on the both sides in a mirror symmetric manner. Figure **5.7** shows the layout of the TGC system on one side.
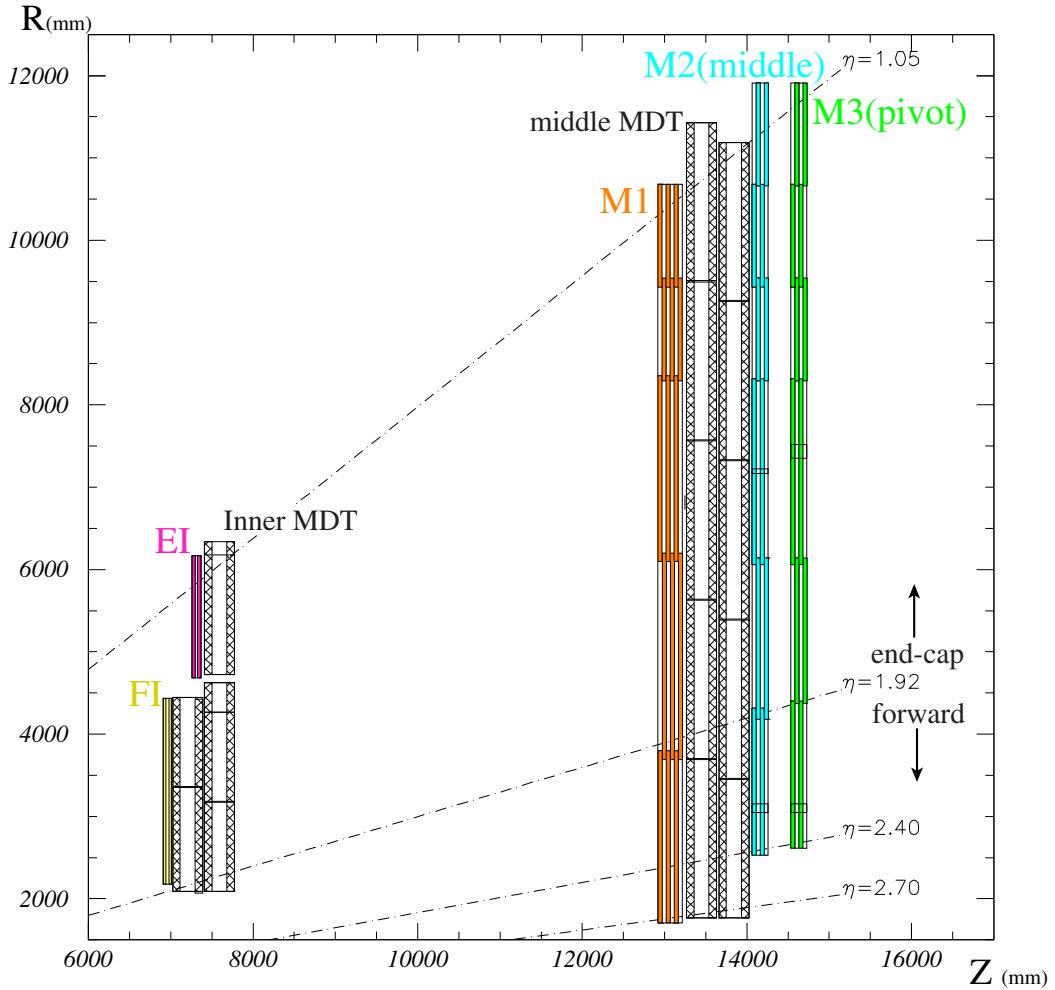
Figure 5.7: The cross section in $R - Z$ plane of the TGC system.

The TGC consists of five stations namely EI (Endcap Inner), FI (Forward Inner), M1, M2, and M3 from inside to the outside. The M1 station is using triplet chambers and M2 and M3 station are using doublet chambers as depicted in Figure **4.30**. M3 station is also referred to as the pivot plane. The TGC stations cover $1.05 < |\eta| < 2.4$ region for triggering except for the innermost stations (EI / FI) which covers $1.05 < |\eta| < 1.9$. In this section, the trigger algorithm, detector segmentation and its implementation of the TGC are given.

Trigger Algorithm

Figure **5.8** shows a scheme of muon p_T decision performed by the TGC. The basic principle of the TGC trigger algorithm is summarized as follows.
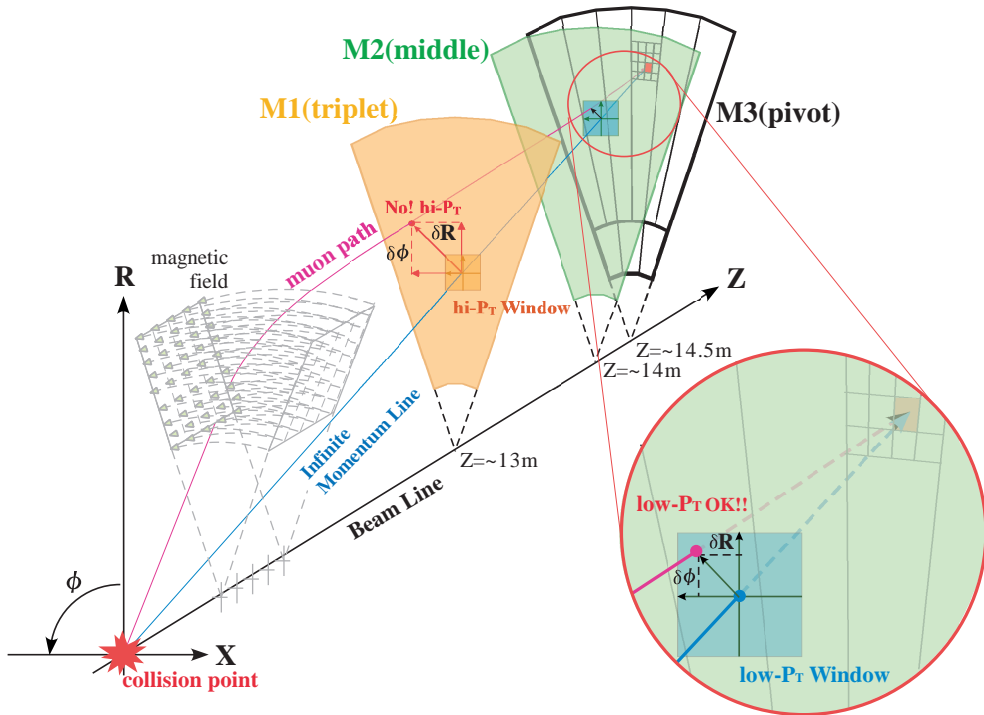
Figure 5.8: The p_T decision scheme in the TGC.

- The trigger algorithm extrapolates a given hits on the M3 to the interaction point with straight line assuming an infinite momentum upon a passage of a muon. Then a window is constructed around the infinite momentum path on each non-pivot plane (M1, M2) in $r - \phi$ coordinates separately.

- Hits are searched on non-pivot planes to take coincidence first between M2 and M3 then between M1 and M3. The coincidence between doublet pair of M2 and M3 requires 3-out-of-4 condition within a window. This is called low-p_T coincidence for its relatively short lever arm. On the top of low-p_T coincidence, the coincidence between M1 and M3 is taken requiring 2-out-of-3 condition in η and 1-out-of-2 condition in ϕ within the M1 triplet layers. The coincidence conditions are adjustable. In both coincidences, deviations of hits from the infinite momentum path, which is considered as pseudo-sagitta are measured to calculate p_T of muons.

- The final p_T measurement is made by merging the results in both coordinates referring the map which describes the correspondence between measured deviations and p_T of muon. This map is prepared for each RoI. Then the six levels of the p_T threshold is applied and muons are classified according to the highest threshold they passed.

Detector Segmentation

The coverage of the TGC is divided into several types of logical units. The segmentation in a M3 octant is shown in Figure **5.9**.
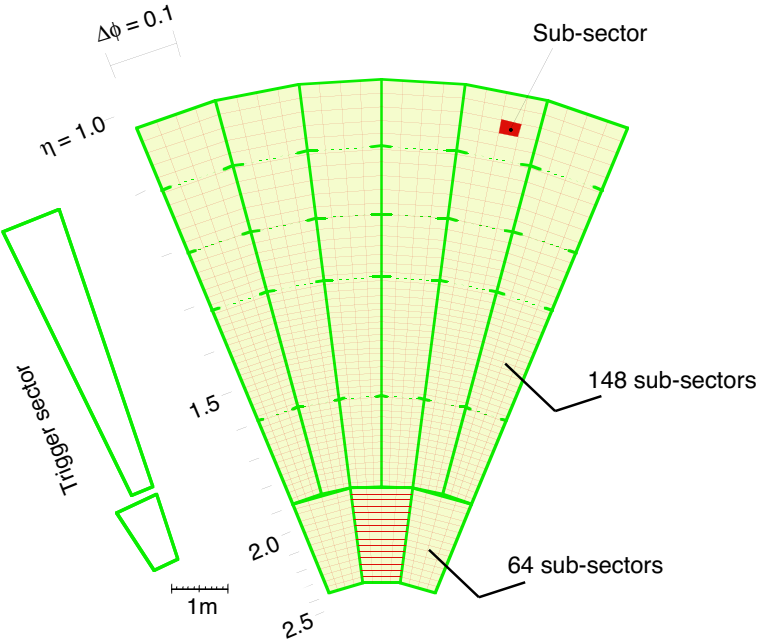
Figure 5.9: A schematic view of the segmentation of a TGC octant.

The TGC coverage is divided into two regions namely endcap ($|\eta| < 1.92$) and forward ($|\eta| > 1.92$) in η. The endcap region of each octant is divided into six trigger sectors in ϕ. The forward octant contains three trigger sectors. There are hence 48 endcap trigger sectors and 24 forward trigger sectors on one side of the TGC. Each trigger sector consists of independent sub-sectors, which corresponds to the TGC RoIs. The number of sub-sectors contained in a trigger sector is 148 in endcap and 64 in forward.

System Implementation

The trigger algorithm outlined above is implemented in purpose-built electronics, partly mounted on and near the TGC chambers, and partly located in the underground counting room. A schema of the trigger and readout chain is shown in Figure **5.10**.

- **ASD:** The wire and strip signals emerging from the TGC are fed into a two-staged amplifier in an Amplifier Shaper Discriminator (ASD [95]) circuit. Four ASD circuits are built into a single ASD chip and four ASD chips are incorporated into an ASD board hence each ASD board handles 16 channels of signals. The ASD board is physically attached to the edge of a TGC and enclosed inside shielding boxes.

- **Patch-Panel:** Signals from the ASD boards are sent to a so-called PS board where Patch-Panel (PP) ASICs and Slave Board (SLB) ASICs are implemented. Figure **5.11** shows a
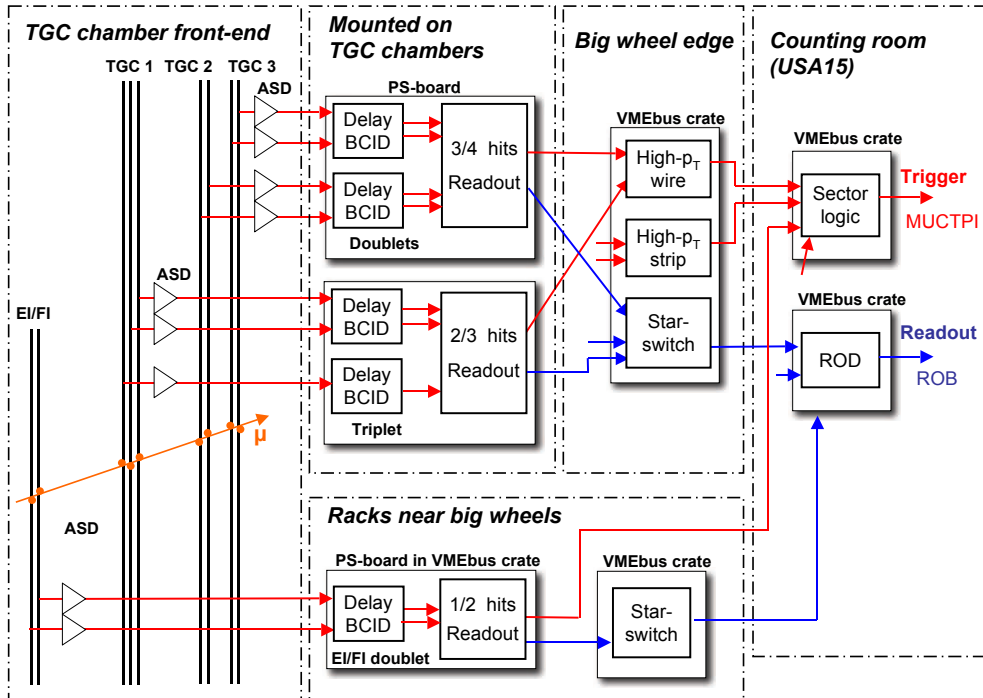
Figure 5.10: A schematic view of the TGC electronics system.

block diagram of the Patch-Panel ASIC. The number of input channels is 32. The main functionality of the Patch-Panel is summarized as follows.

1. **Signal Delay:** The signals from the ASD board are fed into the variable delay logic at first to adjust the delay difference from TOF, cable length and so forth. The delay can change from 0 to 25 ns with sub-nanosecond resolution. The Patch-Panel ASIC is sub-divided to two-parts and each part is responsible to 16 channels come from the same ASD board. Setting of the delay is common to these 16 channels.

   A block diagram of the variable delay logic is shown in Figure **5.12**. The delay logic consists of two parts – delay part (upper side in the figure) and control part (bottom side in the figure) – both parts deploy 32 stages of delay unit and inverter gate. In the control part, delay units form a Voltage Controlled Ring Oscillator (VCON) and the total delay length of VCON is locked to 25 ns using Phase Lock Loop (PLL) logic. The number of delay unit in VCON (N_{con}) is adjustable. This phase lock realizes the situation that all the delay units via common voltage control line have the same delay time of 25 / N_{con} ns. The number of delay units used in the delay line (N_{delay}) is also adjustable from 0 to 31.

2. **Channel Mask:** The Patch-Panel ASIC also can mask individual noisy or malfunctioning channels. This functionality is implemented in the BCID circuit shown in Figure **5.13**.

3. **Bunch Crossing IDentification (BCID):** Figure **5.13** shows the conceptual design
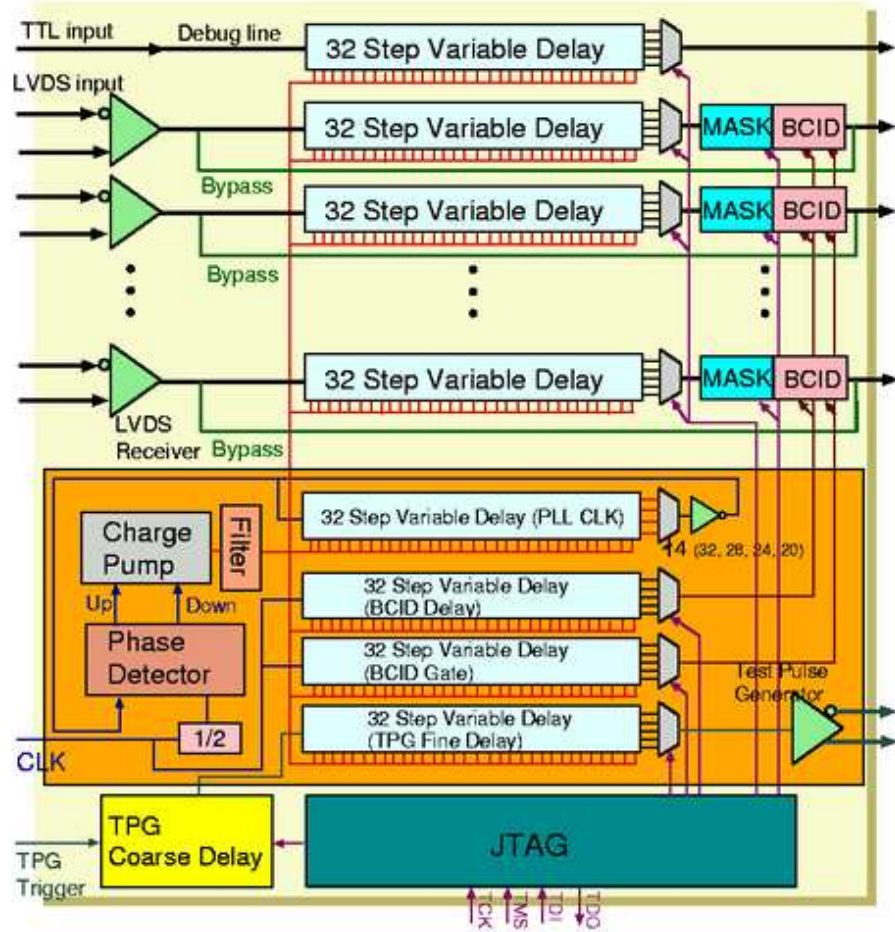
Figure 5.11: A block diagram of the Patch-Panel.
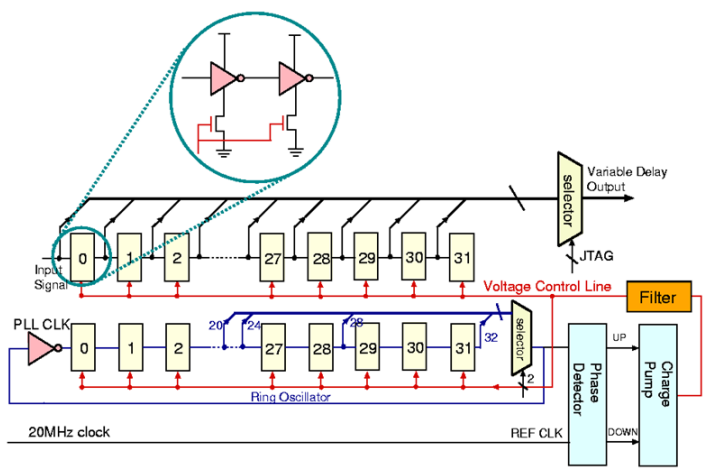
Figure 5.12: A block diagram of the variable delay logic in the Patch-Panel ASIC.

of the BCID circuit which contains two variable delays. The first delay is used to adjust the phase difference between the signals and 40 MHz clock provided by the LHC. The second delay is used to adjust the effective gate width from 26 ns to 48 ns. Values set for each delay are common to a group of 16 channels from an ASD board.
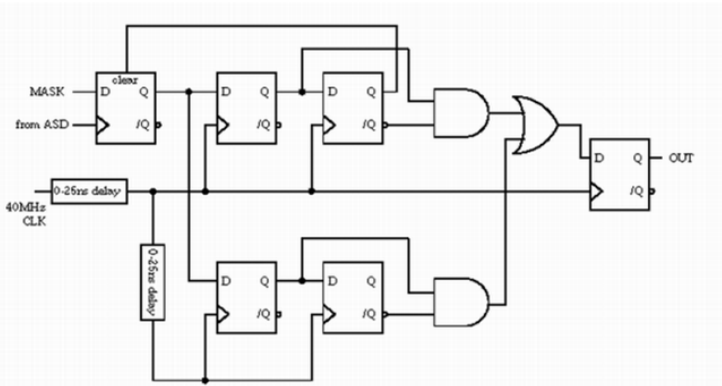
Figure 5.13: A schematic of the BCID circuit on the Patch-Panel ASIC.

The outputs from the Patch-Panel are fed to the on-board logic to solve physical overlap in the TGCs.

- **Slave Board:** SLB ASIC typically receives 32 channels of BCID assigned wire and strip signals from the Patch-Panel and fed them into a so-called coincidence matrix. The SLB ASIC can be configured to have different five types of coincidence matrices namely for triplet-wire, triplet-strip, doublet-wire, doublet-strip and EI / FI. Figure **5.14** shows a block diagram of the SLB ASIC. The functionalities of the SLB are divided into two parts, namely trigger part and readout part. Overviews of each part is as follows.

  1. As mentioned above, the trigger part of the SLB deploys so-called coincidence matrix. The coincidence matrix can be configured to perform different five types of coincidence pattern. Figure **5.15** shows the detailed structure of the coincidence matrix for wire doublets in 3-out-of-4 configuration.

  2. The hit data from the Patch-Panel is stored in the pipe-line memory mounted on the SLB ASIC called L1 buffer during the period of L1 latency. They are read out upon an arrival of the L1 accepted signal together with the data taken in neighboring bunches (previous and next bunch). Otherwise the stored data will be discarded.

     The read out data are sent to the so-called Star Switch module which collects the formatted hit data from the SLBs then multiplexes and randomize them. After that the data is sent to the ROD module and shaped into an ATLAS standard readout format. Finally, the hit data is sent to the ROB i.e. the central DAQ buffer.
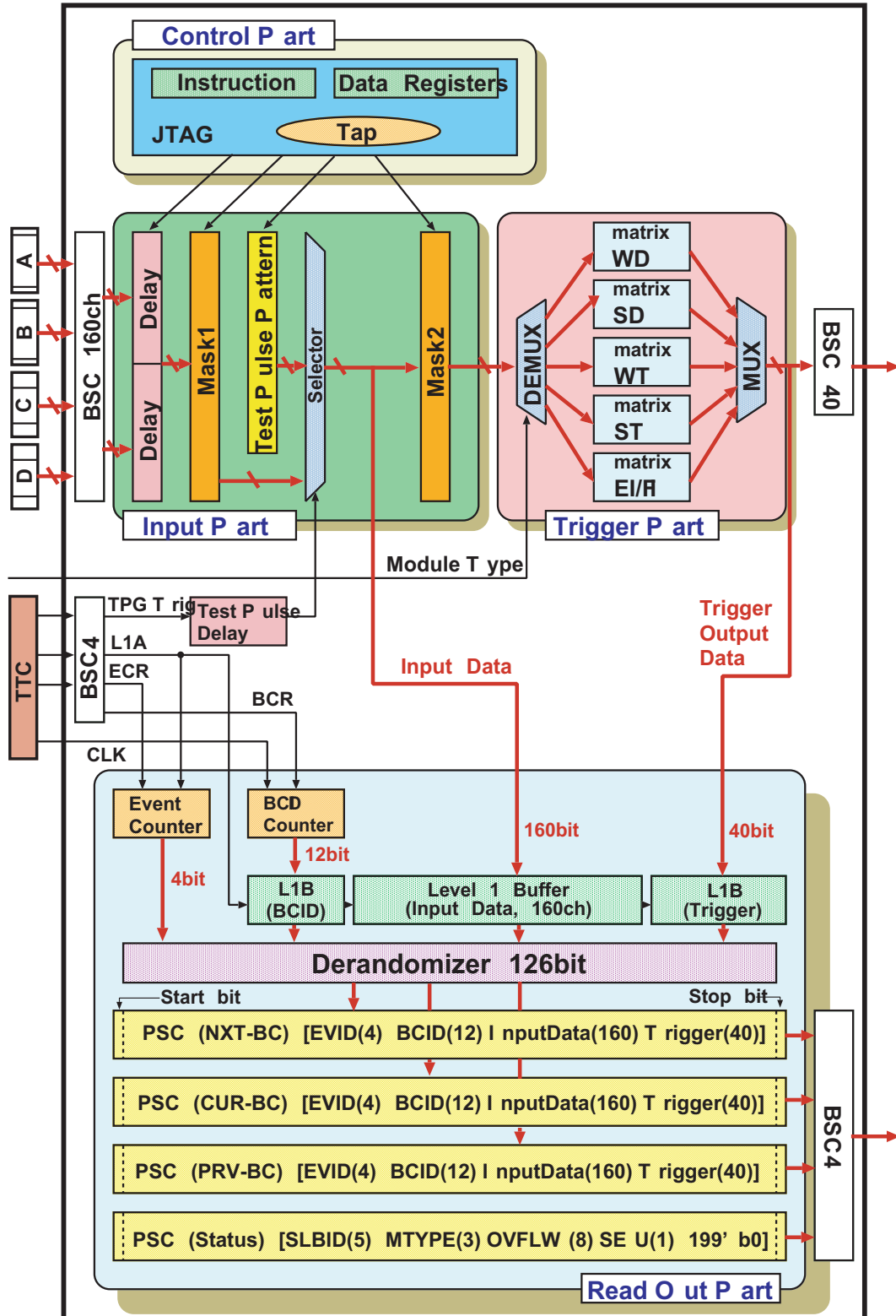
Figure 5.14: A block diagram in the SLB ASIC.

12x2 (middle doublet) inputs

4x2 (pivot doublet) inputs

OR'ed Y

8 outputs to encoder section

a
b —▭—▸ C   C = a & $\overline{b}$ & c + $\overline{a}$ & b & $\overline{c}$
c

A B
C ·······▭—▸ Y
D

X = Y = A & C + A & D + B & D

-7 -6 -5 -4 -3 -2 -1   0   1   2   3   4   5   6   7

δR

OR'ed X

SOS043V05
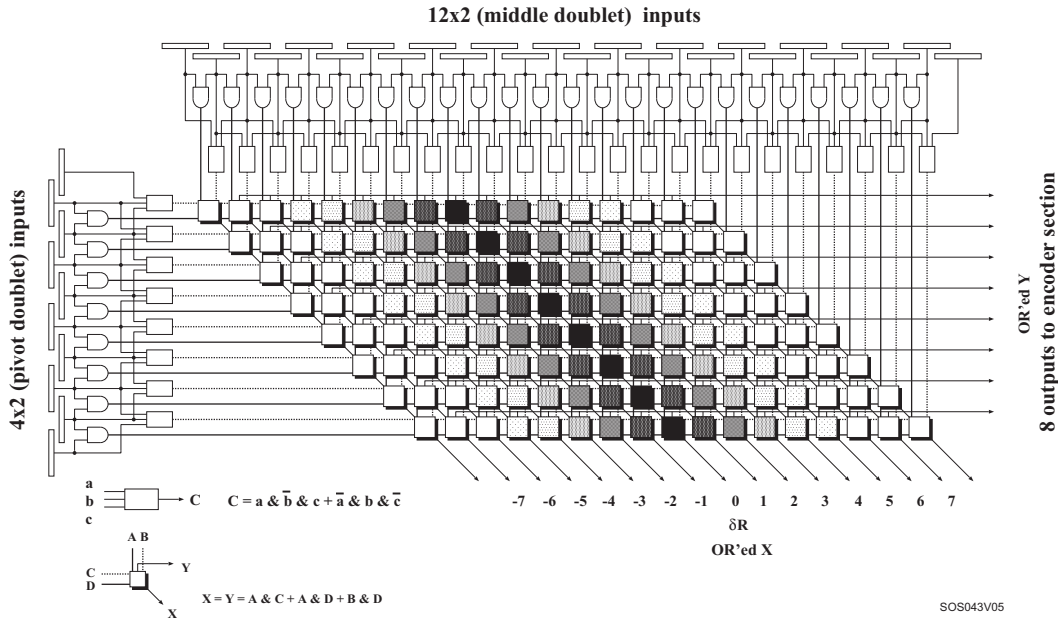
Figure 5.15: A schematic illustration of the wire doublet coincidence matrix in SLB ASIC.

- **High-p_T Board:** Trigger signals from the SLBs are combined to identify high-p_T track candidates in coincidence boards combining all three trigger planes (M1, M2 and M3), so-called high-p_T boards, located in dedicated mini-racks around the outer rim of the triplet wheel. Wire (r-coordinate) and strip (ϕ-coordinate) information is still treated separately at this point. Figure **5.16** shows the functional structure of a wire high-p_T ASIC.

from 4 wire triplet
Slave Boards

18 Phase adjust
18 Phase adjust
18 Phase adjust
18 Phase adjust

Clock

from 3 wire doublet
Slave Boards

18 Phase adjust
18 Phase adjust
18 Phase adjust

Decoder

Decoder

192 x 232
2-fold
Coin. Matrix

window size: ±20

H/L Pt   hit position δR

x 2

track selector

Position + δR
7-bit x 6

Position + δR
10-bit x 2

SOS063V11
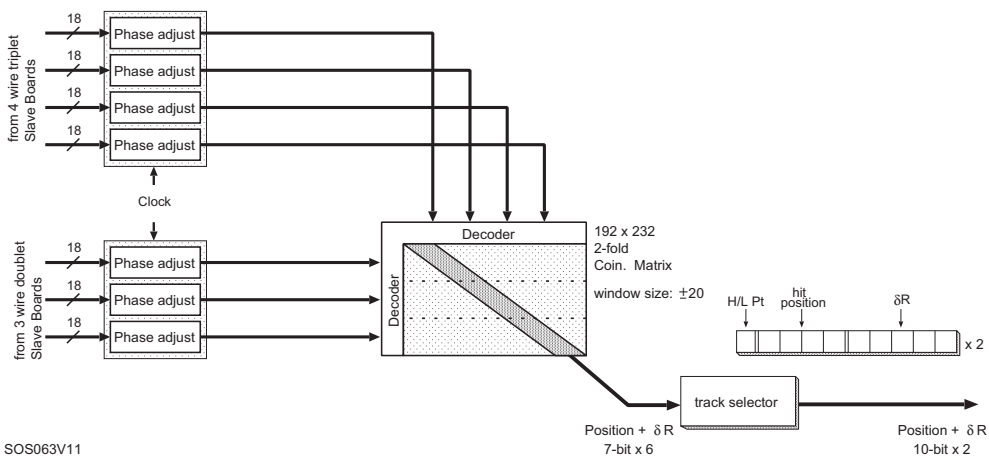
Figure 5.16: A schematic illustration of the functionalities in a wire high-p_T ASIC.

- **Sector Logic:** Signals from high-p_T boards are sent to Sector Logic (SL) boards containing an $r - \phi$ coincidence unit and a track selector to select the highest-p_T candidate. The SL also receives directly the signals from the EI / FI slave boards and can incorporate them into the trigger logic. The resulting trigger information for 72 separate trigger sectors per side are sent to the MUCTPI. Figure **5.17** shows an example of the coincidence matrix configured in the SL.
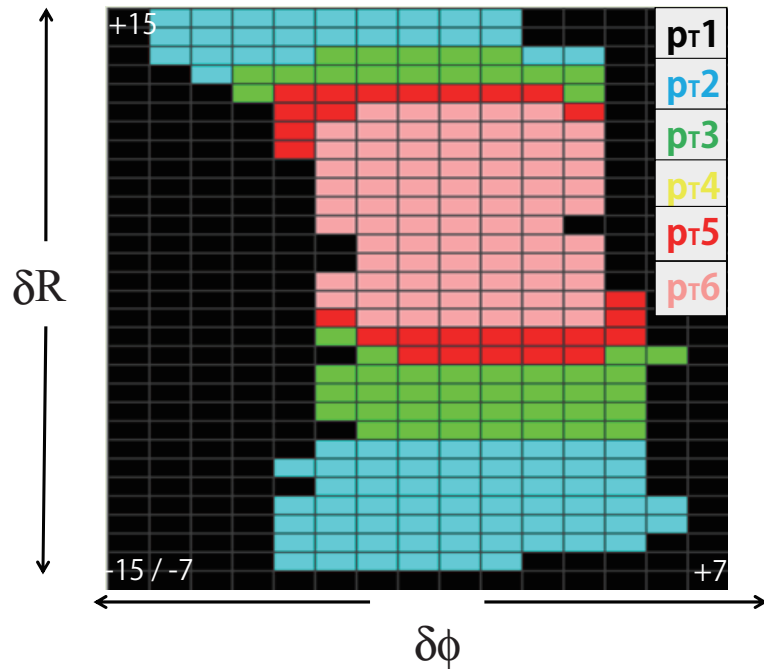
Figure 5.17: A coincidence matrix configured in the SL.

5.2.2   Level-1 Barrel Muon Trigger

The L1 barrel muon trigger is performed by the RPC [96]. For the detector specification and the layout in the ATLAS detector, see section 4.4.5. In this section, the trigger algorithm, detector segmentation and its implementation of the RPC are given.

Trigger Algorithm

The trigger algorithm in the RPC consists of two parts – the low-p_T algorithm and high-p_T algorithm. A schematic view of the both algorithms are shown in Figure **5.18**.
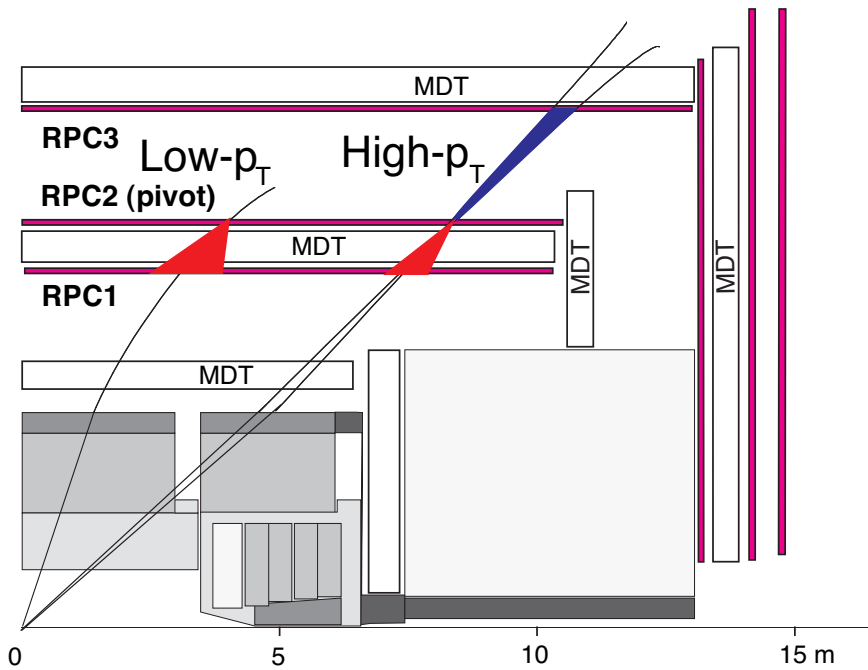
Figure 5.18: A schematic view of the trigger principle in the RPC.

The low-p_T algorithm deploys two RPC stations attached on the inner surfaces (RPC1) and the outer surface (RPC2) of the MDT inner station. The RPC2 is also referred to as the pivot plane. When a hit is generated by a muon in the RPC2, a search for a corresponding hit in the RPC1 is made within a road centered at the infinite momentum track line. The width of the road is related to the three p_T thresholds assigned to the low-p_T algorithm. The algorithm is performed in both η and ϕ coordinates. A 3-out-of-4 coincidence of the four layers in the two stations is required.

The high-p_T algorithm is performed on the top of a low-p_T result. The algorithm operates in a similar way to the low-p_T algorithm but requiring 1-out-of-2 coincidence in the outermost RPC station (RPC3). As in the low-p_T algorithm, three p_T thresholds are assigned to the high-p_T algorithm resulting six thresholds in total.

Detector Segmentation

The RPC is divided into 64 logically identical trigger sectors (32 trigger sectors for each half barrel), each one covers a region of $\Delta\eta \times \Delta\phi \sim 1.0 \times 0.2$. This trigger sector should be distinguished from the physical sector which is sub-divided into two trigger sectors as depicted in Figure **5.19**. Both large and small physical sectors contain two trigger sectors. A trigger sector is further divided into the fine granularity corresponds to ranges of each electronics element. Descriptions for each electronics element are given in the next section.
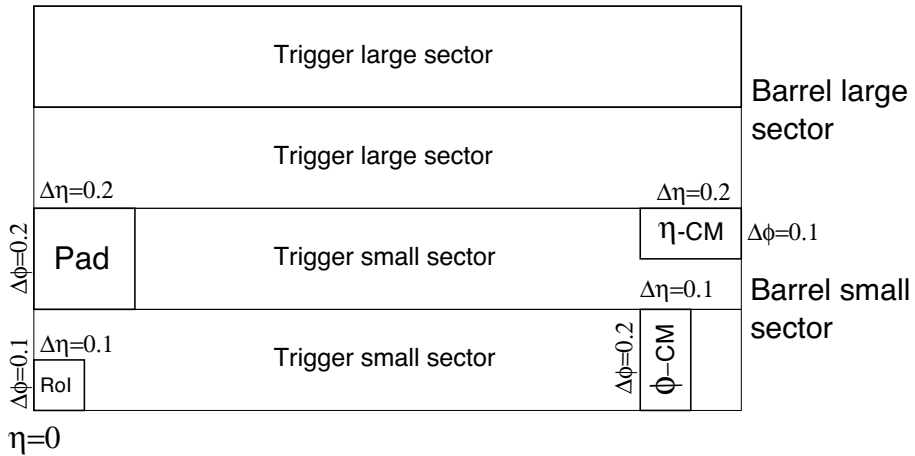
Figure 5.19: The RPC trigger segmentation.

System Implementation

Figure **5.20** shows a schematic view of the RPC trigger slice in front-end and off detector electronics. The description for each component is as follows.

- The Coincidence Matrix ASIC (CMA) [97] covers a region of $\Delta\eta \times \Delta\phi = 0.2 \times 0.1$ or $\Delta\eta \times \Delta\phi = 0.1 \times 0.2$. A CMA performs high-$p_T$ and low-p_T trigger algorithms, have pipeline memory to store event information during the L1 latency and encode data to a serial readout format. A CMA has two input arrays which correspond to the row and column input for a coincidence matrix, each one is called as pivot input (for RPC2) and confirm input (for RPC1, RPC3).

  In the low-p_T algorithm the pivot inputs are connected to the RPC2 and the confirm inputs are connected to the RPC1. In the high-p_T algorithm one of the pivot input is connected to the low-p_T trigger output and the confirm inputs are connected to the RPC3.

- The Splitter board provides a fan-out to serve adjacent inputs to a neighboring CMAs.

- The Pad logic board combines the trigger and readout information from four CMAs, both in the low and high-p_T algorithms. The Pad logic board associates the muon candidates with a region $\Delta\eta \times \Delta\phi = 0.1 \times 0.1$ and with a correct bunch crossing, solves overlaps
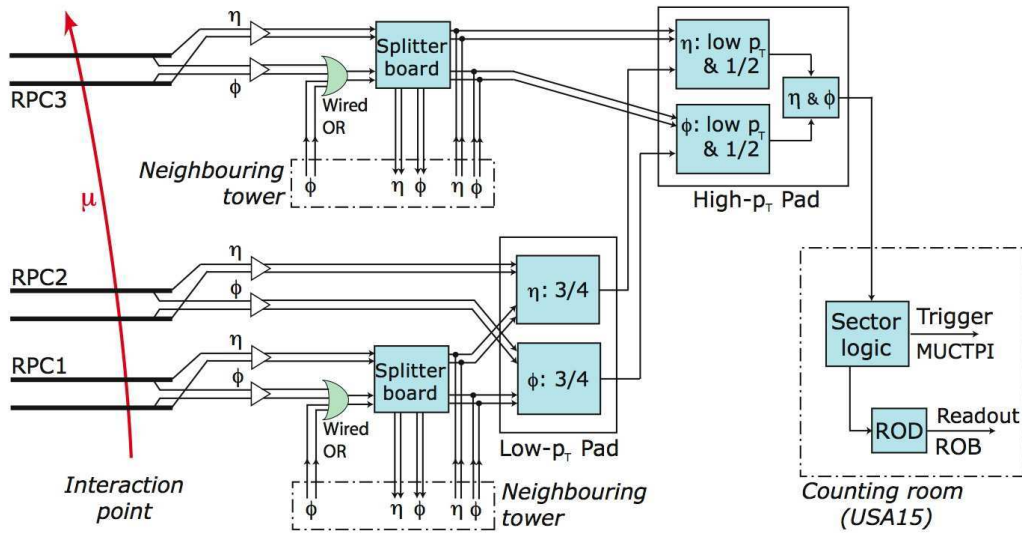
Figure 5.20: A schematic view of the RPC trigger slice.

and selects the highest p_T muon candidate in a coverage of $\Delta\eta \times \Delta\phi = 0.2 \times 0.2$. The low-$p_T$ board sends trigger and readout data to the corresponding high-p_T boards, while the high-p_T board sends trigger and readout data to the Sector Logic.

• The Sector Logic (SL) [98] covers a region of $\Delta\eta \times \Delta\phi = 1.0 \times 0.2$ receiving data from 7 high-p_T Pad Logic boards in a small physical sectors and 6 high-p_T Pad Logic boards in a large physical sectors. The trigger part of the SL solves the overlap inside a sector, performs some optional algorithm and selects the two highest p_T muon candidates in a sector, associating each muon to a RoI ($\Delta\eta \times \Delta\phi = 0.1 \times 0.1$) and to a correct bunch crossing. A trigger output from the SL is sent via parallel LVDS links to the MUCTPI. The readout part of the SL board multiplexes event packets and sends them to the event builder.

5.2.3   Muon to Central Trigger Processor Interface (MUCTPI)

The MUCTPI receives information on up to two muon candidates per trigger sector from both the TGC and the RPC then combines the information from all the trigger sectors and calculates total multiplicity values for each of six p_T thresholds. The maximum overall multiplicity is set at seven. The formatted information are sent to the CTP, the L2 trigger and the DAQ.

In the calculation, the overlaps between the TGC and the RPC or different trigger sectors are solved to avoid double counting. If a muon produces hits in both the TGC and the RPC, the priority is given to the RPC muon candidate.

In addition the MUCTPI can hold the trigger data within ± 3 bunch crossings around the L1 trigger. This is needed for setting up the timing of the system and also for monitoring the timing alignment of the trigger chambers.

5.3   Level-2 Muon Trigger

The L2 muon trigger algorithms are seeded by the ROI information provided by the L1 trigger and use all available detector data around the ROI with full granularity and precision. The role of the L2 is to confirm muon candidates flagged by the L1 and to give precise physics quantities associated to the muon candidate such as p_T.

The muFast algorithm performs a standalone feature extraction using the muon spectrometer data providing a fast selection of the muon event rated from L1. Subsequently, the muon track confirmed by muFast is passed to the muComb algorithm which refines the measurement by using track information reconstructed in the inner detector. The muIso algorithm select isolated muon candidates using calorimeter information. In this section, descriptions about each muon L2 algorithm are given.

MuFast

The muFast algorithm consists of the following three steps. The exact procedures are different between endcap and barrel.

- A global pattern recognition is performed to select clusters in MDT tubes belonging to a muon track without using drift time measurement. First, a pattern recognition is performed on the trigger chamber hits followed by a pattern recognition on the MDT hits. This is a recursive procedure in which the mean position of the track cluster is computed and a hit tube having the highest deviation from the mean is removed. It terminates when a single hit tube on each MDT layer is left

- A track fit is performed using drift time measurement and approximated $r - t$ relation assuming a straight line. A track segment is built if at least four MDT hits (two per MDT multilayer) can be used and fitted. The position on the middle of the MDT chamber crossed by the fitted result with the best χ^2 is chosen and used to sagitta measurement as a precision position measurement.

- The p_T is calculated from the position measurements obtained in the previous step referring a pre-calculated look-up table.

MuComb

The muComb algorithm matches a muon track confirmed by the muFast to a L2 ID tracks. The L2 ID tracks are reconstructed without TRT measurements. The matching algorithm between muFast and ID tracks are proceeded in the following two steps:

- A pre-selection of ID tracks is made using the difference in η and ϕ between muFast and ID tracks. Also the difference in the z-position at the radius of barrel calorimeter surface is used.

- For each of the pre-selected ID tracks, a combined p_T is evaluated with the information of the muFast track. The combined p_T is calculated as a resolution weighted average of p_T given by the muFast and ID tracks. A χ^2 is calculated and the ID track which gives the minimum χ^2 is selected as the best matching candidate.

MuIso

The muIso is seeded by a result of muFast or muComb. The algorithm decodes LAr and Tile calorimeter quantities (i.e. transverse energy deposit or sums of calorimetric cells above a predefined energy threshold) in cones centered around the muon direction. To remove the contribution of the muon track itself, two different concentric cones are defined.

5.4   Muon Event Filter

In the Event Filter, offline muon reconstruction algorithms have been adopted to work in the HLT framework. The two offline packages MOORE (Muon Object Oriented REconstruction) and MuId (MuonIdentification) have been used so far for this purpose. These two packages make up a family of muon reconstruction chain. The detailed description for the reconstruction algorithm itself is described in chapter 6. The HLT version of the MOORE family is called TrigMoore, which is modified to work as the RoI seeded mode in online environment. The TrigMoore has two main strategies,

- **Seeded strategy:** In this strategy TrigMoore accesses ad hoc algorithms that perform a seeded search only around the Region of Interest.

- **Full scan strategy:** In this strategy TrigMoore accesses directly the pointers of the offline version of the algorithms allowing it to execute the algorithms as they are in the offline package.

Chapter 6

The Muon Reconstruction at the ATLAS Experiment

The ATLAS experiment employs a variety of strategies for identification and reconstruction of muon tracks. Among them, two of those are intensively used in the analysis of this thesis.

- Standalone muon tracks are reconstructed only from the information in the muon spectrometer and then extrapolated to the beam line to obtain the track parameters at the closest approach to the beam axis.

- Combined muon tracks are found by matching standalone muon tracks to nearby inner detector tracks and then combined the measurement from the two systems.

This chapter is organized as follows. A description about the tracking objects in the ATLAS is given in section 6.1 followed by an overview of the Hough transformation, a common technique for pattern recognitions, in section 6.2 and tracking in the inner detector presented in section 6.3. Section 6.4 focuses on the standalone muon track reconstruction strategies. Finally, an overview of the track combination procedure is given in section 6.5.

6.1 The ATLAS Tracking Event Data Model

The ATLAS experiment has developed a common design of data objects which handles the various tracking related stuff by the C++ software framework, ATHENA. This common design is called Tracking Event Data Model (EDM) [99–101].

6.1.1 The Concept of a Track

A reconstructed track is represented by an array of the Track State On Surface (TSOS) objects as depicted in Figure **6.1**. A single TSOS is able to hold polymorphic tracking information such as track parametrization on a given surface of detector or materials, measurements in various types of detectors, inert material or integrated material effects and results of fittings.

Among them, the track parametrization and the expression of the detector measurements are of the most important. The details of these two items are described in the following subsections.
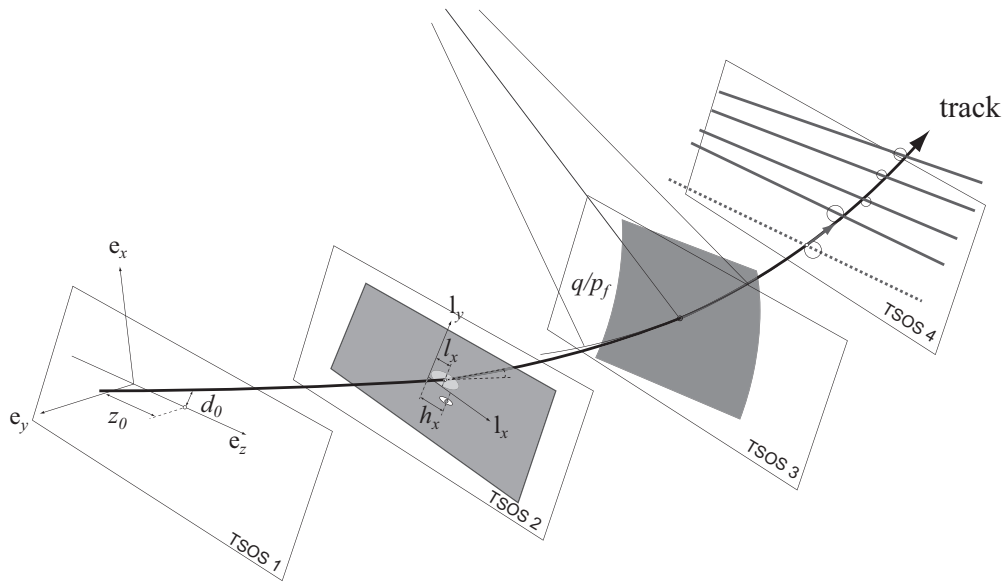
Figure 6.1: An image of a reconstructed track in the ATLAS Event Data Model.

6.1.2   The Track Parametrization

A reconstructed track is parametrized on each of detector or material surfaces where the track passed. The parametrization is done by a set of five parameters as,

$$L_i = (\ell_1, \ \ell_2, \ \phi, \ \theta, \ q/p), \tag{6.1}$$

where ℓ_1 and ℓ_2 denote the position in two coordinates in the intrinsic local frame on the surface under consideration. The surface is also expressed by a C++ object which represents various types of planes or lines. ϕ, θ, and q/p represent the signed momentum of a track in the ATLAS global frame.

The ATLAS tracking EDM can deal with five different types of surfaces namely cylinder, disc, plane, straight line and perigee. In most of the cases, a fitted result of a track is represented by a track parameters at a perigee, the closest approach of a track to the beam line.

d_0 and z_0 are defined as the transverse and longitudinal impact parameters. In this thesis, both d_0 and z_0 are defined with respect to the IP unless otherwise mentioned. The definition of d_0 and z_0 are illustrated in Figure **6.1**.

6.1.3   The Expression of Detector Measurements

An abstract common base class (MeasurementBase) is developed so that it is able to represent various kind of detector measurements. For example, a drift circle from the MDT or TRT, a 3-D position information from Pixel or SCT. These measurement is to be transformed at each level of the reconstruction or after an application of a calibration.

Figure **6.2** shows a simplified UML diagram which represents the inheritance tree of representative five types of measurements extended from MeasurementBase. A short description about these items are given below.
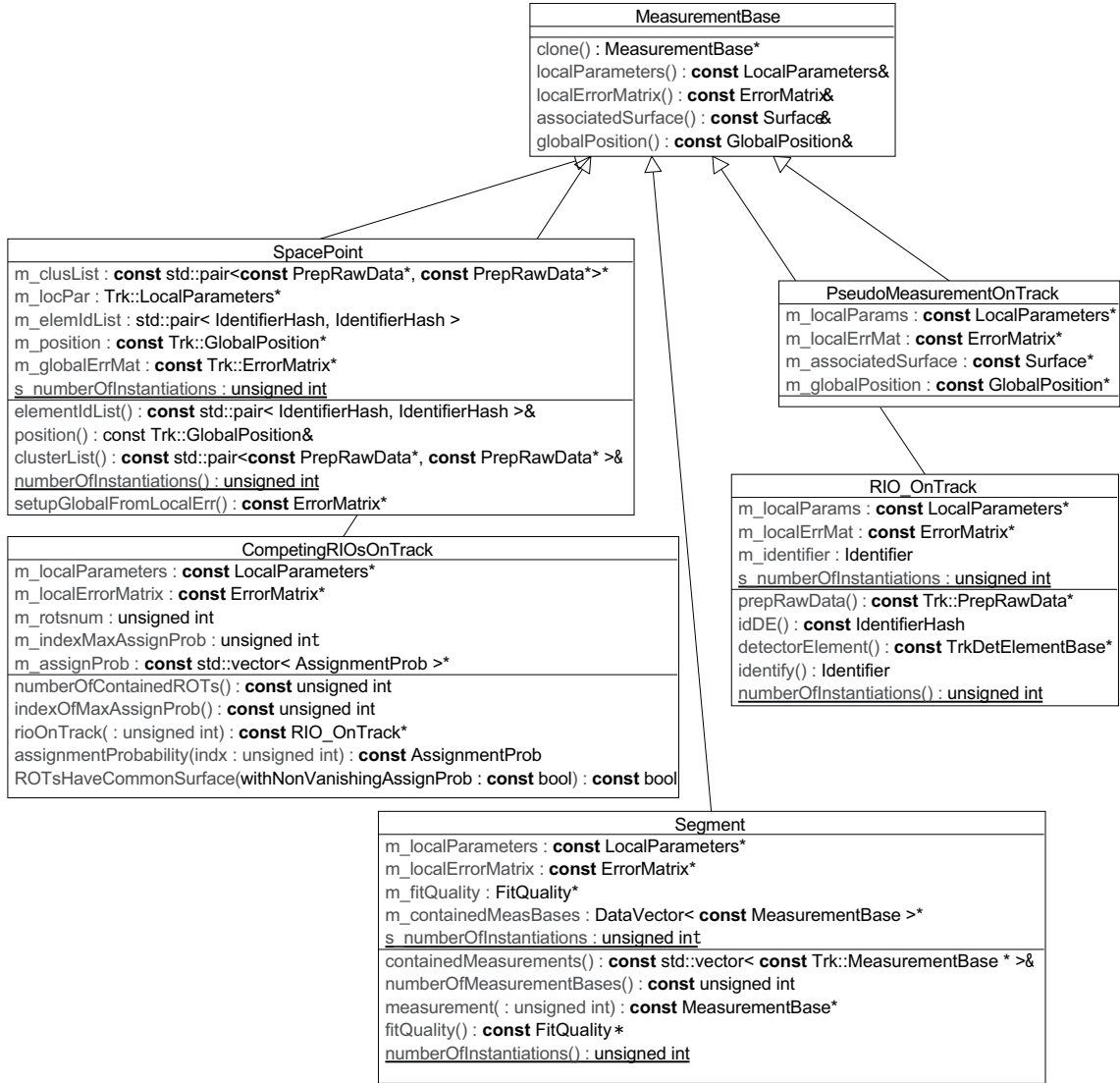
Figure 6.2: A simplified UML diagram showing the extended class of the MeasurementBase.

- RIO_OnTrack (Reconstruction Input Object on Track) is an object which represents a drift circle or 3-D position of a hit after applying additional calibrations.

- CompetingRIOsOnTrack is a group of RIO_OnTracks on the same detector surface, which is used to represents unresolved ambiguous measurements compatible with an estimated track positions on a surface.

- Segment contains an array of RIO_OnTrack and result of local fitting of them. Figure **6.3** shows a segment reconstructed in the MDT (an array of MDT drift circles). In the MDT

segment reconstruction, a straight line approximation is made since the effect of magnetic field is negligible in such a small region.
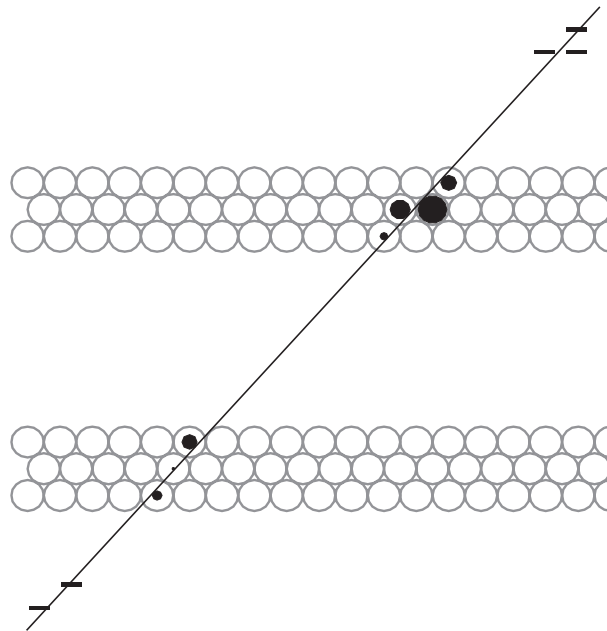
Figure 6.3: A schematic view of a segment in the MDT.

- SpacePoint is a set of a 3-D spatial information of a measurement and its error.

- PseudoMeasurmentOnTrack represents a measurement that can not determine the full track parametrization without information from other detectors.

6.2   The Hough Transformation

The Hough transformation is a feature extraction technique used in image analysis for its robustness in identification of varieties of shapes and patterns. Hough transformation was developed by Paul Hough in 1962 to analyze bubble chamber pictures at CERN [102, 103]. In the ATLAS track reconstruction, the Hough transformation is used in track pattern recognitions in individual hits in a detector.

The Hough transformation projects a point in normal space into a curve in a certain parameter space called Hough space.

$$P(\vec{x}) = H(\vec{x}, \vec{\alpha}). \tag{6.2}$$

The simplest example of the Hough transformation is a linear transformation for finding lines in a 2-D space. A line in a 2-D space can be generally expressed as,

$$x\cos(\phi) + y\sin(\phi) = r. \tag{6.3}$$

Eq.(6.3) represents a line perpendicular to another line which is drawn from the origin to (r, ϕ) in polar coordinates. Meanwhile, Eq.(6.3) also represents a curve in $r - \phi$ space for every (x, y) on the original line in 2-D space. Figure **6.4** shows that every curve in $r - \phi$ space which is on the same line in 2-D space intersect at one point and the intersection corresponds to the (r, ϕ) parameters for the original line. As such, a line in 2-D space is recognized by the Hough transformation.
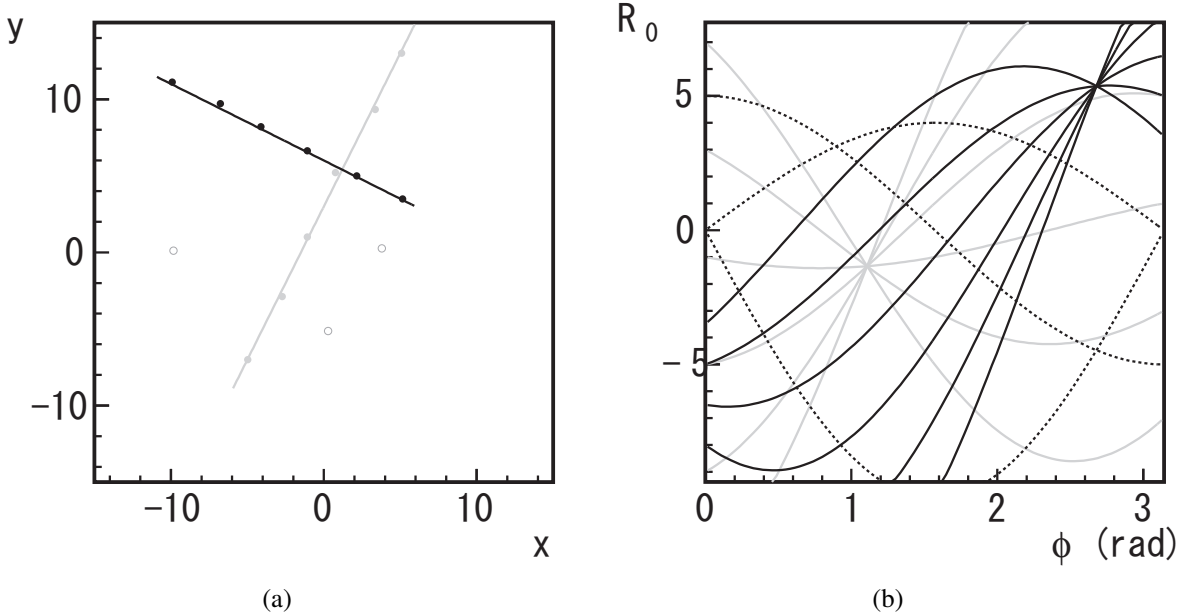
Figure 6.4: Set of points (a) and their representation in the Hough Space (b).

The calculation time of the Hough transformation increases linearly ($O(n)$) when the number of points in original space increases whereas a combinatorial approach would be of $O(n^3)$. This property of the Hough transformation have huge advantage in the ATLAS experiment where the

expected number of hits at the design luminosity reaches up to 20,000 in an event in the muon spectrometer.

In practice a search for overlapping points is made in binned Hough space. Figure **6.5** shows the Hough histogram which corresponds the the curves shown in Figure **6.4** (b). The peaks in the former correspond to overlaps in the latter.
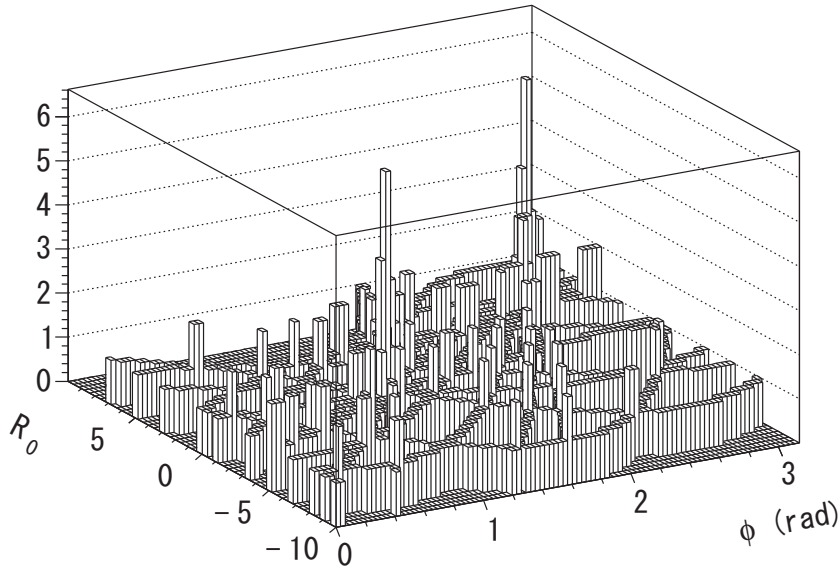
Figure 6.5: A Hough histogram for the curves in Figure **6.4** (b).

6.3   Tracking in the Inner Detector

The track reconstruction in the inner detector consists of two steps of successive strategies namely Inside-Out sequence and Outside-In sequence [101, 104, 105]. The Inside-Out sequence is the primary strategy for the track reconstruction in the inner detector whereas Outside-In sequence is a complementary approach to find tracks which unlikely to have hits in the silicon detectors (PIXEL and SCT) such as tracks coming from V_0 or photon conversion. An overviews of each sequence are given in the following sub-sections.

6.3.1   Inside-Out Sequence

Inside-Out sequence starts with measurements in the silicon detectors then try to extend the tracks into TRT region following the procedures listed below.

1. The measurements in the silicon detectors, which are bounded on the detector surfaces, are transformed to a set of 3-D positions in the ATLAS global frame.

2. Track seeds are searched with or without vertex constraint in z axis taking a balance between time consumption and seed finding efficiency. Once seeds are found, a track building is performed with a Kalman filter [106] smoother formalism which follows the road and include successive hits in the track candidate fit.

3. Ambiguities of shared hits are solved by so-called track scoring strategy [107]. In this strategy, a penalty and a benefit are assigned to each morphological features of a track such as penalty for overlapping hits or benefit for innermost layer hits in the PIXEL. A likelihood is calculated also taking into account the track fit qualities, then an ambiguous hits are assigned to the most favorable track.

4. Tracks are extended into TRT region finding comparable TRT measurements with a Kalman filter based tools [108, 109]. Then a track quality is calculated by track scoring strategy described above and if the quality is improved with additional TRT measurements, the extended track is stored.

6.3.2 Outside-In Sequence

The Outside-In sequence consists of following two separate steps. In the both steps all the measurements that have already been assigned to a Inside-Out track are excluded.

1. TRT segments are searched with both a global pattern search and a subsequent local pattern recognition. Since segments from a track with p_T above 500 MeV appear as almost straight line, the linear Hough transformation is made.

2. The resulting track candidates are then back-extended if at least two comparable measurements are found in the outer three SCT layers. This back-extension uses a Kalman filter smoother formalism. An ambiguity resolving and a track refitting are performed adequately.

6.4 Tracking in the Muon Spectrometer

The ATLAS experiment deploys two independent muon reconstruction algorithm chains – MuId (Muon Identification) [110–112] and the STACO (Statistical Combined) [113, 114]. Both chains contain entire reconstruction algorithms hence able to provide both standalone and combined tracks. In the analysis, the STACO chain is used as the primary algorithm. as well as MuId chain for cross checks and systematic estimations.

6.4.1 Tracking in the STACO Algorithm

This section describes an overview of the standalone muon track reconstruction in the STACO chain. The standalone muon track reconstruction package in the STACO is called Muonboy which reconstructs muons in following four procedure.

1. Region of Activity (ROA), a geometrical region defined in the η - ϕ space with the size of about $\eta \times \phi = 0.4 \times 0.4$, are identified using information from the trigger chambers. The center of ROA is placed where there exist at least one TGC or RPC hit in both $\eta - \phi$ coordinate.

2. Local segments of a straight track are reconstructed in multilayers of each muon station in ROA. The basic procedure is summarized below.

   (a) Segment seeds are searched in the region where more than one ϕ hits are expected by taking any combinations of two hits in different multilayers in an MDT chamber with a loose IP constraint. Then a seed is matched with other hits in the same chamber using drift time information and fitting results are examined if the segment is valid or not. In this matching, δ−ray effect and efficiency of the MDT tubes are considered. Segments are required to be associated with at least one ϕ hit and sufficiently good fitting quality. Such segments are called strict segments.

   (b) CSC segments are reconstructed in 3-D requiring at least one ϕ hit.

   (c) A looser search, in which no ϕ hit is required and less stringent χ^2 cut, is performed. The position in the ϕ is determined by trying five positions along the tube.

   In each of these steps, segments are searched in two consecutive passes. The first pass reconstructs segments which cross both multilayer in an MDT chamber while the second pass reconstructs the segments which cross only one multilayer to retain efficiency. In the second pass, in order to reduce fake combinations, only the hits left unused in the first pass are used and a fit quality cut is applied tightly.

3. Segments in different stations are combined by a 3-D tracking to form track candidates. Effects of the magnetic field is taken into account.

   (a) The strict segments are used as seeds for the first rough momentum estimation. Each segment is then extrapolated to the neighboring stations assuming several different values of momentum around the estimation. If some matching exist with one or more loose segments, the one with the best matching is included in the track candidate and a fit is performed leading to a more accurate momentum estimation.

   (b) The resulting track candidates are extrapolated to the all potentially crossed stations with a finer momentum scan. Any matching loose segment is included in the candidate track and a new fit is performed using all the segments belonging to the track candidates. Only track candidates with two or more segments are kept after this stage.

4. A global fit is performed, starting from the best result of the previous fits, but using raw hit information, such as TDC values and hit strips. In this process all the hits are classified into good or bad and only good hits are kept. After that, the final fit including the material effect is performed to achieve a more realistic result.

The covariance matrices of the track candidates are then computed by varying the fitted parameters taking their correlations into account. To have track parameters at the perigee, the

candidate tracks are back-extrapolated to the beam axis and their covariance matrices are propagated taking into account the energy loss and the scattering in the calorimeters.

6.4.2 Tracking in MuId Algorithm

In this section, an overview of the standalone muon track reconstruction in Muid chain is given. The standalone muon track reconstruction package in Muid is called MOORE (Muon Object Oriented Reconstruction) [115–118] which reconstructs muons in following procedures.

- CSC segments are reconstructed in 3-D assuming straight line.

- A global track pattern finding is performed deploying the Hough transformation using MDT, TGC, RPC hits and CSC segments. The suitable assumption for track model depends on the magnetic field distribution which varies region by region. Hence several types of Hough transformation are performed. The resulting patterns serve as seeds in the next stage.

- A straight line MDT segment reconstruction is performed. In each station, two hits in the outermost layer in both sides are taken and four possible tangent lines are drawn. If the line direction is within 0.2 rad from the pattern direction and more than three hits are found in the same station within a road with width of 1.5 mm, a straight line fit is performed. If the χ^2/ndf is over 10, the hit with the largest contribution is dropped and the segment is refitted. This procedure is repeated until the χ^2/ndf become smaller than 10 and if the number of hits in the segments becomes less than 3, the segment is discarded. Then ϕ hits are associated to the segment.

  The ambiguous segments, with shared hits, are solved by using track scoring strategy taking into account the δ-ray effect, noise-induced hits and tracking holes. Then the shared hits are assigned to the track with the highest score.

- The MDT and CSC segments are combined to build track candidates gathering compatible segments along track patterns. For each track candidate, a segment in the outermost station is used as the seed of the track fit. The seed segment is extrapolated to the next segment, the second-outermost segment, and this procedure is repeated for all segments.

  The resulting set of tracks are sorted by its quality taking into account the number of hits and the χ^2/ndf. Shared hits are assigned to the track with the highest score. Then the track is refitted with a detailed geometry description.

Finally tracks are extrapolated to the beam axis to evaluate the track parameters at the the perigee.

6.5   Combined Tracking

Both MuId and the STACO algorithms perform an inner detector track selection for a given muon spectrometer track using track parameters and covariance matrices. The same definition of the match χ^2 is used in both algorithms as the difference between the inner detector and the muon spectrometer track vectors weighted by the combined covariance matrix,

$$\chi^2_{match} = (\mathbf{T_{MS}} - \mathbf{T_{ID}})^{\mathbf{T}}(\mathbf{C_{MS}} - \mathbf{C_{ID}})^{-1}(\mathbf{T_{MS}} - \mathbf{T_{ID}}). \tag{6.4}$$

Here $\mathbf{T}$ denotes a vector of track parameters expressed at the perigee and $\mathbf{C}$ is its covariance matrix.

In the STACO algorithm, several track selection criteria, such as requirement of the same charge, crude $\eta - \phi$ matching, are applied on both the inner detector and the muon spectrometer track in addition to match χ^2 cut. The track parameters for the combined track is obtained by the statistical combination as,

$$\mathbf{T} = (\mathbf{C_{ID}^{-1}} - \mathbf{C_{MS}^{-1}})^{-1}(\mathbf{C_{ID}^{-1}T_{ID}} - \mathbf{C_{MS}^{-1}T_{MS}}). \tag{6.5}$$

In MuId algorithm, a combined refit is performed after the inner detector track selection using match χ^2. This combined refit accounts all the measurements, scatterer effect, energy loss and magnetic field effect throughout the path of the track. The resulting track parameters at the at the perigee is stored as the combined track parameters.

Chapter 7

Experimental Conditions and the Datasets

This study is based on the data sample of $\sqrt{s} = 7$ TeV proton-proton collisions collected from April to July, 2010. The operation of the LHC and the experiment, as well as the setup of the trigger, during this period are summarized in this chapter.

7.1 Good Quality Event Selection

The experimental data used in this study are selected in accordance with the good run list (GRL) criterion developed by the ATLAS experiment to ensure that every analyzer can share the identical events with good quality for the physics analysis in consideration [119].

The concept of GRL criterion based on the selection of luminosity blocks (LB) which are the unit of time for data-taking ($\sim$ 2 minutes period). A GRL is created by applying a Data Quality (DQ) criterion to list all of the valid physics runs and luminosity blocks. Usually physics groups hold their own GRL by selecting appropriate Data Quality flags (DQ flags), which is simple indicator of a specific part of DQ such as TGC detector or muon reconstruction in the STACO algorithm, to be applied on the data used in their analysis. DQ is assessed and DQ flags are filled in following two stages,

- Each sub-system is responsible for filling their DQ flags. The lowest level flags such as for nominal voltages, temperature, humidity are filled automatically. Sub-systems fill flags at a number of different stages, flagging possible hardware and data-taking problems. Automatic online flags are set and can be overwritten by the detector shifter during data taking.

- DQ flags are then reviewed by an offline expert. For the dedicated combined performance groups (such as for muons, taus, jets) the flags are set by a combination of automatic consistency checks and also by DQ shifters. A distilled summary of these stages are stored in the database.

Table **7.1** shows the DQ flags required for the W/Z analysis (these requirements are made upon a requirement of the stable running of the LHC). Due to the different requirements in the GRL, the resulted integrated luminosities used in $W \to \mu\nu$ and $Z \to \mu\mu$ are not the same (310 nb^{-1} for the $W \to \mu\nu$ and 331 nb^{-1} for the $Z \to \mu\mu$ as listed in Table **7.2**).

DQ flag	description
ATLGL	DQ information has been reviewed
ATLTOR	Good solenoid magnet status
ATLSOL	Good toroid magnet status
L1CTP	L1 trigger is working without problems
MMUIDCB	Requirements for MUID algorithm is fulfilled
MSTACO	Requirements for Staco algorithm is fulfilled
MET	Requirements for E_T^{miss} reconstruction is fulfilled (for W analysis only)

Table 7.1: DQ flags selected for the W / Z analysis

7.2 Operation of the LHC and the Experiment

The LHC has ran stably during the period with good data collection efficiency of $\sim 95\%$ with the ATLAS detector. The recorded instantaneous peak luminosity is $\sim 1.6 \times 10^{30}$ cm^{-2}s^{-1}. Figure **1.3** shows the integrated luminosity versus day delivered to (green), and recorded by the ATLAS (yellow) during stable beams condition. The details for the luminosity calculation is given in section 8.2.

   This period is divided into sub-periods according to the changes of the LHC operation modes or configurations of the ATLAS detector. A summary of the integrated luminosity used in each $W \rightarrow \mu\nu$ and $Z \rightarrow \mu\mu$ analysis is given in Table **7.2** with remarks on the LHC operation.

	Integrated Luminosity (nb^{-1})		
Run number range	$W \rightarrow \mu\nu$ GRL	$Z \rightarrow \mu\mu$ GRL	LHC comments
A: 152884 – 153200	0.13	0.15	unsqueezed beam ($\beta^* = 10$ m)
B: 153565 – 155160	8.07	8.76	first squeezed beam ($\beta^* = 2$ m)
C: 152228 – 156682	8.47	8.72	increased number of bunches
D1: 158045 – 158392	26.89	28.64	increased beam intensity ($\sim$0.9E11 protons/bunch), $\beta^* = 3.5$ m
D2: 158443 – 158582	29.03	31.76	–
D3: 158632 – 158975	32.85	34.71	–
D4: 159041 – 159086	79.40	87.82	–
D5: 159113	28.04	28.38	–
D6: 159179 – 159224	97.05	101.85	–
Total: 152844 – 159224	310.0	330.8	–

Table 7.2: A summary of data taking periods

   The ATLAS detector have been also operated stably. Table **7.3** shows the luminosity weighted relative fraction of good quality data delivery by each detector during LHC fills with stable beams and after ramped up the tracking detectors on between 30 March and 16 July, 2010.

	Sub-detector	Good quality fraction (%)
Inner Detector	PIXEL	97.1
	SCT	98.2
	TRT	100.0
Calorimeter	LAr EM	93.8
	LAr hadronic	98.8
	LAr forward	99.1
	Tile	100.0
Muon	MDT	97.9
	RPC	96.1
	TGC	98.1
	CSC	97.4

Table 7.3: Luminosity weighted relative detector uptime and good quality.

7.3   Trigger Setups

There were several physics streams operated during the data taking period. Each stream consists of a particular set of trigger chains. A trigger chain consists of three trigger items, each comes from different trigger stages (L1, L2 and EF). An event which passes a certain trigger chain is classified into the corresponding stream then stored in a dedicated file. If an event passes more than one trigger chain, the event is stored in all the corresponding files.

Among streams, the MuonswBeam (stands for *Muons with Beam*) stream and L1Calo stream are of a particular interest since the former is used in the *W* / *Z*-boson cross sections measurement and the latter is in the single muon trigger efficiency estimation. A brief description for each trigger stream is given below.

- The MuonswBeam stream consists of trigger items which are designed to collect events with muons generated in proton - proton collisions. Most of the HLT items are driven by a L1 muon trigger.

- The L1Calo stream consists of trigger items which are designed to collect events with jets, taus, $E_\mathrm{T}^\mathrm{miss}$, photons and electrons.

The *W* / *Z*-boson cross sections measurement utilizes the lowest threshold un-prescaled L1 single muon trigger available – the L1_MU6 – to avoid the trigger bias as possible. During the data taking period, there exist trigger chains in which trigger decisions are sorely performed with a L1 trigger item – called L1ItemStreamer. Table **7.4** shows the summary of the L1ItemStream for single muons with its prescale factor during lumiblock 746 – 813 in run 159224 (The last stable beam period of the data taking) as an example. The prescale factor for previous runs are smaller than the values in the table – i.e. all the L1ItemStreamer have not been prescaled except for L1_MU0.

Trigger Menu	L1_MU0	L1_MU6	L1_MU10	L1_MU0_COMM	L1_MU15	L1_MU20
Prescale	116.7	1.0	1.0	1.0	1.0	1.0

Table 7.4: L1 single muon trigger items for ItemStreamer chain in run 159224, LB 746 – 813.

Special Setups for MUCTPI

A Remark should be made on the special configuration on the MUCTPI.

- In design, the MUCTPI can hold L1 trigger information in ± 3 bunches with respect to the beam collision bunch. Normally only the L1 trigger information coincidenced with the collision bunch is sent to the L2 trigger but this acceptance has been stretched for the commissioning of the L1 muon trigger. The resulted timing acceptance for L1 muon trigger is [-2, -1, 0] in terms of the BCID difference ([BCID for an muon RoI] - [BCID for the event]).

- Since the muon rate is not so high during the data taking period, the overlap solving between the TGC and RPC have not been operated.

Level-1 Jet Trigger Configuration

L1 jet trigger is used in the relative trigger efficiency measurement with respect to single muons to ensure that muons are free from muon trigger biases. Hence a brief description on the L1 jet trigger is made here [120].

The ATLAS EM and hadronic calorimeters are segmented into trigger towers with granularity of about 0.1×0.1 in $\eta \times \phi$ coordinates. The exact size of trigger towers depends on its location. The analog signals from calorimeters are transmitted to the L1 hardware and the L1 hardware digitizes the trigger tower signals, associates them with a corresponding bunch crossings and subtracts pedestals. The L1 system also performs a noise suppression and E_T calibration. The L1 jet trigger constructs so-called jet elements made of four (2×2) trigger towers in both EM and hadron calorimeters. The resulted granularity of the jet element is about 0.2×0.2.

The L1 jets are reconstructed with an algorithm which consists of a sliding window with programmable size. The size of the window could be changed as 2×2, 3×3 and 4×4 jet elements. The step size for the sliding window is set at 0.2 in both η and ϕ. To prevent overlapping jets, E_T of a cluster defined as a region spanned by 2×2 jet elements, should be a local maximum within $\pm$ 0.4 units. Then a jet is reconstructed if the total E_T withing a given window is above a given threshold. The L1 jet algorithm is performed within $|\eta| < 3.2$. Figure **7.1** shows a schematic diagram of the jet reconstruction algorithm at L1.
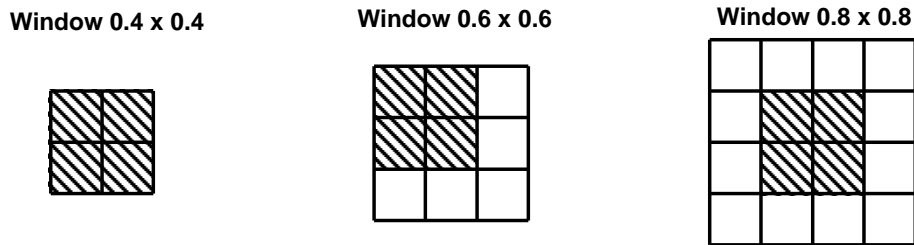
Figure 7.1: A schematic diagram of the L1 jet algorithm showing a window of 2×2, 3×3 and 4×4 jet trigger elements spanning the EM and hadronic calorimeter.

The L1 jet trigger items are summarized in Table **7.5** with E_T thresholds, window size and prescale factor in lumiblock 746 - 813 in run 159224.

Trigger Item (L1_XX)	J5	J10	J15	J30	J55	J75	J95	J115
E_T threshold (GeV)	5	10	15	30	55	75	95	115
Window size	2×2	4×4	4×4	4×4	4×4	4×4	4×4	4×4
Prescale factor	115	8.0	1.0	1.0	1.0	1.0	1.0	1.0

Table 7.5: A summary of the Level-1 jet trigger items.

Chapter 8

W / Z Boson Event Reconstruction and Selection

8.1 Cross Section Measurement Overview

The total production cross-section times branching ratio of the W / Z events, such as $Z \to \mu\mu$ or $W \to \mu\nu$, can be factorized into several components as in Eq.(8.1).

$$\sigma_{W/Z} \times BR(W/Z) = \frac{N^{obs} - N^{bkg}}{A \cdot C \cdot L_{int}}, \tag{8.1}$$

where

- $\sigma_{W/Z}$ means the production cross section for W / Z boson, and $BR(W/Z)$ represents its branching fraction to the $W \to \mu\nu$ or $Z \to \mu\mu$.

- N^{obs} represents the number of events in the experimental data which passed all the selection criteria applied in the analysis.

- N^{bkg} is the estimated number of background events in the signal region in each analysis.

- A (*Acceptance*) denotes the acceptance in the phase space. C (*Correction factor*) denotes the correction for the detector effect. These values are derived from MC simulation for each $W \to \mu\nu$ or $Z \to \mu\mu$ process by calculating the following numbers (for details of MC samples, see section 4.7.2).

  N_1: the total number of generated events

  N_2: the number of events generated in the fiducial acceptance defined in the phase space (the exact definitions are specific to each analysis). The fiducial acceptance is defined using Monte Calro truth variables before any QED radiation.

  N_3: the number of events which pass the analysis specific selection criteria after event reconstruction. The selection is made using reconstructed variables.

Then, the *A* and *C* are defined as

$$A = \frac{N_2}{N_1}, \quad C = \frac{N_3}{N_2},$$ (8.2)

In this study, data driven corrections, such as for muon trigger and reconstruction efficiencies, are applied on *C* to fairly reflect the actual experimental condition.

- L_{int} represents the integrated luminosity used in each analysis. Current uncertainty for the L_{int} is estimated as 11 %. Details for the luminosity calculation is described in section 8.2.

This section is organized as follows: Section 8.2 describes the methodology and current situation of the luminosity calculation. In section 8.3, the high-p_T muon selection and E_T^{miss} reconstruction used in the W / Z cross sections measurement as well as an overview of the vertex reconstruction and reweighing technique, and the requirement on the jet quality are presented. Section 8.4 is devoted to describe the systematic uncertainties which are common to both W / Z-boson cross sections measurement.

Cross sections measurement in $W \rightarrow \mu\nu$ and $Z \rightarrow \mu\mu$ processes are given in section 11 and 12 respectively.

8.2 Luminosity Calculation

The instantaneous luminosity of pp collision can be written as follows [121].

$$L = \frac{\mu n_b f_r}{\sigma_{inel}} = \frac{\mu^{meas} n_b f_r}{\epsilon \sigma_{inel}} = \frac{\mu^{meas} n_b f_r}{\sigma_{vis}},$$ (8.3)

where μ is the mean number of inelastic pp interactions per bunch crossing (BC), σ_{inel} represents the inelastic pp cross section, n_b is the number of bunches colliding at the IP and f_r is the revolution frequency. Also ϵ is the efficiency of the luminosity calculation algorithm of the detector used in the measurement, $\mu^{meas} = \mu\epsilon$ is the average number of interactions per BC that pass the selection requirements of the algorithm and the visible cross section σ_{vis} is the detector calibration constant for the luminosity measurements. As one can see in the Eq.(8.3) the luminosity calculation is done with knowledge of the four parameters, namely μ^{meas}, σ_{vis}, n_b and f_r (11245.5 Hz for LHC).

μ^{meas} is measured by the several detectors such as MBTS, LUCID, LAr calorimeter and the inner detectors for charged particle event counting. The uncertainty for the μ^{meas} measurement is about 5 % for each method. For the central value used in this study, the one measured with LUCID is adopted.

As described in the section 4.5, the ATLAS will perform an absolute σ_{vis} calibration using the ALFA detector. Since the ALFA was not ready at the data taking period, σ_{vis} is predicted by MC event generators and measured by the **van der Meer (vdM) Scan**. The details of the vdM scan are described in section 8.2.1. The dominant uncertainty for the luminosity measurement in this study is coming from the determination of σ_{vis}. Estimation using MC event generators gives ~20% uncertainty mainly coming from the modeling of the diffractive components of

the pp cross section. Estimations obtained from vdM scans have better uncertainty of ~11% which is dominated by the uncertainty on the proton beam current measurement, especially by the accuracy of DC transformers [122]. For its smaller uncertainty, the vdM scan result is used for the luminosity calculation. n_b, f_r are the operation parameters of the LHC and those uncertainties are zero. The σ_{vis} value used for this study is measured by the LUCID as

$$\sigma_{vis} = 40.2 \pm 0.1 \text{ (stat)} \pm 4.4 \text{ (syst)}. \tag{8.4}$$

8.2.1   van der Meer (vdM) scan

This method was invented in 1968 by S. van der Meer who found that it was possible to measure the effective height of the colliding ISR beams by observing the counting rate R in a suitable detector while scanning one of the two beams in the vertical plane with respect to the other one.

   In terms of colliding beam parameters, luminosity is defined as

$$L = n_b f_r I_1 I_2 \int \rho_1(x, y)\rho_2(x, y)dxdy, \tag{8.5}$$

where $I_{1(2)}$ is the number of particles per bunch in beam 1 (2) and $\rho_{1(2)}(x, y)$ is the particle density in the transverse $(x - y)$ plane of beam 1 (2) at the IP. Assuming no correlation between x and y, then the particle densities can be factorized and Eq.(8.5) can be rewritten as

$$L = n_b f_r I_1 I_2 \Omega_x(\rho_1(x)\rho_2(x))\Omega_y(\rho_1(y)\rho_2(y)), \tag{8.6}$$

where

$$\Omega_x(\rho_1, \rho_2) = \int \rho_1(x)\rho_2(x)dx, \tag{8.7}$$

is the beam overlap integral in the x direction, and it is calculated as

$$\Omega_x(\rho_1, \rho_2) = \frac{R_x(0)}{\int R_x(x)dx}, \tag{8.8}$$

where $R_x(x)$ is the rate measured by the several detectors during a scan. We define Σ_x by the equation

$$\Sigma_x = \frac{1}{\sqrt{2\pi}} \frac{\int R_x(x)dx}{R_x(0)}. \tag{8.9}$$

Using the last two equations, Eq.(8.5) can be rewritten as

$$L = \frac{n_b f_r I_1 I_2}{2\pi \Sigma_x \Sigma_y}. \tag{8.10}$$

   Three vdM scans have been performed at the ATLAS IP on April 26 and May 9 (2 successive scans), 2010. In each scan, MBTS, Inner Detector and LUCID is used for the rate measurement and analysis. The results from every detector agreed well within the error. We adopted the result from the LUCID as the official value, because of the following three reasons.

- The LUCID has good time resolution and event counting capability to provide robust luminosity measurements for the ATLAS up to luminosities about $10^{34} \text{cm}^{-2}\text{s}^{-1}$

- The luminosity information provided from the LUCID is independent of the TDAQ, so less sensitive to TDAQ downtime than the other detectors

- The background in LUCID is lower than the other detectors

8.3 *W / Z* **Event Reconstruction and Selection**

$W \rightarrow \mu\nu$ events are characterized by a high-p_T isolated muon and a large $E_\mathrm{T}^\mathrm{miss}$ and $Z \rightarrow \mu\mu$ events are by two oppositely charged high-p_T isolated muons with a Z-boson consistent invariant mass. In this section, the high-p_T muon selection procedure used in the both $W \rightarrow \mu\nu$ and $Z \rightarrow \mu\mu$ analysis and how $E_\mathrm{T}^\mathrm{miss}$ is reconstructed are given.

Also, the cross sections measurement in $W \rightarrow \mu\nu$ and $Z \rightarrow \mu\mu$ processes share common selection on primary vertices. In each analysis, a event-by-event reweighing on the number of vertices is applied. A description on these cuts and reweighing are given as well.

Finally, a description on the so-called jet cleaning procedure, which is to reject bad jet induced by non-physics effect is presented.

8.3.1 High Quality Muon Selection

A set of selections is applied on combined tracks as a part of the $W \rightarrow \mu\nu$ and $Z \rightarrow \mu\mu$ event candidate selection. The aim of the selections is to extract prompt muons from W / Z-bosons. Three types of backgrounds, namely muons from decay-in-flight of π / K mesons, cosmic ray and QCD processes are mainly considered.

Shown in Figure **8.1** is a distribution of the difference in p_T measured in the inner detector (p_T^{ID}) and in the muon spectrometer (p_T^{MS}) for combined tracks with $p_\mathrm{T} > 20\,\mathrm{GeV}$ and $|\eta| < 1.05$. The events are required to pass the $Z \rightarrow \mu\mu$ pre-selection (see section 12.1). Since a part of the energy of π / K meson is lost through in-flight decay, the $p_\mathrm{T}^{ID} - p_\mathrm{T}^{MS}$ tend to be larger than that of prompt muons as seen in Figure **8.1** (see a bump in the right-hand side of the distribution).

Making use of this feature, we applied the following cuts.

1. $|p_\mathrm{T}^{ID} - p_\mathrm{T}^{MS}| < 15\,\mathrm{GeV}$

2. $p_\mathrm{T}^{MS} > 10\,\mathrm{GeV}$

The definition of p_T^{MS} is a extrapolated p_T measurement at the perigee originally measured in the muon spectrometer then back-extrapolated to the IP. A cut of $p_\mathrm{T} > 20\,\mathrm{GeV}$ is applied on the p_T of combined tracks in both W / Z-boson cross sections measurement thus cut 2 contributes to reduce decay-in-flight background.

To reject cosmic ray background, combined tracks are required to point the IP by a cut of

3. $|z_0 - z_{vtx}| < 10\,\mathrm{mm}$

with z_0 the longitudinal impact parameter with respect to the IP and z_{vtx} is the z-position of the good primary vertex which minimizes $|z_0 - z_{vtx}|$. Figure **8.2** shows the distribution of $z_0 - z_{vtx}$ for combined tracks with $p_\mathrm{T} > 20\,\mathrm{GeV}$ in the events which passed the $W \rightarrow \mu\nu$ pre-selection
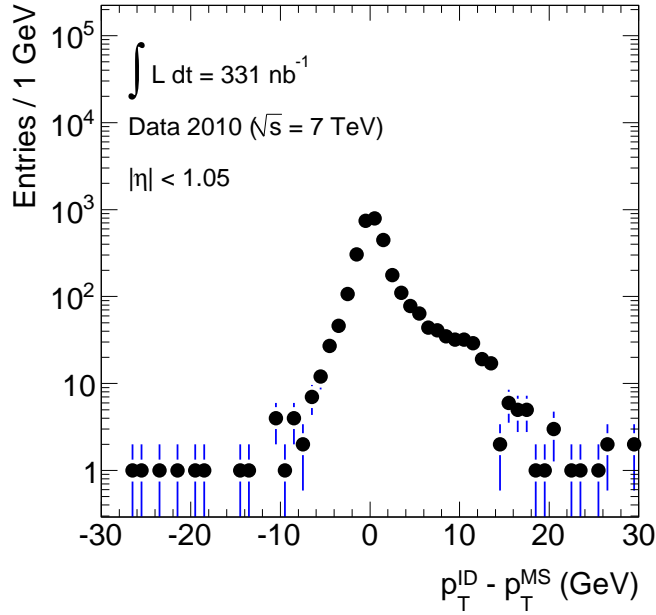
Figure 8.1: $p_T^{ID} - p_T^{MS}$ distribution for combined tracks with $p_T > 20$ GeV and $|\eta| < 1.05$ for the events which passed the $Z \to \mu\mu$ pre-selection

and all the $W \to \mu\nu$ selection (see section 11.1). The figures show that $z_0 - z_{vtx}$ is well modeled by the MC for both QCD and EW events.

Muons from QCD processes are tend to be surround by hadrons. To reject such non-isolated tracks, the following cut is applied

4. $\Sigma p_T^{ID} / p_T < 0.2$ ($\Delta R = 4$)

where the sum is taken for all inner detector tracks with $p_T > 1$ GeV within a cone with ΔR of 0.4. The denominator is the p_T of the combined track in consideration. The contribution from the combined track is subtracted from the numerator. This isolation variable is referred to as relative track isolation hereunder.

Figure **8.3** shows the distribution of relative track isolation for combined tracks with $p_T > 20$ GeV in the events which passed the $W \to \mu\nu$ pre-selection and all the $W \to \mu\nu$ selection (see section 11.1). The figures show that relative track isolation is well modeled by the MC for both QCD and EW events.
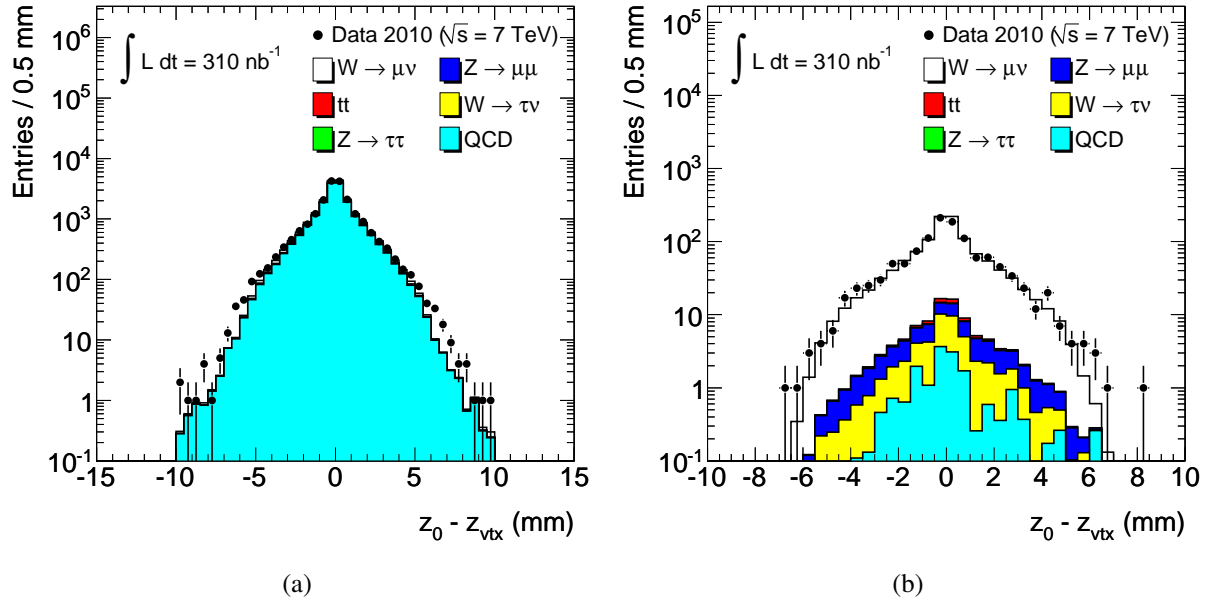
Figure 8.2: $z_0 - z_{vtx}$ distributions for combined tracks with $p_T > 20$ GeV in the events which passed the (a) $W \to \mu\nu$ pre-selection (b) all $W \to \mu\nu$ selection.
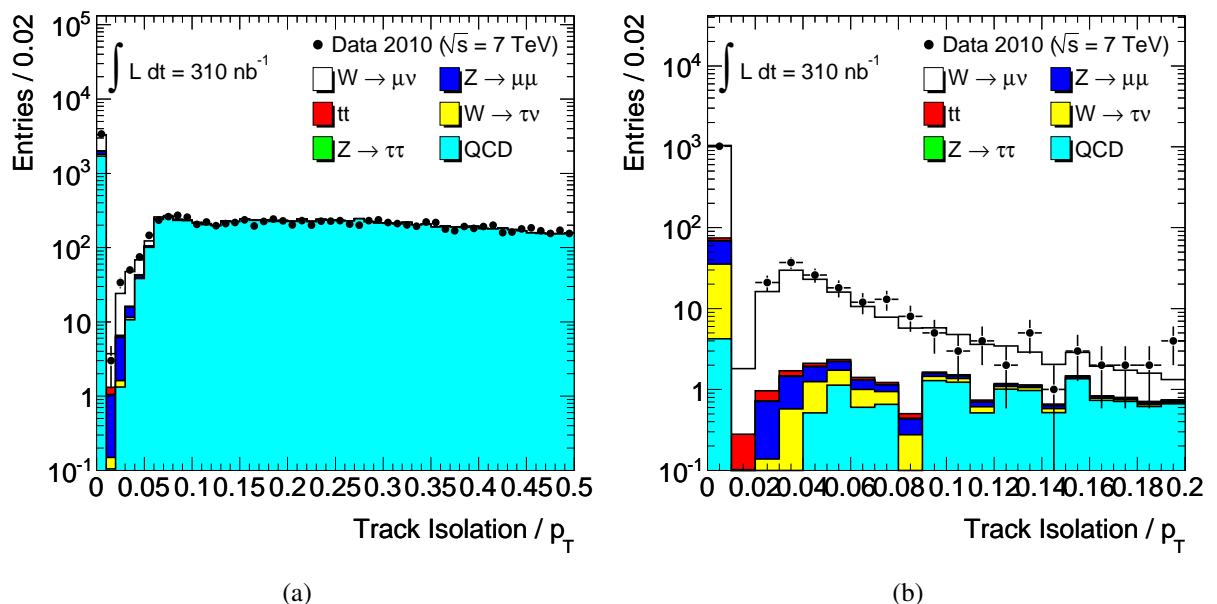
Figure 8.3: Relative track isolation distributions for combined tracks with $p_T > 20$ GeV in the events which passed the (a) $W \to \mu\nu$ pre-selection (b) all $W \to \mu\nu$ selection.

8.3.2 Missing Transverse Energy Reconstruction

The missing transverse energy (E_T^{miss}) is defined as a vector with same magnitude and inverse direction of the vectorial sum of all visible transverse energy. The definition of the E_T^{miss} used in the *W* / *Z* analyses is based on the energy deposits in the calorimeter and reconstructed muons.

$$E_T^{miss} = -\left(\sum_{\text{calo cluster}} \vec{E_T} + \sum_{\text{muon}} \vec{p_T} \right).$$

(8.11)

The first term means the vectorial sum of all calorimeter clusters reconstructed by a three dimensional topological clustering algorithm [123]. Clusters are seeded by a cell which has an energy significance, which is defined as $|E_{cell}|/RMS_{noise}$ with E_{cell} the energy of the cell and RMS_{noise} the expected RMS of the electronics noise, above 4. Then the neighboring cells are added to the cluster if their energy significance is above a defined threshold. The resulted clusters are classified into EM-like or hadron-like by their shape and calibrated their energy scale locally depending on their classification [124].

For the E_T^{miss} calculation, muons are classified into two classes. Isolated muon is defined as muons with no jets within a cone with radius of $\Delta R \leq 0.3$. The energy deposition of the isolated muon in the calorimeter can be measured explicitly then removed from the first term. The energy deposition of non-isolated muons cannot be separated from the nearby jet energy. Therefore, the p_T of muon reconstructed as a muon spectrometer standalone track is used unless there is a significant mismatch between the track parameters of standalone and corresponding combined tracks. If there is a mismatch, the p_T of the combined track is used and a parametrized energy loss in the calorimeter is removed from the first term. For muons in $|\eta| > 2.5$, outside the inner detector acceptance ,the p_T of standalone track is used. Details on the performances of missing transverse energy is found in [125].

8.3.3 Primary Vertex Reconstruction

In the cross sections measurement in $W \to \mu\nu$ and $Z \to \mu\mu$ processes, events are required to have one or more good quality primary vertices to reject events induced by cosmic rays. The definition of the good vertex is as follows.

- To have three or more tracks

- Position in z is within 150 mm from the IP

In this section, an overview of the primary vertex reconstruction in the ATLAS is given.

Primary vertices are reconstructed from tracks reconstructed in the inner detector. Descriptions about the tracking in the inner detector is presented in section 6.3 and Ref.[126, 127]. During the data taking period, tracks are reconstructed from track candidates with p_T above 100 MeV in the Inside-Out Sequence and above 300 MeV in the Outside-In Sequence. The primary vertex reconstruction in the ATLAS consists of two steps [2],

- Primary vertex finding algorithm associates tracks to vertex candidates

- Vertex fitting algorithm reconstructs vertices position and error matrices. This algorithm also refits associated tracks constraining them to a reconstructed interaction point.

In the vertex reconstruction, following cuts are applied on the inner detector tracks.

- $p_T > 150$ MeV

- $|d_0| < 4$mm

- $\sigma(d_0) < 5$ mm

- $\sigma(z_0) < 10$ mm

- at least 4 hits in the SCT

- at least 6 hits in the pixel and SCT

Here d_0 and z_0 denote the transverse and longitudinal impact parameters of tracks with respect to the center of the beam-spot. Beam-spot is the luminous region in the ATLAS detector reconstructed during physics run typically in every 10 minutes [128].

Shown in Figure **8.4** and **8.5** are the distributions of reconstructed primary vertices in 6 nb^{-1} of integrated luminosity taken by L1_MBTS trigger. Shown in Figure **8.6** is the position and RMS in each (x, y, z) coordinate of primary vertices reconstructed in each run. Both position and RMS vary depending on the run number due to the changes in the LHC operation parameters. The events are required to fulfill the $W \to \mu\nu$ GRL selection, L1_MU6 trigger requirement and have one or more combined tracks in $|\eta| < 2.4$ and $p_T > 6$ GeV.
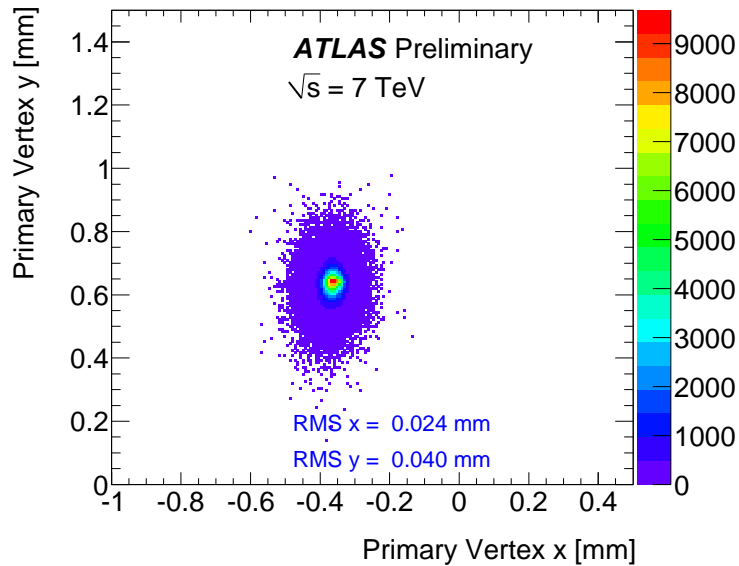
Figure 8.4: Two dimensional distribution of reconstructed primary vertices in 6 nb^{-1} of 7 TeV data taken by MBTS trigger in $x − y$ plane [2].
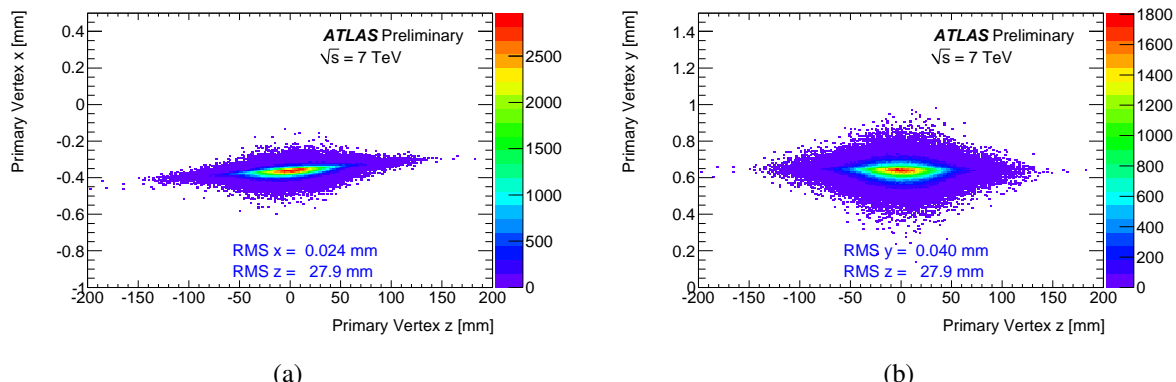
Figure 8.5: Two dimensional distribution of reconstructed primary vertices in 6 nb^{-1} of 7 TeV data taken by MBTS trigger in the $x − z$ (a) and the $y − z$ (b) [2].

(a)

(b)

(c)
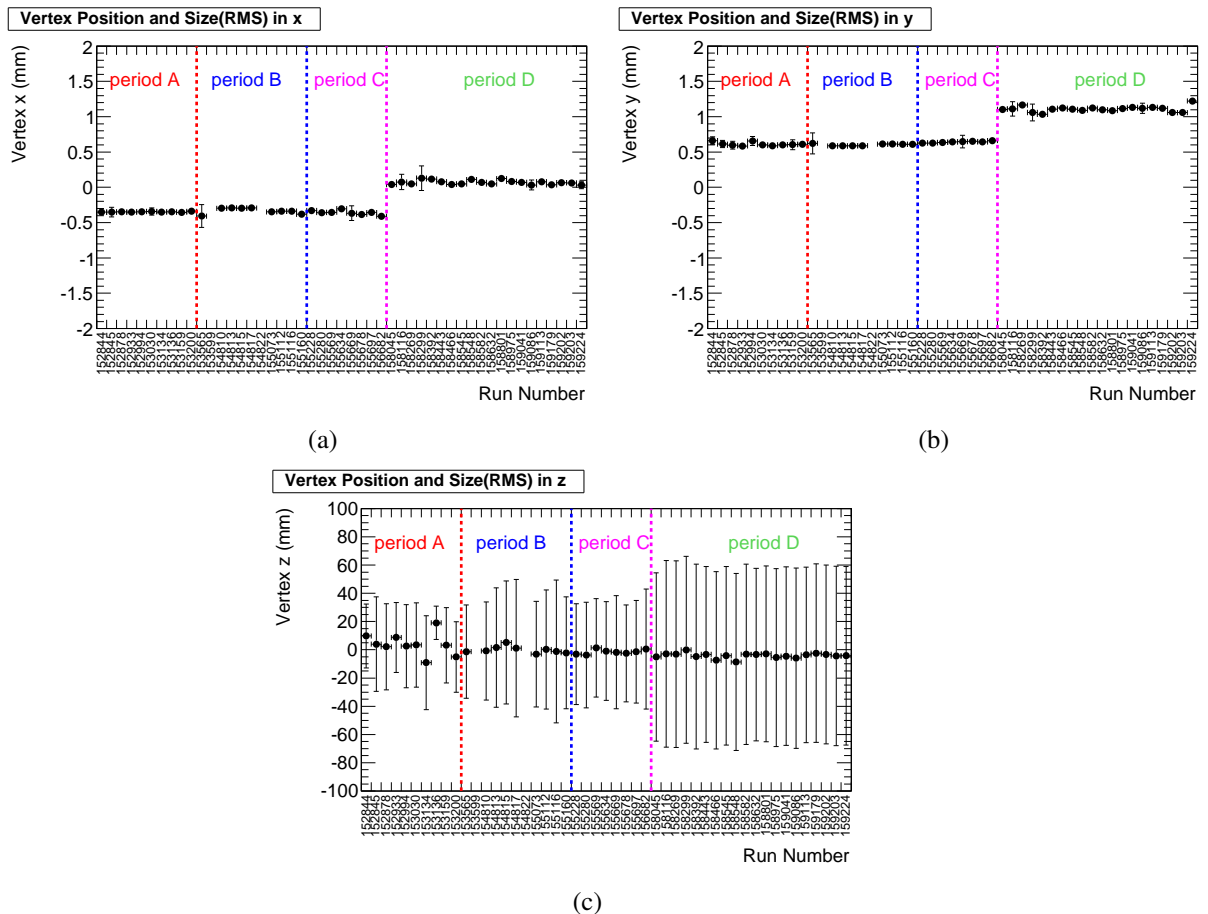
Figure 8.6: The mean position and RMS of primary vertices in (a) *x*, (b) *y* and (c) *z* coordinate in each run.

Pile-up Event Reweighting

As mentioned in section 4.7.2, simulated minimum bias events are overlaid over the original hard-scattering events in the $W \rightarrow \mu\nu$ and $Z \rightarrow \mu\mu$ MC samples to model the pile-up effect. Since the pile-up modeling is not perfect, a event-by-event reweighing is applied as described hereunder.

Shown in Figure **8.7** (a) is the distribution of the number of good vertices in an event in data and $W \rightarrow \mu\nu$ MC. The events are required to pass $W \rightarrow \mu\nu$ pre-selection (see section 11.1). Also, the distribution of the z-position of primary vertices reconstructed with three or more tracks is shown in Figure **8.7** (b). In Figure **8.7** (a), there is a significant difference between data and MC.

To compensate this difference, an event-by-event weight is applied on the number of good vertices in an event in the W / Z analyses. The total effect of the reweighing on the acceptance is about 0.2 %. The reweighing factors for both $W \rightarrow \mu\nu$ and $Z \rightarrow \mu\mu$ is given in Table **8.1**.

(a)   (b)
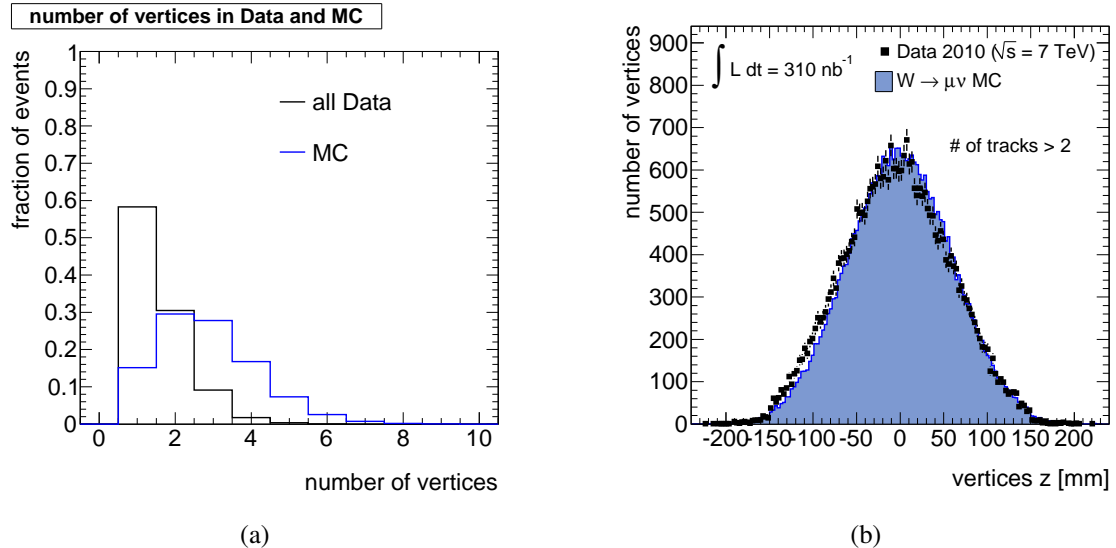
Figure 8.7: (a) The number of good vertices in an event in data and $W \rightarrow \mu\nu$ MC. (b) z-position of primary vertices reconstructed with three of more tracks.

Number of good Vertices	W event weight	Z event weight
0	1	1
1	3.85143	3.76055
2	1.03051	1.06299
3	0.32755	0.35412
4	0.10374	0.11341
5	0.05154	0.05356
6	0.00766	0.00980
7	0.00671	0.03498

Table 8.1: Event reweighing factors in terms of number of good vertices in an event.

8.3.4 Jet Cleaning

To reduce spurious $E_{\mathrm{T}}^{\mathrm{miss}}$ generated from detector effects and cosmic rays, the events with jets with E_T in EM scale larger than 10 GeV and at least one of the following characteristics are rejected in the $W \rightarrow \mu\nu$ analysis.

- A jet with the least number of cells accounting for 90 % of the jet energy (n90) is less or equal to 5 and the energy fraction in the hadronic endcap calorimeter (f_{HEC}) is larger than 0.8. This cut is to remove noise bursts in the HEC where most of fake energy deposit is found in a single or neighboring cells.

- A jet with the fraction of jet energy from bad-quality calorimeter cells (f_{QLAr}) is larger than 0.8 and the energy fraction in the EM calorimeter (f_{EM}) is larger than 0.95. f_{QLAr} is the fraction of LAr cells with a cell Q-factor greater than 4000. The cell Q-factor is the difference between measured and predicted pulse shape used for a cell energy reconstruction. This cut is to remove fake jets arise from noise bursts in the EM calorimeter.

- A jet with relative timing of the calorimeter deposits from the event time is larger than 50 ns. This cut is to remove out-of-time energy depositions in the calorimeter like cosmics.

Shown in Figure **8.8** are the jet cleaning variables in the events which pass the $W \rightarrow \mu\nu$ GRL and L1_MU6 trigger with one or more combined tracks with $|\eta| < 2.4$ and $p_{\mathrm{T}} > 6$ GeV. The effect of the jet cleaning on the $W \rightarrow \mu\nu$ acceptance is below 0.01 %.
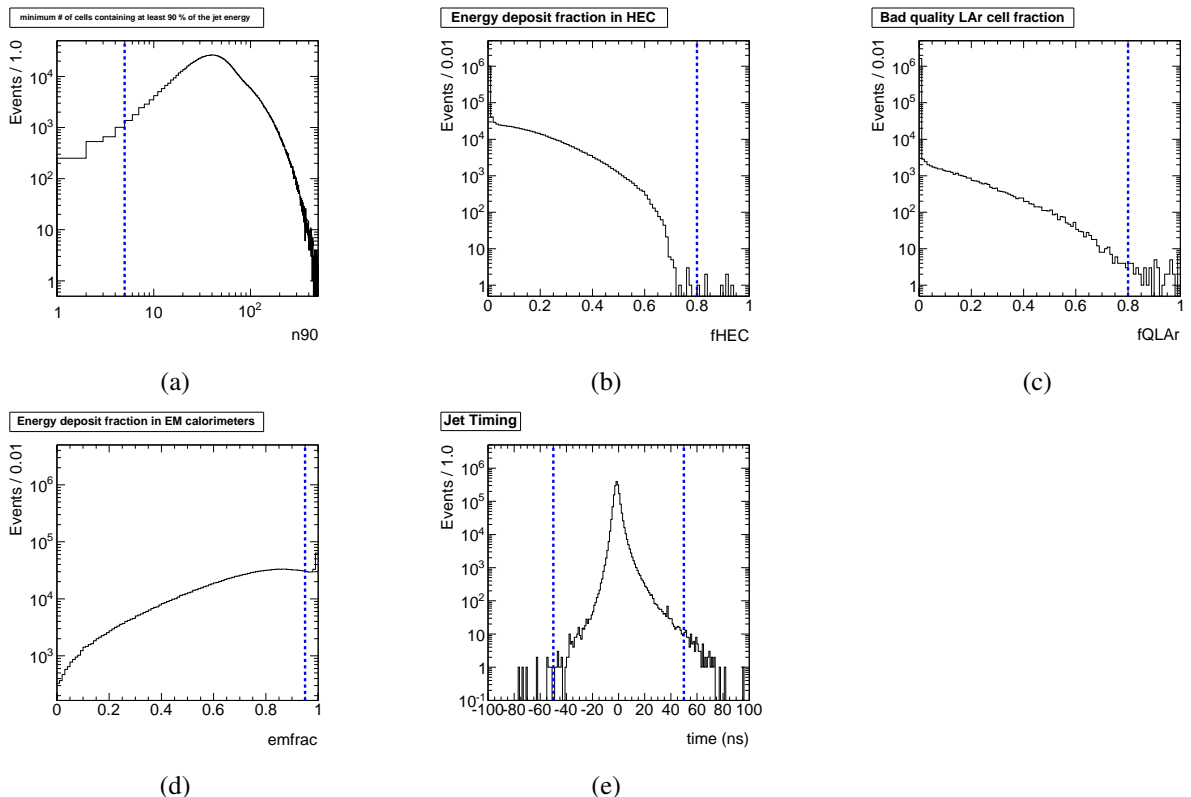
Figure 8.8: Jet cleaning variables: (a) n90, (b) f_{HEC}, (c) f_{QLAr}, (d) f_{EM}, (e) Jet timing.

8.4   Common Systematic Uncertainties

The following three systematic uncertainties which are common to both W / Z cross sections measurement are evaluated in this section.

- The uncertainty from the muon momentum resolution and scale

- The uncertainty from the muon isolation efficiency

- The theoretical uncertainty on the acceptance (A and C)

8.4.1   Muon Momentum Resolution and Scale

The uncertainty on the momentum scale and resolution of the muon spectrometer are deduced by investigating di-muon invariant mass distributions in $Z \rightarrow \mu\mu$ events. The following two methods are performed.

1. Fitting with Breit-Wigner function convoluted with a gaussian

2. Chi-square test

In both methods, the muon p_T is parametrized as

$$\left(\frac{1}{p_\mathrm{T}}\right)_{smear} = \frac{1}{C_1} \times \left(\frac{1}{p_\mathrm{T}}\right)_{MC} \times (1 + x \times C_2),\tag{8.12}$$

where $(1/p_\mathrm{T})_{smear}$ is the reconstructed muon curvature smeared by the detector effects which is not included in the MC. $(1/p_\mathrm{T})_{MC}$ is the reconstructed muon curvature in MC. C_1 is the momentum scale term and C_2 is the additional momentum smearing term, x fluctuates as a gaussian distribution with zero mean and unit width.

   In the method 1, distributions are fitted with a Breit-Wigner function convoluted with a gaussian. The C_1 and C_2 are determined as the value that fitted mean and gaussian width in data and MC agree the best. Shown in Table **8.2** is the summary of the determined C_1 and C_2.

	C_1	C_2
All	0.991 ± 0.005	0.055 ± 0.012
endcap	0.980 ± 0.012	0.063 ± 0.031
barrel	0.992 ± 0.010	0.031 ± 0.020

Table 8.2: The determined C_1 and C_2 parameters by di-muon invariant mass distribution fitting.

   In the method 2, di-muon invariant mass distributions are investigated by the Chi-square test. χ^2 between smeared distribution in data and in MC is calculated with various C_1 and C_2. Shown in Figure **8.9** is the $\Delta\chi^2$ distribution in $C_1 - C_2$ plane and the di-muon invariant mass

distribution in data and MC. The distributions in MC are smeared with C_1 and C_2 which report the minimum χ^2 value (summarized in Table **8.3**). Figure **8.9** (a) and (b) are the results for all $Z \to \mu\mu$ events, (c) and (d) are for events in which both muons are generated into the endcap and (e) and (f) are for events in which both muons are generated into the barrel. The χ^2 is calculated within the mass window of $66 < M_{\mu\mu} < 116$ with the binning shown in Figure (b), (d) and (f). The yellow lines in Figure **8.9** (a), (c) and (e) indicate contour lines where $\Delta\chi^2 = 1, 4, 9....$ The results by the method 2 are well consistent with the results from the method 1 within the region in which $\Delta\chi^2 < 1$.

	C_1	C_2	χ^2
All	0.99	0.07	0.49
endcap	0.99	0.07	0.77
barrel	0.985	0.035	0.58

Table 8.3: The determined C_1 and C_2 parameters with calculated χ^2 value by Chi-square test on the di-muon invariant mass distributions.

The results from both methods are consistent with the estimations from the ATLAS muon combined performance group based on the comparisons between the measurements in the inner detector and the muon spectrometer for given combined tracks [129]. Hence the uncertainties in Ref.[129] are adopted as 0.01 for muon momentum scale and 5 (9) % in endcap (barrel) for muon momentum resolution.

8.4.2   Muon Isolation Efficiency

In the W / Z-boson cross sections measurement, a requirement of relative track isolation is applied ($\sum p_{\mathrm{T}}^{ID}/p_{\mathrm{T}} < 0.2$ within a cone of $\Delta R < 0.4$). The difference in efficiency for the isolation cut in data and MC is considered as a systematic component.

This effect is estimated using muons selected by tag-and-probe method (see section 10) and resulted efficiency is 0.984 ± 0.010 in data and 0.993 in MC with negligible statistical error. The difference of ~ 1 % is observed. This value is taken as a conservative systematic uncertainty with the central value calculated in MC.

(a)

(b)

(c)

(d)

(e)

(f)
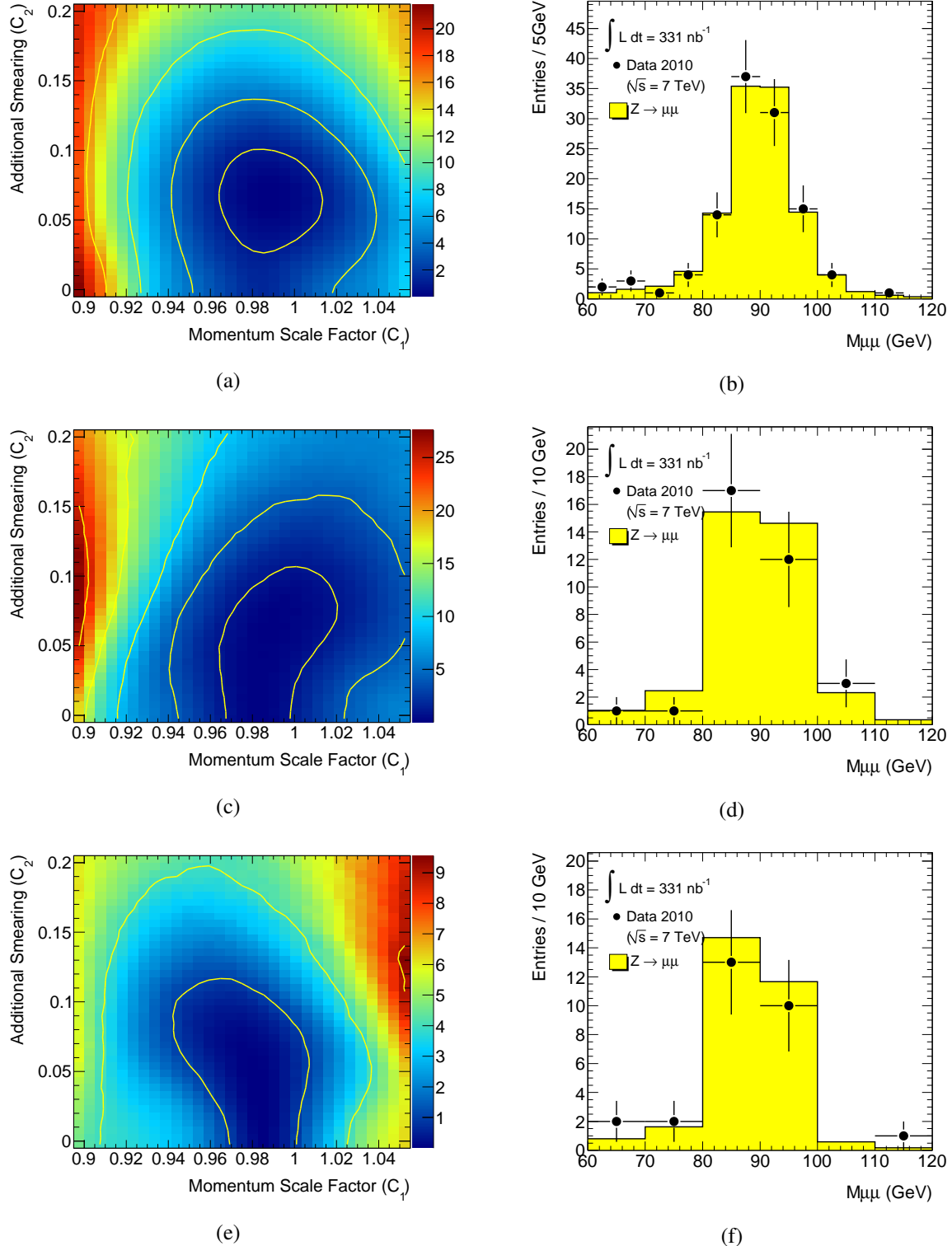
Figure 8.9: The calculated distributions of $\Delta\chi^2$ between the di-muon invariant mass distribution in data and MC in $C_1 - C_2$ plane ((a), (b), (c)). (a) is for all $Z \to \mu\mu$ events, (c) is for events in which both muons are generated into the endcap and (e) is for events in which both muons are generated into the barrel. The yellow contour lines indicate where $\Delta\chi^2 = 1, 4, 9....$ The di-muon invariant mass distributions in data and MC with C_1 and C_2 which reports the minimum χ^2 are also shown ((b), (d), (f)).

8.4.3   Theoretical Uncertainty on Acceptance

As described in section 4.7.2, the central values for the acceptances (A, C) are estimated by using PYTHIA event generator with the MRST LO* [93] PDFs. The uncertainty on these acceptance is estimated by a method which is common to $W \rightarrow \mu\nu$ and $Z \rightarrow \mu\mu$ analyses [130].

Uncertainties on A

The systematic uncertainties on the acceptances A are dominated by a limited knowledge on PDFs and the modeling of W / Z-boson production at the LHC. In the uncertainty estimation, the following three components are considered as independent contributions.

- The uncertainty within a PDF set is estimated using PDF error eigenvectors of the CTEQ6.6 NLO PDF set [131]. The error eigenvectors are obtained by PDF reweighing of a single sample of events generated using MC@NLO [132] and the CTEQ6.6 NLO PDF set. The estimated amount of uncertainty on acceptance is 1.8 % for $W \rightarrow \mu\nu$ and 1.6 % for $Z \rightarrow \mu\mu$, respectively.

- The uncertainty between different PDF sets is estimated by comparing three different PDF sets (MRST LO*, CTEQ6.6 and HERAPDF1.0 [133] NLO PDF). The events are generated with PYTHIA. The estimated amount of uncertainty on acceptance is 1.1 % for $W \rightarrow \mu\nu$ and 2.0 % for $Z \rightarrow \mu\mu$, respectively.

- The uncertainty due to the modeling of W / Z-boson production is estimated from the difference of the results between PYTHIA and MC@NLO using CTEQ6.6 PDF set. The estimated amount of uncertainty on acceptance is 1.6 % for $W \rightarrow \mu\nu$ and 2.8 % for $Z \rightarrow \mu\mu$, respectively.

The results are added in quadrature. The resulted uncertainty on A is 3.0 % for $W \rightarrow \mu\nu$ analysis and 4.0 % for $Z \rightarrow \mu\mu$ analysis.

Uncertainties on C

The theoretical uncertainty on C is obtained by a PDF reweighing technique due to the limited statistics. The three PDF sets (MRST LO*, CTEQ6.6 and HERAPDF1.0) are used and the 0.3 % of uncertainty is obtained for both $W \rightarrow \mu\nu$ and $Z \rightarrow \mu\mu$ processes.

Besides, the uncertainty coming from low energy (< 1 GeV) FSR is independently estimated as 0.2 %, and the resulted total theoretical uncertainty on C is 0.4 % for both $W \rightarrow \mu\nu$ and $Z \rightarrow \mu\mu$ processes.

Chapter 9

Muon Trigger Efficiency Estimation using Collision Data

The methods and results for the muon trigger efficiency estimation are presented in this chapter. In this study, the muon trigger efficiency relative to a combined track is estimated since both W / Z-boson cross sections measurement requires at least one combined track in the event selection. Independent two methods are utilized in this efficiency measurement.

1. Using high-p_T combined track samples which pass a selection based on the ones used in the W / Z-boson cross sections measurement (this method is referred to as the single combined track method hereunder)

2. Using combined track samples identified as a muon by so-called tag-and-probe method in $Z \rightarrow \mu\mu$ events

This section is organized as follows. In section 9.1, a description of the situation of the Level-1 muon trigger in the data taking period is given. Section 9.2 describes the relative trigger efficiency estimation by the single combined track method. In section 9.3, an overview of tag-and-probe method in $Z \rightarrow \mu\mu$ events is presented followed by a description of actual analysis and results. Finally the relative trigger efficiency results for the W / Z-boson cross sections measurement are summarized in section 9.4.

9.1   Level-1 Muon Trigger Configuration

The TGC and RPC are designed to be operated with six levels of p_T threshold. Both detectors share a common set of five thresholds throughout the data taking period. Each of them are named as L1_MU0, L1_MU6, L1_MU10, L1_MU15 and L1_MU20. Remaining one threshold have been used for a commissioning purpose.

All the thresholds except for L1_MU0 deploy dedicated coincidence window on the top of the high-p_T coincidence condition. The coincidence window is set to have a p_T threshold at the value as their name indicates, i.e. L1_MU6 is tuned to have its threshold around 6 GeV. The efficiency for the L1_MU6 is tuned to be about 80 % at the threshold.

In the TGC case, the low-p_T and high-p_T coincidence are set as the nominal configuration. low-p_T coincidence requires 3-out-of-4 hit coincidence both for wires and strips. High-p_T coincidence requires 2-out-of-3 coincidence for wires and 1-out-of-2 for strips on the top of the low-p_T coincidence. The BCID gate width is set at 35 (45) ns for wires (strips).

Figure **9.1** shows a simulated L1_MU6 efficiency map in the endcap ($1.05 < |\eta| < 2.4$) for muons with p_T = 20 GeV. This trigger item is used in the W / Z analysis as the event trigger. An inefficient region at the outer edge of the TGC is due to the presence of magnetic field where muons bend away from TGC acceptance depending on their charges. Ineffective areas in the TGC are due to the presence of the holes for the laser optical alignment and the physical boundary of the TGC chambers.
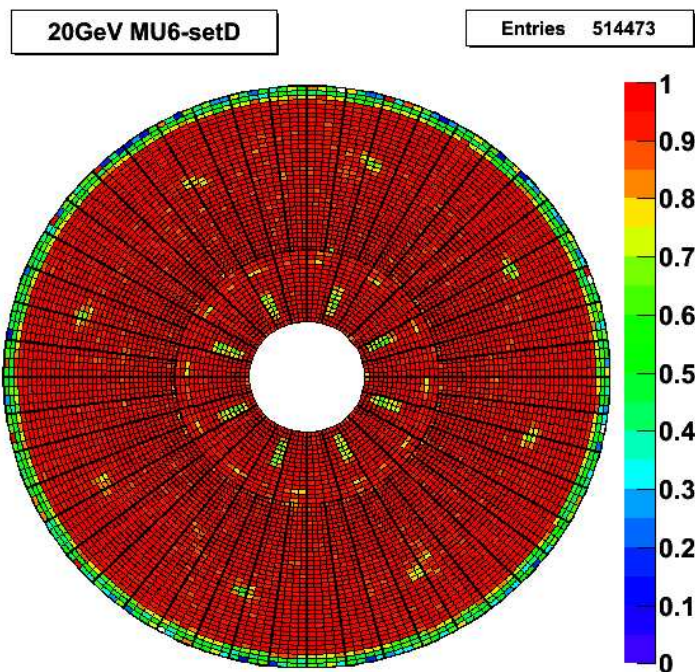
Figure 9.1: Simulated TGC L1MU6 trigger efficiency for muons with p_T of 20 GeV generated in $1.05 < |\eta| < 2.4$ in the $r - \phi$ plane.

Figure **9.1** shows a simulated L1_MU0 efficiency map in the barrel ($|\eta| < 1.05$) for muons with p_T = 10 GeV. This map indicates the acceptance holes in the barrel. Due to the presence of the detector support structure (Feet), magnet support, services for the calorimeters and elevator, the overall coverage of the RPC is about 80 % in the entire barrel region.
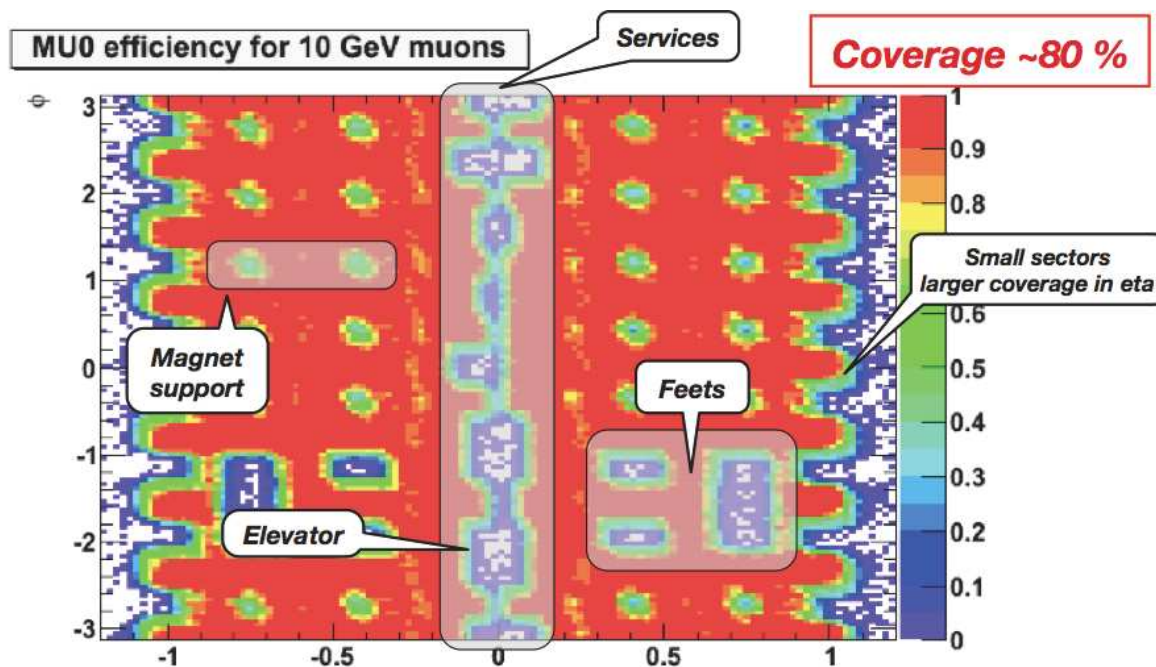
Figure 9.2: A map of the RPC trigger coverage in $\eta - \phi$ plane.

9.1.1   Timing Acceptance Stretch for Muon Level-1 Trigger Commissioning

As described in section 7.3, the timing acceptance of the MUCTPI is stretched as [-2, -1, 0] in terms of BCID difference ([BCID for a muon RoI] - [BCID for the event]). In the muon trigger efficiency calculation, RoIs in the stretched time window are adopted.

To see how BCID difference distributes, combined tracks are selected by the following selection and the BCID difference of the muon RoIs matched with any of the combined tracks are plotted.

– Reconstructed in the MuId algorithm chain

– Matching $\chi^2 < 50$

– Number of SCT hits ≥ 4

– Number of Pixel hits ≥ 1

– $|z_0 - z_{vtx}| < 10$ mm

In the matching between a given combined track and a muon RoI, $\Delta R = \sqrt{(\Delta\eta)^2 + (\Delta\phi)^2}$ of 0.5 is used. If a combined track matches with more than one RoI, the RoI which has larger BCID is adopted.

Figure **9.3** shows the distributions of the BCID difference for the TGC and the RPC trigger with respect to the L1_MBTS trigger. The events used in the figures are taken by L1_MBTS trigger, hence the figures show the difference in BCID between muon RoIs and event timings.

(a)   (b)
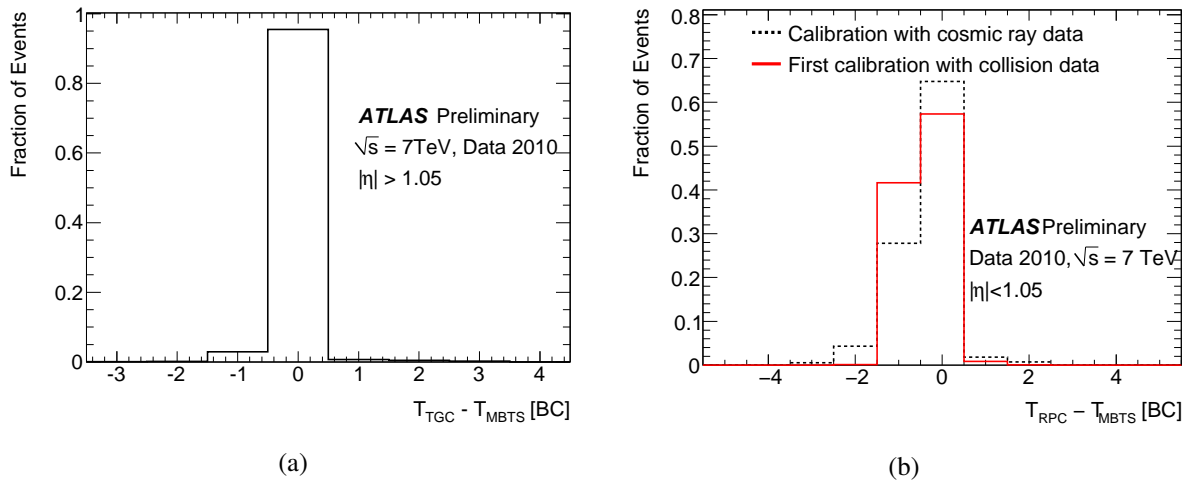
Figure 9.3: Distribution of the trigger time difference in units of bunch crossing (BC) with respect to the L1_MBTS for the TGC (a) and the RPC (b) triggers.

9.2 Trigger Efficiency Estimation by the Single Combined Track Method

This section describes the relative trigger efficiency estimation with respect to combined tracks which pass a selection based on the one used in the W / Z-boson cross sections measurement. The estimation is done with the following procedures.

1. Select a combined track

2. Extrapolate the trajectory of the combined track toward the TGC or RPC then define an RoI search range on the pivot plane

3. Search muon RoIs in the search range

If more than one muon RoIs are found in the search range, the RoI is flagged as fired by the combined track.

    This analysis is done with the data taken via L1Calo stream upon a request that at least one L1 single jet trigger is issued in a given event (the exact requirement is the OR of all L1 single jet trigger items, see Table **7.5**). Since the single jet triggers are independent to the muon trigger, no trigger bias is caused in the estimation.

9.2.1 The Combined Track Selection

The selection on combined tracks used is given in Table **9.1**. The selection is based on the W / Z event pre-selection (see Table **11.1** and **12.1**).

Collision event selection	
Good Run List & BCID	$Z \rightarrow \mu\mu$ GRL
Primary vertex	$N_{\text{vtx}} \geq 1$ with $N_{\text{tracks}} \geq 3$
	$|z_{vtx}| < 150$ mm
Trigger	OR of all L1 single jet triggers
High-p_{T} muon selection	
Muon selection	STACO combined tracks
	$p_T > 20$ GeV, $|\eta| < 2.4$
Muon quality	$p_T^{MS} > 10$ GeV
	$|p_T^{MS} - p_T^{ID}| < 15$ GeV
	$|z_0 - z_{vtx}| < 10$ mm

Table 9.1: Event and muon selection for trigger efficiency measurement.

    The $Z \rightarrow \mu\mu$ GRL is applied with resulted integrated luminosity is 331 nb^{-1}. Then the events are required to pass any of L1 single jet triggers and have one or more good vertices (for the definition of the good vertex, see section 8.3.3).

    Muons are required to be a combined track reconstructed with STACO algorithm with $p_{\text{T}} > 20$ GeV in $|\eta| < 2.4$. p_{T}^{MS}, p_{T}^{ID} are the p_{T} measured only with the muon spectrometer or the

inner detector. z_0 means the longitudinal impact parameter with respect to the IP and z_{vtx} is the z-position of a good vertex which minimizes $|z_0 - z_{vtx}|$. Details for the cuts related to p_T^{MS}, p_T^{ID}, z_0 and z_{vtx} are found in section 8.3.1.

The differences between Table **9.1** and the W/Z pre-selection are summarized as follows.

1. $p_T > 20$ GeV, which is consistent with W/Z final selection, is required in the efficiency estimation.

2. The OR of all L1 single jet triggers is required in this analysis to avoid trigger biases instead of L1_MU6 in W/Z cross sections measurement

3. No isolation is required since additional activities around a combined track are considered not to cause any bias in the trigger efficiency estimation (confirmed in section 9.2.4) and isolation requirements largely reduce the available statistics

Figure **9.4** shows event displays for a sample of events used in this efficiency estimation. All the five samples are taken from the run 159224. The red lines are muons, the purple cones are jets, the yellow lines are tracks reconstructed in the inner detector and the yellow blocks are calorimeter clusters. The gray circle represents the projection plane of the endcap TRT. Since the events are taken by single jet triggers, muons are tend to be immersed in a jet.

Figure **9.5** shows the η, ϕ and p_T distributions for the muons which pass all the selections, hereafter referred to as denominator muons (the cut of $p_T > 20$ GeV is omitted in the p_T distributions just to show the lower p_T components). In this figure, positive and negative charged muons are shown separately and histograms are stacked. In this trigger efficiency estimation, the entire muon spectrometer acceptance is divided into two bins, namely the endcap (1.05 $< \eta <$ 2.4) and the barrel ($|\eta| <$ 1.05), each corresponds to the TGC and RPC respectively. The number of denominator muons are 2307 (+ :1187, − :1120) in the endcap and 3173 (+ :1670, − :1503) in the barrel.

9.2.2   Track Extrapolation and Search Range Definition

Two independent methods are deployed in the track extrapolation and search range calculation. In this analysis, the track extrapolator method is used by default. The straight line extrapolation method is used for a validation of the results and a systematic uncertainty estimation.

Track Extrapolator Method

This method utilizes a tool called track extrapolator [134, 135] to extrapolate the trajectory of the denominator muons. In the extrapolation process, the track extrapolator takes into account the effect of magnetic field [136] and materials [137].

Extrapolations are done toward artificially defined pseudo trigger pivot planes.

- A cylinder with $r = 7500$ mm and half-length = 16000 mm along the beam axis for denominator muons in $|\eta| < 1.05$ (barrel)

- Two disks with $r = 20000$ mm at $|z| = 15525$ mm placed perpendicular to the beam axis for denominator muons with $1.05 < |\eta| < 2.4$ (endcap)
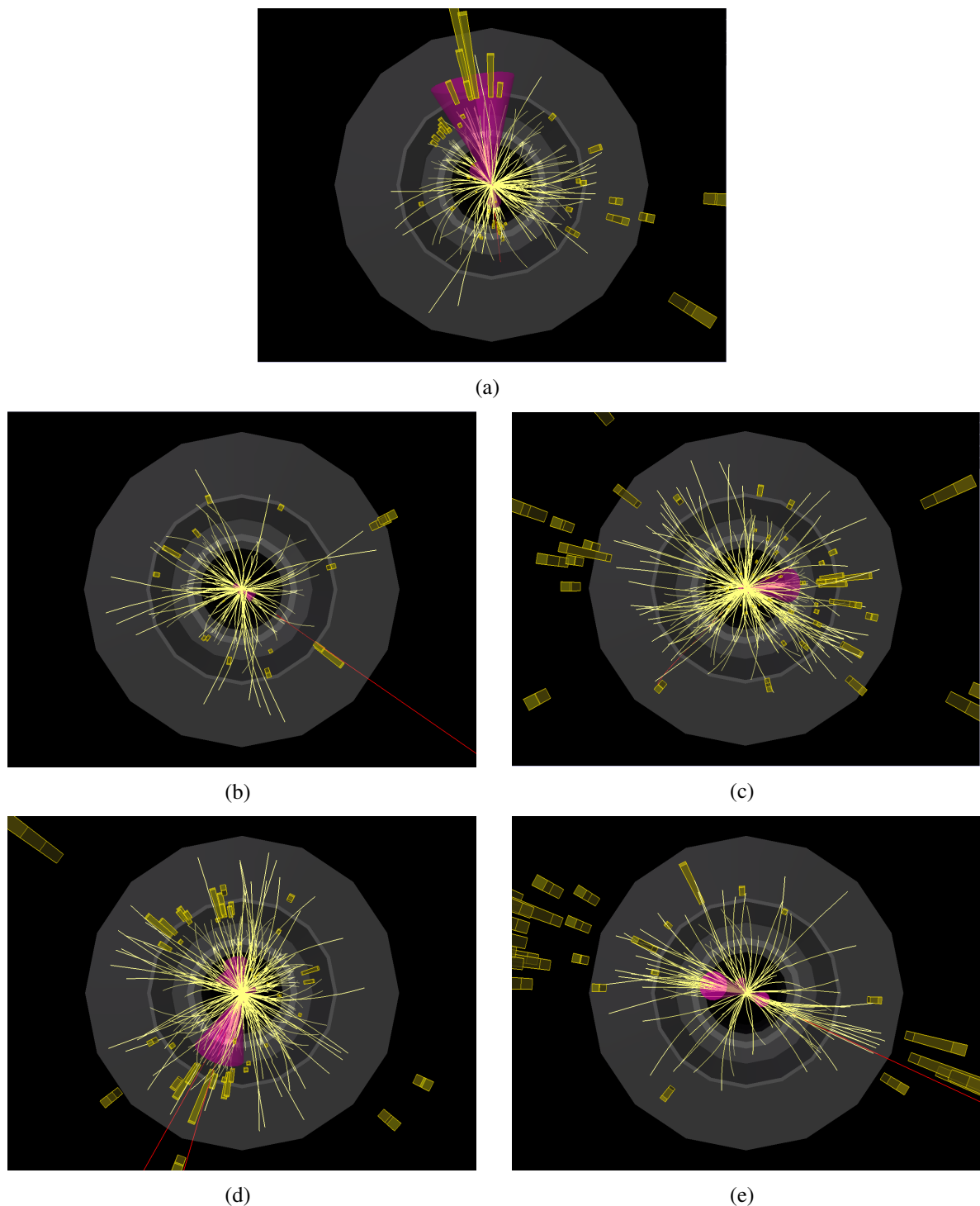
Figure 9.4: Event displays of the events used in the efficiency estimation. Red lines are muons, yellow lines are tracks reconstructed in the inner detector, purple cones are jets and yellow blocks are clusters in the calorimeter. Most of muons are immersed in a jet. All events are taken from RunNumber = 159224, LumiBlock = 260 and (a) EventNumber = 4628851 (b) EventNumber = 4634992 (c) EventNumber = 4636444 (d) EventNumber = 4659650 and (d) EventNumber = 4665286.
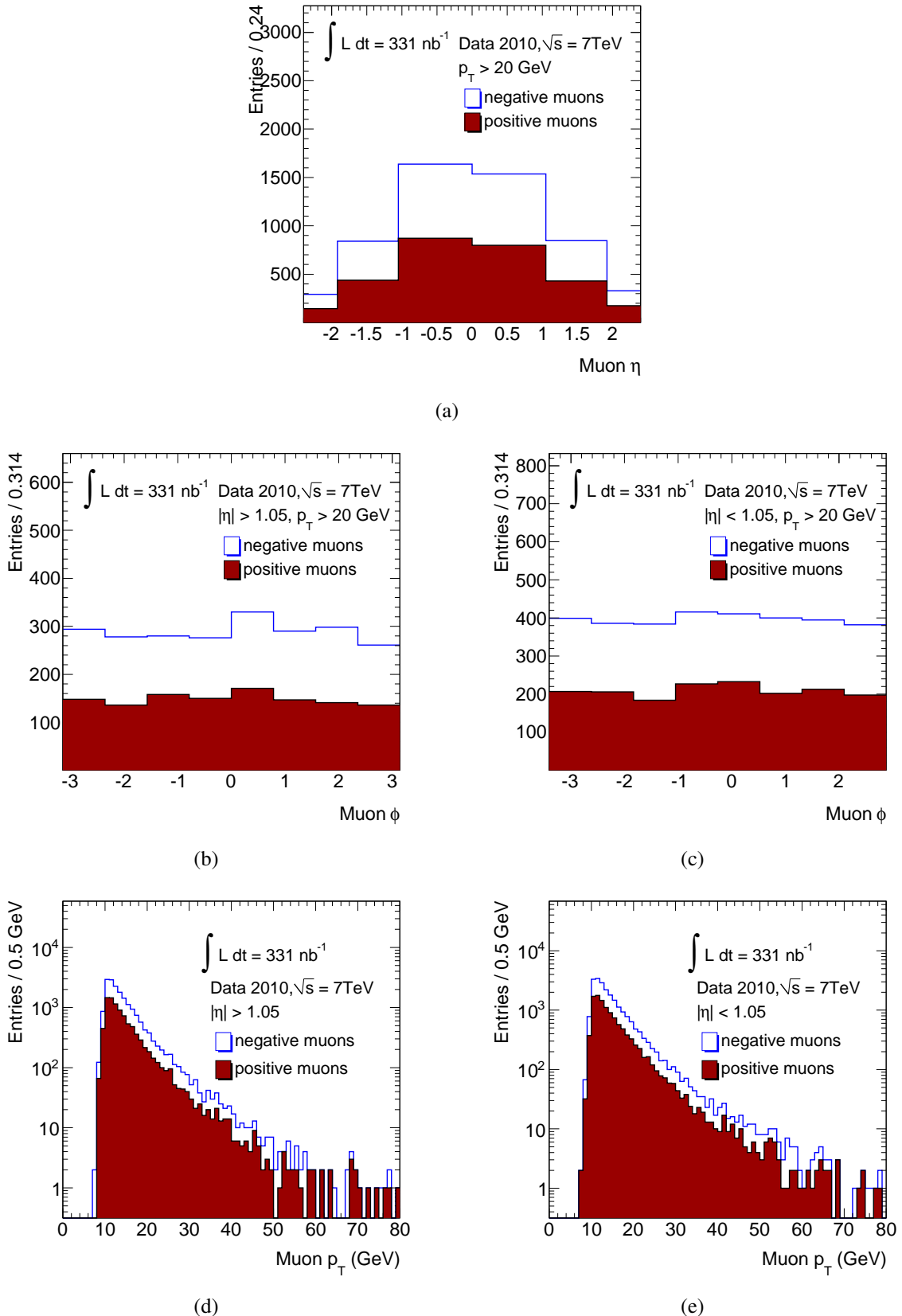
Figure 9.5: η, ϕ and p_T distributions of muons which passed all the selections listed in Table 9.1 except for the p_T distributions (the cut of $p_T > 20$ GeV is not applied on these distributions). Positive and negative muons are shown separately and both are stacked. The ϕ and p_T distributions are shown for the endcap ((b), (d)) and the barrel ((c), (e)) separately.

After an extrapolation, track extrapolator reports calculated extrapolation errors, $\delta\eta$ and $\delta\phi$. The search range is calculated based on this extrapolation error as

$$\textbf{search range} = (\text{matching tolerance}) \times \sqrt{\delta\eta^2 + \delta\phi^2} + (\text{ RoI size }). \tag{9.1}$$

The RoI size represents the half-diagonal length of RoI. The region dependence of RoI size is summarized in Table **9.2**.

Region	barrel ($|\eta| < 1.05$)	endcap ($1.05 < |\eta| < 1.95$)	forward ($|\eta| > 1.95$)
RoI size	0.071	0.019	0.034

Table 9.2: Region dependence of RoI size.

Matching tolerance is an adjustable number and set at 3.0 by default. ΔR is defined as,

$$\Delta R = \sqrt{(\eta_{ex} - \eta_{RoI})^2 + (\phi_{ex} - \phi_{RoI})^2}, \tag{9.2}$$

where (η_{ex}, ϕ_{ex}) represents the extrapolated position on the pseudo pivot plane and (η_{RoI}, ϕ_{RoI}) is the center position of the RoI in the $\eta - \phi$ plane.

Straight Line Extrapolation Method

In this method, a track trajectory is extrapolated assuming a straight line ignoring the effects of magnetic field and materials. This approximation is valid for high-p_T tracks used in W/Z cross sections measurement. A constant size of search range is defined. The default value is $\Delta R = 0.3$. This method is much simpler and robust compared to the track extrapolator method.

9.2.3   RoI Finding in a Search Range

If an RoI is found in the search range, the RoI is flagged as fired by the denominator muon. In case that more than one RoI are found in a search range, one must choose an RoI to be taken. In searching an RoI, two procedures – called the highest p_T procedure and the nearest position procedure – are deployed. The order of priority adopted in each procedure is as follows.

The Highest p_T Procedure

1. The RoI with the highest p_T threshold value

2. The RoI at the nearest position from the extrapolated point

3. The RoI with the largest BCID in the stretched timing acceptance

The Nearest Position Procedure

1. The RoI at the nearest position from the extrapolated point

2. The RoI with the highest p_T threshold value

3. The RoI with the largest BCID in the stretched timing acceptance

The highest p_T procedures is used by default. The nearest position procedures is used for a cross check and a systematic uncertainty estimation.

9.2.4 Estimated Efficiency and Scale Factor

The L1_MU6 trigger efficiencies are estimated using the following combination as the default.

- The track extrapolator method in track extrapolation and search range definition

- The highest p_T procedure in RoI finding

Shown in Figure **9.6** is a two dimensional map of the estimated trigger efficiency for the L1_MU6. A low efficiency region with $\eta < $ -1.9 and $\phi \sim$ -1.8 is due to a problematic electronics board which applies threshold voltages. The condition of the board has not changed throughout the data taking period. Another low efficiency region around $\phi \sim$ -1.6 in the barrel is due to the acceptance hole on the RPC for the detector support structure (see Figure **9.2**). For the figure, p_T cut value is relaxed from 20 GeV to 15 GeV to gain statistics.

Shown in Figure **9.7** is the estimated trigger efficiency for the L1_MU6 as a function of η, ϕ and p_T. The results for the endcap and the barrel shown separately for the figure in terms of ϕ and p_T. The Figure **9.7** (a) shows the η dependence, which shows the low efficiency in $\eta < $ -1.9 due to the above mentioned problematic electronics board. The efficiency in the barrel is lower than the endcap reflecting the lower acceptance in the barrel. The Figure **9.7** (c) shows the ϕ dependence in the barrel. The above mentioned support structure region is clearly seen.

A list of the estimated efficiencies for all the L1 single muon trigger items in $p_T > 20$ GeV are summarized in Table **9.3** along with the trigger efficiencies estimated in MC and trigger efficiency scale factors (The definition of the scale factor is described later). As shown in the table, the estimated trigger efficiency is consistent between positive and negative muons within $1\,\sigma$. Hence no charge dependence in the trigger efficiency is assumed in this study.
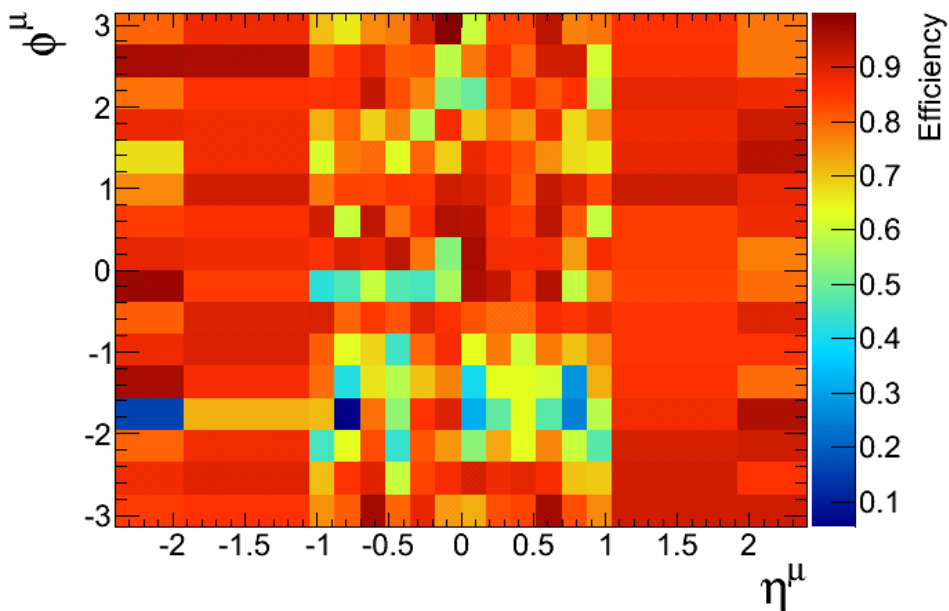
Figure 9.6: Estimated trigger efficiency for L1_MU6 in data in the $\eta - \phi$. The track selection is based on Table **9.1** but p_T cut value is relaxed to 15 GeV.
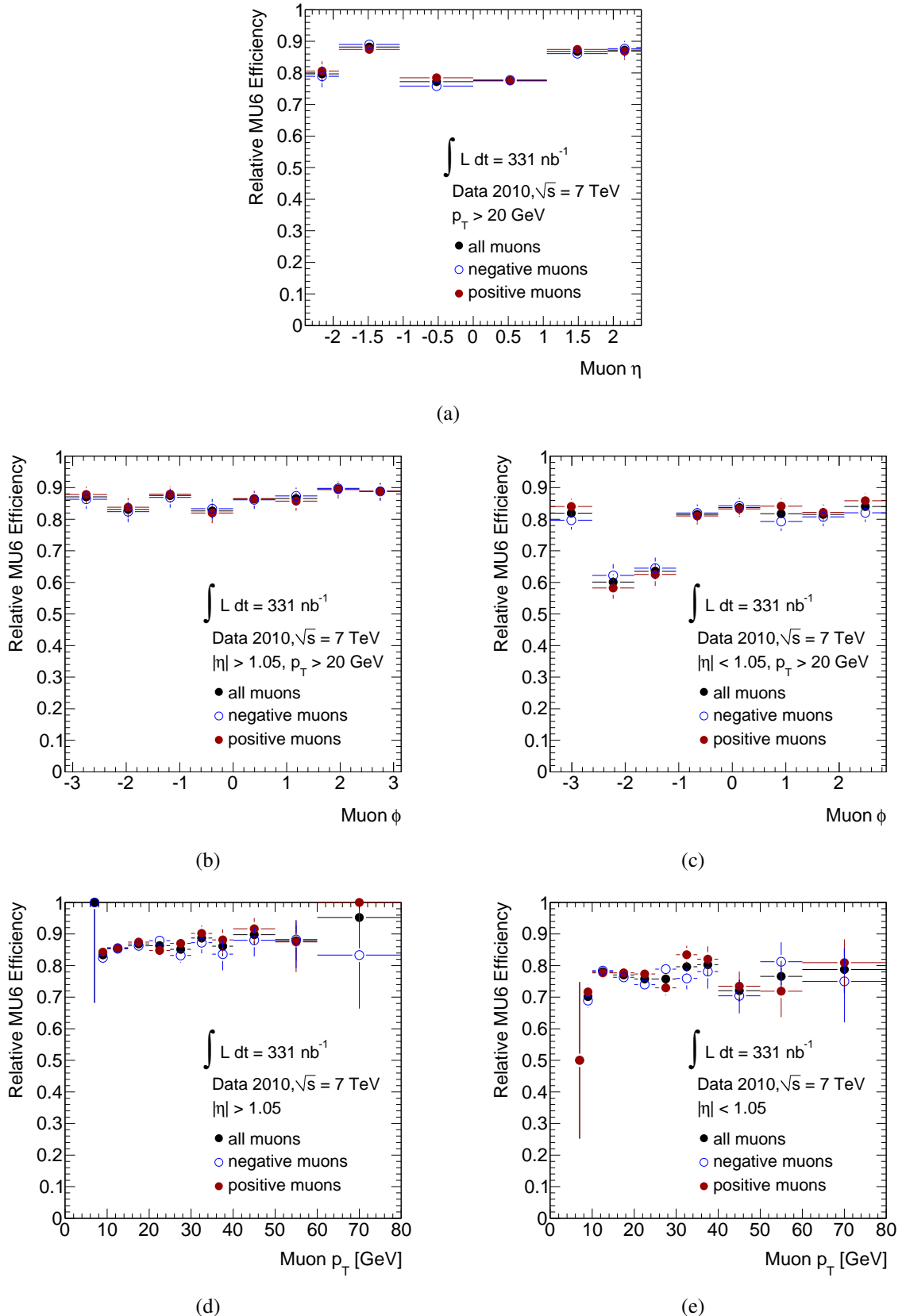
Figure 9.7: Estimated L1_MU6 trigger efficiency as a function of η, ϕ and p_T for muons which passed all the selections listed in Table **9.1** except for the cut of $p_T > 20$ GeV in p_T distributions. Efficiencies for positive, negative and all muons are shown separately. The ϕ and p_T distributions are shown for the endcap ((b), (d)) and the barrel ((c), (e)) separately.

Isolation Effect on Trigger Efficiencies

As shown in Figure **9.4**, denominator muons are tend to be not isolated. The basic concept of this relative trigger efficiency measurement is to use the muons with the same quality for trigger efficiency as the one used in the W / Z-boson cross sections measurement. A naive guess is that, since both the TGC and RPC utilize hit coincidence in its algorithm, additional hits will not deteriorate the efficiency unless the density of hits becomes huge. The dependence of the trigger efficiency on isolation is investigated to ensure this assumption.

Two types of isolation variables are defined. One is utilizing a sum of transverse energy in the calorimeter within a cone centered at the direction of the muon in consideration with a certain ΔR divided by the p_T of the muon.

$$(\text{ relative } E_T \text{ isolation }) = \frac{\Sigma^{\Delta R} E_T(\text{calo})}{p_T(\text{track})}. \tag{9.3}$$

Another is utilizing a sum of p_T of charged tracks reconstructed in the inner detector within a cone centered at the direction of the muon in consideration with a certain ΔR divided by the p_T on the muon. In the calculation, p_T of tracks with $p_T < 1$ GeV and the p_T of muon itself is not added.

$$(\text{ relative } p_T \text{ isolation }) = \frac{\Sigma^{\Delta R} p_T(\text{track})}{p_T(\text{track})}. \tag{9.4}$$

The contribution from the muon itself is subtracted from the numerator in both types of isolation variables.

Figure **9.8** shows the dependence of L1_MU6 trigger efficiency on the two isolation variables with different ΔR values. One can see that relative trigger efficiencies do not depend on the isolation variables. Figure **9.9** shows distributions for both isolation variables in the endcap and the barrel. The one used in the cross sections measurement of the W / Z is the relative p_T isolation with $\Delta R = 0.4$.
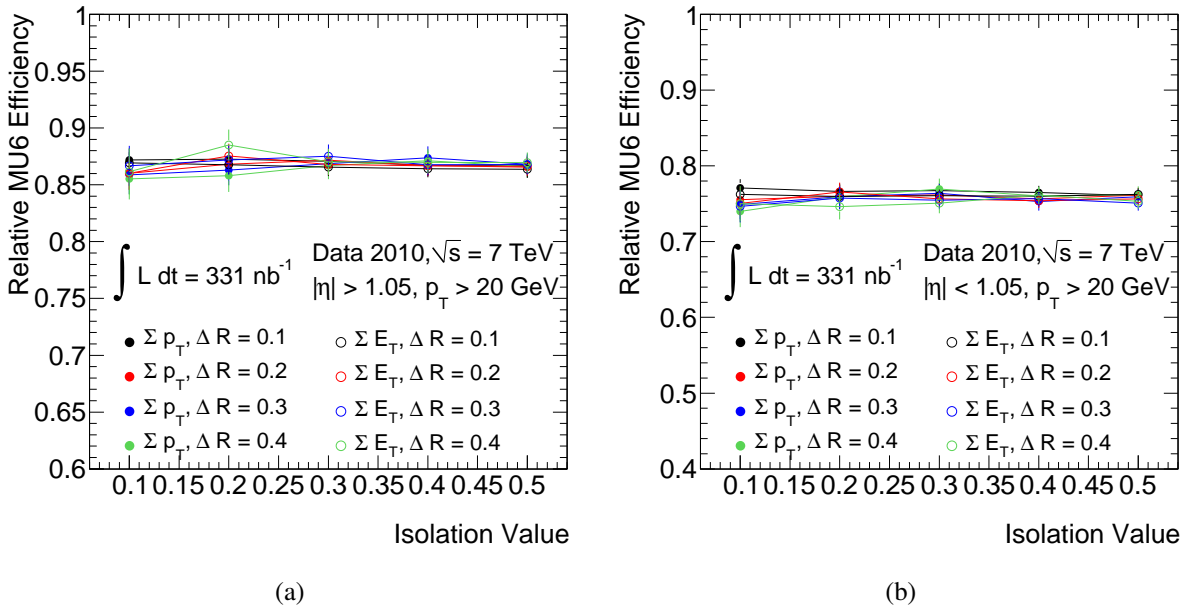
Figure 9.8: Isolation dependence of L1_MU6 efficiency in the endcap (a) and the barrel (b).
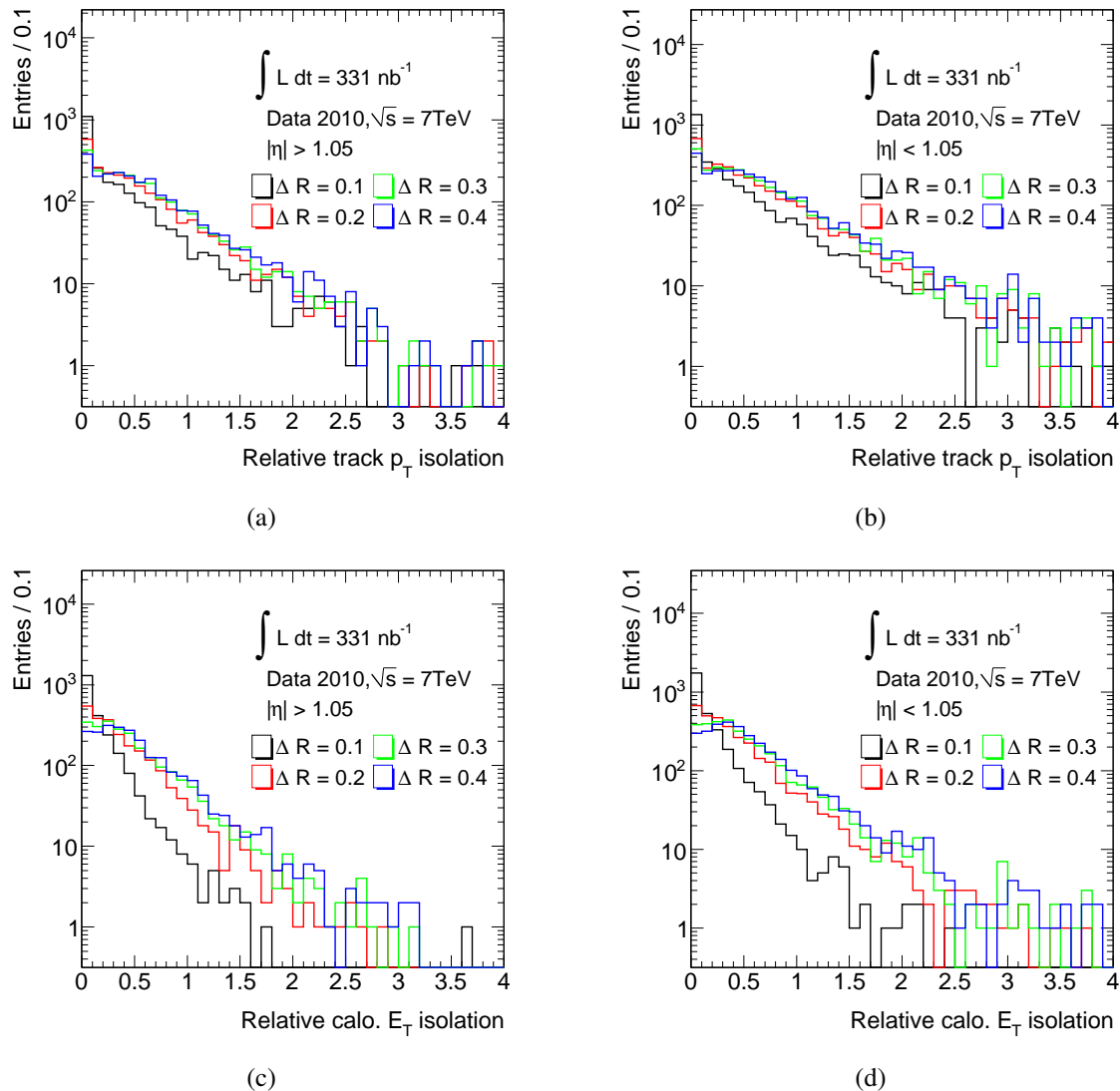
Figure 9.9: Relative p_T and E_T isolation variables for denominator muons in endcap ((a), (c)) and barrel ((b), (d)) with various cone sizes.

Trigger Efficiency Scale Factor

In the *W / Z*-boson cross sections measurement, trigger efficiencies measured in data are used for the correction of MC efficiency (see section 8.1), thus the actual value used in the cross sections measurement is so called scale factor, the ratio of data efficiency to MC efficiency.

$$\textbf{scale factor} = \frac{\text{efficiency in data}}{\text{efficiency in MC}}. \tag{9.5}$$

In this section the scale factor for single muons is derived. The MC sample used in this derivation is of $W \to \mu\nu$ process.

In the efficiency estimation in both data and MC, the completely same method is deployed, i.e. no truth information is used for MC. In this study, efficiency for L1_MU6 has a special importance since it is used for the *W / Z*-boson cross sections measurement. Figure **9.10** shows the estimated single muon efficiency for L1_MU6 in the endcap and the barrel as a function of p_T. The selection in Table **9.1** is applied except for the $p_T > 20$ GeV just to show the efficiency in the p_T region below the cut value. In the cross sections measurement, the muons with $p_T > 20$ GeV is used thus the single muon scale factor is derived using the average efficiency in the $p_T > 20$ GeV region. Table **9.3** summarizes the efficiencies and scale factors for denominator muons with $p_T > 20$ GeV.

One can see a discrepancy between the efficiency in data and MC for L1_MU6 especially in the endcap. Currently this is understood as a combination effect of the inefficiency of the TGC chambers and lack of calibration for the trigger road programmed in the L1 trigger electronics.

trigger	charge	efficiency in data endcap (%)	efficiency in data barrel (%)	efficiency in MC endcap (%)	efficiency in MC barrel (%)	scale factor endcap (%)	scale factor barrel (%)
L1_MU0	all	95.1 ± 0.4	76.8 ± 0.7	98.2 ± 0.1	79.5 ± 0.2	96.9 ± 0.5	96.6 ± 1.0
	μ^+	95.2 ± 0.6	77.4 ± 1.0	98.2 ± 0.1	79.4 ± 0.3	97.0 ± 0.6	97.4 ± 1.3
	μ^-	95.0 ± 0.7	76.2 ± 1.1	98.2 ± 0.1	79.6 ± 0.3	96.7 ± 0.7	95.7 ± 1.4
L1_MU6	all	86.5 ± 0.7	76.3 ± 0.8	95.0 ± 0.1	79.3 ± 0.3	91.1 ± 0.8	96.1 ± 1.0
	μ^+	86.5 ± 1.0	76.9 ± 1.0	94.9 ± 0.1	79.3 ± 0.3	91.2 ± 1.1	97.1 ± 1.3
	μ^-	86.4 ± 1.0	75.5 ± 1.1	95.1 ± 0.2	79.5 ± 0.3	90.9 ± 1.1	95.0 ± 1.4
L1_MU10	all	86.3 ± 0.7	76.2 ± 0.8	94.8 ± 0.1	79.3 ± 0.2	91.0 ± 0.8	96.1 ± 1.0
	μ^+	86.3 ± 1.0	76.9 ± 1.0	94.7 ± 0.1	79.2 ± 0.3	91.1 ± 1.1	97.1 ± 1.3
	μ^-	86.3 ± 1.0	75.4 ± 1.1	94.8 ± 0.2	79.4 ± 0.3	91.0 ± 1.1	95.0 ± 1.4
L1_MU15	all	85.1 ± 0.7	61.1 ± 0.9	94.1 ± 0.1	73.2 ± 0.2	90.4 ± 0.8	83.6 ± 1.2
	μ^+	85.1 ± 1.0	62.0 ± 1.2	94.0 ± 0.1	73.2 ± 0.3	90.5 ± 1.1	84.8 ± 1.7
	μ^-	85.1 ± 1.1	60.1 ± 1.3	94.2 ± 0.2	73.2 ± 0.3	90.3 ± 1.1	82.2 ± 1.8
L1_MU20	all	82.6 ± 0.8	60.6 ± 0.9	93.6 ± 0.1	73.1 ± 0.2	88.2 ± 0.8	82.9 ± 1.2
	μ^+	82.8 ± 1.1	61.5 ± 1.2	93.6 ± 0.1	73.1 ± 0.3	88.5 ± 1.1	84.2 ± 1.7
	μ^-	82.4 ± 1.1	59.5 ± 1.3	93.8 ± 0.2	73.1 ± 0.3	87.9 ± 1.2	81.5 ± 1.8

Table 9.3: A summary of the L1 single muon trigger efficiencies. Assigned errors contain only statistical components.
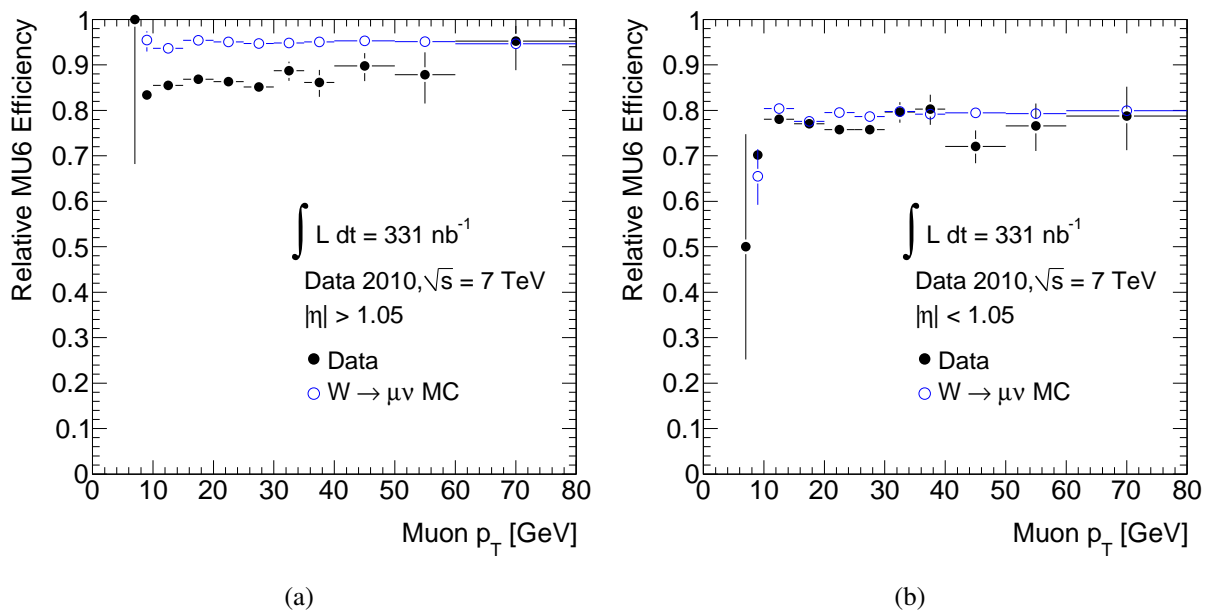
Figure 9.10: L1_MU6 trigger efficiencies estimated in data and MC in the endcap ((a)) and the barrel ((b)). Muons are selected by the selection in Table **9.3** except for p_T cut of 20 GeV. In the scale factor calculation, the average efficiency in the $p_T > 20$ GeV is used.

9.2.5 Systematic Uncertainty

The L1_MU6 is solely used in the W/Z-boson cross sections measurement since it is the lowest threshold un-prescaled trigger during the data taking period. In this section, systematic uncertainty on the L1_MU6 efficiency and scale factor is investigated. The results are summarized in Table **9.4**. The detailed description for each component is given in the following subsections.

	eff. in data (%)		eff. in MC (%)		scale factor (%)	
	endcap	barrel	endcap	barrel	endcap	barrel
Reconstruction algorithm dependence	0.4	2.8	0.0	1.3	0.5	1.5
p_T cut value ($\pm$ 5 GeV)	0.8	1.1	0.1	0.2	0.8	1.0
$\lvert p_T^{ID} - p_T^{MS} \rvert$ cut value ($\pm$ 5 GeV)	0.4	0.1	0.0	0.2	0.4	0.1
Track extrapolation method	1.3	0.4	0.3	0.1	1.0	0.4
RoI finding criteria	1.5	0.1	0.3	0.0	1.2	0.1
Size of search range in RoI finding	0.5	0.1	0.4	0.0	0.2	0.1
η distribution re-weight	—	—	—	—	0.3	0.5
Total	2.3	3.0	0.6	1.3	1.9	1.9

Table 9.4: Relative systematics for the L1_MU6 trigger efficiencies and scale factors.

Reconstruction algorithm dependence STACO algorithm, which is used as the default in this analysis, requires at least one trigger hit in both η and ϕ coordinates in ROA search whereas MuId algorithm does not. This requirement could bias the relative trigger efficiency. The size of bias differs place by place reflecting the variation in acceptance and efficiency of the trigger chambers. However the current binning, which divides the muon spectrometer into only two bins namely the endcap ($\lvert\eta\rvert > 1.05$) and the barrel ($\lvert\eta\rvert < 1.05$), is so coarse that we cannot be sensitive to this effect.

To cover this effect, we take the difference in measured efficiency between STACO and MuId as a systematic component. The L1_MU6 trigger efficiencies for STACO is summarized in Table **9.3** and for MuId are summarized in Table **9.5**. The estimated relative uncertainties, estimated uncertainty divided by the efficiency or scale factor of STACO muons, on efficiency in data are 0.4 (2.8) % and in MC are 0.0 (1.3) % in the endcap (barrel) resulting uncertainties on the scale factors of 0.5 (1.5) %.

charge	eff. in data (%)		eff. in MC (%)		scale factor (%)	
	endcap	barrel	endcap	barrel	endcap	barrel
all	86.1 ± 0.7	74.2 ± 0.8	95.0 ± 0.1	78.3 ± 0.2	90.6 ± 0.8	94.7 ± 1.0
μ^+	86.6 ± 1.0	75.0 ± 1.0	94.9 ± 0.1	78.2 ± 0.3	91.2 ± 1.0	95.9 ± 1.4
μ^-	85.6 ± 1.0	73.3 ± 1.1	95.1 ± 0.2	78.5 ± 0.3	89.9 ± 1.1	93.3 ± 1.4

Table 9.5: A summary of the L1_MU6 trigger efficiencies and scale factors with respect to muons reconstructed in MuId algorithm.

p_T **Cut Value**   To take into account the muon momentum scale and resolution fluctuation resulting an instability of the averaged efficiency in plateau region, the p_T cut value is shifted by $\pm$ 5 GeV with 0.5 GeV steps. The results are shown in Figure **9.11** for both in the endcap and the barrel. The assigned errors are statistical only.

Though fluctuations of the central efficiency / scale factor values are relatively small compared to the statistical error, the maximum shift of central values are counted as a conservative systematic component. The estimated relative uncertainties on efficiency in data are 0.8 (1.1) % and in MC are 0.1 (0.2) % in the endcap (barrel), resulting uncertainties on the scale factors of 0.8 (1.0) %.

(a)   (b)
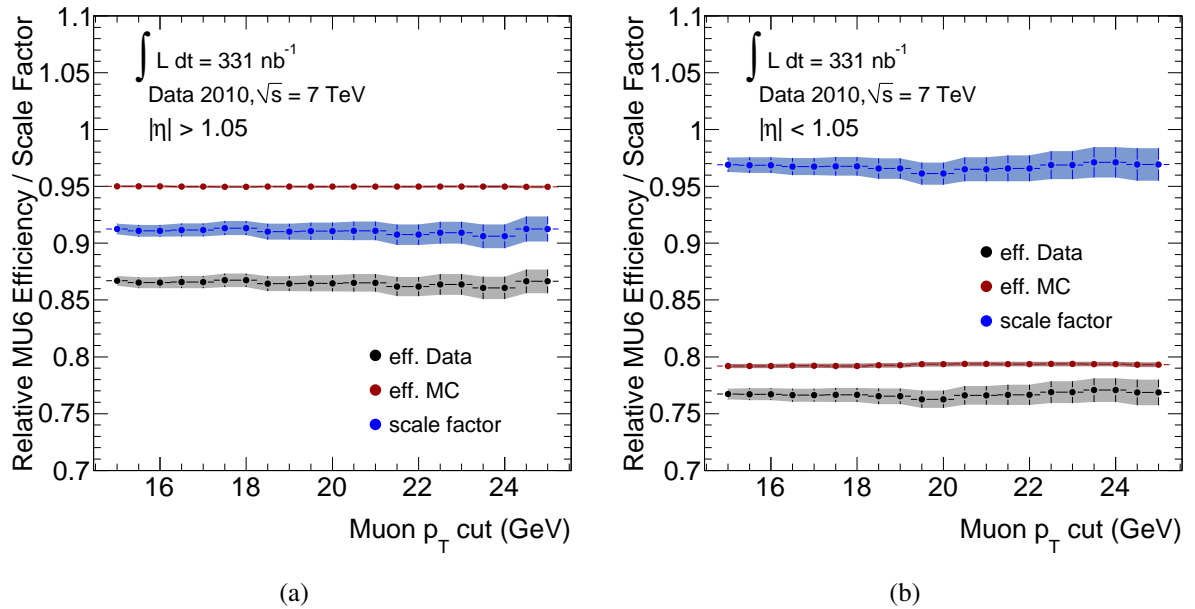
Figure 9.11: Fluctuation of averaged L1_MU6 efficiency for muons with p_T > 20 GeV and scale factor with shifting p_T cut.

$|p_T^{ID} - p_T^{MS}|$ **cut value**   To estimate the impact of the decay-in-flight contamination in the denominator muons, the effect of changing $|p_T^{ID} - p_T^{MS}|$ cut value is investigated.

In the estimation, the cut value is shifted by 0.5 GeV step and the maximum shift of the central value between 10 GeV and 20 GeV are counted as a systematic component. The resulting plots are shown in Figure **9.12**. The estimated relative uncertainties on efficiency in data are 0.4 (0.1) % and in MC are 0.0 (0.2) % in the endcap (barrel), resulting uncertainties on the scale factors of 0.4 (0.1) %.

Track extrapolation method dependence   As described in section 9.2.3, two methods are deployed for the track extrapolations. By default, the track extrapolator is used but the straight line extrapolation method is also utilized. The difference in the estimated efficiencies between both methods are taken as a systematic component.

The estimated relative uncertainties on efficiency in data are 1.3 (0.4) % and in MC are 0.3 (0.1) % in the endcap (barrel), resulting uncertainties on the scale factors of 1.0 (0.4) %.
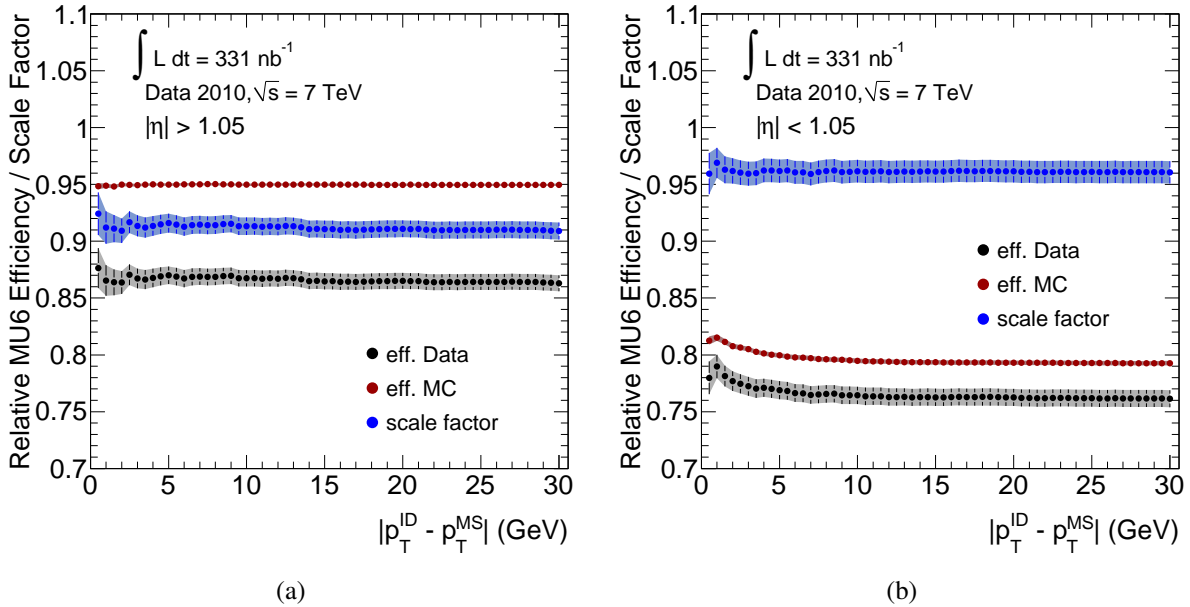
Figure 9.12: Fluctuation of L1_MU6 efficiency and scale factor with shifting $|p_T^{ID} - p_T^{MS}|$ cut. The maximum shift of the central value between 10 GeV and 20 GeV are counted as a systematic component.

RoI finding criteria dependence   As described in section 9.2.3, two procedures are deployed for RoI finding in a search range.

By default, in case of more than one RoIs are found in the search range, the first priority is given to an RoI with the highest p_T threshold number. However one can not guarantee that this procedure always selects the RoIs actually fired by the muon. One can give the first priority to the RoI which is the nearest to the extrapolated point instead and this procedure is equally valid as the default one. Thus we take the efficiency difference between this two procedures as a systematic component. The estimated relative uncertainties on efficiency in data are 1.5 (0.1) % and in MC are 0.3 (0.0) % in the endcap (barrel), resulting uncertainties on the scale factors of 1.2 (0.1) %.

Size of search range in RoI finding   The search range in the RoI finding is defined as in Eq.(9.1). The dependence of efficiencies and scale factors on matching tolerance is shown in Figure **9.13**. The full width of the fluctuation of central values when we change the matching tolerance by ± 1 σ from default value (3 σ) are counted as a systematic component.

The estimated relative uncertainties on efficiency in data are 0.5 (0.1) % and in MC are 0.4 (0.0) % in the endcap (barrel), resulting uncertainties on the scale factors of 0.2 (0.1) %.

η distribution re-weight   Most of the muons used in this trigger efficiency measurement are considered to be coming from semi-leptonic decay of heavy flavor mesons. Thus the η distribution of the muons are different from the muons from W or Z boson decay. Figure **9.14** shows the difference in η distribution on denominator muons and muons in $Z \to \mu\mu$ and $W \to \mu\nu$ MCs. This difference could enhance or suppress the L1_MU6 trigger efficiency in specific
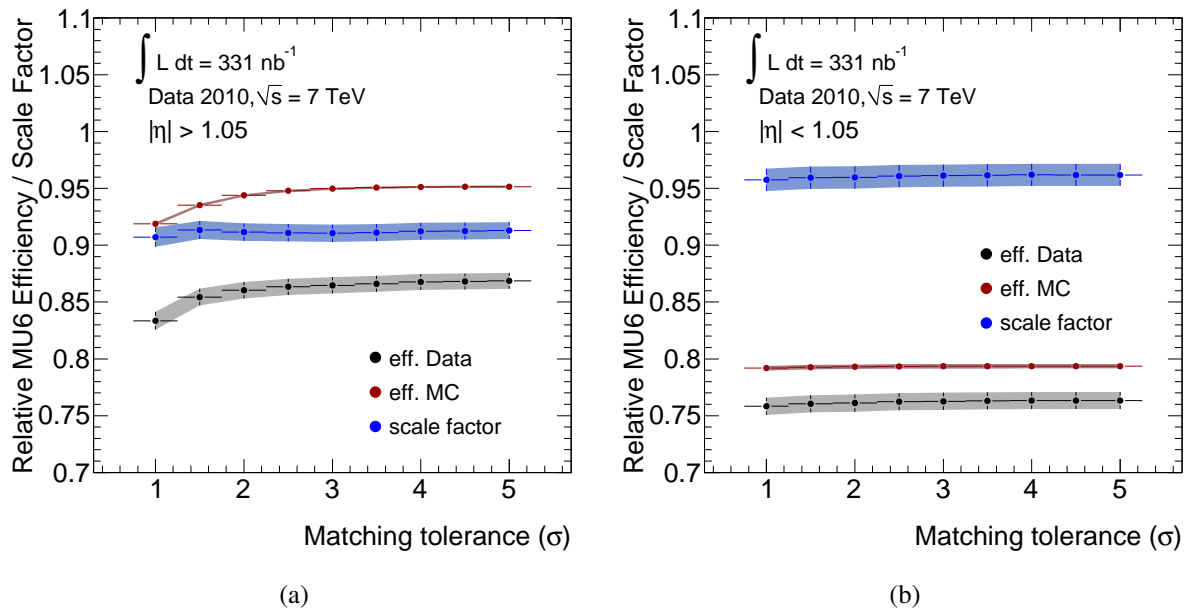
Figure 9.13: Fluctuation of L1_MU6 efficiency and scale factor against the change of matching tolerance. The maximum shift of the central value between 2 σ and 4 σ are counted as a systematic component.

regions then make the overall efficiency value different from that of true *W* or *Z*'s. To evaluate this uncertainty, the following procedures are taken.

- create L1_MU6 trigger efficiency map as a function of η in data

- apply $Z \to \mu\mu$ and $W \to \mu\nu$ muon distributions on the efficiency map and calculated overall efficiency in the endcap and the barrel bins

The efficiency map is created with two sets of granularity. One is dividing $|\eta| < 2.4$ region into 20 and the other into 40. Both binning report very consistent results. The derived overall efficiency in the endcap and the barrel is summarized in Table **9.6**.

	reweighed eff. (20 bins)		reweighed eff. (40 bins)	
sample for η distribution	endcap (%)	barrel (%)	endcap (%)	barrel (%)
data	86.5 ± 0.8	76.3 ± 0.7	86.5 ± 0.7	76.3 ± 0.7
$Z \to \mu\mu$	86.2 ± 0.8	75.8 ± 0.8	86.2 ± 0.8	75.8 ± 0.8
$W \to \mu\nu$	86.2 ± 0.7	75.9 ± 0.8	86.2 ± 0.7	75.9 ± 0.8

Table 9.6: A summary of the derived L1_MU6 efficiencies in the endcap and the barrel after reweighed by the η distributions of muons obtained in $Z \to \mu\mu$ and $W \to \mu\nu$ MC. The assigned errors are statistical only.

The central values in data is the same as in Table **9.3**, as expected. The systematic uncertainties assigned to this effect are 0.3 (0.5) % in the endcap (barrel) taking the maximum difference between data and MC. This effect is directly counted on the scale factor uncertainty.
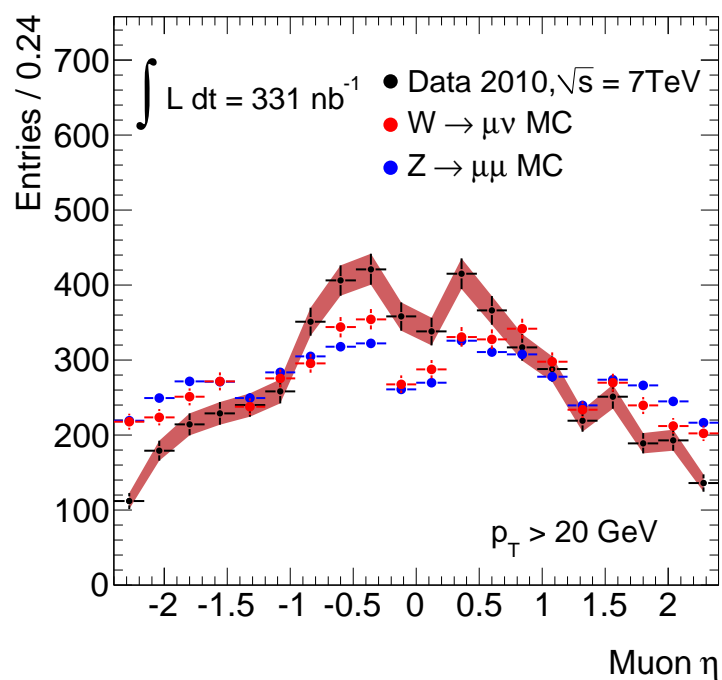
Figure 9.14: η distribution of muons in data, $Z \rightarrow \mu\mu$ and $W \rightarrow \mu\nu$ MC.

9.2.6 Trigger Efficiency Stability

The stability of the L1_MU6 trigger efficiency during the data taking period is shown in Figure **9.15**. The period is divided into seven sub-periods and each sub-period has at least about 20 nb^{-1} of data. The results for every period are consistent with the overall average within the error.

(a)

(b)
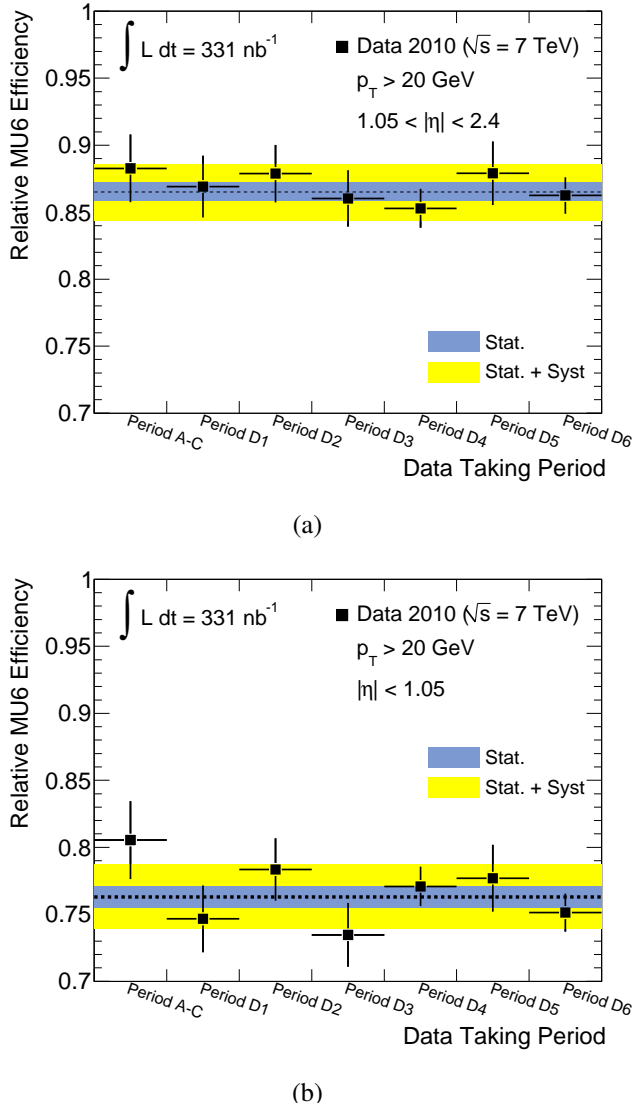
Figure 9.15: L1_MU6 trigger efficiency stability over the data taking period in the endcap (a) and barrel (b). The dotted line shows the overall average, the light blue band shows the statistical error and the yellow band shows the total uncertainty. The error bars on the black square points shows the statistical error only.

9.3   Trigger Efficiency Estimation by $Z \to \mu\mu$ Tag-and-Probe Method

9.3.1   Tag and Probe Method

Tag-and-probe method is a concrete application of a data-driven technique to collect pure, unbiased samples of probe-like object. In the performance measurement of the muon spectrometer in high-p_T regime, tag-and-probe method utilizing $Z \to \mu\mu$ process is deployed. In this case, probe-like object is a high-p_T muon.

The basic procedure of $Z \to \mu\mu$ tag-and-probe method is as follows.

1. A high-p_T combined track with high track qualities is taken. This muon is called tag muon. The tag muon is required to be matched with one or more L1_MU6 RoIs.

2. Another combined track which has Z-boson consistent invariant mass with the tag muon is adopted as a probe muon.

In the procedure, the event trigger is ascribed to the tag muon. Hence the probe muon is free from trigger biases. Furthermore, due to the high background rejection power of the invariant mass cut, very pure muon samples can be collected.

9.3.2   Event Selection and Muon Distribution

$Z \to \mu\mu$ candidate are chosen utilizing the same selection criteria used in the $Z \to \mu\mu$ cross sections measurement (see Table **12.1**). Note that the trigger item used for the event selection is L1_MU6. There are 109 Z-boson candidates found. For the relative trigger efficiency estimation, both muons can be used for the measurement. Thus number of muon candidates is doubled from the number of Zs, i.e. total of 218 muons are used for the efficiency measurement. Figure **9.16** shows the distribution of muons coming from $Z \to \mu\mu$ decays. In these figures, MC histograms are normalized to the number of events yielded in data. As described in section 12.4, the estimated amount of the background events is below % level, hence ignored in these figures.

9.3.3   Estimated Efficiency and Scale Factor

The relative trigger efficiencies are measured by using both muons in $Z \to \mu\mu$ candidate events following the steps listed below.

1. Find $Z \to \mu\mu$ candidate events with two muons (each of them is called μ_1 and μ_2 hereunder)

2. First, μ_1 is used for the efficiency measurement using the same procedure described in section 9.2. In this measurement, prior to the μ_1 trial, μ_2 is required to be matched with an L1_MU6 RoI to remove a trigger bias from the μ_1 measurement.

3. Then μ_2 is used for the measurement upon the condition that μ_1 is matched with an L1_MU6 RoI.
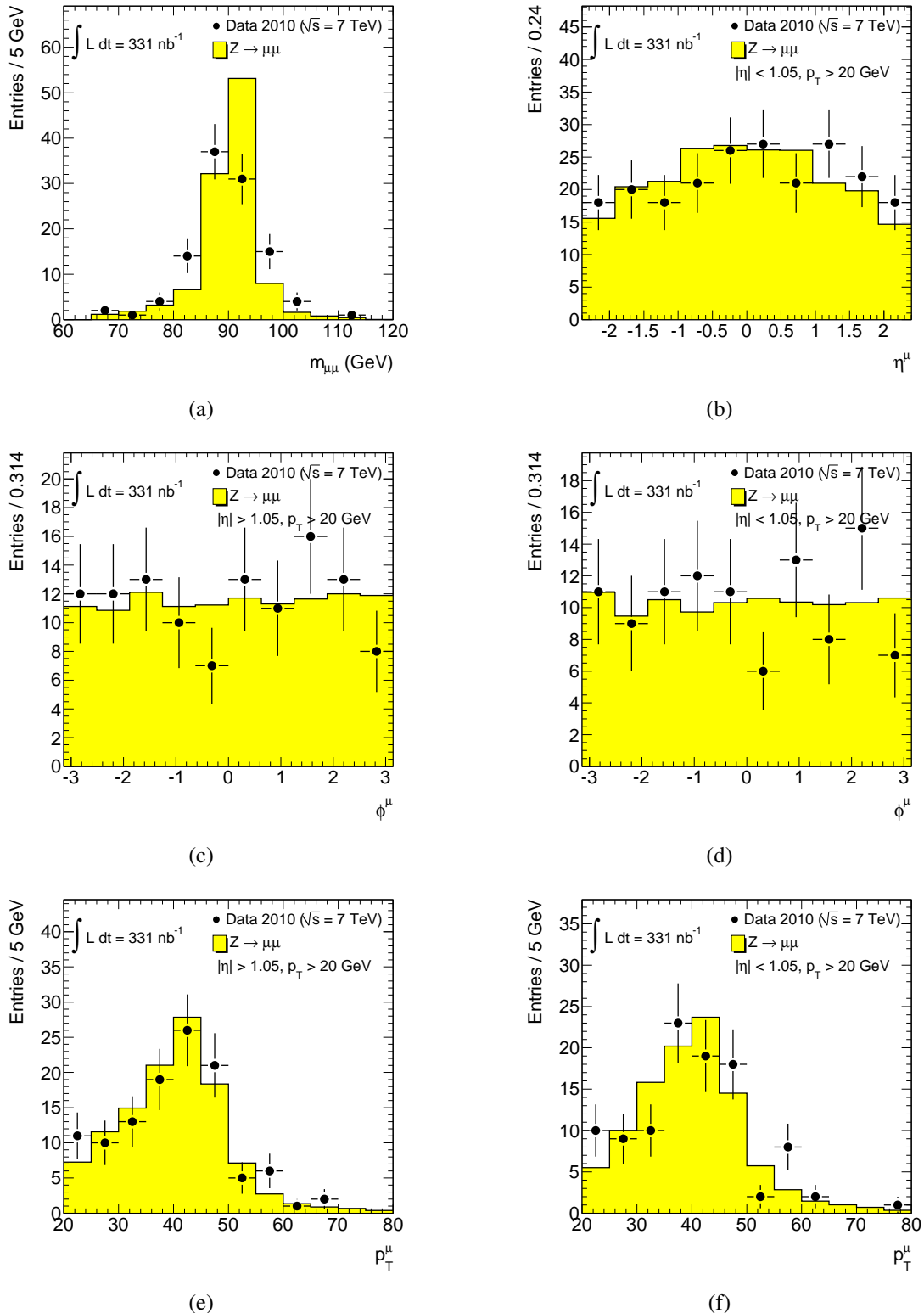
Figure 9.16: (a): Invariant mass distribution of tag and probe muons. (b) (c) (d) (e) (f): η, ϕ and p_{T} distribution for probe muons.

The results of the relative L1_MU6 efficiency measurement using $Z \to \mu\mu$ tag-and-probe are shown in Figure **9.17** compared to the results from the single combined track method. Table **9.7** summarizes the efficiencies and scale factors of $p_T > 20$ GeV. One can see that the results from tag-and-probe method is well consistent with the result from the single combined track method.

	charge	eff. in data endcap (%)	eff. in data barrel (%)	eff. in MC endcap (%)	eff. in MC barrel (%)	scale factor endcap (%)	scale factor barrel (%)
	all	86.5 ± 3.5	74.7 ± 4.7	95.2 ± 0.2	79.4 ± 0.4	90.8 ± 3.7	94.1 ± 5.9
L1_MU6	μ^+	84.8 ± 5.3	71.4 ± 6.5	94.9 ± 0.3	79.3 ± 0.5	89.3 ± 5.6	90.1 ± 8.2
	μ^-	88.0 ± 4.6	78.9 ± 6.6	95.4 ± 0.3	79.6 ± 0.5	92.2 ± 4.8	99.2 ± 8.3

Table 9.7: Estimated L1_MU6 trigger efficiencies and scale factors with tag-and-probe method.

9.4   Single Muon Trigger Efficiency Scale Factor

Here, the single muon trigger efficiency measurements described in this section is summarized. The needed information in the measurement of the W / Z-boson cross sections is the efficiency scale factor for single muons. The results for independent two methods, namely

1. Single combined track method

2. Tag-and-probe method with $Z \to \mu\mu$ events

were presented. The central values for the scale factors agree well between both methods. As for the uncertainty, the one from the method 1 is adopted since the available statistics are much higher than the method 2. The single muon trigger efficiency scale factors for the W / Z cross sections measurement are summarized in Table **9.8**.

region	parameter	result
	eff. in data	0.865 ± 0.007 (stat) ± 0.016 (syst)
endcap	eff. in MC	0.950 ± 0.001 (stat) ± 0.006 (syst)
	single muon scale factor	0.911 ± 0.008 (stat) ± 0.017 (syst)
	eff. in data	0.763 ± 0.008 (stat) ± 0.015 (syst)
barrel	eff. in MC	0.793 ± 0.002 (stat) ± 0.010 (syst)
	single muon scale factor	0.961 ± 0.010 (stat) ± 0.018 (syst)

Table 9.8: A summary of the L1_MU6 trigger efficiency and scale factor
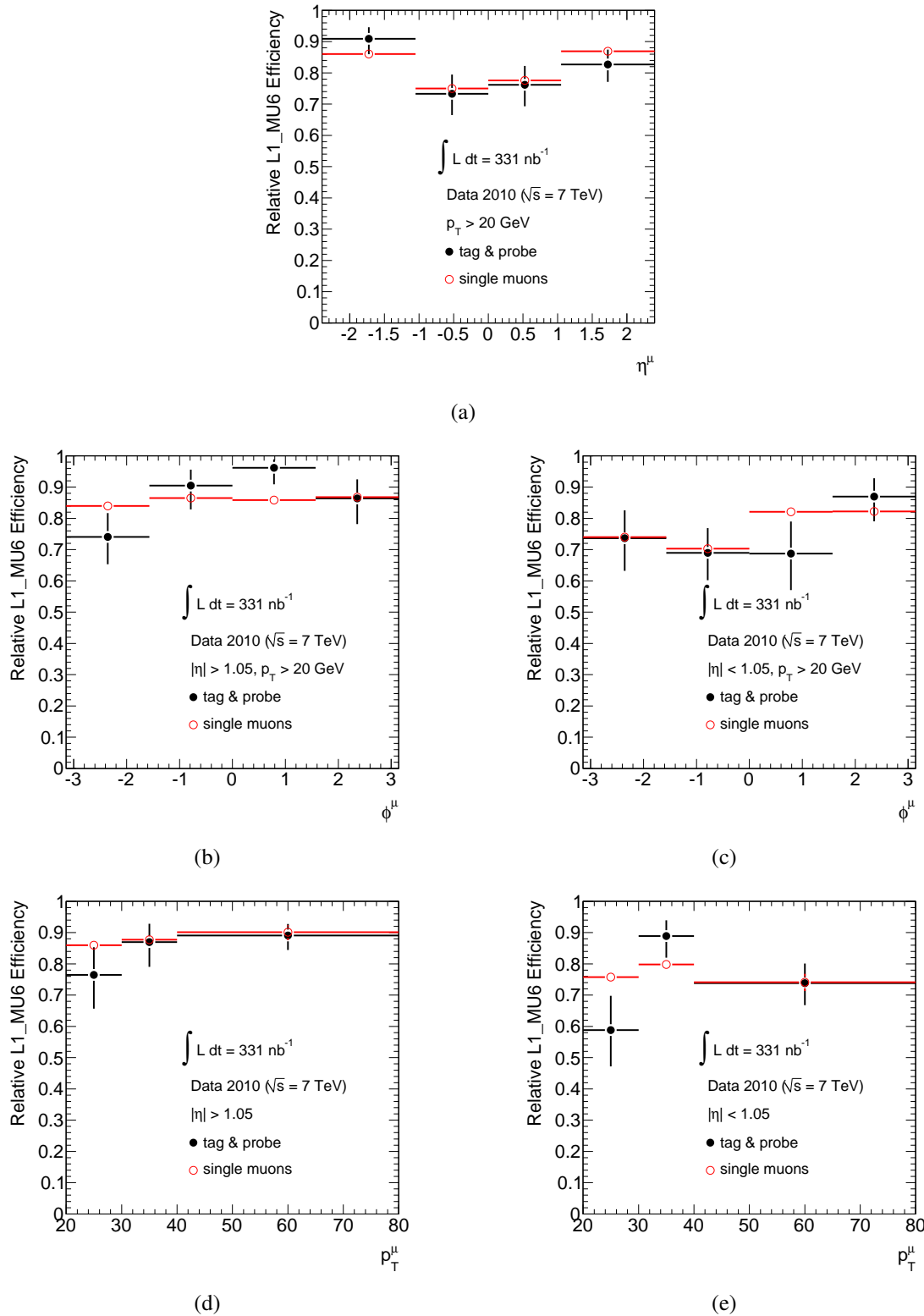
Figure 9.17: Estimated L1_MU6 trigger efficiency by tag-and-probe and single combined track methods as a function of η, ϕ and p_T for probe muons.

Chapter 10

Muon Reconstruction Efficiency Estimation using Collision Data

The methods and results for the muon reconstruction efficiency estimation are presented in this chapter. In this study, muon reconstruction efficiency is estimated in the following steps.

1. Identify an ID track which is created by a muon

2. Search a combined track which is considered to be created by the same muon

In proton-proton collisions at the LHC, the average number of ID tracks reconstructed in an event reaches some tens or hundreds. Most of the reconstructed ID tracks are hadrons and these tracks form significant background hence the rejection of this background becomes the most crucial issue for the reconstruction efficiency estimation.

In this study, two methods are used for this purpose. The first one is called the Muon Spectrometer (MS) Hit Tagging Method, described in detail in section 10.1. The other is the tag-and-probe method using $Z \rightarrow \mu\mu$ events. The details and results for the tag-and-probe method are presented in section 10.2. The results to be used in W / Z-boson cross sections measurement are summarized in section 10.3.

10.1   MS Hit Tagging Method

In principle, the muon is only particle which can penetrate hadronic calorimeter. Thus, if one requires activities in the muon spectrometer ahead of an ID track, most of hadron tracks fail this requirement. A tool which counts the associated number of hits in the muon spectrometer around the extrapolated path of an ID track has been developed. The details of the tool is described hereunder.

10.1.1   MDT Hits – ID Track Association

The number of MDT hits associated with an ID track is counted by this tool. The word a hit represents a fired tube. The reason why the MDT hits are utilized is as follows.
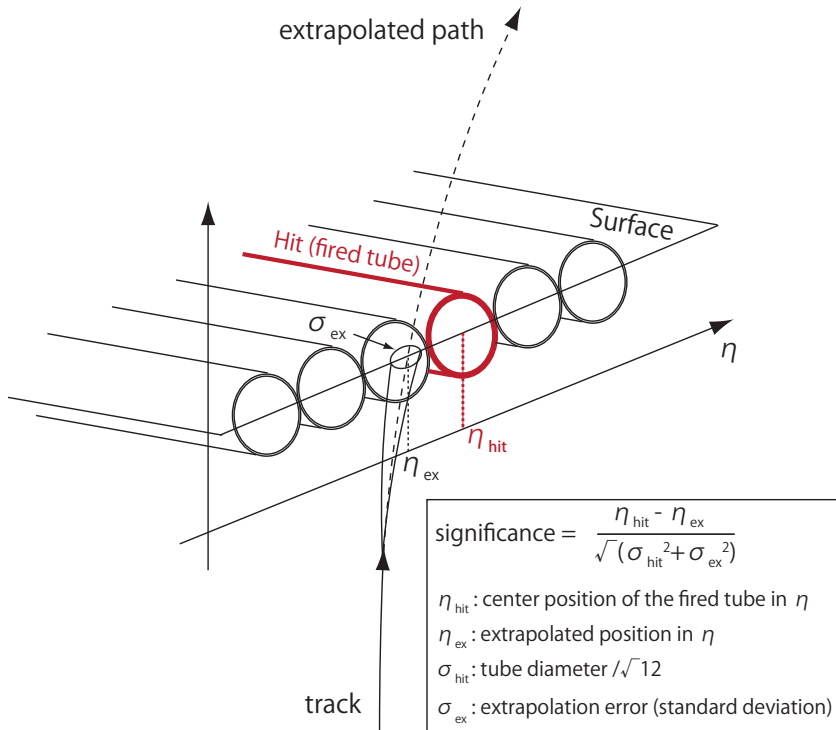
Figure 10.1: A schematic illustration of the MDT Hits – ID track association.

- One main concern of this method is the measurement bias for the efficiency estimation inevitably caused by requiring activities in the target detector. Since the MDT covers the entire η range of the muon spectrometer, the bias is more or less uniform. Hence the treatment of the bias becomes easy.

- The average number of MDT hits on a combined track is about 20. This is large enough to adjust the amount of bias in case-by-case basis.

To associate MDT hits to an ID track, the track extrapolator [134, 135] is deployed. The number of MDT hits within a road of certain width around extrapolated track path is counted. The concrete procedure is summarized as follows.

1. Extrapolate an ID track to an MDT tube layer surface, a plane in which MDT hits are contained (see Figure **10.1**),

2. Calculate a significance from the extrapolated position and error, the center position of the hit and the tube width as

$$\text{significance} = \frac{\eta_{hit} - \eta_{ex}}{\sqrt{\sigma_{hit}^2 + \sigma_{ex}^2}}, \tag{10.1}$$

where η_{ex} is the extrapolated position in η coordinate and η_{hit} is the center position of the tube in consideration. σ_{ex} is the extrapolation error reported by the track extrapolator and σ_{hit} is the tube diameter divided by $\sqrt{12}$.

3. If the calculated significance is smaller than a certain cut value, the hit is counted. The cut value is set at 3.0 by default.

This procedure is repeated over all MDT hits.

10.1.2   Event Selection and Muon Distribution

The ID track selection deployed in the reconstruction efficiency estimation using MS hit tagging method is summarized in Table **10.1**.

	Event selection
Quality	$W \rightarrow \mu\nu$ Good Runs List
Primary vertex	$N_{\text{vtx}} \geq 1$ with $N_{\text{tracks}} \geq 3$
	$\|z_{vtx}\| < 150$ mm
Trigger	L1_MU6
	Tagged ID track selection
p_T	> 20 GeV
Pixel Hits	≥ 1
Silicon Hits	≥ 6
TRT Hits	≥ 10
Isolation	$\sum p_{\text{T}}^{ID}/p_{\text{T}} < 0.2$ $(\Delta R = 0.4)$
Associated MDT hits	2 of 3: inner ≥ 4, middle ≥ 3, outer ≥ 3

Table 10.1: The event and track selections for muon reconstruction efficiency estimation using MS hit tagging method.

In this estimation, the GRL for $W \rightarrow \mu\nu$ cross sections measurement is used resulting an integrated luminosity of 310 nb^{-1}. Events are required to have one or more vertices reconstructed with at least three ID tracks.

Then the ID tracks are required to pass the cuts of p_{T} and ID hits requirements. Silicon hits mean the sum of the number of SCT hits and Pixel hits. Relative track isolation of $\leq$ 0.2 is applied in terms of p_{T} sum of ID tracks within the cone of $\Delta R = 0.4$. In the isolation calculation, the contributions from the track in consideration itself and tracks with $p_{\text{T}} < 1$ GeV are subtracted. Finally, the associated MDT hits requirements are applied as in Table **10.1**. The resulting distributions of the selected ID tracks are shown in Figure **10.2**.

Combined tracks are looked for within a cone of $\Delta R = 0.4$ centered at a selected ID tracks in consideration. This matching is done simply using track parameters, not using the track extrapolator. The efficiency denominator in this estimation is the number of selected ID tracks, and the efficiency numerator is the number of the ones matched with one or more combined tracks.

The efficiency is measured regarding the entire muon spectrometer as a single bin. The estimation results are summarized in Table **10.2**. As one can see, a significant discrepancy is seen between the efficiency in data and in $W \rightarrow \mu\nu$ MC. This is considered as mainly coming from decay-in-flight contamination. A background rejection method against this decay-in-flight component is described in the next subsection.
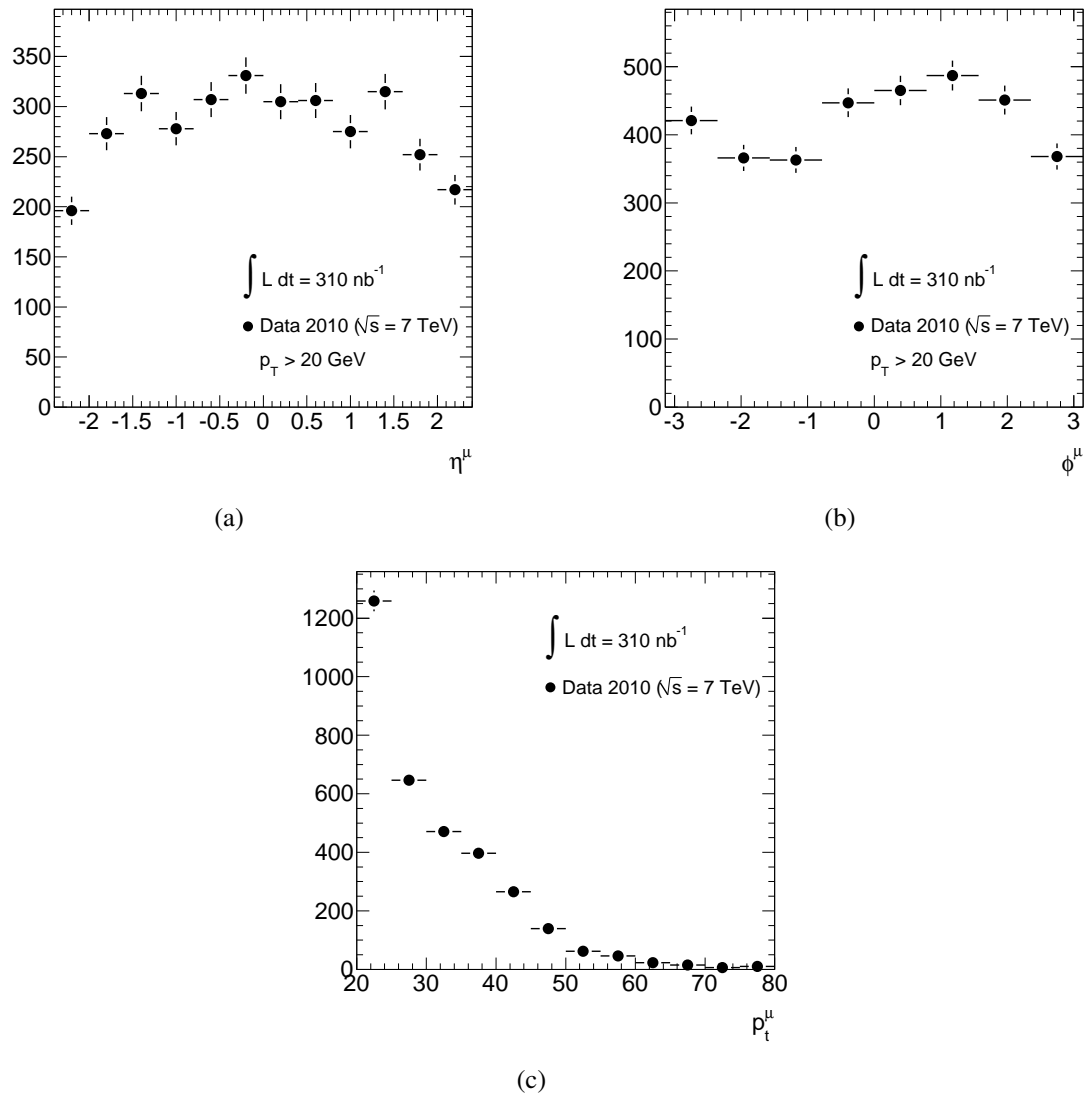
Figure 10.2: (a) η (b) ϕ and (c) p_T distribution of selected ID tracks for the muon reconstruction efficiency estimation by the MS hit tagging method.

eff. in data (%)	eff. in $W \to \mu\nu$ MC (%)	scale factor
94.7 ± 0.4	98.6 ± 0.1	96.1 ± 0.4

Table 10.2: Measured muon reconstruction efficiency by the MS hit tagging method without background subtraction.

10.1.3   Decay in Flight Background Subtraction

To investigate the reason of the discrepancy between the measured muon reconstruction efficiency by the MS hit tagging method in data and MC, the method is factorized into two steps.

1. Search standalone tracks around a selected ID track in consideration

2. Search combined tracks around a selected ID track in consideration which is matched with an standalone track

Figure **10.3** shows the ΔR distribution between a selected ID tracks and the corresponding standalone and combined track. The ΔR value used in the step 1 is set at 0.4 and in step 2 at 0.1.
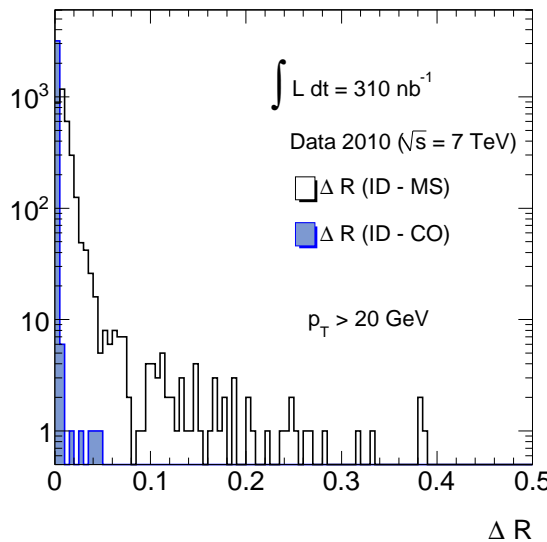
Figure 10.3: Matching ΔR between ID tracks and standalone tracks (black) and ID tracks and combined tracks (blue).

The resulted efficiency for the standalone and combined tracks are listed in Table **10.3**. As one can see, the main efficiency drop happens in the combining stage.

Sample	eff. standalone (%)	eff. combined (%)	total (%)
Data	98.2 ± 0.2	96.5 ± 0.4	94.5 ± 0.5
$W \to \mu\nu$ MC	99.4 ± 0.1	99.2 ± 0.0	98.6 ± 0.1

Table 10.3: The breakdown of the measured muon reconstruction efficiency drop in the MS hit tagging method.

Figure **10.4** shows the distribution of the selected ID tracks which succeeded to pass a matching with an standalone track but failed to match with a combined track. Figure **10.4** (a) is a distribution of ΔR between the ID tracks and their nearest standalone tracks.

Figure **10.4** (b) is the distribution of the p_T difference between the ID tracks and their nearest standalone tracks. The ID tracks tend to have harder p_T than their nearest standalone tracks.

Figure **10.4** (c) is the 2-D distribution of (a) and (b). Combinations may fail even when the directions of ID and standalone tracks are reasonably close. This tend to happen when the ID tracks are much harder than that of the standalone tracks. This suggests the contribution of decay-in-flight events. The rejection of these decay-in-flight events is crucial for this estimation.

(a)

(b)

(c)
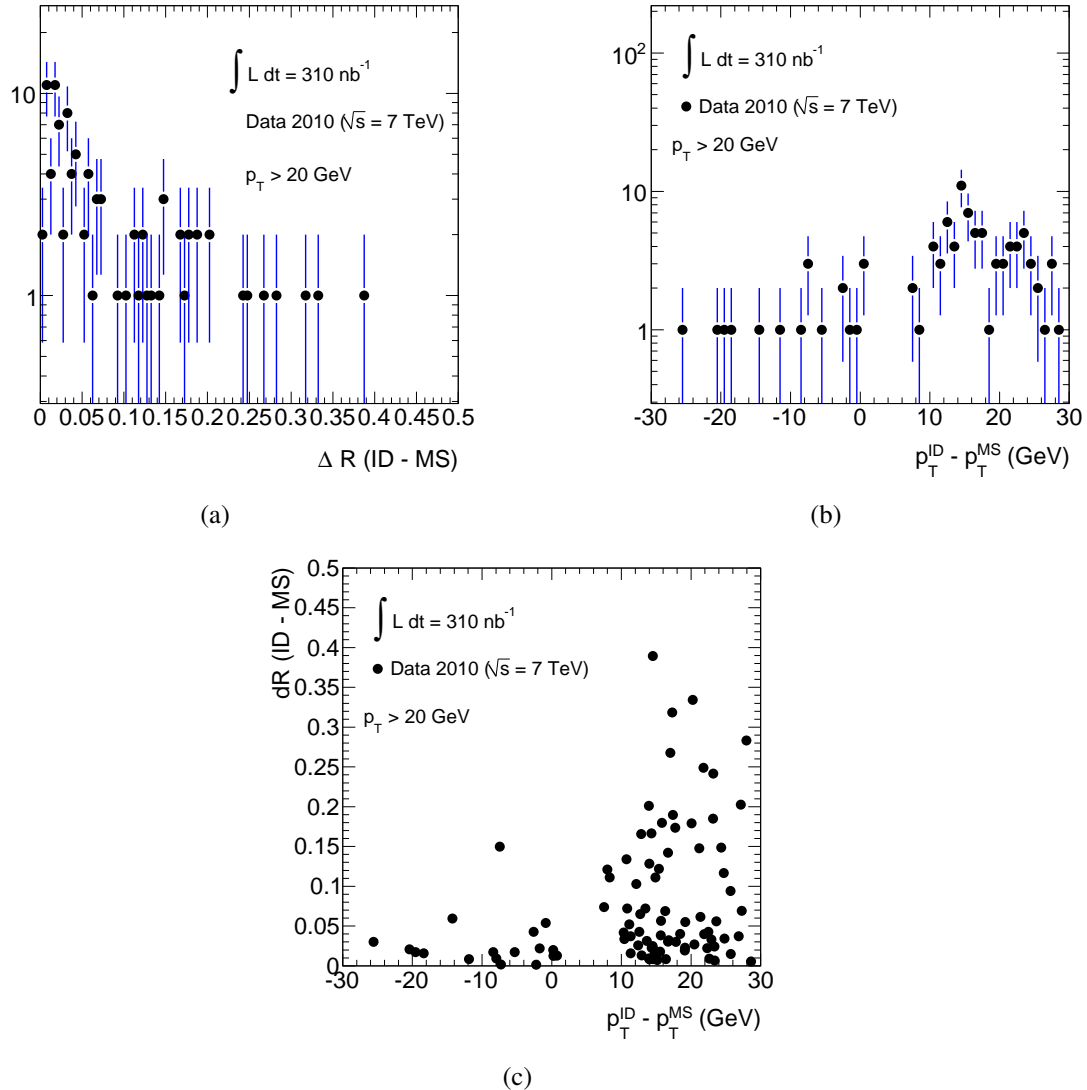
Figure 10.4: (a) ΔR between the selected ID tracks and their nearest standalone tracks (b) difference in p_T between the selected ID tracks and their nearest standalone tracks (c) two dimensional histogram of (a) and (b).

MDT Hit Residual Template Fit

To subtract the decay-in-flight contamination, template fits for the distribution of MDT hit residuals (distance in η between extrapolated position of selected ID tracks and center of MDT hits)

are performed.The templates are made for the $W \rightarrow \mu\nu$ MC as a prompt muon samples and a single charged pion MC as the decay-in-flight component. The single pions are flatly generated in p_T between 1 GeV to 100 GeV, thus a reweighing is done according to one over the true pion p_T to the third power based upon a fit to ID track distributions in minimum bias data samples. Then the two templates are fitted to the residual distribution in data using RooFit [138].

A template fit example for selected ID tracks is shown in Figure **10.5** and derived prompt muon fraction in the selected ID tracks and that matched with a combined track are summarized in Table **10.4**. Then the derived decay-in-flight components are subtracted from both denominator and numerator. Resulting reconstruction efficiency for prompt muons are in Table **10.5**.
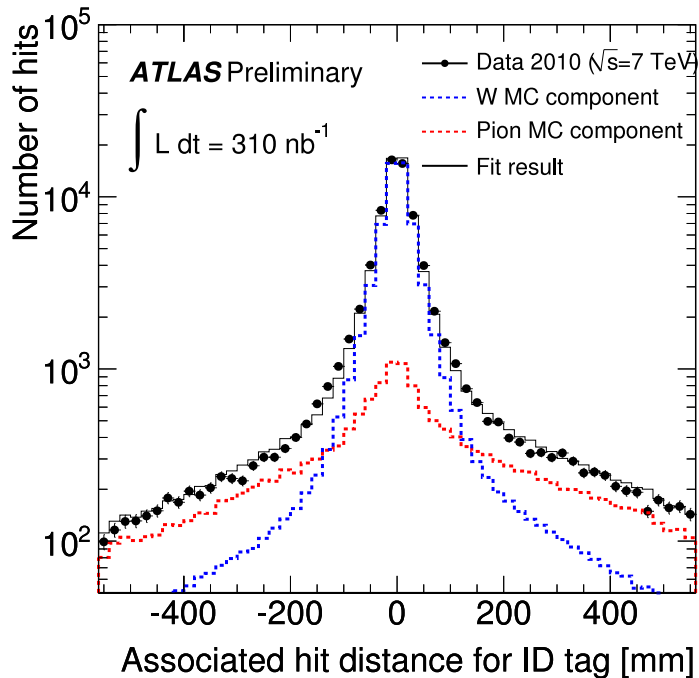
Figure 10.5: Fitting result for MDT hit residuals of tagged ID tracks in data and MC.

Selected ID tracks (%)	Matched with a combined track (%)
79.3 ± 0.3	83.0 ± 0.3

Table 10.4: Derived prompt muon fractions by the MDT hit residual template fits.

eff. in data (%)	eff. in MC (%)	scale factor (%)
99.2 ± 0.4	98.6 ± 0.1	100.5 ± 0.4

Table 10.5: Muon reconstruction efficiency for prompt muons with the MDT hits residual template fits.

10.1.4   Systematic Uncertainty

Systematic	Value
decay-in-flight Contamination	2.0%
ID tracking efficiency	1.0%
Cut stability	0.5%
Trigger bias	0.4%
Total	2.4%

Table 10.6: Systematics for the muon reconstruction efficiency by the MS hit tagging method.

The systematic components for the muon reconstruction efficiency estimation using the MS hit tagging method are summarized in Table **10.6**.

The largest component is coming from the uncertainty for the amount of decay-in-flight contamination. To evaluate the maximum effect of this, so-called factorizing method is used. Basically, decay-in-flight components cause negative effect on the reconstruction efficiency estimation in the combining stage. In the factorizing method, reconstruction efficiency estimation is divided into two parts as in the evaluation in section 10.1.3 and requirements for decay-in-flight rejection are made before the combination efficiency estimation. The requirements are,

- The selected ID track is matched with a standalone track within $\Delta R < 0.1$

- The p_T of the standalone track is > 10 GeV

- The difference in p_T between the ID and standalone track is < 15 GeV

The resulted efficiency is $98.2 \pm 0.2\%$ for standalone tracks and $98.9 \pm 0.2\%$ for combined tracks and the overall reconstruction efficiency is $97.1 \pm 0.3\%$. These requirements can not reject all decay-in-flight contamination. However, compared to the efficiency derived in the template fit method in Table **10.4**, both results are consistent within 2.0 %. Hence a conservative uncertainty coming from decay-in-flight of 2.0 % is taken, assuming all the efficiency difference is coming from decay-in-flight contamination.

The reconstruction efficiency is measured on reconstructed ID tracks. Hence uncertainties should be put on ID track reconstruction efficiency. The ID tracking efficiency is well modeled (see section 10.2.3) in the MC hence a conservative uncertainty of 1 % is put on it from a MC study.

The requirement of L1_MU6 trigger causes a bias on the estimation. The amount of the effect is estimated using truth information in MC and 0.4 % is counted for this effect.

The stability of the efficiency results with respect to variations in the cuts on matching ΔR, number of required hits and road size is also examined. The variations are covered by a systematic uncertainty of 0.5 %.

10.2 $Z \to \mu\mu$ **Tag-and-Probe Method**

The muon reconstruction efficiency is also measured with the tag-and-probe method. In this case, probe tracks should be reconstructed only with the inner detector. The corresponding combined tracks are searched as is done in the previous section.

10.2.1 **Event Selection and Muon Distribution**

Collision event selection	
Good Run List & BCID	$Z \to \mu\mu$ GRL
Primary vertex	$N_{vtx} \geq 1$ with $N_{tracks} \geq 3$
	$|z_{vtx}| < 150$ mm
Trigger	L1_MU6
Tag track selection	
Track Type	combined tracks
Kinematics	$p_T > 15$ GeV, $|\eta| < 2.4$
Muon quality	$p_T^{MS} > 10$ GeV
	$|p_T^{MS} - p_T^{ID}| < 15$ GeV
	$|z_0 - z_{vtx}| < 10$ mm
Trigger	Matched with L1_MU6 trigger
Probe track selection	
Track Type	ID tracks
Kinematics	$p_T > 20$ GeV, $|\eta| < 2.4$
Isolation	$\sum p_T^{ID}/p_T < 0.2$
ID hit	Pixel ≥ 1, SCT ≥ 4, Silicon ≥ 6, TRT ≥ 10
Vertex (w.r.t PV)	$|d_0^{tag} - d_0^{probe}| < 2$mm, $|z_0^{tag} - z_0^{probe}| < 2$mm
Opposite Charge	$q_{tag} \cdot q_{probe} < 0$
Invariant Mass	$|M_Z - M_{TP}| < 15$ GeV

Table 10.7: Event and muon selection for muon reconstruction efficiency estimation by the $Z \to \mu\mu$ tag-and-probe method.

Table **10.7** summarizes the selection criteria used in the tag-and-probe estimation. The collision event selection, which is intended to reject events with non-collision origin, is identical to the one used in the $Z \to \mu\mu$ cross section measurement.

Tag tracks are required to be a combined track with $p_T > 15$ GeV generated within the muon trigger chamber acceptance. To reject muons from decay-in-flight events, the cuts on $p_T^{MS} > 10$ GeV and $|p_T^{MS} - p_T^{ID}| < 15$ GeV are required. $|z_0 - z_{vtx}|$ should be within 10 mm to reject cosmic muons. Finally tag muons are required to be matched with an L1_MU6 RoI. This matching is done by the method described in section 9.2.

Probe tracks are required to be an ID track with $p_T > 20$ GeV and $|\eta| < 2.4$. Relative track p_T isolation and a certain number of inner detector hits are required to reject backgrounds. d_0 and z_0 measured with respect to the reconstructed primary vertex is required to be with 2 mm

from that of the corresponding tag track. An opposite charge requirement is applied as well as the mass window cut of $|M_Z - M_{TP}| < 15$ GeV.

Figure **10.6** shows the distributions of resulting probe tracks and invariant mass of tag and probe tracks. The total number of $Z \rightarrow \mu\mu$ events found is 135 and 205 probe tracks are adopted.
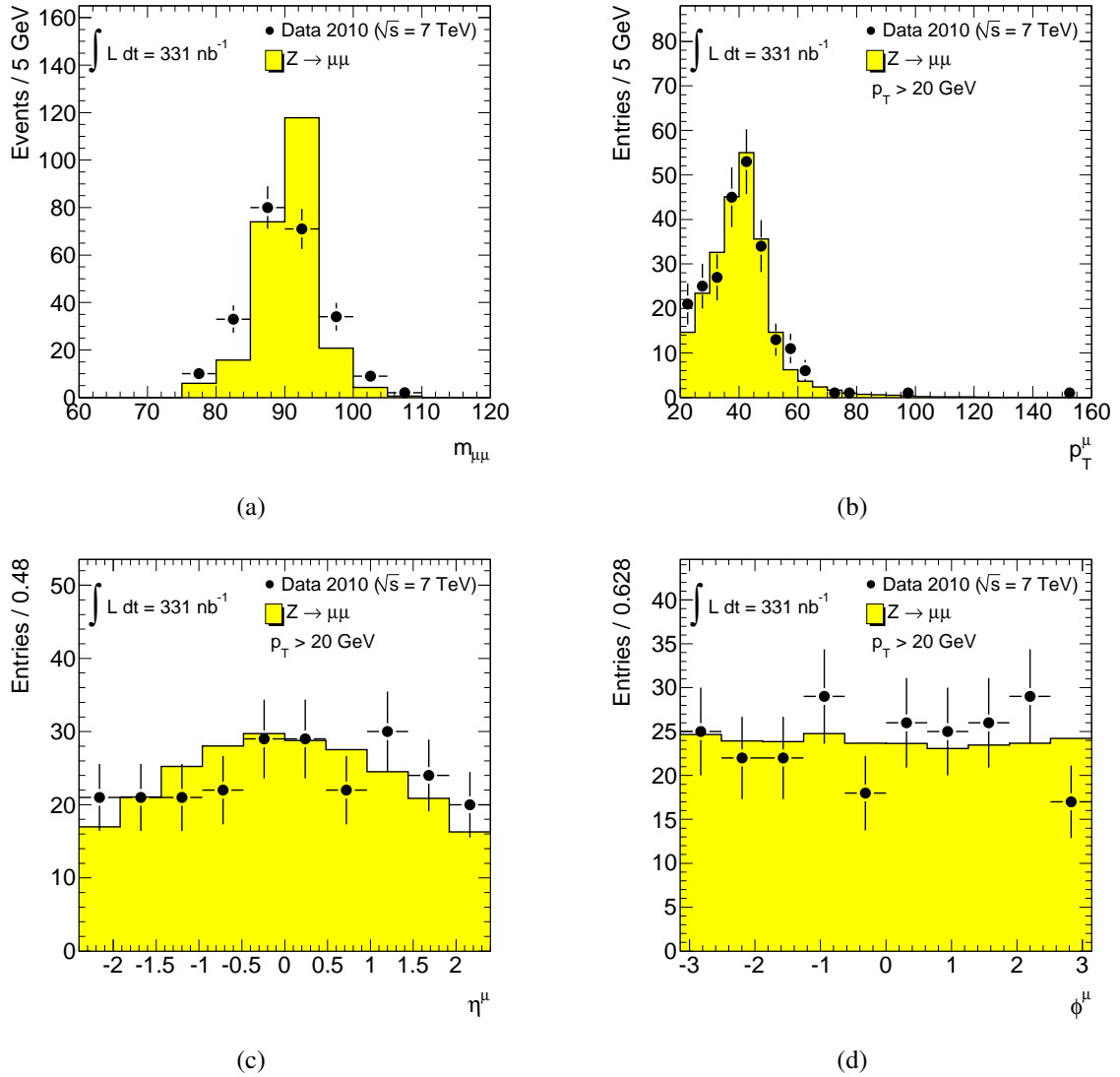
Figure 10.6: (a) Invariant mass of tag and probe tracks. (b) p_T (c) η and (d) ϕ distributions of the probe tracks.

10.2.2 Efficiency and Scale Factor

After the probe track selection, a combined track is searched within a cone of $\Delta R = 0.01$ from each of adopted probe tracks. The combined tracks are required to satisfy the following cuts.

- $|p_T^{MS} - p_T^{ID}| < 15$ GeV

- $p_T^{MS} > 10$ GeV

These requirements are to ensure that combined tracks have the same quality as the one used in the W / Z-boson cross sections measurement. The resulting reconstruction efficiencies and scale factors are summarized in Table **10.8** and Figure **10.7**. The results in data and MC agrees well.

eff. in data (%)	eff. in MC (%)	scale factor (%)
92.2 ± 1.9	92.6 ± 0.2	99.6 ± 2.0

Table 10.8: Measured reconstruction efficiency by the $Z \to \mu\mu$ tag-and-probe method.

(a)

(b)

(c)
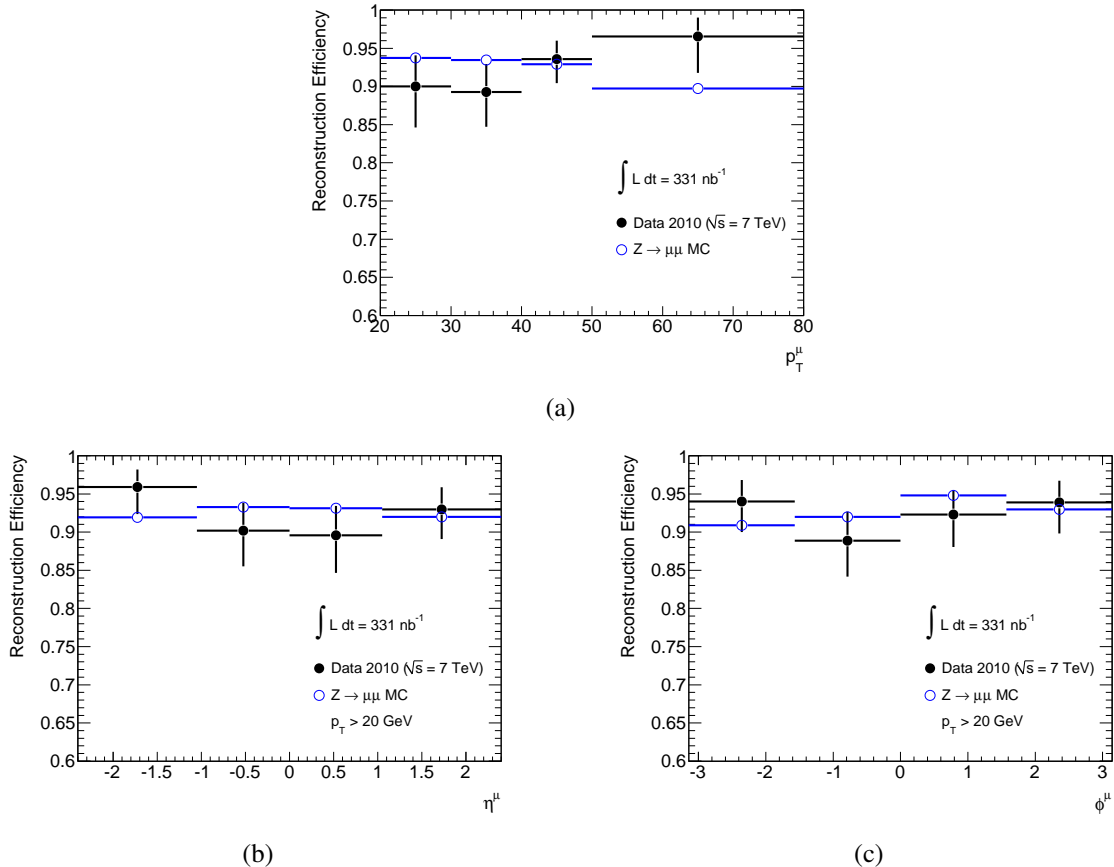
Figure 10.7: (a) p_T (b) η and (c) ϕ distribution of the measured muon reconstruction efficiency by the $Z \to \mu\mu$ tag-and-probe method.

10.2.3   ID Track Reconstruction Efficiency

The track reconstruction efficiency in the inner detector is measured by tag-and-probe method by using a muon spectrometer standalone track as a probe. In this case, the event and tag selection is identical to the one summarized in Table **10.7**. The probe track selection is summarized in Table **10.9**.

Probe track selection	
Track Type	muon spectrometer stand alone tracks
Kinematics	$p_T > 20 \, \text{GeV}, |\eta| < 2.4$
Vertex (w.r.t PV)	none
Opposite Charge	$q_{tag} \cdot q_{probe} < 0$
Invariant Mass	$|M_Z - M_{TP}| < 15 \, \text{GeV}$

Table 10.9: standalone probe track selection for ID reconstruction efficiency estimation.

ID tracks are looked for within a cone of $\Delta R = 0.03$. The following requirements are applied on the ID tracks to reject noise or non prompt tracks.

- number of Pixel hits ≥ 1

- number of SCT hits ≥ 4

- $|d_0^{tag} - d_0^{probe}| < 2$ mm (d_0: w.r.t primary vertex)

- $|z_0^{tag} - z_0^{probe}| < 2$ mm (z_0: w.r.t primary vertex)

The resulting ID tracking efficiencies are summarized in Table **10.10** and Figure **10.8**. The reconstruction efficiency in the ID is very close to 100 % both in data and MC. This support an assumption made in this study that the ID tracking efficiency is well modeled in MC (see section 10.1.4).

eff. in data (%)	eff. in MC (%)	scale factor (%)
99.5 ± 0.5	99.5 ± 0.0	99.9 ± 0.6

Table 10.10: Measured ID track reconstruction efficiency by the $Z \rightarrow \mu\mu$ tag-and-probe method.
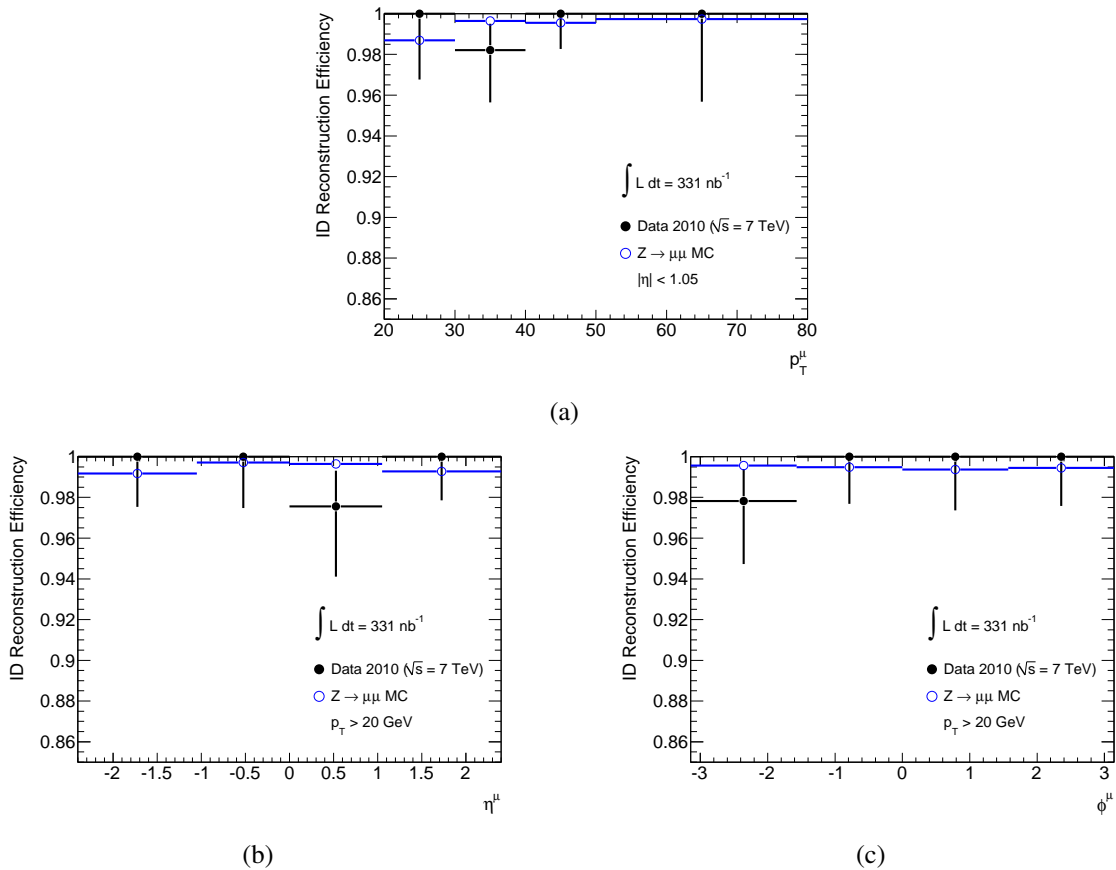
Figure 10.8: (a) p_T (b) η and (c) ϕ distributions of the measured ID tracking efficiency by the $Z \to \mu\mu$ tag-and-probe method.

10.3 Single Muon Reconstruction Efficiency Scale Factor

As in the case for the muon trigger efficiency, the needed information in W / Z-boson cross sections measurement is the efficiency scale factor for single muons. The results for independent two methods, namely

1. MS hit tagging method & MS hit residual template fit

2. Tag-and-probe method with $Z \to \mu\mu$ events

were presented so far and results for both methods show that single muon reconstruction efficiency is well modeled in the MC. Hence the scale factor center value of 1.000 is taken. As for the uncertainty, the one from method 1 is adopted since the available statistics are much higher in this method. The single muon reconstruction efficiency scale factor result is

single muon reconstruction efficiency scale factor = 1.000 ± 0.004 (stat) ± 0.024 (syst)

Chapter 11

Measurement of *W* Boson Cross Section

11.1 Event Selection

Collision event selection	
Good Run List & BCID	$W \to \mu\nu$ GRL
Primary vertex	$N_{\text{vtx}} \geq 1$ with $N_{\text{tracks}} \geq 3$
	$|z_{vtx}| < 150$ mm
Jet cleaning	cleaning cuts
Trigger	L1_MU6
High-p_T event selection	
Muon selection	combined tracks
	$p_T > 15$ GeV, $|\eta| < 2.4$
Muon quality	$p_T^{MS} > 10$ GeV
	$|p_T^{MS} - p_T^{ID}| < 15$ GeV
	$|z_0 - z_{vtx}| < 10$ mm
$W \to \mu\nu$ event selection	
Tight kinematics	$p_T > 20$ GeV, $|\eta| < 2.4$
ID isolation	$\sum p_T^{ID}/p_T < 0.2 \quad (\Delta R = 0.4)$
Missing transverse energy	$E_T^{\text{miss}} > 25$ GeV
Transverse Mass	$M_T > 40$ GeV

Table 11.1: A summary of the requirements for the $W \to \mu\nu$ candidate event selection.

    A summary of the requirements for the $W \to \mu\nu$ candidate event selection is given in Table **11.1**. The requirements are classified into three stages namely collision event selection, high-p_T event selection and the $W \to \mu\nu$ event selection. The collision event selection and high-p_T event selection are called pre-selection as a whole.

    In the collision event selection, events coming from proton-proton collisions are selected. First, the official GRL for the $W \to \mu\nu$ analysis (see section 7.1) is applied and events are required to have BCIDs of proton-proton collisions. Events are then required to have one or more reconstructed primary vertices with at least three inner detector tracks. The vertex position

along the *z*-axis required to be within 150 mm from the ATLAS origin to reduce cosmic ray background. To reduce spurious missing transverse energy from jets generated by detector effects or cosmic rays, the jet cleaning procedure is applied. The trigger used for this analysis is L1_MU6.

In the high-p_T event selection, first, events are require to have at least one muon reconstructed as a combined track with $p_T > 15$ GeV and $|\eta| < 2.4$. Then, the p_T^{MS} is required to be greater than 10 GeV. This is to remove the π/K decay-in-flight contamination as well as combined tracks resulting from a poor combination of inner detector and muon spectrometer standalone tracks. To increase further the robustness against π/K background and track reconstruction mistakes, the requirement of $|p_T^{MS} - p_T^{ID}| < 15$ GeV is applied. Then, $|z_0 - z_{vtx}|$ should be within 10 mm to reject cosmic muons.

Finally, the $W \to \mu\nu$ event selection is applied. The selection places a $p_T > 20$ GeV on the selected combined track. Also, a requirement of relative track isolation within a cone of $\Delta R = 0.4$ is applied to reject QCD background events. Then E_T^{miss} is required to be greater than 25 GeV and final *W* candidates are counted in the region above transverse mass of 40 GeV.

11.2 Signal Acceptance and Efficiencies

11.2.1 Overall Acceptance of $W \rightarrow \mu\nu$ Selection

The acceptance is defined as the number of events passing all of the selection divided by the number of generated events. The acceptance is estimated with a $W \rightarrow \mu\nu$ MC sample which is described in section 4.7.2. The yielded acceptance is 36.32 % with a negligible statistical error. The GRL and BCID requirements are omitted from the selection since these are not relevant for simulated samples. The number of signal events passing each step of the selection, and the efficiencies of each step relative to the previous one and total generated number (denoted as reduction factor) are given in Table **11.2**.

Then the acceptance is corrected to compensate the discrepancy between data and MC in the number of vertices (see section 8.3.3), muon trigger and reconstruction efficiency. Details of the corrections are summarized in section 11.2.2.

selection	number of events	reduction factor (%)	rel. eff. (%)
All	999885	100.00	—
Jet cleaning	999877	100.00	100.00
L1_MU6	630689	63.08	63.08
Vertex	629399	62.95	99.80
combined track, $\|\eta\| < 2.4$, $p_T > 15$ GeV, $p_T^{MS} > 10$ GeV, $\|p_T^{MS} - p_T^{ID}\| < 15$ GeV, $\|z_0 - z_{vtx}\| < 10$ mm,	532776	53.28	84.65
$p_T^\mu > 20$ GeV,	483712	48.38	76.85
isolation	479974	48.00	99.23
$E_T^{miss} > 25$ GeV	395955	39.60	82.50
$M_T > 40$ GeV	392144	39.22	99.04
	(W$^+$:234454, W$^-$:157690)	(W$^+$:39.93, W$^-$:38.21)	—
Correction (vertex)	391358	39.14	99.80
Correction (trigger)	363141	36.32	92.83
Correction (reconstruction)	363141	36.32	100.00
	(W$^+$:217117, W$^-$:146025)	(W$^+$:36.98, W$^-$:35.38)	—

Table 11.2: Effect of the $W \rightarrow \mu\nu$ selection criteria on simulated $W \rightarrow \mu\nu$ events.

11.2.2   Efficiency Scale Factors

The three correction factors for the $W \to \mu\nu$ acceptance, namely for the number of vertices, muon trigger and reconstruction efficiency, are applied on the calculated acceptance in MC as in Table **11.2**. The details for these corrections are given in the following subsection. In these calculation, no difference between positive and negative muons are assumed. All the resulted scale factor on the $W \to \mu\nu$ acceptance are summarized in Table **11.3**.

Number of Vertices

The discrepancy in the number of vertices between data and MC is corrected as described in section 8.3.3. An efficiency of 99.8 % is adopted (see Table **11.2**) to take into account this effect in acceptance calculations. The amount of correction on acceptance is estimated as about 0.2 %. To be conservative, a full range of systematic uncertainty is assigned. The resulted scale factor is 0.998 ± 0.000 (stat) ± 0.002 (syst).

Trigger Efficiency

The single muon trigger efficiency and scale factor for L1_MU6, which is used in this analysis, is derived in two bins (endcap and barrel) as in Table **9.8**. Since only one muon is required in an event, the single muon trigger scale factor equals to the needed correction for the $W \to \mu\nu$ acceptance.

   To apply the correction, the fraction of muons flying to each bin is calculated by the $W \to \mu\nu$ MC as 0.550 (endcap) and 0.450 (barrel) with a negligible statistical error. In this calculation, muons are required to pass all the $W \to \mu\nu$ selection except for the L1_MU6 requirement. The weighted mean of single muon trigger efficiency is calculated as

  - 0.819 ± 0.005 (stat) ± 0.014 (syst) (weighted average efficiency in data)

  - 0.879 ± 0.001 (stat) ± 0.007 (syst) (weighted average efficiency in MC)

After that the ratio of weighted average in data to MC is taken as the trigger efficiency scale factor for the $W \to \mu\nu$ acceptance. The resulting scale factor is 0.931±0.006 (stat)±0.017 (syst).

Muon Reconstruction Efficiency

The single muon reconstruction efficiency scale factor also equals to that of the needed correction for the $W \to \mu\nu$ acceptance. Hence the scale factor for muon reconstruction efficiency is taken from section 10.3 as 1.000 ± 0.004 (stat) ± 0.024 (syst).

11.2.3   Acceptance Decomposition

The overall acceptance is factorized into two parts as in Eq.(8.1). Each component is referred to as A_W and C_W hereafter. The concrete definition and estimated values of A_W and C_W are as follows. The values for A_W and C_W are summarized in Table **11.3**.

- A_W: Fraction of the generated $W \rightarrow \mu\nu$ events satisfying $p_T^\mu > 20$ GeV, $|\eta^\mu| < 2.4$, $p_T^\nu > 25$ GeV and $M_T(\mu, \nu) > 40$ GeV, where all of these quantities refer to the truth-level muon before any final state radiation. A_W is estimated as 0.480. The acceptances for both W^+ and W^- are estimated separately as 0.484 (W^+) and 0.474 (W^-). A common systematic uncertainty of 3.0 % is assigned to all of them (see section 8.4.3).

- C_W: The denominator of C_W is the number of events passing the generator-level requirements which equals to the numerator of A_W. The numerator is the fraction of events passing the full analysis selections then corrections by the scale factors are applied. The resulted C_W value is 0.758. The acceptances for both W^+ and W^- are estimated separately as 0.765 (W^+) and 0.748 (W^-). A common systematic uncertainty of 4.0 % is assigned to all of them (see section 11.3).

11.2.4   Summary of Acceptance and Efficiency

The acceptance for the $W \rightarrow \mu\nu$ event is summarized in Table **11.3**. The uncertainty on the total acceptance is assigned as 5.0 % which is the quadrature sum of the uncertainties of A_W and C_W. The scale factors are also summarized.

	W (all)	W^+	W^-
A_W	0.480 ± 0.014	0.484 ± 0.015	0.474 ± 0.014
C_W	0.758 ± 0.031	0.765 ± 0.031	0.748 ± 0.030
total acceptance	0.364 ± 0.018	0.370 ± 0.019	0.355 ± 0.018
number of vertices SF		0.998 ± 0.002	
trigger efficiency SF		0.931 ± 0.018	
reconstruction efficiency SF		1.000 ± 0.024	

Table 11.3: A summary of the acceptance and scale factors for the $W \rightarrow \mu\nu$ events.

11.3   Systematic Uncertainty on Acceptance

A summary of the systematic uncertainties is reported here. The decomposition of the systematic uncertainties for C_W is given in Table **11.4** as well as a theoretical uncertainty for A_W. The uncertainties on C_W coming from muon energy scale and resolution and the cut of $E_T^{miss} > 25$ GeV have not described yet. The description is given in the following subsections.

parameter	intrinsic uncertainty (%)	$\delta C_W(\%)$
number of vertices	0.2	0.2
trigger efficiency	2.4 (barrel), 2.1 (endcap)	1.8
reconstruction efficiency	2.4	2.4
muon momentum scale	1.0	1.2
muon momentum resolution	5.0 (barrel), 9.0 (endcap)	0.2
associated to the E_T^{miss} cut (> 25 GeV)		2.0
isolation efficiency	1.0	1.0
theoretical uncertainty	0.2 (FSR), 0.3 (PDF)	0.4
total uncertainty		4.0

parameter	$\delta A_W(\%)$
theoretical uncertainty	3.0

total uncertainty	5.0

Table 11.4: A summary of the systematic uncertainty on the $W \to \mu\nu$ acceptance.

Muon Momentum Scale and Resolution

The uncertainty on muon momentum scale and resolution are estimated in section 8.4.1 by fitting the *Z*-boson mass distribution with the Breit-Wigner function convoluted with a gaussian. The resulted uncertainties are 1.0 % for momentum scale and 9.0 (5.0) % for momentum resolution in endcap (barrel). The acceptance uncertainties coming from them are estimated as follows.

(a) Shifting C_1 in Eq.(8.12) by ± 1.0 % in the acceptance calculation while keeping $C_2 = 0$.

(b) Setting $C_1 = 1.0$ and $C_2 = 9.0$ (5.0) % in endcap (barrel) and calculate the acceptance

To take into account the correlation between muon momentum, E_T^{miss} and relative track isolation, these values are recalculated in event-by-event basis. The uncertainty for (a) is -1.2 (+1.0) % when shifting C_1 by -1 (+1) %, hence 1.2 % is adopted as the uncertainty coming from the muon momentum scale. Also, the uncertainty for (b) is 0.2 % and this value is adopted as the uncertainty coming from the muon momentum resolution.

Uncertainty Associated to the $E_T^{miss} > 25$ GeV Cut

The $W \rightarrow \mu\nu$ analysis includes a cut of $E_T^{miss} > 25$ GeV. The systematic uncertainty related to this cut is estimated as 2.0 % in total [139].

The maximum contribution to the uncertainty is coming from the uncertainty on the energy scale of the topological calorimeter clusters in the central region ($|\eta| < 3.2$). This uncertainty is derived as the difference between data and MC from E/p studies. At the high-p_T region currently in consideration, the uncertainty on the energy scale is estimated as $\pm$ 5 %. The uncertainty on acceptance from this effect through the cut of $E_T^{miss} > 25$ GeV is estimated by MC as $\pm$ 1.5 %.

The next largest uncertainty is coming from the imperfect MC modeling of the detector response. The effect is estimated as the difference between the acceptance calculated E_T^{miss} at the MC truth level and after reconstruction. The resulted uncertainty through the cut of $E_T^{miss} > 25$ GeV is 1.0 %.

Also, the uncertainty from E_T^{miss} resolution (0.4 %), pile-up (0.01 %), dead regions in the calorimeter (< 0.2 %), imperfect modeling of the underlying event (0.4 %), energy scale of the topological calorimeter clusters in the forward ($3.2 < |\eta| < 4.9$) region (0.1 %) and FCal displacement with respect to the beam spot (0.04 %) are considered.

11.4   Background Estimation

11.4.1   QCD Background

Number of Background Events Derived by Matrix Method

The estimated number of QCD backgrounds used in this study is derived by so-called matrix method. In this method, a loose muon sample with N_{loose} events is defined and impose a tight muon requirement especially the track isolation criterion used in the analysis upon it. The number of events in the isolated sample are defined as N_{isol}. Also $\epsilon_{\mathrm{nonQCD}}$ and ϵ_{QCD} are defined as relative isolation efficiencies for non-QCD and QCD processes. Here, non-QCD represents the $W \to \mu\nu$ signals and other electroweak sources. Then the following equations are obtained.

$$N_{\mathrm{loose}} \quad = \quad N_{\mathrm{nonQCD}} + N_{\mathrm{QCD}}, \tag{11.1}$$

$$N_{\mathrm{isol}} \quad = \quad \epsilon_{\mathrm{nonQCD}} N_{\mathrm{nonQCD}} + \epsilon_{\mathrm{QCD}} N_{\mathrm{QCD}}, \tag{11.2}$$

then

$$N_{\mathrm{QCD}} = \frac{N_{\mathrm{loose}} \epsilon_{\mathrm{nonQCD}} - N_{\mathrm{isol}}}{\epsilon_{\mathrm{nonQCD}} - \epsilon_{\mathrm{QCD}}}. \tag{11.3}$$

If one obtains $\epsilon_{\mathrm{nonQCD}}$ and ϵ_{QCD}, the estimated number of QCD backgrounds can be expressed as $\epsilon_{\mathrm{QCD}} N_{\mathrm{QCD}}$. The procedure for data driven derivation of these isolation efficiencies are summarized as follows.

- ϵ_{QCD} : This efficiency is estimated from muons between 15 and 20 GeV after the preselection. In this region, ϵ_{QCD} in data and jet MC samples are almost flat, yielding confidence that the region picked out has only small non-QCD contamination.

  In the high-p_{T} region, the efficiency for jet MC falls with p_{T}. Hence the efficiency for 15 – 20 GeV data is scaled by the ratio of isolation efficiency in jet MC above and below 20 GeV cut. Then the scaled efficiency of $\epsilon_{\mathrm{QCD}} = 0.227 \pm 0.006$ is obtained. The systematic uncertainty is assigned as the full range of this extrapolation.

- $\epsilon_{\mathrm{nonQCD}}$: As the electroweak sample, muons in the $Z \to \mu\mu$ selection is taken. The efficiency $\epsilon_{\mathrm{nonQCD}} = 0.984 \pm 0.010$.

As the loose sample, the events passing all the requirements except for the isolation are chosen. The loose sample has $N_{\mathrm{loose}} = 1272$ events and isolated sample has $N_{\mathrm{isol}} = 1181$ events.

Finally, from Eq.(11.3), the estimated number of QCD background $\epsilon_{\mathrm{QCD}} N_{\mathrm{QCD}} = 21.1 \pm 4.5$ (stat) $\pm$ 8.7 (syst) is obtained. The systematic uncertainty emerging from comparing to the number with unscaled QCD efficiency.

QCD Scaling Factor Derivation

The QCD scaling factor is derived by comparing the events with non-isolated high-p_{T} muons in data and MC. As a control sample, events passed all W selection criteria before muon isolation and reversed muon isolation requirement are used.

Figure **11.1** (a) shows the $E_{\mathrm{T}}^{\mathrm{miss}}$ distribution of the events with $p_{\mathrm{T}} > 20$ GeV in di-jet MC and data. MC distribution is normalized to data, and shapes agree well. When the distributions are

normalized to integrated luminosity of 310 nb^{-1}, we found 6843.9 muons with $p_T > 20$ GeV in MC distribution and 4186 muons in data. Thus the scaling factor of 0.61 $\pm$ 0.01 (stat) $\pm$ 0.23 (syst) is derived.

The systematic uncertainties are obtained by comparing the scaling factor with that of the events with $E_T^{\text{miss}} > 25$ GeV, replacing the relative track isolation with the same cut imposed on relative calorimeter based isolation and taking absolute difference of the scaling factors between left and right of the peak. The numbers are summarized in Table **11.5**.
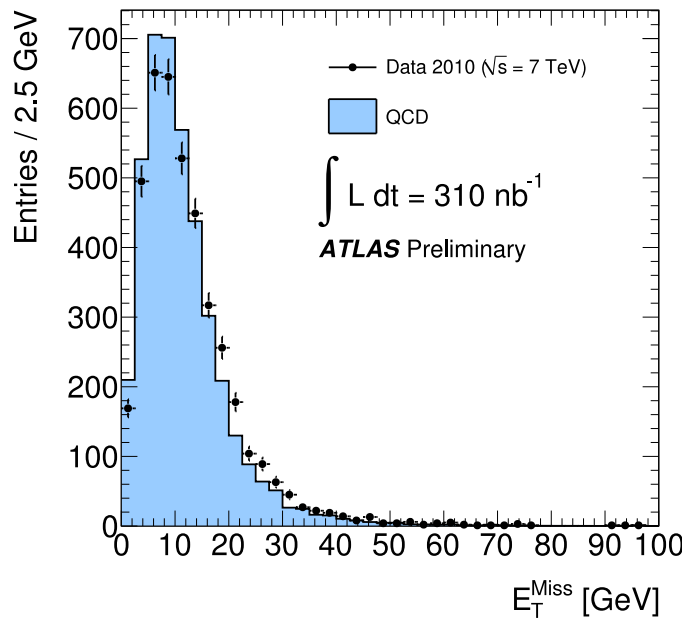
Figure 11.1: Shape comparison between di-jet MC and data for $p_T > 20$ GeV.

QCD scaling factor	Stat. uncertainty	High E_T^{miss} syst.	Isolation syst.	Shape syst.	Total uncertainty
0.61	0.01	0.21	0.04	0.08	0.23

Table 11.5: QCD scaling factor derived with events with non-isolated muons with $p_T > 20$ GeV

11.4.2 Electroweak and $t\bar{t}$ Backgrounds

Another background contribution is from sources with real W or Z-bosons, i.e. $W \rightarrow \tau\nu$, $Z \rightarrow \mu\mu$, $Z \rightarrow \tau\tau$ and $t\bar{t}$ processes are considered as this type of backgrounds.

The yielded number of these backgrounds is estimated using MC samples. The cross section are scaled and normalized to the integrated luminosity. Also, the corrections for the number of vertices, trigger and muon reconstruction are applied. The acceptances and predicted number

of events for the various backgrounds are shown in Table **11.6**. For the $Z \rightarrow \mu\mu$ process, a scale factor of 109 / 121.9 is applied to compensate the discrepancy observed between the data and MC in the $Z \rightarrow \mu\mu$ analysis (see Table **12.7**).

Systematic components for these background predictions are listed as follows.

- Uncertainty on C_W of 4.0 % as summarized in the Table **11.4**

- Uncertainty on the PDF dependence of 3.0 % for $t\bar{t}$

- Theoretical cross section uncertainty of 5.0 % for electroweak processes and 6.0 % for $t\bar{t}$

The total systematic uncertainty is 7.8 % for $t\bar{t}$ and 6.4 % for electroweak backgrounds. We treat these uncertainties as 100 % correlated among all the electroweak backgrounds, except for the $t\bar{t}$ cross section uncertainty, which is treated as uncorrelated with the other theoretical uncertainties. The total number of predicted events from electroweak background process is 77.8 ± 0.3 (stat) ± 4.8 (syst).

11.4.3   Cosmic Ray Background

The number of cosmic ray backgrounds is estimated in this section. The following two cases are considered.

1. The events in which cosmic muons overlap with a in-time minimum bias event

2. The events which contain cosmic activity only

For case 1, the cosmic background cross section is written as in Eq.(11.4).

$$\sigma_{\text{cosmic}} = \sigma_{\text{MB}} \cdot p_{\text{cosmic}}^{\text{trig}} \cdot p_{\text{cosmic}}^{\text{reco}} \cdot L_{\text{int}}, \tag{11.4}$$

where σ_{MB} is the minimum bias cross section, $p_{\text{cosmic}}^{\text{trig}}$ is the probability that a cosmic ray fires L1_MU6 trigger in time and $p_{\text{cosmic}}^{\text{reco}}$ is the probability that a triggered cosmic background event passes the $W \rightarrow \mu\nu$ event selection without the requirement on primary vertices. L_{int} is the integrated luminosity used for the $W \rightarrow \mu\nu$ analysis.

σ_{MB} is assumed as 50 ± 10 (syst) mb. $p_{\text{cosmic}}^{\text{trig}}$ is derived as 3.3×10^{-5} by a study of muon trigger rate in the bunch with no beam. $p_{\text{cosmic}}^{\text{reco}}$ is estimated with the data in non-colliding bunch and resulted probability is $(0.34 \pm 0.13) \cdot 10^{-5}$. The charge asymmetry of the cosmic muons are also considered as $N^+/N^- = 1.235 \pm 0.004$ (stat) ± 0.025 (syst). At the $L_{\text{int}} = 310$ nb^{-1}, the number of cosmic background in the $W \rightarrow \mu\nu$ acceptance for each charge is estimated as

$$N_{\text{cosmic}}^+ = 0.9 \pm 0.4 \text{ (stat)} \pm 0.2 \text{ (syst)},$$
$$N_{\text{cosmic}}^- = 0.8 \pm 0.3 \text{ (stat)} \pm 0.2 \text{ (syst)}.$$

The main source of the statistical uncertainty is the reconstruction probability for cosmic events. The main source of the systematic uncertainty is about 20 % of uncertainty on minimum bias cross section.

For case 2, a study utilizing non-colliding bunch is performed. With the data which corresponds to the delivered luminosity of 8.4 nb^{-1}, we have 55581 events in the MuonswBeam stream. When requirements of more than one muon with $p_T > 6$ GeV and more than one primary vertex are applied, no events remain. Taking into account the calculated results of $p_{\mathrm{cosmic}}^{\mathrm{trig}}$ and $p_{\mathrm{cosmic}}^{\mathrm{reco}}$, the cosmic ray backgrounds entirely induced by cosmic activities are assumed safely negligible in this study.

11.4.4   Background Summary

The overall estimated backgrounds are summarized in Table **11.6**.

	Sample	Acceptance (%)	Predicted Events
W	$Z \to \mu\mu$	11.4	34.8 ± 0.2 (stat) ± 2.2 (syst)
	$Z \to \tau\tau$	0.5	1.4 ± 0.0 (stat) ± 0.1 (syst)
	$W \to \tau\nu$	3.4	38.3 ± 0.2 (stat) ± 2.5 (syst)
	$t\bar{t}$	8.7	4.3 ± 0.0 (stat) ± 0.3 (syst)
	QCD	–	21.1 ± 4.5 (stat) ± 8.7 (syst)
	Cosmic	–	1.7 ± 0.8 (stat) ± 0.4 (stat)
	Total	–	101.7 ± 10.9
W^+	$Z \to \mu\mu$	5.9	18.2 ± 0.1 (stat) ± 1.2 (syst)
	$Z \to \tau\tau$	0.2	0.7 ± 0.0 (stat) ± 0.1 (syst)
	$W \to \tau\nu$	2.0	22.4 ± 0.2 (stat) ± 1.4 (syst)
	$t\bar{t}$	4.4	2.2 ± 0.0 (stat) ± 0.2 (syst)
	QCD	–	11.1 ± 2.7 (stat) ± 5.2 (syst)
	Cosmic	–	0.9 ± 0.4 (stat) ± 0.2 (syst)
	Total	–	55.5 ± 6.4
W^-	$Z \to \mu\mu$	5.4	16.7 ± 0.1 (stat) ± 1.1 (syst)
	$Z \to \tau\tau$	0.2	0.7 ± 0.0 (stat) ± 0.0 (syst)
	$W \to \tau\nu$	1.4	15.9 ± 0.1 (stat) ± 1.7 (syst)
	$t\bar{t}$	4.3	2.1 ± 0.0 (stat) ± 0.2 (syst)
	QCD	–	10.1 ± 1.8 (stat) ± 3.5 (syst)
	Cosmic	–	0.8 ± 0.4 (stat) ± 0.2 (syst)
	Total	–	46.3 ± 4.5

Table 11.6: The predicted number of electroweak, QCD and cosmic ray background events after corrections of number of vertices, trigger and muon reconstruction efficiency scale factors. The predicted number of events are normalized to 310 nb^{-1}.

11.5   Results for *W*-Boson Analysis

11.5.1   Event Cut Flow in the $W \rightarrow \mu\nu$ Selection

Table **11.7** summarizes the cut flow of the $W \rightarrow \mu\nu$ selection on the events in the 310 nb^{-1} of data in MuonswBeam stream. Total of 1181 (W$^+$:709, W$^-$:472) $W \rightarrow \mu\nu$ candidates are found in this analysis.

selection	number of events	reduction factor (%).	relative eff. (%))
All	50204964	100.00	—
Good Run List	33613684	66.95	66.95
Jet cleaning	33611292	66.95	99.99
L1MU6	5133936	10.23	15.27
Vertex	4789670	9.54	93.29
Combined μ, $\|\eta\| < 2.4$, $p_T > 15$ GeV, $p_T^{MS} > 10$ GeV, $\|p_T^{MS} - p_T^{ID}\| < 15$ GeV, $\|z_0 - z_{vtx}\| < 10$ mm,	20721	4.13×10^{-2}	0.43
$p_T > 20$ GeV,	7052	1.41×10^{-2}	34.03
isolation	2921	5.82×10^{-3}	41.42
$E_T^{\mathrm{miss}} > 25$ GeV	1220	2.43×10^{-3}	41.77
$M_T > 40$ GeV	1181	2.35×10^{-3}	96.80
	(W$^+$:709, W$^-$:472)		

Table 11.7: Event cut flow of the $W \rightarrow \mu\nu$ selection on data.

Shown in Figure **11.2** is the cut flow of the $W \rightarrow \mu\nu$ signal events as well as the background processes. In the figure, the result in data and MC prediction does not agree before preselection. This is because the di-jet MC sample (denoted as QCD in the figure) is filtered by the cut which requires the events to have at least one muon with $p_T > 8$ GeV as described in section 4.7.2.

11.5.2   Kinematics of Pre-Selected Samples

Figure **11.3**, **11.4** show the distributions of selected events in data as well as the MC prediction after the pre-selection. MC predictions are scaled by the cross section and normalized to the number of events in the data. The event-by-event basis weight is applied according to the number of vertices distribution. Also the trigger and muon reconstruction efficiency scale factor is applied. The QCD histogram represents the sum of the contributions from di-jet samples after 0.61 of QCD scale factor applied on them.

Figure **11.3** is the distributions in η, ϕ and p_T of the highest-p_T muons. Trigger and reconstruction scale factors are applied according to the direction (endcap or barrel) a given muon generated. The figures show a good agreement between data and MC prediction.
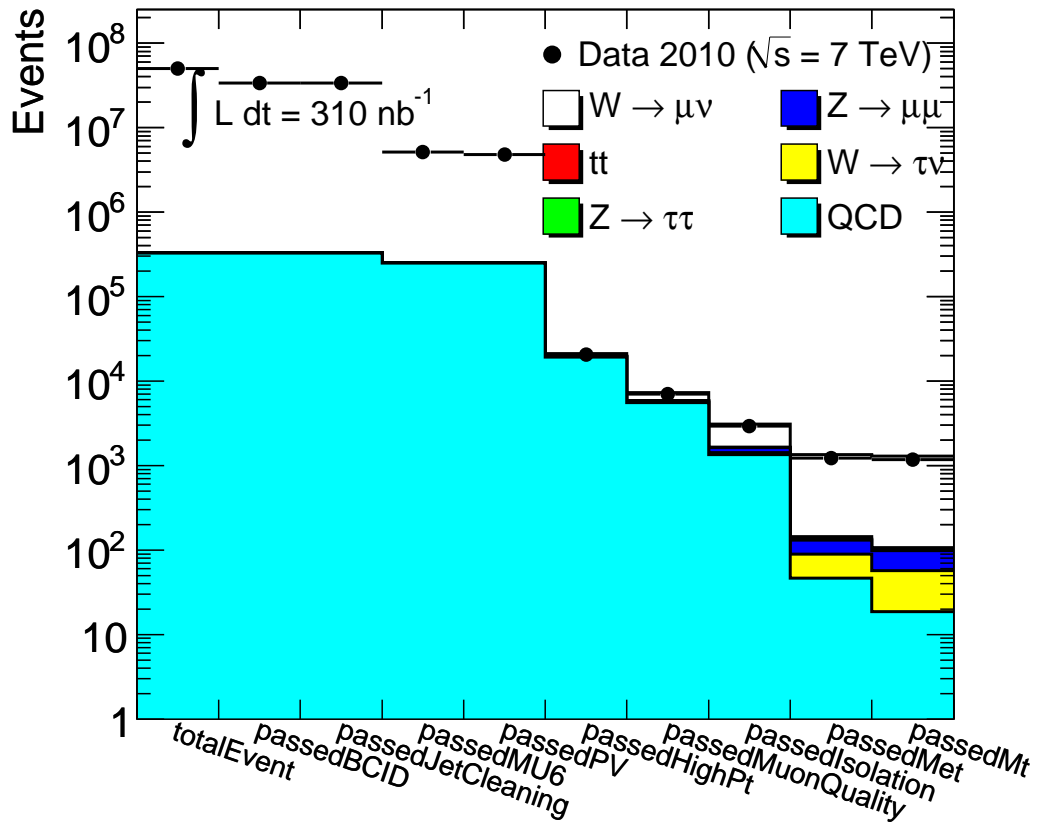
Figure 11.2: A cut flow of the $W \rightarrow \mu\nu$ event selection with backgrounds.

Figure **11.4** shows the E_T^{miss} and M_T distributions after pre-selection. In the M_T distribution, if there are more than one muons in an event, the muon which gives the M_T value nearest to m_W = 80.399 GeV [36] is adopted. The trigger scale factor is applied according to the direction of the muons selected by this procedure.
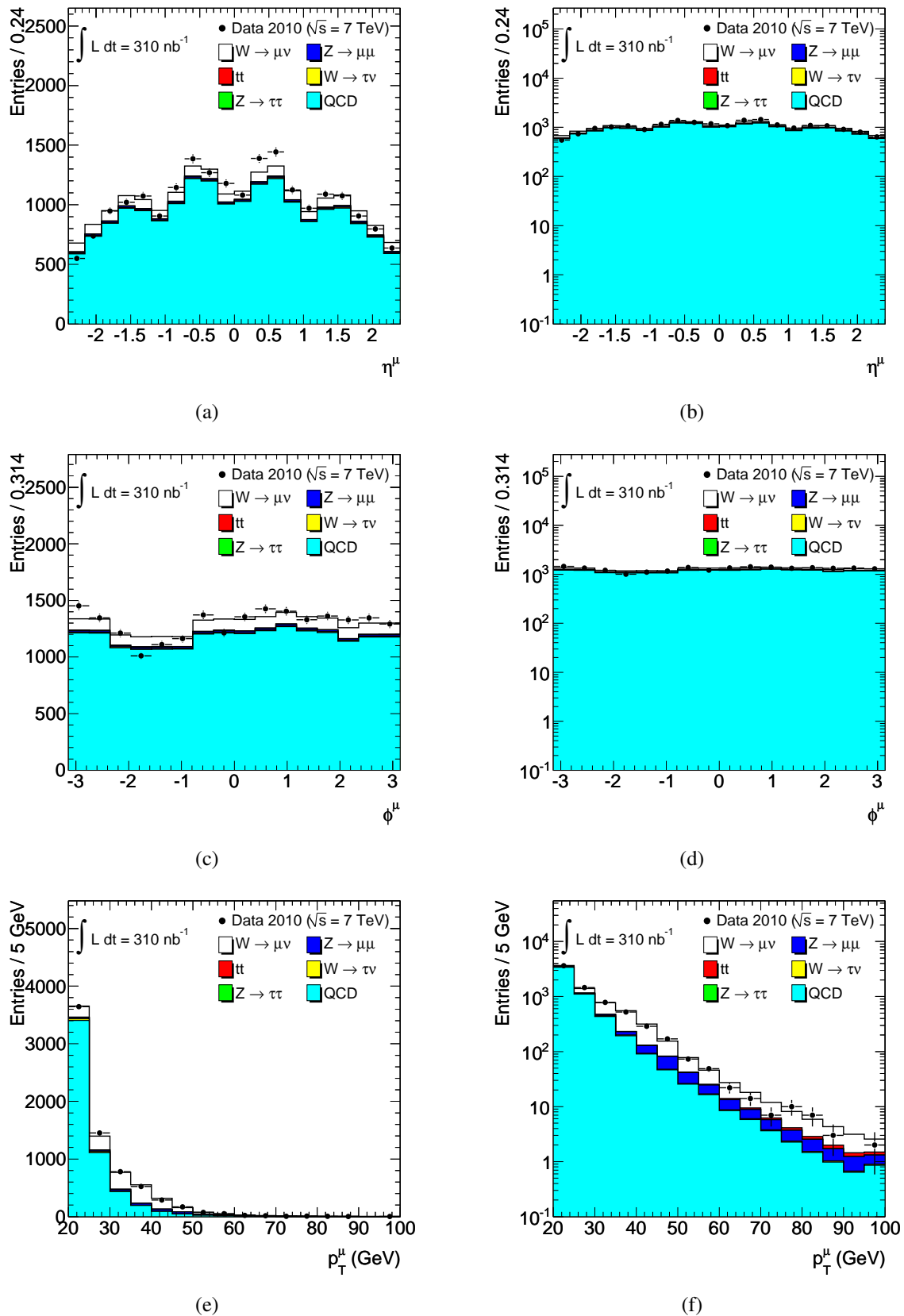
Figure 11.3: Distributions of the highest-p_T muons in events after pre-selection. Histograms are scaled by the cross section and normalized to the number of events in data. The number of vertices, trigger and muon reconstruction efficiency scale factors are applied as well as the QCD scaling factor.
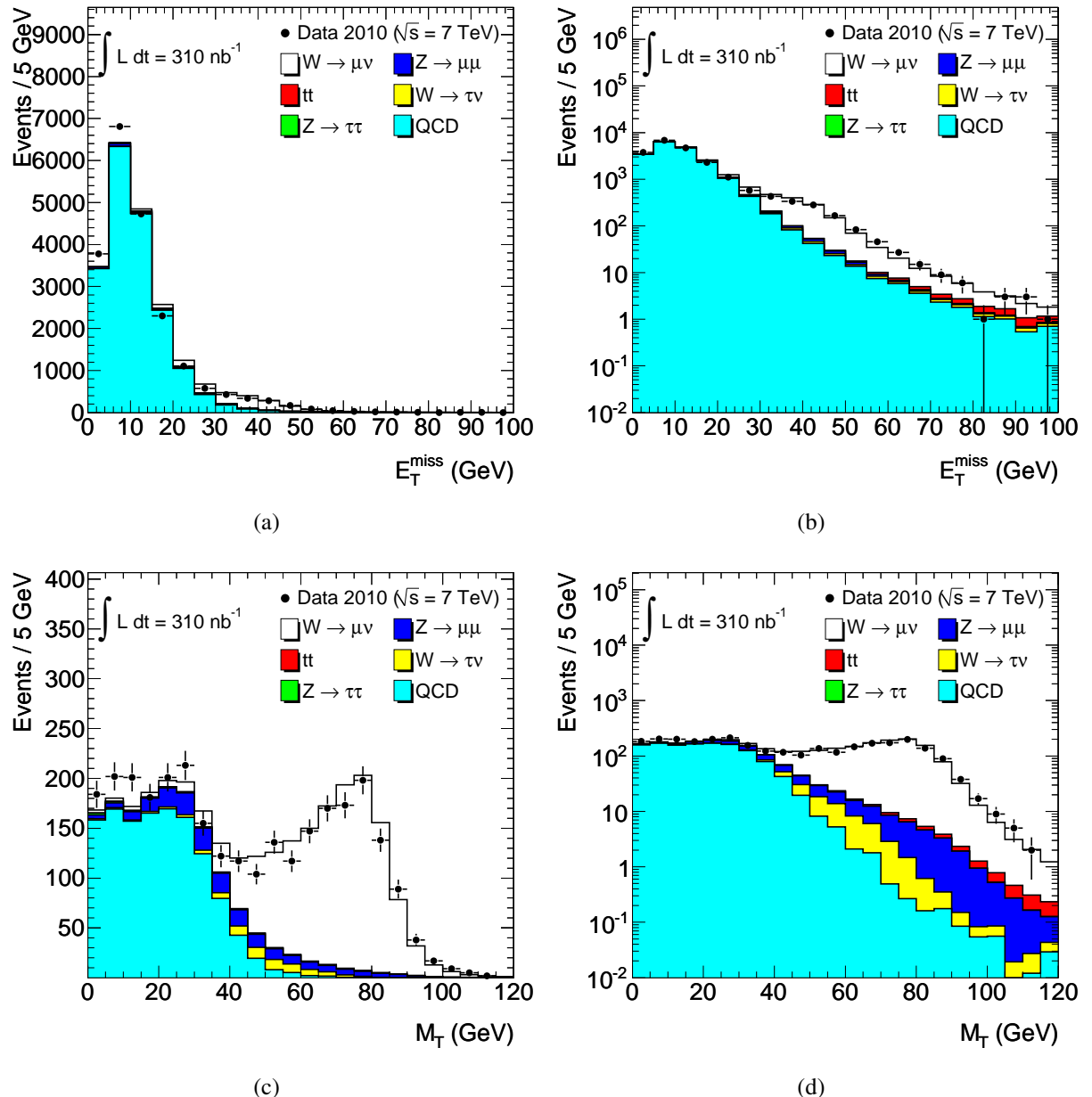
Figure 11.4: E_T^{miss} and M_T distributions of the events after pre-selection. The muon which gives the M_T nearest to m_W is selected. Histograms are scaled by the cross section and normalized to the number of events in data. The number of vertices, trigger and muon reconstruction efficiency scale factors are applied as well as the QCD scaling factor.

11.5.3   Kinematics of the $W \to \mu\nu$ Candidate Events

Shown in Table **11.8** is the number of events after all the $W \to \mu\nu$ selection in data and MC. The numbers are separated into the ones coming from W^+ and W^- according to the charge of muons which is used to calculate the M_T. The indicated uncertainties do not include the systematic contribution from the luminosity.

Sample	W	$W+$	$W-$
$Z \to \mu\mu$	34.8 ± 2.2	18.2 ± 1.2	16.7 ± 1.1
$Z \to \tau\tau$	1.4 ± 0.1	0.7 ± 0.0	0.7 ± 0.0
$W \to \tau\nu$	38.3 ± 2.5	22.4 ± 1.4	15.9 ± 1.0
$t\bar{t}$	4.3 ± 0.3	2.2 ± 0.2	2.1 ± 0.2
QCD	21.1 ± 9.8	11.1 ± 5.4	10.1 ± 4.8
Cosmic	1.7 ± 0.8	0.9 ± 0.4	0.8 ± 0.4
Total background	101.7 ± 10.9	55.5 ± 6.4	47.1 ± 4.6
$W \to \mu\nu$ signal	1194.0 ± 76.4	712.1 ± 45.6	481.5 ± 30.8
Total predicted	1295.7 ± 87.3	767.6 ± 52.0	528.6 ± 35.4
Number observed	1181	709	472

Table 11.8: The number of events which passed the $W \to \mu\nu$ selection in data and MC with its error. The error does not contain contributions coming from luminosity uncertainty.

Figure **11.5** and **11.6** show the distributions of selected muons / events in data as well as the MC prediction after all the $W \to \mu\nu$ selection. In Figure **11.5**, muons are selected as the ones which give the M_T result nearest to the m_W in an event. In Figure **11.6**, in case if there are more than one muons in an event, the M_T result nearest to the m_W is adopted. MC predictions are scaled by the cross section and normalized to the number of events in data. The event-by-event basis weight is applied according to the number of vertices distribution. Also the trigger and muon reconstruction efficiency scale factor is applied as well as the QCD scaling factor.
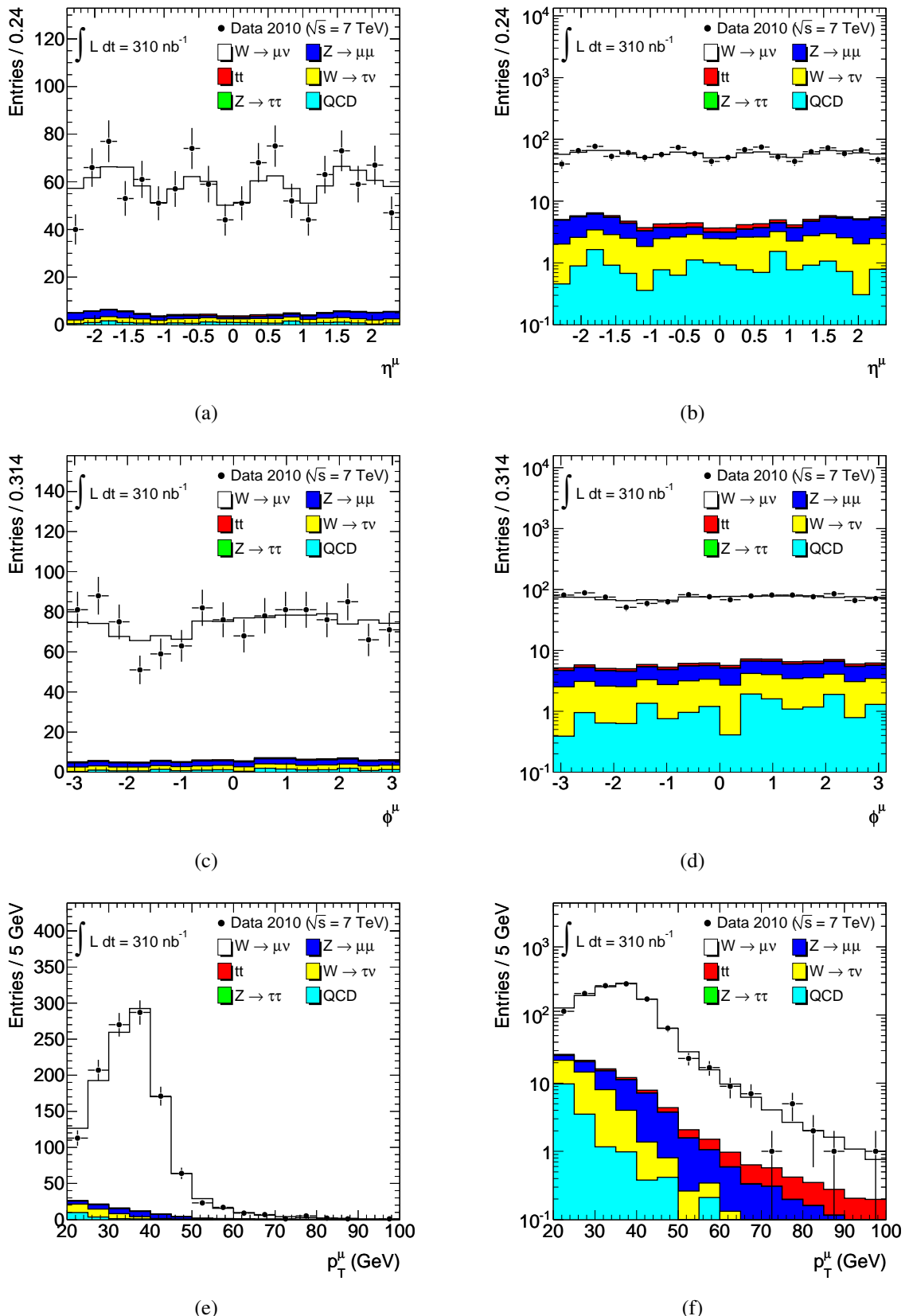
Figure 11.5: Distributions of the muons used in M_T calculation after all the $W \to \mu\nu$ selection. Histograms are scaled by the cross section and normalized to the number of events in data. The number of vertices, trigger and muon reconstruction efficiency scale factors are applied as well as the QCD scaling factor.
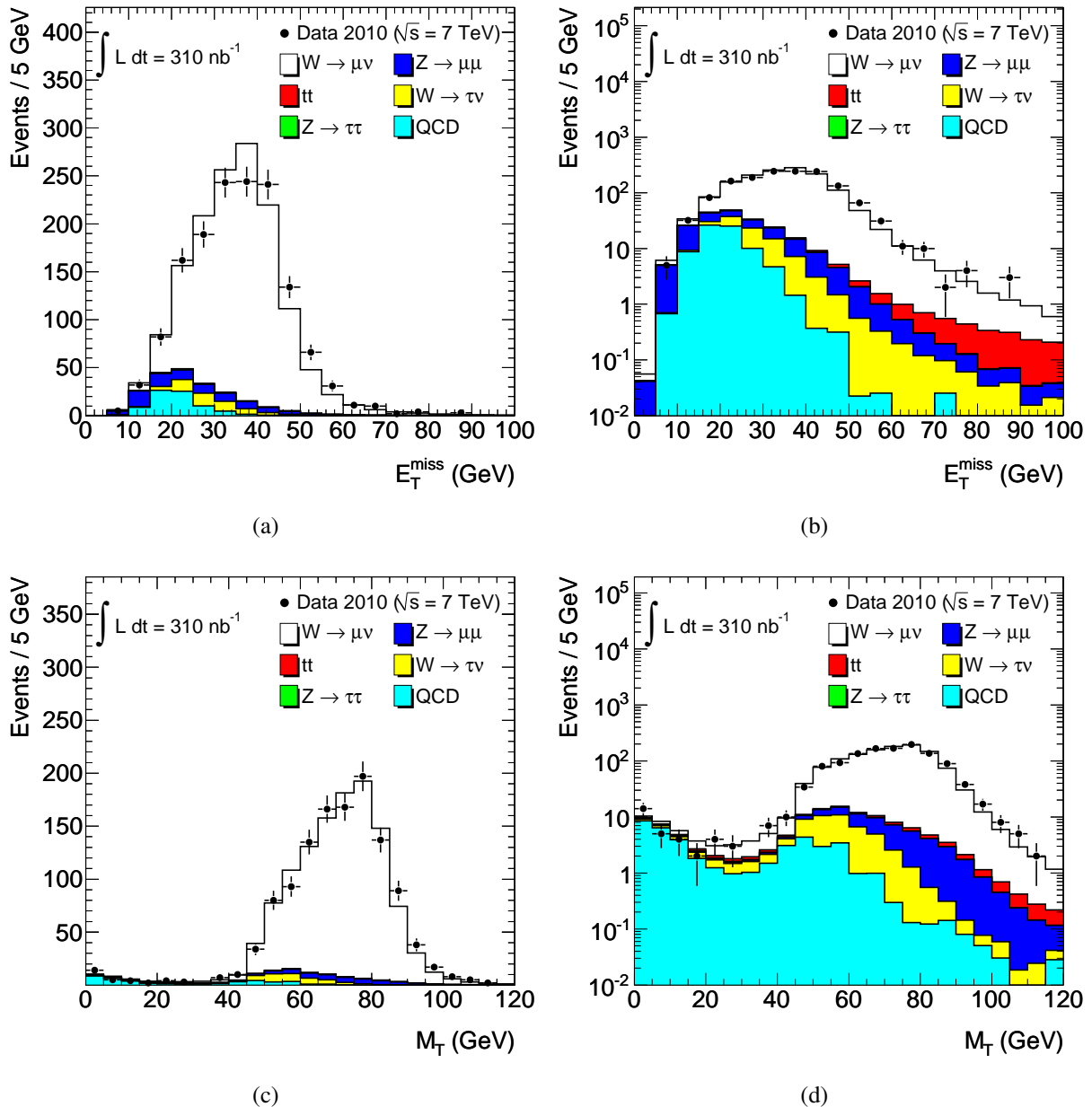
Figure 11.6: E_T^{miss} and M_T distributions of the events after all the $W \to \mu\nu$ selection. The muon which gives the M_T nearest to m_W GeV is selected. Histograms are scaled by the cross section and normalized to the number of events in data. The number of vertices, trigger and muon reconstruction efficiency scale factors are applied as well as the QCD scaling factor.

11.5.4 Cross Section Measurement

The production cross sections times branching ratio of the $W \to \mu\nu$ process is calculated according to Eq.(11.5) is summarized in Table **11.9**.

$$\sigma_W \times BR(W \to \mu\nu) = \frac{N_W^{obs} - N_W^{bkg}}{A_W \cdot C_W \cdot L_{int}}. \tag{11.5}$$

N^{obs} for inclusive cross section is 1181, in them, the number of W^+ is 709 and the number of W^- is 472 as listed in Table **11.8**. N^{bkg} is also taken from Table **11.8**. A_W and C_W are summarized in Table **11.3** with the correction factors applied on them. L_{int} is 310 nb^{-1} with the uncertainty of 11 %.

$\sigma_W \times BR\,(W \to \mu\nu)$	=	9.57 ± 0.31 (stat) ± 0.48 (syst) ± 1.05 (lumi) nb.
$\sigma_W \times BR\,(W^+ \to \mu^+\nu)$	=	5.69 ± 0.23 (stat) ± 0.29 (syst) ± 0.63 (lumi) nb.
$\sigma_W \times BR\,(W^- \to \mu^-\nu)$	=	3.87 ± 0.20 (stat) ± 0.20 (syst) ± 0.43 (lumi) nb.

Table 11.9: Results for the $W \to \mu\nu$ total cross section measurements.

Figure **11.7** and **11.8** show the comparison of distributions between data and inclusive MC prediction. Histograms are scaled by the cross section and normalized to the integrated luminosity of 310 nb^{-1}. For MC, the luminosity uncertainty of 11 % is assigned as the error. In these figure, all the scale factors (QCD scaling, number of vertices, trigger and muon reconstruction efficiency) are applied.

(a)

(b)

(c)
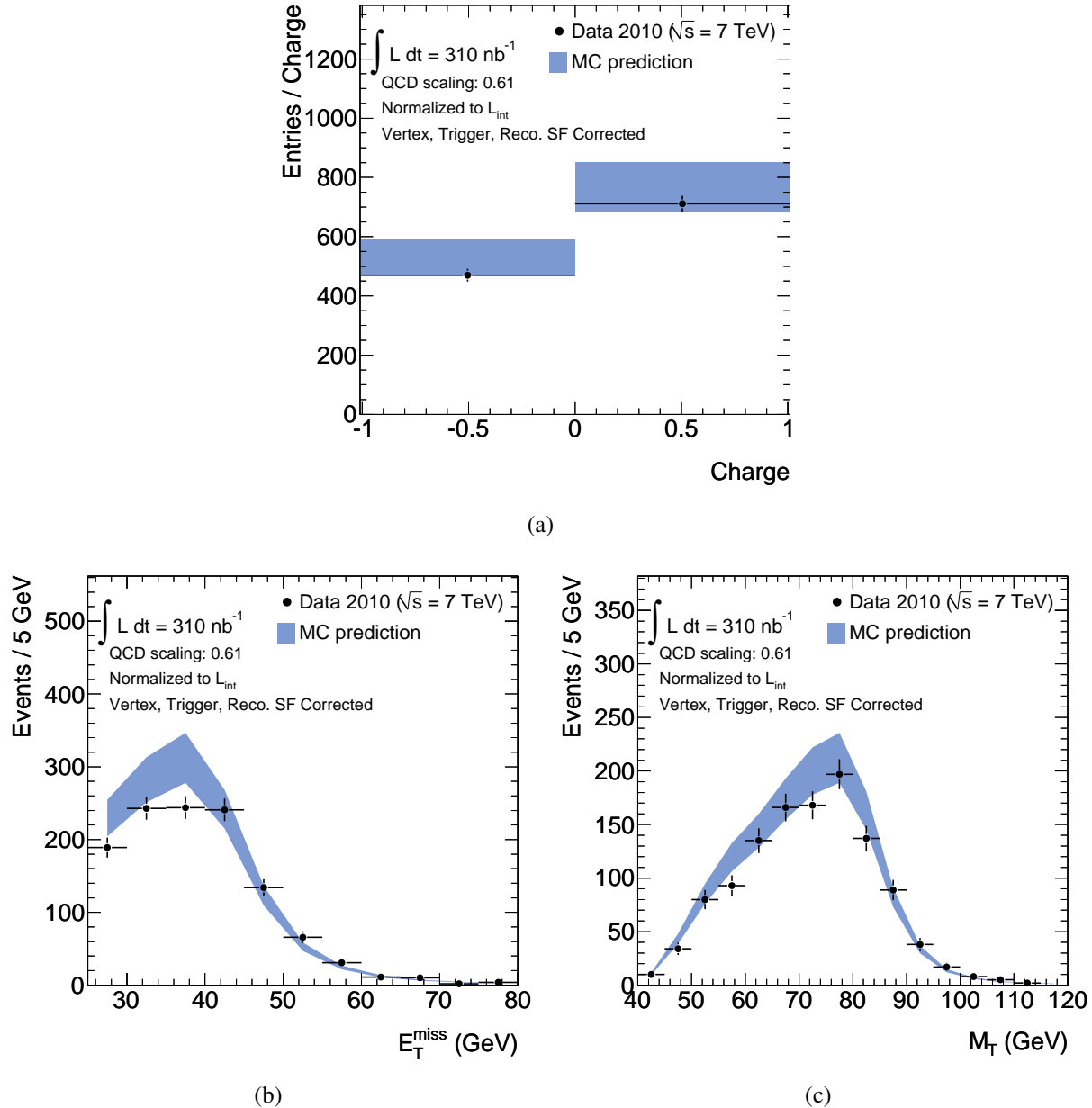
Figure 11.7: Muon charge, E_T^{miss} and M_T distributions of the events after all the $W \rightarrow \mu\nu$ selection. The muon which gives the M_T nearest to m_W GeV is selected. MC predictions are given as an integrated histogram with 11 % of the luminosity uncertainty as the error. MC predictions are scaled by the cross section and normalized to integrated luminosity of 310 nb^{-1}. The number of vertices, trigger and muon reconstruction efficiency scale factors are applied as well as the QCD scaling factor.
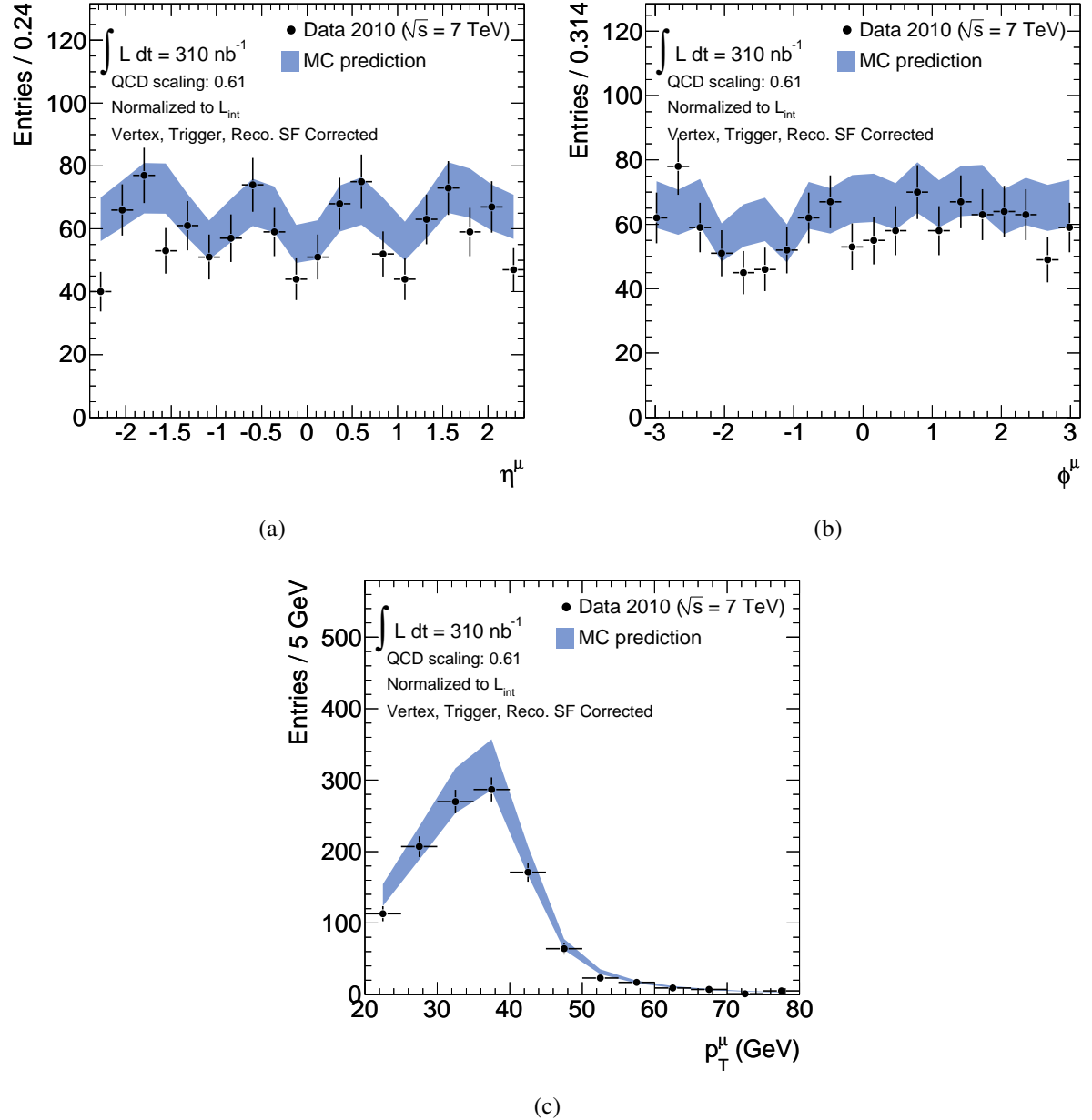
Figure 11.8: η, ϕ and p_T distributions of muons after all the $W \rightarrow \mu\nu$ selection. The muons which give the M_T nearest to m_W GeV are selected. MC predictions are given as an integrated histogram with 11 % of the luminosity uncertainty as the error. MC predictions are scaled by the cross section and normalized to integrated luminosity of 310 nb^{-1}. The number of vertices, trigger and muon reconstruction efficiency scale factors are applied as well as the QCD scaling factor.

Chapter 12

Measurement of Z Boson Cross Section

12.1 Event Selection

Collision event selection	
Good Run List & BCID	$Z \to \mu\mu$ GRL
Primary vertex	$N_{vtx} \geq 1$ with $N_{tracks} \geq 3$
	$|z_{vtx}| < 150$ mm
Trigger	L1_MU6
High-p_T event selection	
Muon selection	combined tracks
	$p_T > 15$ GeV, $|\eta| < 2.4$
Muon quality	$p_T^{MS} > 10$ GeV
	$|p_T^{MS} - p_T^{ID}| < 15$ GeV
	$|z_0 - z_{vtx}| < 10$ mm
$Z \to \mu\mu$ event selection	
Tight kinematics (both muons)	$p_T > 20$ GeV
Muon quality (both muons)	(as above)
ID isolation (both muons)	$\sum p_T^{ID}/p_T < 0.2$ ($\Delta R = 0.4$)
Charge	$q_1 \cdot q_2 < 0$
Invariant Mass	$66 < M_{\mu\mu} < 116$ GeV

Table 12.1: A summary of the requirements for the $Z \to \mu\mu$ candidate event selection.

A summary of the requirements for $Z \to \mu\mu$ candidate events selection is given in Table **12.1**. Alike the $W \to \mu\nu$ event selection, the $Z \to \mu\mu$ event selection is divided into three parts. The collision event selection and high-p_T event selection are identical to the $W \to \mu\nu$ selection except for GRL (each analysis uses the dedicated GRL) and jet cleaning. Note that the high-p_T event selection only requires a single combined track.

In the $Z \to \mu\mu$ event selection, two isolated, oppositely charged muons are required in an event. Both muons are required to satisfy the same quality as the one in the high-p_T event selection but $p_T > 20$ GeV. The Mass window is set at $66 < M_{\mu\mu} < 116$ GeV.

12.2 Signal Acceptance and Efficiencies

12.2.1 Overall Acceptance of $Z \to \mu\mu$ Selection

The definition of the acceptance is the same as in the $W \to \mu\nu$ analysis, i.e. the number of events passing all selections divided by the number of generated events. The acceptance is estimated with a $Z \to \mu\mu$ MC sample which is described in section 4.7.2. The yielded acceptance is 36.90 % with a negligible statistical error. The GRL and BCID requirements are omitted from the selection since these are not relevant for simulated samples. The number of signal events passing each step of the selection, and the efficiencies for each step relative to the previous one and total generated number (denoted as reduction factor) are given in Table **12.2**.

Then the acceptance is corrected to compensate the discrepancy between data and MC in the number of vertices, trigger and reconstruction efficiency. The correction procedure of the difference in the number of vertices effect is the same as the one used in $W \to \mu\nu$ analysis. Details of the corrections are summarized in section 12.2.2.

selection	number of events	reduction factor (%)	rel. eff. (%)
Total Events	299811	–	–
L1_MU6	257330	85.83	85.83
Vertex	256810	85.66	99.80
combined track, $\lvert\eta\rvert < 2.4$, $p_\mathrm{T} > 15$ GeV, $p_\mathrm{T}^{MS} > 10$ GeV, $\lvert p_\mathrm{T}^{MS} - p_\mathrm{T}^{ID}\rvert < 15$ GeV, $\lvert z_0 - z_{vtx}\rvert < 10$ mm,	232787	77.64	90.65
Tight Kinematics ($\mu \times 2$)	118080	39.38	50.72
Isolation	116035	38.70	98.27
Opposite Charge	116034	38.70	100.00
Mass Window	112858	37.64	97.26
Correction (vertex)	112608	37.56	99.78
Correction (trigger)	110615	36.90	98.23
Correction (combined track)	110615	36.90	100.00

Table 12.2: Effect of the $Z \to \mu\mu$ selection criteria on simulated $Z \to \mu\mu$ events.

12.2.2   Efficiency Scale Factors

Number of Vertices

The effect of the correction in terms of the number of vertices is the same as in the $W \rightarrow \mu\nu$ analysis. The resulted scale factor is 0.998 ± 0.000 (stat) ± 0.002 (syst).

Muon Trigger Efficiency

In the $Z \rightarrow \mu\mu$ analysis, two muons are required in an event. Thus the single muon trigger efficiency scale factor does not coincides with the needed correction on the $Z \rightarrow \mu\mu$ acceptance. The event trigger efficiency and its uncertainty are expressed as follows.

$$\epsilon_{event} = 1 - (1 - \epsilon_1)(1 - \epsilon_2), \tag{12.1}$$

$$\delta\epsilon_{event} = (1 - \epsilon_1)\,\delta\epsilon_2 \,\oplus\, (1 - \epsilon_2)\,\delta\epsilon_1. \tag{12.2}$$

ϵ_1 and ϵ_2 are the L1_MU6 efficiency for each muon. Since the single muon trigger efficiencies are measured in endcap and barrel separately, events are categorized into three types according to the direction to which each muon is generated. EE represents the events in which both muons are generated to the endcap, BB represents the events in which both muons are generated to the barrel, and EB represents the events in which one muon is generated to the endcap and the other is generated to the barrel. Event trigger efficiency is computed following the procedure summarized below.

- Estimate the fraction of Z events of each type EE, BB and EB in MC. Events are required to pass all the Z selection criteria except for the trigger. The resulted fractions are 0.230 (EE), 0.286 (BB) and 0.484 (EB).

- Apply Eq.(12.1) on each type of events. Using the single muon trigger efficiency, we estimated the event trigger efficiency for each type in data and MC.

- Using the fractions, take weighted average of the efficiency separately in data and MC as a scale factor.

  - 0.965 $\pm$ 0.002 (stat) $\pm$ 0.005 (syst) (weighted average efficiency in data)
  - 0.983 $\pm$ 0.000 (stat) $\pm$ 0.001 (syst) (weighted average efficiency in MC)

After that the ratio of weighted average in data to MC is taken as the trigger efficiency scale factor for the $Z \rightarrow \mu\mu$ acceptance. The resulting scale factor is 0.982 ± 0.002 (stat) ± 0.005 (syst).

Muon Reconstruction Efficiency

Given that $Z \rightarrow \mu\mu$ events have two combined muons, the muon reconstruction efficiency scale factor on the acceptance and its uncertainty are given as

$$\epsilon_{event} = \epsilon^2, \tag{12.3}$$

$$\delta\epsilon_{event} = 2\epsilon\delta\epsilon. \tag{12.4}$$

The scale factor for muon reconstruction efficiency is taken from section 10.3. The scale factor on the $Z \to \mu\mu$ acceptance become 1.000 ± 0.008 (stat) ± 0.048 (syst).

12.2.3 Acceptance Decomposition

As in $W \to \mu\nu$ analysis, the overall acceptance is decomposed into A_Z and C_Z. The definition and the estimated number are summarized in following.

- A_Z: Fraction of the generated $Z \to \mu\mu$ events which passed the kinematic and geometrical selection of $p_T > 20$ GeV, $|\eta| < 2.4$ and $66 < M_{\mu\mu} < 116$ GeV, where all of these quantities refer to the truth-level muon before any final state radiation. Estimated value for A_Z is 0.486 with 3.0 % of common uncertainty (see section 8.4.3).

- C_Z: The denominator is the number of events passing the generator-level requirements that form the numerator of A_Z, and the numerator is the fraction of events passing the full analysis selections. The uncorrected value of C_Z is estimated as 0.788. The systematic uncertainty is assigned as 5.5 %, the details are presented in 12.3.

12.2.4 Summary of Acceptance and Efficiency

The $Z \to \mu\mu$ signal acceptance is summarized in Table **12.3**. The correction for the number of vertices distribution, trigger and muon reconstruction efficiency is already applied on the overall acceptance and C_Z. The scale factors are also summarized in the table. The uncertainty on the overall acceptance is assigned as 6.2 % as the quadrature sum of the uncertainties of A_Z and C_Z.

	Z
A_Z	0.486 ± 0.015
C_Z	0.774 ± 0.043
overall acceptance	0.369 ± 0.023
number of vertices SF	0.998 ± 0.002
trigger efficiency SF	0.982 ± 0.006
reconstruction efficiency SF	1.000 ± 0.008 (stat) ± 0.048 (syst)

Table 12.3: A summary of the acceptance and scale factors for the $Z \to \mu\mu$ events.

12.3   Systematic Uncertainty on Acceptance

Table **12.4** summarizes the systematic components on the $Z \rightarrow \mu\mu$ acceptance. The uncertainty on A_Z is estimated as 3.0 % and on C_Z is estimated as 5.5 %. The effects from muon momentum scale and resolution are estimated by the same method as in section 11.3. The differences from the uncertainty on $W \rightarrow \mu\nu$ acceptance are coming from the fact that, in the $Z \rightarrow \mu\mu$ analysis, two muon are required and calorimeter information is not used. The overall uncertainty on the acceptance is 6.2 %.

parameter	parameter uncertainty (%)	acceptance uncertainty (%)
number of vertices	0.2	0.2
trigger efficiency	2.4 (barrel), 2.1 (endcap)	0.6
reconstruction efficiency	2.4	4.8
muon momentum scale	1.0	0.5
muon momentum resolution	5.0 (barrel), 9.0 (endcap)	0.5
isolation cut efficiency	1.0	2.0
theoretical uncertainty	0.2 (FSR), 0.3 (PDF)	0.4
total uncertainty		5.5

parameter		$\delta A_Z (\%)$
theoretical uncertainty		3.0

total uncertainty		6.2

Table 12.4: A summary of the systematic uncertainty on the $Z \rightarrow \mu\mu$ acceptance.

12.4 Background Estimation

12.4.1 QCD Background

Estimation by Simulated Samples

The combinatorial muon pair comes from QCD process is one of the main background source for the $Z \to \mu\mu$ process due to its huge cross section. The muons originate from semileptonic decay of heavy flavor hadrons or decay-in-flight of π/K meson.

Since the statistics used in this analysis is so small, the number of QCD background events are estimated using MC simulation samples. We used same di-jet MC samples used in the $W \to \mu\nu$ analysis with QCD scaling factor of 0.61. Also, due to the fact that the jet production cross section is not know accurately, the The corrections for the number of vertices, muon trigger and reconstruction efficiency are applied as well. systematic uncertainty of 100 % is assigned. In 331 nb^{-1} of data, the predicted QCD background is 0.138 ± 0.085 (stat)± 0.138 (sys). Since the amount of QCD background is expected to be very small, this estimation is used in the Z-boson cross section calculation.

Estimation from the Number of Same Charged Muon Pair

One of the most straight forward data driven estimations for the number of QCD background is to count the number of like-sign muon pairs fallen in the invariant mass window passed all the $Z \to \mu\mu$ selection. However, the yielded number of such muon pair is zero. Thus only an upper limit of the number of expected QCD events smaller than 3 is obtained in 95 % C.L.

Estimation using Sideband with Reversed Isolation

In this method the $M_{\mu\mu} - -Isolation$ space is divided into following four areas.

A: Isolated muons in $66 < M_{\mu\mu} < 116$ GeV

B: Isolated muons in $40 < M_{\mu\mu} < 60$ GeV

C: Non-Isolated muons in $66 < M_{\mu\mu} < 116$ GeV

D: Non-Isolated muons in $40 < M_{\mu\mu} < 60$ GeV

Figure **12.1** shows the $M_{\mu\mu}$ distributions for isolated and non-isolated muons. An assumption that the ratio of isolated to non-isolated muons from jets is independent of $M_{\mu\mu}$ is made. Upon this assumption, the number of QCD events in the signal region is given by

$$N_A \sim \frac{N_B \times N_C}{N_D}. \tag{12.5}$$

The number of events in each area is $N_B = 2$, $N_C = 3$ and $N_D = 5$. Hence the expected number of events are

$$N_A \sim \frac{(4.0 \pm 2.0) \times (3 \pm 1.7)}{5.0 \pm 2.2} = 2.4 \pm 2.1. \tag{12.6}$$

The assigned error is only statistical component.
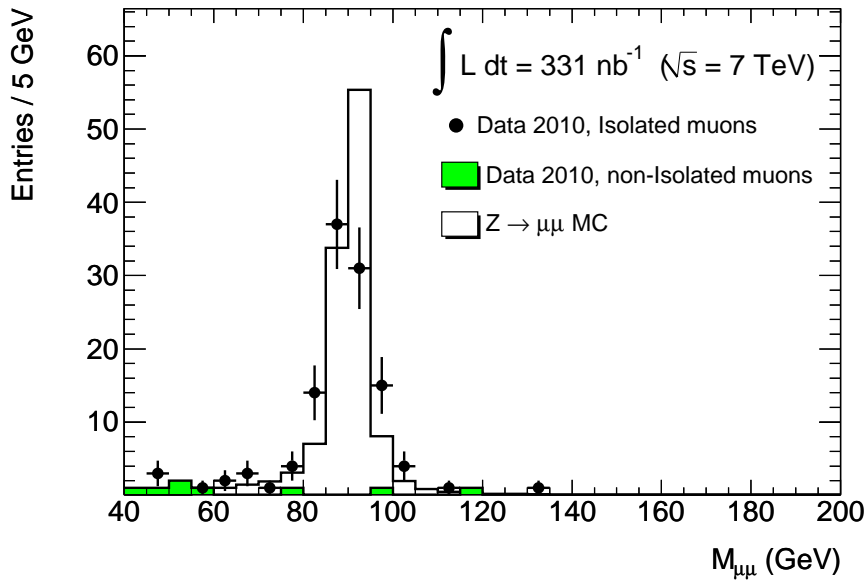
Figure 12.1: Dimuon invariant mass distributions for isolated and non-isolated muons.

12.4.2 Electroweak and $t\bar{t}$ Backgrounds

The same set of the processes as in the $W \to \mu\nu$ analysis, $W \to \mu\nu$, $W \to \tau\nu$ and $Z \to \tau\tau$, are considered as electro weak background process. Since the total amount of the electroweak background is expected to be very small, we use MC simulation to estimate the various components. For the $W \to \mu\nu$ process, a scale factor of 1181 / 1194.0 is applied on the number of events to compensate the discrepancy observed between the data and MC (see Table **11.8**).

For the electroweak and $t\bar{t}$ backgrounds, the following errors are assigned as systematic components.

- Uncertainty on C_Z of 5.5 % as summarized in the Table **12.4**

- Uncertainty on the PDF dependence of 3.0 % for $t\bar{t}$

- Theoretical cross section uncertainty of 5.0 % for electroweak processes and 6.0 % for $t\bar{t}$.

The systematics total to 8.7 % for $t\bar{t}$ and 7.4 % for electroweak backgrounds. All the electroweak backgrounds are treated as 100 % correlated except for $t\bar{t}$. In 331 nb^{-1} of data, total of 0.226 ± 0.012 (stat) ± 0.013 (sys) electroweak background events are predicted in this analysis.

12.4.3 Cosmic Ray Background

The model of the cosmic background used in the $W \to \mu\nu$ analysis is also adopted here as

$$\sigma_{cosmic} = \sigma_{MB} \cdot p_{cosmic}^{trig} \cdot p_{cosmic}^{reco} \cdot L_{int}. \tag{12.7}$$

$\sigma_{MB} = 50 \pm 10$ mb and $p_{cosmic}^{trig} = 3.3 \times 10^{-5}$ are adopted as estimated in section 11.4.3. Even with a loosened z_0 cut to $|z_0 - z_{vtx}| < 150$ mm (the cut used in the $Z \to \mu\mu$ cross section measurement is $|z_0 - z_{vtx}| < 10$ mm), no events remain in the non-colliding bunch data of 9.4×10^5 events. The upper limit is calculated by assuming the case if one event remain, the number of expected events which pass the $Z \to \mu\mu$ selection is $1 \times (20/300) = 0.067$. This yields a value of $p_{cosmic}^{reco} = 7.1 \times 10^{-8}$. The resulted value for the upper limit on the cosmic ray background estimation is

$$N_{cosmic} = 50 \cdot 10^6 \times 3.3 \cdot 10^{-5} \times 7.1 \cdot 10^{-8} \times 331 = 0.039. \tag{12.8}$$

Since this value is one order smaller than estimated electro weak background and it is just a upper limit, the background cosmic ray events are considered to be negligible in the $Z \to \mu\mu$ cross sections measurement.

12.4.4 Background Summary

The summary of the backgrounds estimated to $Z \to \mu\mu$ in 331 nb^{-1} of data is presented in Table **12.5**. All the values are taken from the prediction of the MC simulation. As background processes, we consider $W \to \mu\nu$, $W \to \tau\nu$, $Z \to \tau\tau$, $t\bar{t}$ and QCD di-jet events.

As described above, we take 100 % of the predicted number of events as systematics for QCD events. On the other hand, the uncertainty of the acceptance, PDF and theoretical cross sections are considered for electroweak processes. In 331 nb^{-1} of data, total of 0.365 ± 0.085 (stat) ± 0.139 (sys) background events are predicted.

sample	Acceptance (%)	Number of events
$W \to \mu\nu$	8.68×10^{-4}	0.030 ± 0.010 (stat) ± 0.002 (syst)
$W \to \tau\nu$	1.00×10^{-4}	0.001 ± 0.001 (stat) ± 0.000 (syst)
$Z \to \tau\tau$	2.65×10^{-2}	0.087 ± 0.004 (stat) ± 0.006 (syst)
$t\bar{t}$	2.04×10^{-1}	0.108 ± 0.005 (stat) ± 0.009 (syst)
EW Total	—	0.226 ± 0.011 (stat) ± 0.012 (syst)
QCD	—	0.138 ± 0.084 (stat) ± 0.138 (syst)
Total Background	—	0.364 ± 0.085 (stat) ± 0.139 (syst)

Table 12.5: The background contributions predicted by MC. Predictions are normalized to 331 nb^{-1} and vertex, trigger and muon reconstruction scale factors are applied.

12.5   Results of Z-Boson Analysis

12.5.1   Event Cut Flow in the $Z \to \mu\mu$ Selection

Table **12.6** summarizes the effect of each step of $Z \to \mu\mu$ event selection. The number of events passing each step of the selection, the efficiencies of each step relative to the previous one and all the processed events (denoted as reduction factor) are given in Table **12.2**. In the 331 nb^{-1} of data triggered by L1_MU6, total of 109 $Z \to \mu\mu$ candidates are found.

selection	number of Events	reduction factor (%)	relative eff. (%)
All	49655492	100.00	100.00
Good run List	35883824	72.27	72.27
L1_MU6	5476542	11.03	15.26
Vertex	5113446	10.30	93.37
Combined μ, $|\eta| < 2.4$, $p_{\mathrm{T}} > 15$ GeV, $p_{\mathrm{T}}^{MS} > 10$ GeV, $|p_{\mathrm{T}}^{MS} - p_{\mathrm{T}}^{ID}| < 15$ GeV, $|z_0 - z_{vtx}| < 10$ mm,	22120	4.45×10^{-3}	4.33×10^{-3}
Tight Kinematics ($\mu \times 2$)	144	2.90×10^{-4}	6.51×10^{-3}
Isolation	117	2.36×10^{-4}	81.25
Opposite Charge	117	2.36×10^{-4}	100.00
Mass Window	109	2.20×10^{-4}	93.16

Table 12.6: Event cut flow of the $Z \to \mu\mu$ selection on data.

12.5.2   Kinematics of Pre-Selected Samples

Figure **12.2** and **12.3** show the distributions of selected events in data as well as the MC prediction after the pre-selection. MC predictions are scaled by the cross section and normalized to the number of events in data. An event-by-event basis weight is applied according to the number of vertices in a given event. Also the trigger and muon reconstruction efficiency scale factors are applied. QCD histogram represents the sum of the contributions from di-jet samples after 0.61 of QCD scale factor is applied on them.

Figure **12.2** is the distributions in η, ϕ and p_{T} of the highest-p_{T} muons. Trigger and reconstruction scale factors are applied according to the direction (endcap or barrel) of a given muon generated. The data and MC results show a reasonable agreement.

Shown in Figure **12.3** is the invariant mass distribution of di-muon pairs. If there are more than two muons in an event, the pair which has the invariant mass nearest to $m_Z = 91.1876$ GeV [36] among any combination is adopted. The data and MC results agree well.
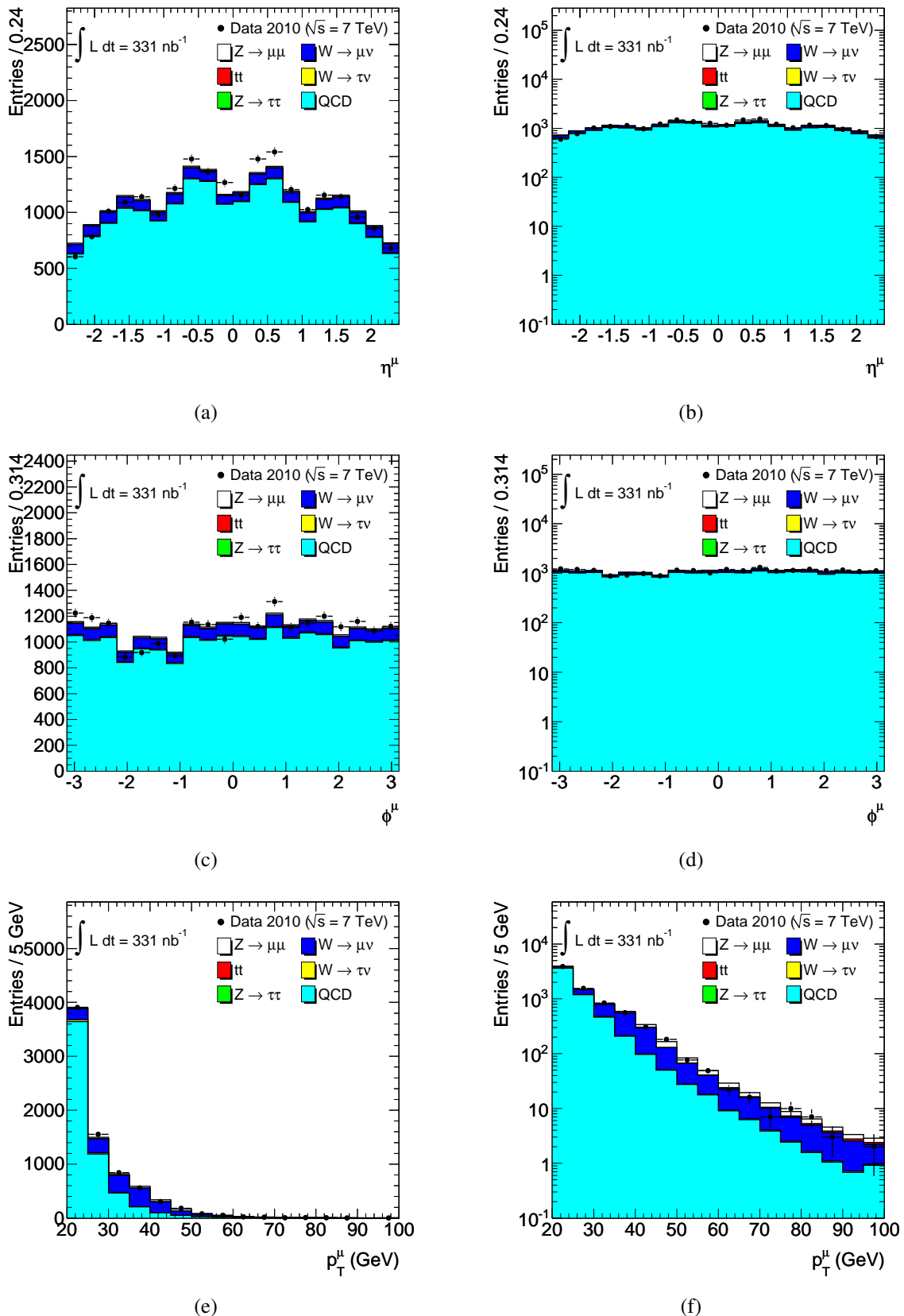
Figure 12.2: Distributions of the highest-p_T muons after pre-selection. Histograms are scaled by the cross section and normalized to the number of events in data. The number of vertices, trigger and muon reconstruction efficiency scale factors are applied as well as the 0.61 of QCD scaling factor.
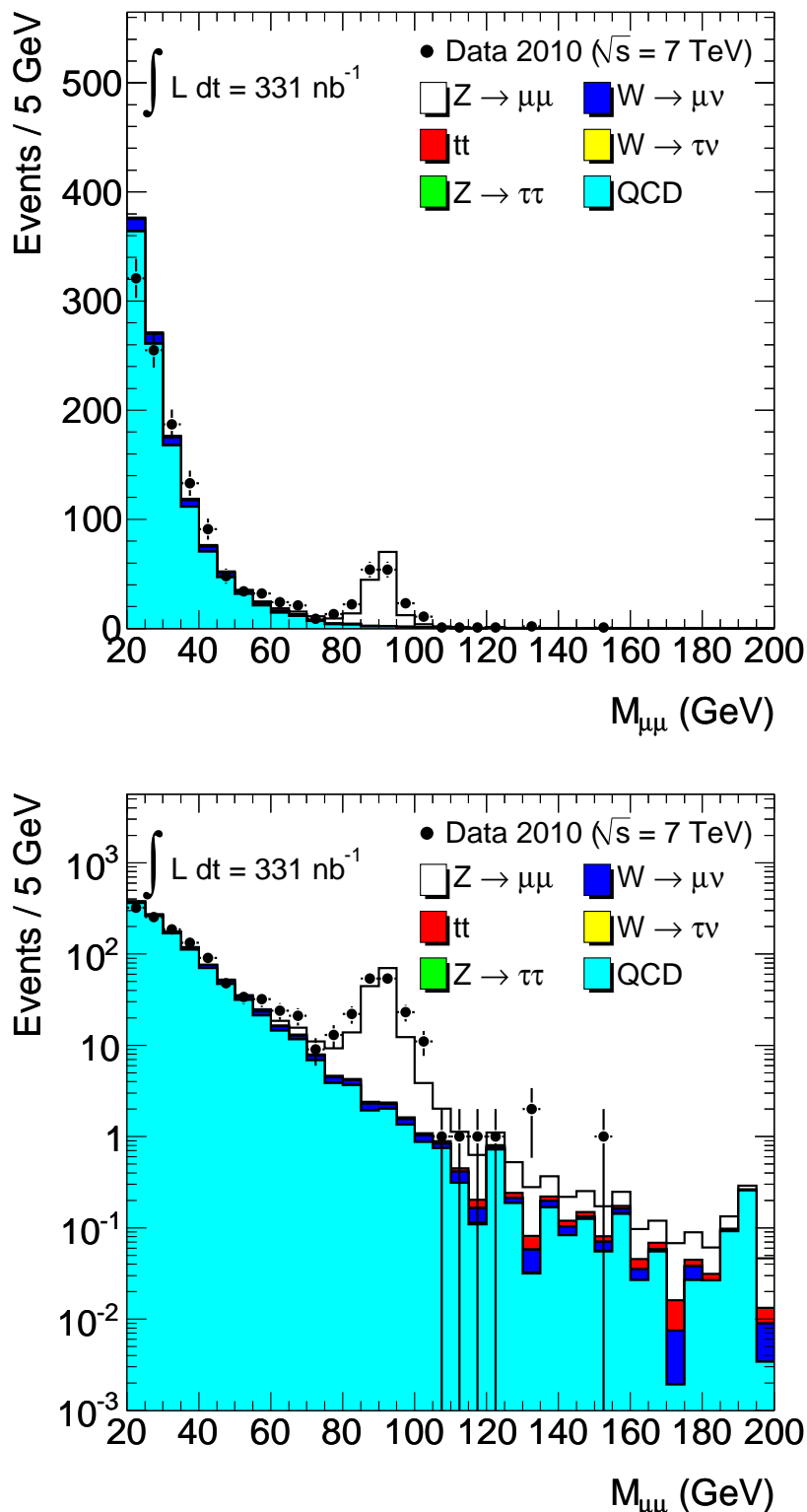
Figure 12.3: *M$_{\mu\mu}$* distributions of the muons after the pre-selection. Histograms are scaled by the cross section and normalized to the number of events in data. The number of vertices, trigger and muon reconstruction efficiency scale factors are applied as well as the 0.61 of QCD scaling factor.

12.5.3   Kinematics of $Z \rightarrow \mu\mu$ Candidate Events

Table **12.7** summarizes the number of events after all the $Z \rightarrow \mu\mu$ selection in data and MC. The indicated uncertainties do not include the contribution from luminosity uncertainty.

$W \rightarrow \mu\nu$	0.030 ± 0.010
$W \rightarrow \tau\nu$	0.001 ± 0.001
$Z \rightarrow \tau\tau$	0.087 ± 0.007
$t\bar{t}$	0.108 ± 0.011
EW Total	0.226 ± 0.018
QCD	0.138 ± 0.162
Total background	0.364 ± 0.163
$Z \rightarrow \mu\mu$ signal	121.5 ± 9.0
Total predicted	121.9 ± 9.2
Number observed	109

Table 12.7: The number of events which passed the $Z \rightarrow \mu\mu$ selection in data and MC with its error. The error does not contain contributions coming from luminosity uncertainty.

Shown in Figure **12.4** is the cut flow of the $Z \rightarrow \mu\mu$ signal events as well as the background processes. In the figure, the result in data and MC prediction does not agree before preselection. This is because the di-jet MC sample (denoted as QCD in the figure) is filtered by the cut which requires the events to have at least one muon with $p_T > 8$ GeV as described in section 4.7.2.

Figure **12.5** and **12.6** show the distributions of selected muons / events in data as well as the MC prediction after all the $Z \rightarrow \mu\mu$ selection. In Figure **12.5**, both muons which comprise Z candidate are plotted. In case if there are more than two muons in an event, the pair with its invariant mass the nearest to m_Z is selected.

Also in Figure **12.6**, the pair with the most Z-like invariant mass is adopted. MC predictions are scaled by the cross section and normalized to the number of events in data. Event-by-event basis weight is applied according to the number of vertices distribution. Also the trigger and muon reconstruction efficiency scale factor is applied as well as the QCD scaling factor.

As can be seen in Figure **12.6**, the invariant mass distribution in data has a broader peak than the MC prediction. This comes from the fact that the momentum resolution of the actual muon spectrometer is worse than that of in MC. The degradation of the momentum resolution is estimated as 5 (9) % in the barrel (endcap) in section 8.4.1 and the effect on the acceptance is counted into the systematic uncertainty.

Figure **12.7** shows the distribution of original Z-boson kinematics after all selections.
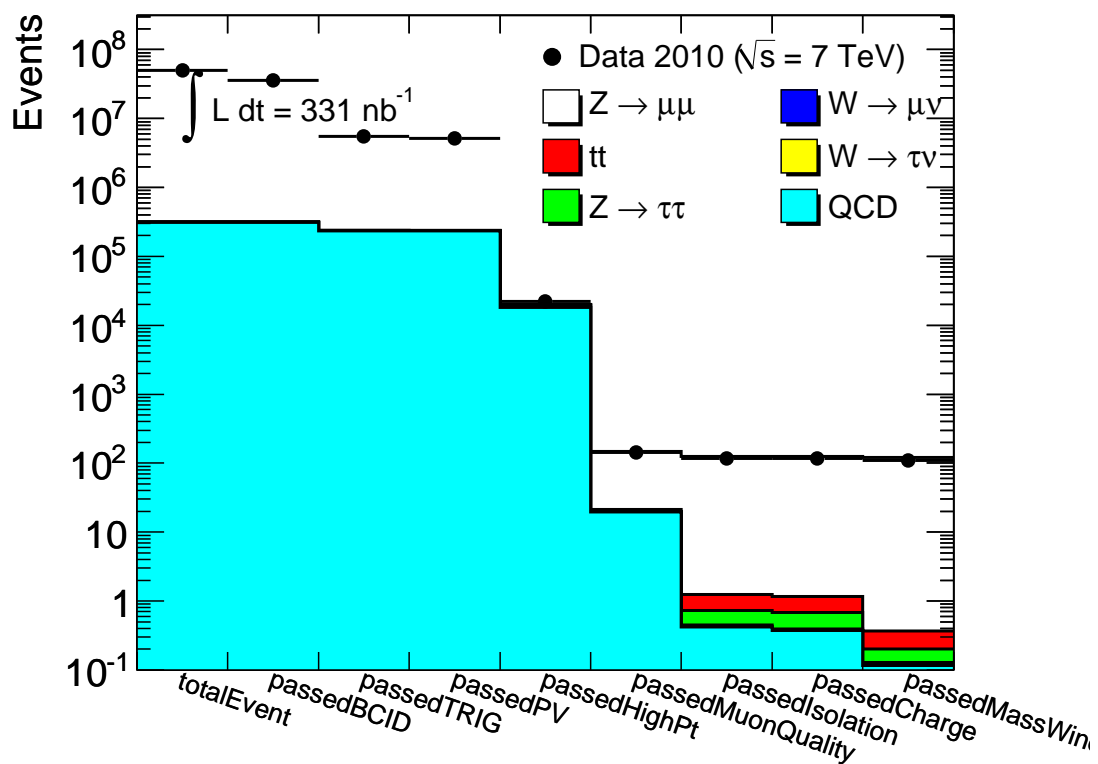
Figure 12.4: A cut flow of the $Z \rightarrow \mu\mu$ event selection with backgrounds.

(a)   (b)

(c)   (d)

(e)   (f)
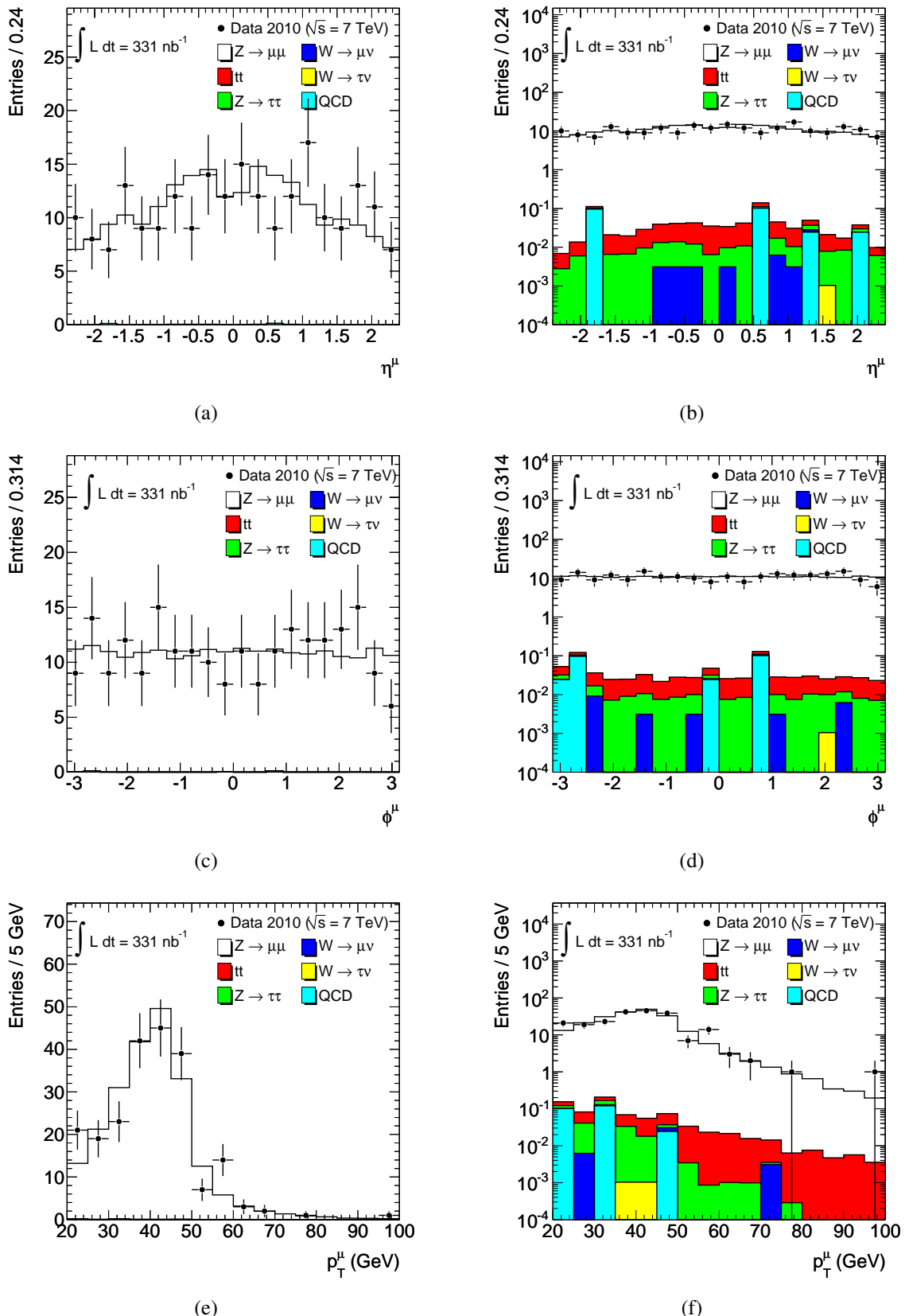
Figure 12.5: Distributions of the muons making up Z candidates after all $Z \rightarrow \mu\mu$ selection. Histograms are scaled by the cross section and normalized to the number of events in data. The number of vertices, trigger and muon reconstruction efficiency scale factors are applied as well as the 0.61 of QCD scaling factor.
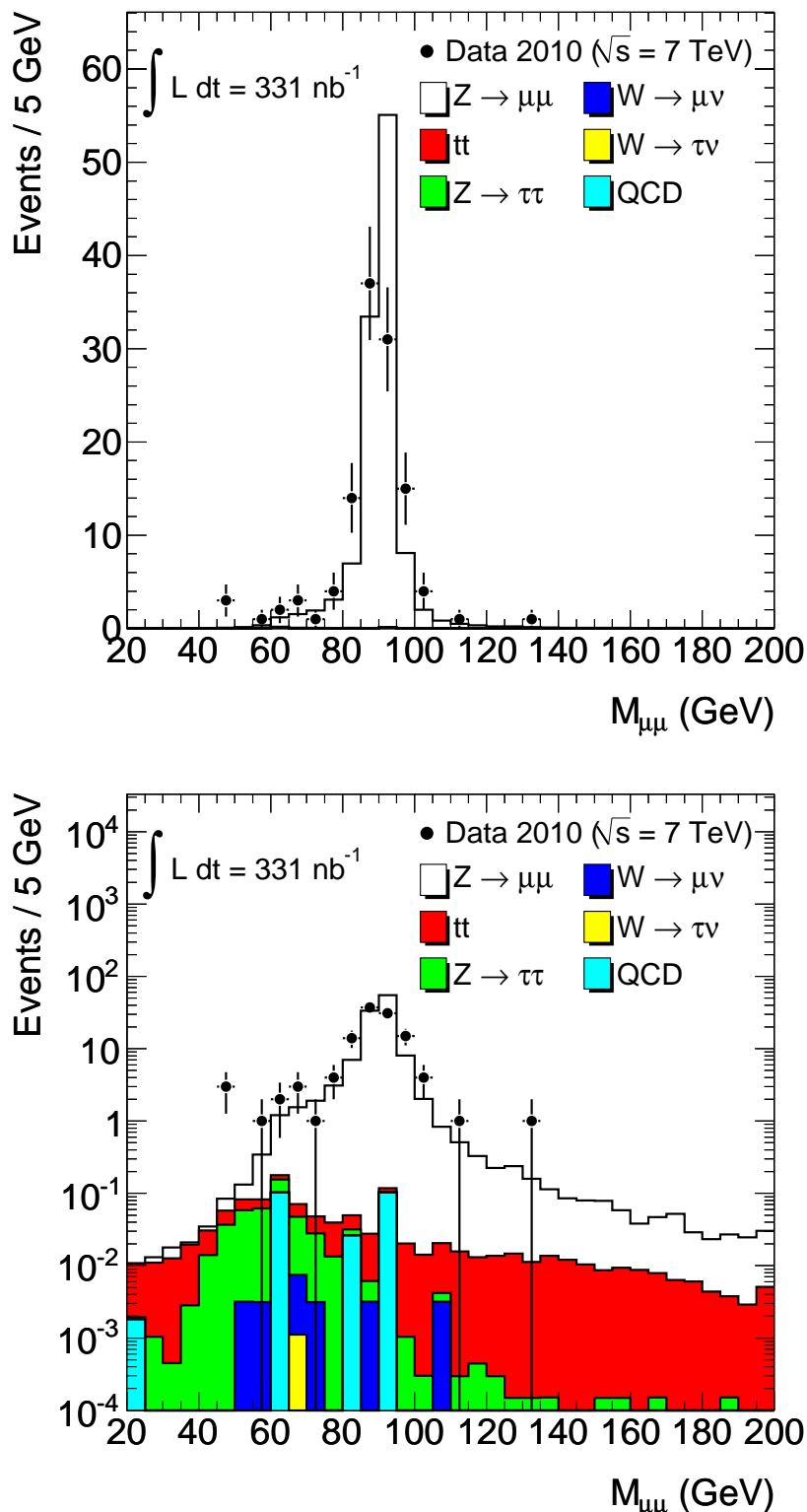
Figure 12.6: $M_{\mu\mu}$ distributions of the muons after all cuts. Histograms are scaled by the cross section and normalized to the number of events in data. The number of vertices, trigger and muon reconstruction efficiency scale factors are applied as well as the 0.61 of QCD scaling factor.

(a)

(b)

(c)

(d)
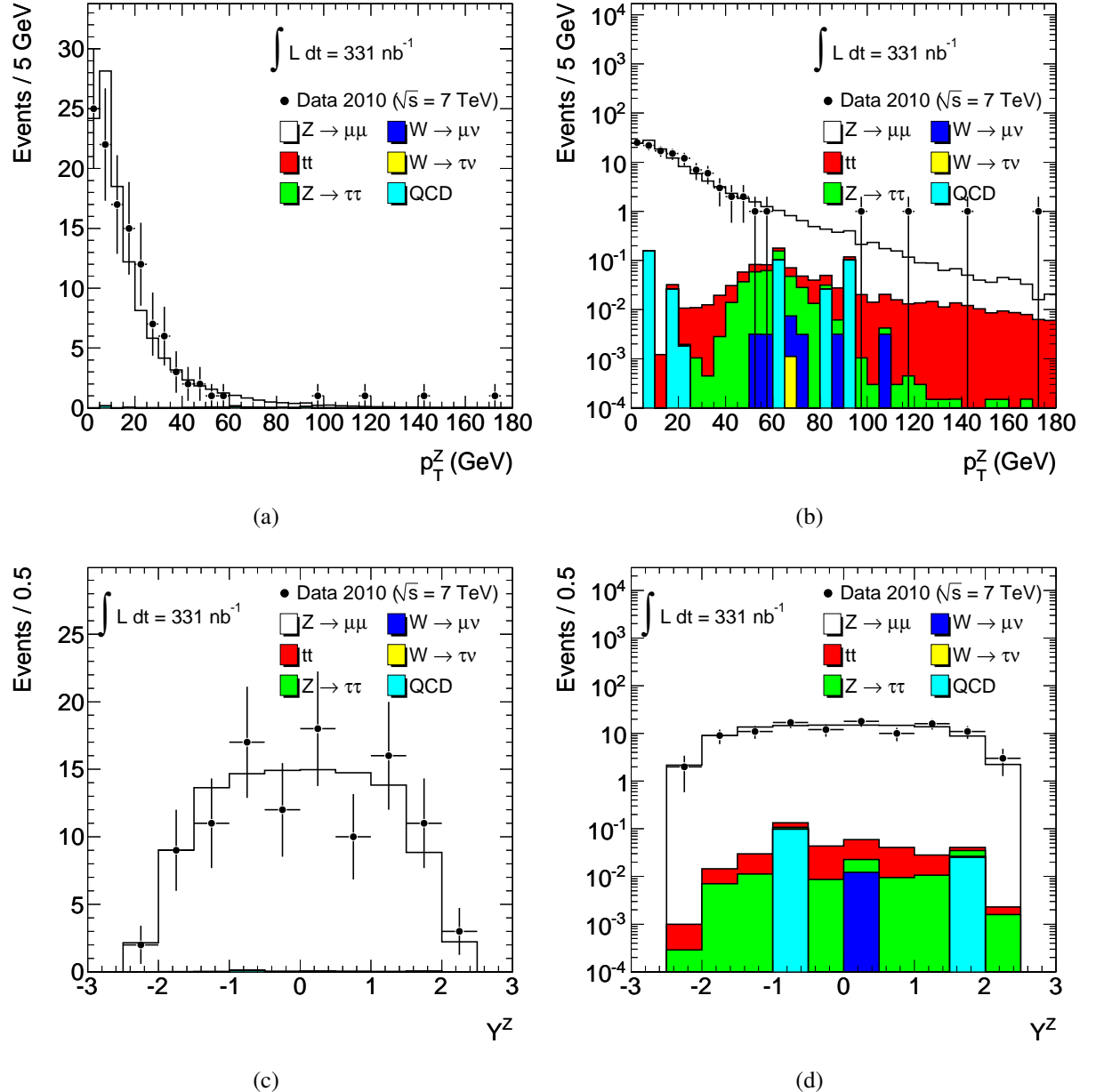
Figure 12.7: p_T and rapidity distribution of the Z-bosons after all selections. Histograms are scaled by the cross section and normalized to the number of events in data. The number of vertices, trigger and muon reconstruction efficiency scale factors are applied as well as the 0.61 of QCD scaling factor.

12.5.4   Cross Section Measurement

The production cross sections times branching ratio of the $Z \to \mu\mu$ process is calculated according to Eq.(12.9) is summarized in Table **12.8**.

$$\sigma_Z \times BR(Z \to \mu\mu) = \frac{N_Z^{obs} - N_Z^{bkg}}{A_Z \cdot C_Z \cdot L_{int}}. \tag{12.9}$$

The 109 $Z \to \mu\mu$ event candidates are observed with an integrated luminosity of 331 nb^{-1} in which 121.9 ± 9.2 events are expected. N_Z^{bkg} are taken from Table **12.5**. A_Z and C_Z are summarized in Table **12.3** with the correction factors applied on them. L_{int} is 331 nb^{-1} with the uncertainty of 11 %.

$$\sigma_{Z/\gamma^*} \times BR(Z/\gamma^* \to \mu^+\mu^-) \quad = \quad 0.87 \pm 0.08 \text{ (stat)} \pm 0.06 \text{ (sys)} \pm 0.10 \text{ (lum)} \quad \text{nb.}$$

Table 12.8: $Z \to \mu\mu$ total and fiducial cross-section measurement.

Figure **12.8** and **12.9** show the comparison of distributions between data and inclusive MC prediction. For MC, the luminosity uncertainty of 11 % is assigned as the error. In these figure, all the scale factors (QCD scaling, number of vertices, trigger and muon reconstruction efficiency) are applied.

(a)

(b)

(c)
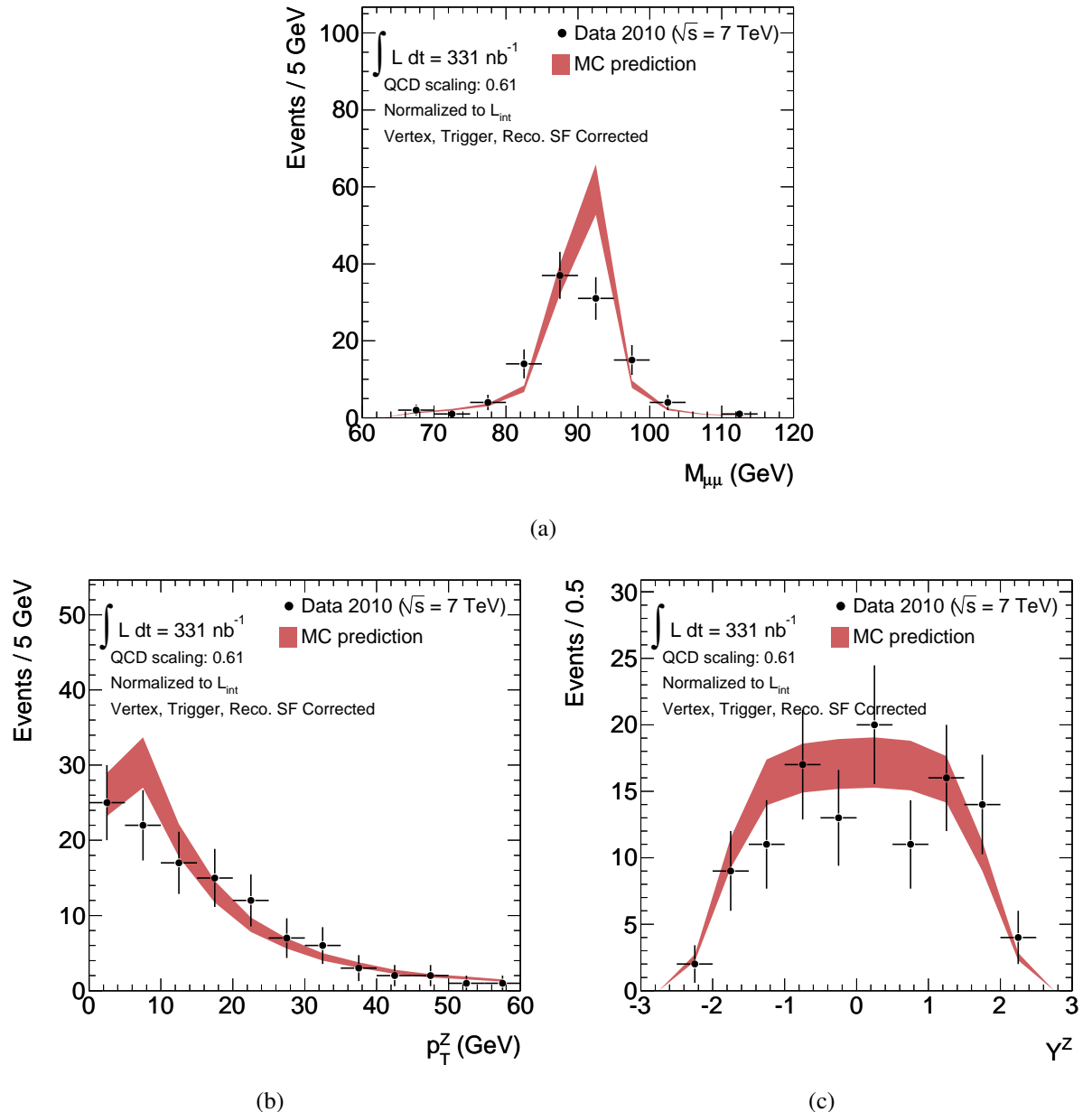
Figure 12.8: $M_{\mu\mu}$ and Z-boson p_T and rapidity distributions after all $Z \to \mu\mu$ selection. The muon pair with $M_{\mu\mu}$ which is the nearest to m_Z is selected. MC prediction is also given as integrated in one histogram with the error of 11 % of luminosity uncertainty. MC prediction is scaled by the cross section and normalized to 331 nb^{-1} of integrated luminosity. The number of vertices, trigger and muon reconstruction efficiency scale factors are applied as well as the QCD scaling factor.
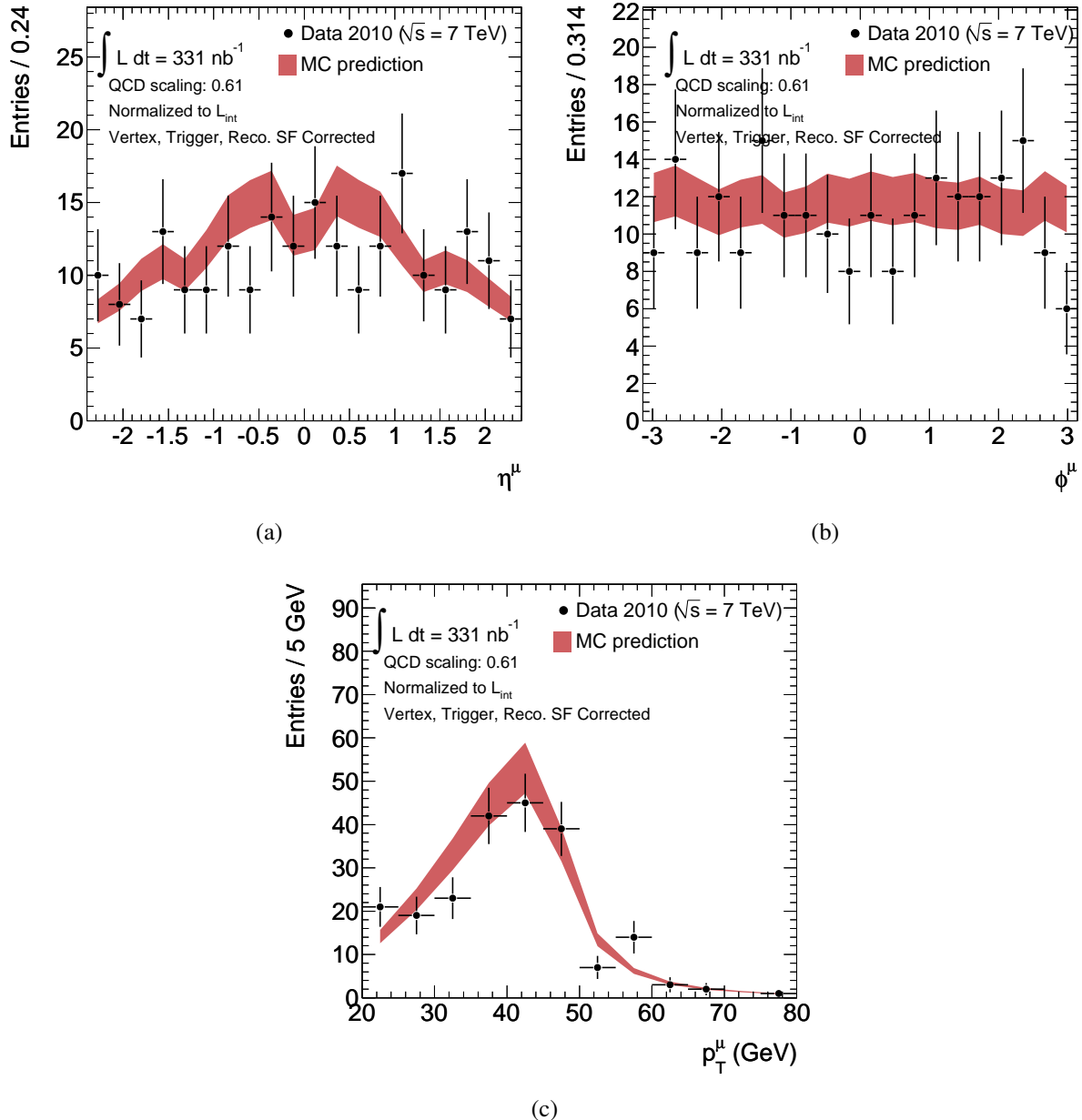
Figure 12.9: η, ϕ and p_{T} distributions of the muons which make up Z-boson candidate after all $Z \to \mu\mu$ selection. The muon pair with $M_{\mu\mu}$ which is the nearest to m_Z GeV is selected. MC prediction is also given as integrated in one histogram with the error of 11 % of luminosity uncertainty. MC prediction is scaled by the cross section and normalized to 331 nb^{-1} of integrated luminosity. The number of vertices, trigger and muon reconstruction efficiency scale factors are applied as well as the QCD scaling factor.

Chapter 13

Discussion and Conclusions

The first measurement of the W and Z-boson production cross sections in proton-proton collisions at $\sqrt{s} = 7$ TeV, the highest center-of-mass energy ever, are performed in the $W \to \mu\nu$ and $Z \to \mu\mu$ processes using the data collected with the ATLAS detector from April to July, 2010. The integrated luminosity used in the $W \to \mu\nu$ analysis is 310 nb^{-1} and in the $Z \to \mu\mu$ analysis is 331 nb^{-1}.

The muon detection efficiency is estimated using the experimental data. The dedicated methods are developed to estimate the efficiencies using single muon tracks since, due to the limited statistics, the yielded number of $Z \to \mu\mu$ events is small.

The muon trigger efficiency is estimated with respect to a reconstructed muon track since one muon track with high transverse momentum is required in both the $W \to \mu\nu$ and $Z \to \mu\mu$ event selection. The efficiency is deduced by counting the number of muon trigger signatures on the path of a given track. The estimation is done using data taken by triggers which are based on the calorimeter information to avoid trigger biases.

The muon reconstruction efficiency is measured with respect to a reconstructed track in the inner detector. The efficiency is deduced by counting the number of tracks in the muon spectrometer which has consistent track parameters with a given muon track's reconstructed in the inner detector. In the estimation, about half the number of the layers in the muon spectrometer are required to be fired on the extrapolated path of the inner detector track to reject non-muon backgrounds.

Event selection criteria for both $W \to \mu\nu$ and $Z \to \mu\mu$ processes are established.

Figure **13.1** shows the distribution of the energy fraction (x) of partons which constitute Z-boson candidates derived from the Z-boson rapidity distribution. The initial transverse momentum of Z-bosons are assumed negligible. The Z-boson flying into the most forward direction is generated with $y_Z = 2.2$, this corresponds to $x = 0.12$ and 0.0014. The previous studies held at the Tevatron [140, 141] measured Z-bosons with $|y_Z| < 2.8$ which corresponds to $x > 0.0028$. The results in this thesis are looking the two times finer parton kinematic region.

Figure **13.2** shows the η distribution for muons in Z-boson events including a parton with x < 0.0038 ($|y_Z| > 2.5$ in the Tevatron). A precise knowledge of the muon spectrometer especially in the endcap region is important to put accurate constraints on PDFs in low-x region.
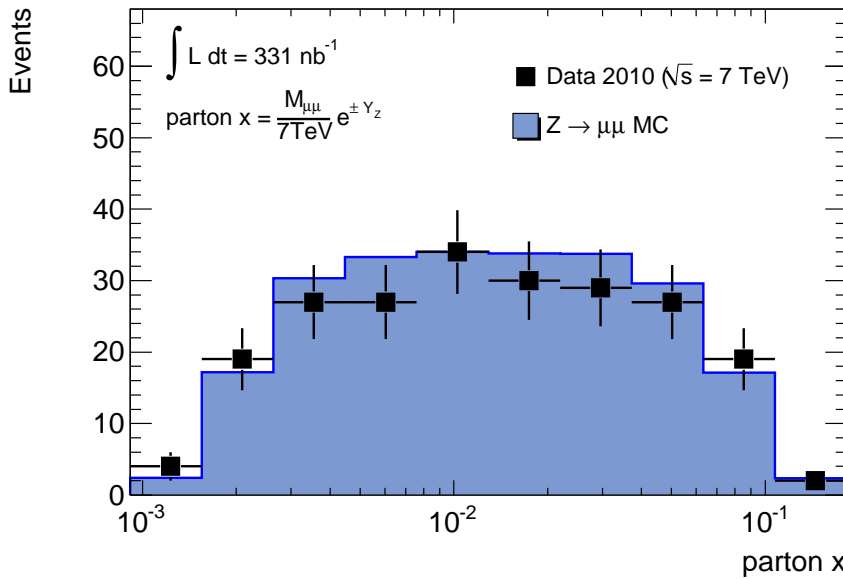
Figure 13.1: (a) Parton *x* distribution in *Z*-boson candidate events obtained from Figure **12.7** (c). The invariant mass of di-muon is used as *Q*. The Monte Calro prediction is normalized to the number of events in data and background components are assumed negligible.
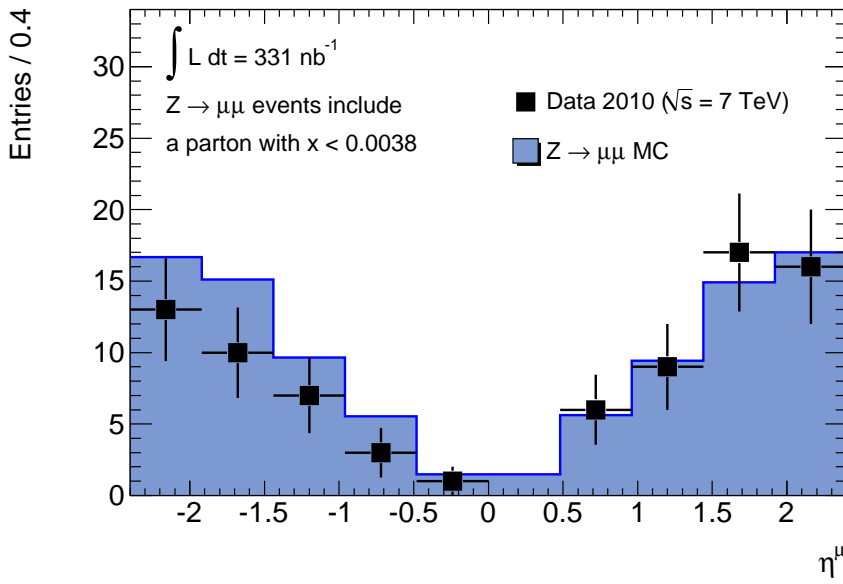
Figure 13.2: η distribution of muons in *Z*-boson candidate events which have a partons with *x* < 0.0038. The Monte Calro prediction is normalized to the number of events in data and background components are assumed negligible.
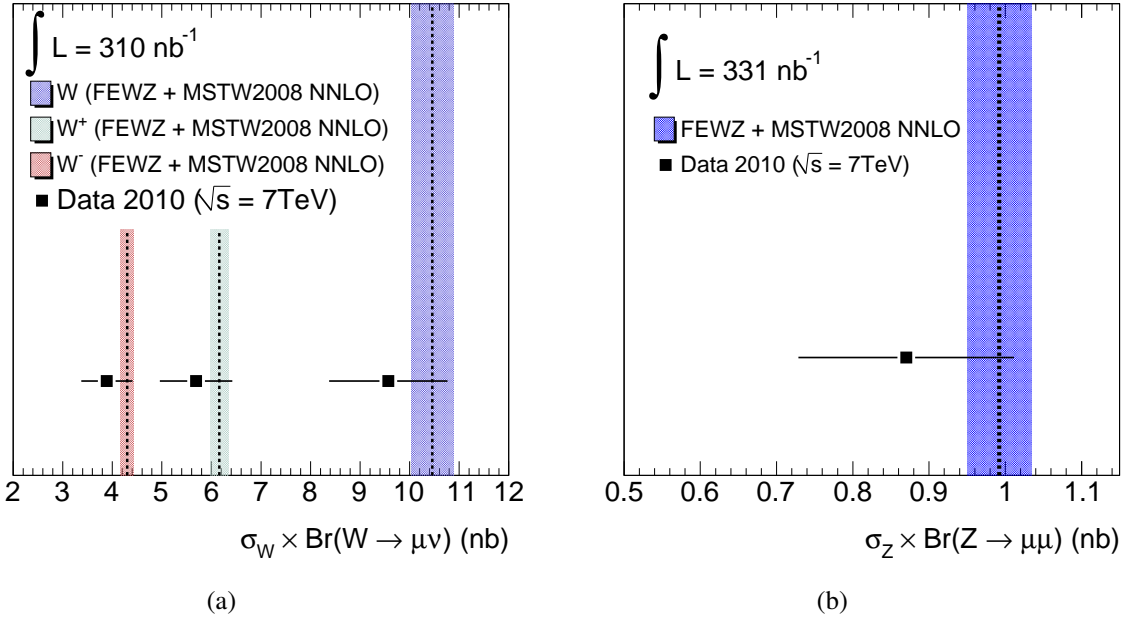
Figure 13.3: Comparisons between the measured cross section times branching ratios and theoretical predictions in (a) $W \to \mu\nu$ (b) $Z \to \mu\mu$ processes.

1181 W-bosons (709 W^+ and 472 W^-) and 109 Z-bosons are observed in data. The $\sigma_W \times BR(W \to \mu\nu)$ are measured with a transverse mass cut of $M_T > 40$ GeV and $\sigma_Z \times BR(Z \to \mu\mu)$ is measured within an invariant mass window of $66 < m_{\mu\mu} < 116$ GeV. The results of both measurements are as follows.

$$\sigma_W \times BR(W \to \mu\nu) = 9.57 \pm 0.31 \text{ (stat)} \pm 0.48 \text{ (syst)} \pm 1.05 \text{ (lumi) nb.}$$
$$\sigma_{W^+} \times BR(W^+ \to \mu^+\nu) = 5.69 \pm 0.23 \text{ (stat)} \pm 0.29 \text{ (syst)} \pm 0.63 \text{ (lumi) nb.}$$
$$\sigma_{W^-} \times BR(W^- \to \mu^-\nu) = 3.87 \pm 0.20 \text{ (stat)} \pm 0.20 \text{ (syst)} \pm 0.43 \text{ (lumi) nb.}$$
$$\sigma_Z \times BR(Z \to \mu\mu) = 0.87 \pm 0.08 \text{ (stat)} \pm 0.06 \text{ (syst)} \pm 0.10 \text{ (lumi) nb.}$$

The next-to-next-to leading order QCD theoretical predictions are obtained as

$$\sigma_W \times BR(W \to \ell\nu) = 10.46 \pm 0.52 \text{ nb.}$$
$$\sigma_W \times BR(W^+ \to \ell^+\nu) = 6.16 \pm 0.31 \text{ nb.}$$
$$\sigma_W \times BR(W^- \to \ell^-\nu) = 4.30 \pm 0.21 \text{ nb.}$$
$$\sigma_Z \times BR(Z \to \ell\ell) = 0.96 \pm 0.05 \text{ nb.}$$

For a description of the calculation method, see section 4.7.2.

Shown in Figure **13.3** (a) is a comparison between the yielded $\sigma_W \times BR(W \to \mu\nu)$ and the theoretical predictions. The results for W^+ and W^- are also shown separately. The asymmetry between the positive and negative charged W-bosons is interpreted as comes from the asymmetry in the number of valence u and d quark constituens in protons colliding at $\sqrt{s} = 7$ TeV. All the results, including the charge asymmetry, are consistent with the theoretical prediction.

Shown in Figure **13.3** (b) is a comparison between the measured $\sigma_Z \times BR(Z \to \mu\mu)$ and the theoretical prediction. The result agrees well with the theoretical prediction within the error.

Shown in Figure **13.4** and **13.5** are the W/Z-boson production cross sections times branching ratios as a function of $\sqrt{s}$. The results of the previous measurements by the UA1 and UA2 experiments at the CERN Sp$\bar{\text{p}}$S, by the CDF and D0 experiments at the Fermilab Tevatron and by the PHENIX experiment at the RHIC are also shown in both figures. Along with the results by the previous experiments, the energy dependence of the W/Z-boson production cross section is also well described.

Though the statistics is limited, the uncertainties of the W/Z cross sections measurement is already dominated by the systematic components.

The largest source is the 11 % uncertainty in the luminosity measurement. This mainly comes from an inaccuracy in the proton beam current measurement and expected to be improved with more dedicated measurements. Also the preparation of the absolute luminosity calibration using the ALFA detector is on going. As described in section 4.5.2, the ALFA detector provide an accurate absolute luminosity calibration measuring elastic proton-proton scattering at small angles in the Coulomb-Nuclear Interference region. The expected accuracy of the calibration is about 3 %.

The second largest systematic source is the uncertainty on the muon detection efficiency. The major contributions are coming from the contamination of the decay-in-flight muons and lack of statistics. These are expected to be improved significantly with more statistics of $Z \rightarrow \mu\mu$ samples. The $Z \rightarrow \mu\mu$ study in this thesis shows that expected background in the $Z \rightarrow \mu\mu$ event selection is below % level. As for statistics, assuming 10 fb^{-1} of data, the 10^7 muon samples from the $Z \rightarrow \mu\mu$ events are expected within the detector acceptance. This leads to a precise muon detection efficiency estimation in a phase-space dependent manner.

Another large systematic source comes from the acceptance calculation (3 % for $W \rightarrow \mu\nu$, 4 % for $Z \rightarrow \mu\mu$). This is dominated by the uncertainty on PDFs in low-x region (2.1 % (W), 2.6 % (Z)) and the W/Z-boson production modeling (1.6 % (W), 2.8 % (Z)). A study shows that, provided well estimated muon detection efficiency, the uncertainty on PDFs improve by a factor of 30 with 10 fb^{-1} of data [46]. The usage of PYTHIA, a leading order event generator, limits the accuracy of the W/Z-boson production modeling. Hence the preparation of the Monte Calro production with a next-to leading order generator is on going and this will improve the situation. Furthermore, the modeling will improve by the feedback from the measurement of an accurate p_T distribution of Z-bosons foreseen in the near future.

In this thesis, muon detection efficiency estimations using the $Z \rightarrow \mu\mu$ process are performed. These are the first trials of the detector calibrations with the $Z \rightarrow \mu\mu$ process. The $Z \rightarrow \mu\mu$ process plays a central role in the precise calibration of both the detector and Monte Calro simulations. These lead to precise electroweak measurements which make a major objective for the ATLAS. A representative measurement is of the W-boson mass. The ATLAS is expected to have a potential to measure the W-boson mass with better than 10 MeV accuracy [46]. This leads to a new indirect constraints on the Higgs boson mass and the properties of the SUSY particles. Furthermore, well constrained PDFs provide a solid basis for every physics analysis and searches performed at the ATLAS. As such, the works in this thesis constitute the first major step for the lasting physics program at the ATLAS.
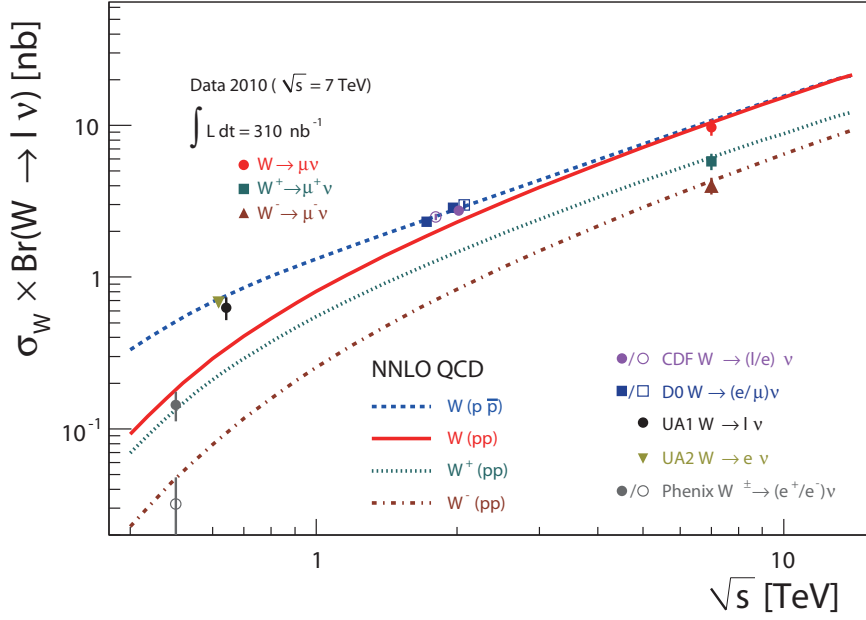
Figure 13.4: Comparison between the measured production cross section times branching ratios for $W \rightarrow \mu\nu$ channels in this thesis with $M_T > 40$ GeV and theoretical predictions including next-to-next-to-leading order QCD corrections. The results of the previous experiments are also shown.
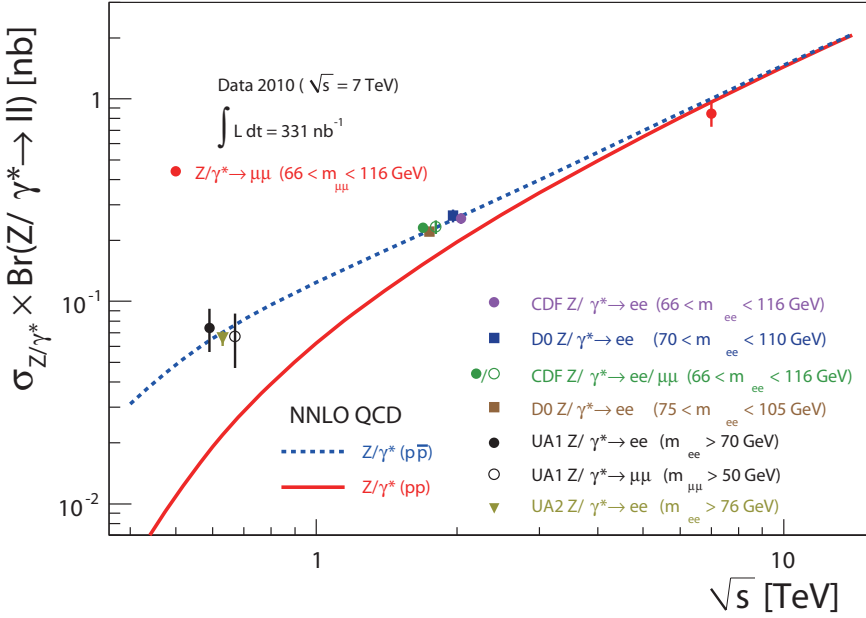
Figure 13.5: Comparison between the measured production cross section times branching ratios for $Z \rightarrow \mu\mu$ channel in this thesis with $66 < m_{\mu\mu} < 116$ GeV and theoretical predictions including next-to-next-to-leading order QCD corrections. The results of the previous experiments are also shown.

Acknowledgments

There are a number of people without whom this thesis would not have been written, and to whom I am greatly indebted.

First of all, I wish to express my sincere thankfulness to my supervisor, Prof. Satoru Yamashita for continuously encouraging and advising me throughout five years of my Ph.D. course. His true love for physics and attitude to open new frontiers, which is not limited within particle physics, have affected me so much. He have always respected his duty of education and guided my primitive curiosities into right directions. It is my great fortune that I have been able to spend my Ph.D course so close to him as his first doctoral student. I am also very grateful to his wife Ms. Fumiyo Yamashita and his daughter Ms. Mayura Yamashita to allow me to discuss with him by phone even around midnight and served the members of our laboratory great dinners many times.

I deeply appreciate Prof. Hiroshi Sakamoto for his constant support over my Ph.D. period. When my study was going well or I was stumbled by a difficulty, his kind and patient assistance always helped me a lot. The home party to which he kindly invited me is a very good memory with delicious dishes prepared by his wife Ms. Riyoko Sakamoto.

I would like to express my gratitude to the director of the International Center of Elementary Particle Physics (ICEPP), Prof. Sachio Komamiya. All the achievement in my study have been made as a student of ICEPP and they are obviously based on his tireless effort as the director. I am also truly thankful to co-spokespersons of the ATLAS Japan group, Prof. Takahiko Kondo, Prof. Tomio Kobayashi and Prof. Katsuo Tokushuku for giving me this excellent opportunity to participate in the great experiment.

I am very grateful to Dr. Nicolas Norman Ellis for becoming my supervisor at CERN. He gave me variety of important advices on my study and career as a researcher and his warmth encouraged me to carry on my study.

Joao Guimaraes da Costa, a co-convener of the W/Z-boson working group at the ATLAS, taught me so many things starting from basic techniques for data analyses. We have discussed a lot for the W/Z cross sections measurement with muons. I really appreciate him for kindly teaching me as if I am one of his students.

I would like to thank members of the University of Tokyo team. Prof. Tatsuo Kawamoto for taking care of many aspects of my life at CERN, such as how to refueling a car or how to pay fines for speeding. Prof. Shoji Asai for kindly arranging my presentation at the ATLAS Japan physics meetings. Prof. Ikuo Ueda, Prof. Junichi Tanaka and Prof. Shimpei Yamamoto for administrating excellent computing facility at CERN. Prof. Naoko Kanaya for many discussions

Bibliography

[1]   C. W. Fabjan and T. Ludlam, *CALORIMETRY IN HIGH-ENERGY PHYSICS*, Ann. Rev. Nucl. Part. Sci. **32** (1982), 335–389.

[2]   *Performance of primary vertex reconstruction in proton-proton collisions at $\sqrt{s}$ =7 TeV in the ATLAS experiment*, Technical Report ATLAS-CONF-2010-069, CERN, Geneva, 2010.

[3]   Steven Weinberg, *A Model of Leptons*, Phys. Rev. Lett. **19** (1967), 1264–1266.

[4]   A Salam, *Elementary Particle Physics*, N.Svartholm.ed. (Nobel Symposium No.8, Almqvist and Wiksell, Stockholm 1968).

[5]   Peter W. Higgs, *Broken symmetries, massless particles and gauge fields*, Phys. Lett. **12** (1964), 132–133.

[6]   Peter W. Higgs, *Spontaneous Symmetry Breakdown without Massless Bosons*, Phys. Rev. **145** (1966), 1156–1163.

[7]   R. Barate et al., *Search for the standard model Higgs boson at LEP*, Phys. Lett. **B565** (2003), 61–75, available at `hep-ex/0306033`.

[8]   B Kilminster, *Higgs boson searches at the Tevatron*, presented at ICHEP 2010, Paris, France, 22 - 28 July, 2010 (`http://indico.cern.ch/contributionDisplay.py?contribId=82&sessionId=13&confId=73513`).

[9]   R. Brandelik et al., *Evidence for Planar Events in e+ e- Annihilation at High- Energies*, Phys. Lett. **B86** (1979), 243.

[10]   D. P. Barber et al., *Discovery of Three Jet Events and a Test of Quantum Chromodynamics at PETRA Energies*, Phys. Rev. Lett. **43** (1979), 830.

[11]   W. Bartel et al., *Observation of Planar Three Jet Events in e+ e- Annihilation and Evidence for Gluon Bremsstrahlung*, Phys. Lett. **B91** (1980), 142.

[12]   Christoph Berger et al., *Evidence for Gluon Bremsstrahlung in e+ e- Annihilations at High-Energies*, Phys. Lett. **B86** (1979), 418.

[13]   Elliott D. Bloom et al., *High-Energy Inelastic e p Scattering at 6-Degrees and 10- Degrees*, Phys. Rev. Lett. **23** (1969), 930–934.

[14]   Martin Breidenbach et al., *Observed Behavior of Highly Inelastic electron-Proton Scattering*, Phys. Rev. Lett. **23** (1969), 935–939.

[15]   T. Eichten et al., *MEASUREMENT OF THE NEUTRINO - NUCLEON ANTI-NEUTRINO - NUCLEON TOTAL CROSS-SECTIONS*, Phys. Lett. **B46** (1973), 274–280.

[16]   J. D. Bjorken, *Asymptotic Sum Rules at Infinite Momentum*, Phys. Rev. **179** (1969), 1547–1553.

[17]   Richard P. Feynman, *Very high-energy collisions of hadrons*, Phys. Rev. Lett. **23** (1969), 1415–1417.

[18]   Yuri L. Dokshitzer, *Calculation of the Structure Functions for Deep Inelastic Scattering and e+ e- Annihilation by Perturbation Theory in Quantum Chromodynamics*, Sov. Phys. JETP **46** (1977), 641–653.

[19]   V. N. Gribov and L. N. Lipatov, Sov.J.Nucl.Phys. **15** (1972), 438.

[20] Guido Altarelli and G. Parisi, *Asymptotic Freedom in Parton Language*, Nucl. Phys. **B126** (1977), 298.

[21] S. Heinemeyer, W. Hollik, D. Stockinger, A. M. Weber, and G. Weiglein, *Precise prediction for M(W) in the MSSM*, JHEP **08** (2006), 052, available at `hep-ph/0604147`.

[22] S. Heinemeyer, W. Hollik, and G. Weiglein, *Electroweak precision observables in the minimal supersymmetric standard model*, Phys.Rept. **425** (2006), 265–368, available at `hep-ph/0412214`.

[23] A. Djouadi, P. Gambino, S. Heinemeyer, W. Hollik, C. Junger, et al., *Supersymmetric contributions to electroweak precision observables: QCD corrections*, Phys.Rev.Lett. **78** (1997), 3626–3629, available at `hep-ph/9612363`.

[24] B. Adeva et al., *A Determination of the Properties of the Neutral Intermediate Vector Boson Z^0*, Phys. Lett. **B231** (1989), 509.

[25] D. Decamp et al., *Determination of the Number of Light Neutrino Species*, Phys. Lett. **B231** (1989), 519.

[26] M. Z. Akrawy et al., *Measurement of the Z^0 Mass and Width with the OPAL Detector at LEP*, Phys. Lett. **B231** (1989), 530.

[27] P. A. Aarnio et al., *Measurement of the Mass and Width of the Z^0 Particle from Multi - Hadronic Final States Produced in e^+e^- Annihilations*, Phys. Lett. **B231** (1989), 539.

[28] Makoto Kobayashi and Toshihide Maskawa, *cp-violation in the renormalizable theory of weak interaction*, Progress of Theoretical Physics **49** (1973), no. 2, 652–657.

[29] H. Weyl, *Electron and gravitation*, Z. Phys. **56** (1929), 330–352.

[30] S. Tomonaga, *On a relativistically invariant formulation of the quantum theory of wave fields*, Prog. Theor. Phys. **1** (1946), 27–42.

[31] S. Tomonaga, *On a relativistically invariant formulation of the quantum theory of wave fields. II*, Prog. Theor. Phys. **2** (1947), 101–116.

[32] S. Tomonaga, *On a relativistically invariant formulation of the quantum theory of wave fields. III*, Prog. Theor. Phys. **2** (1947), 198–208.

[33] Julian S. Schwinger, *On Quantum electrodynamics and the magnetic moment of the electron*, Phys. Rev. **73** (1948), 416–417.

[34] Julian S. Schwinger, *Quantum electrodynamics. I: A covariant formulation*, Phys. Rev. **74** (1948), 1439.

[35] R. P. Feynman, *Relativistic cutoff for quantum electrodynamics*, Phys. Rev. **74** (1948), 1430–1438.

[36] K Nakamura *et al.* (Particle Data Group), *The Review of Particle Physics*, J. Phys. G **37** (2010), 075021.

[37] Y Nagashima, *The standard model of the elemental particle physics and experimental foundation*, Asakura Publishing Co., Ltd, 1999.

[38] T. Muta, *Foundations of quantum chromodynamics: An Introduction to perturbative methods in gauge theories*, World Sci. Lect. Notes Phys. **5** (1987), 1–409.

[39] R. D. Field, *Applications of Perturbative QCD*, Front. Phys. **77** (1989), 1–366.

[40] D. J. Gross and Frank Wilczek, *ULTRAVIOLET BEHAVIOR OF NON-ABELIAN GAUGE THEORIES*, Phys. Rev. Lett. **30** (1973), 1343–1346.

[41] H. David Politzer, *RELIABLE PERTURBATIVE RESULTS FOR STRONG INTERACTIONS?*, Phys. Rev. Lett. **30** (1973), 1346–1349.

[42] S. Chekanov et al., *A ZEUS next-to-leading-order QCD analysis of data on deep inelastic scattering*, Phys. Rev. **D67** (2003), 012007, available at `hep-ex/0208023`.

[43] John C. Collins and Davison E. Soper, *The Theorems of Perturbative QCD*, Ann. Rev. Nucl. Part. Sci. **37** (1987), 383–409.

[44] J Stirling, *MSTW PDFs (*`http://projects.hepforge.org/mstwpdf/plots/plots.html`*).*

[45] G. Aad et al., *Expected Performance of the ATLAS Experiment - Detector, Trigger and Physics* (2009), available at `0901.0512`.

[46] Nathalie Besson, Maarten Boonekamp, Esben Klinkby, Sascha Mehlhase, and Troels Petersen, *Re-evaluation of the LHC potential for the measurement of Mw*, Eur.Phys.J. **C57** (2008), 627–651, available at `0805.2093`.

[47] J. Alcaraz et al., *A Combination of preliminary electroweak measurements and constraints on the standard model* (2006), available at `hep-ex/0612034`.

[48] *Updated Combination of CDF and D0 Results for the Mass of the W Boson* (2009), available at `0908.1374`.

[49] J.C. Collins, Davison E. Soper, and George Sterman, *Transverse momentum distribution in Drell-Yan pair and W and Z boson production*, Nuclear Physics B **250** (1985), no. 1-4, 199 –224.

[50] F. Landry, R. Brock, P. M. Nadolsky, and C.-P. Yuan, *Fermilab tevatron run-1 z boson data and the collins-soper-sterman resummation formalism*, Phys. Rev. D **67** (2003Apr), no. 7, 073016.

[51] C. Balázs and C.-P. Yuan, *Soft gluon effects on lepton pairs at hadron colliders*, Phys. Rev. D **56** (1997Nov), no. 9, 5558–5583.

[52] C. Albajar et al., *Intermediate Vector Boson Cross-Sections at the CERN Super Proton Synchrotron Collider and the Number of Neutrino Types*, Phys. Lett. **B198** (1987), 271.

[53] J. Alitti et al., *A Measurement of the W and Z production cross-sections and a determination of Gamma (W) at the CERN $\bar{p}p$ collider*, Phys. Lett. **B276** (1992), 365–374.

[54] F. Abe et al., *Measurement of $\sigma b(w \rightarrow ev)$ and $\sigma b(z^0 \rightarrow e^+e^-)$ in $p\bar{p}$ collisions at $\sqrt{s}$ = 1.8 tev*, Phys. Rev. Lett. **76** (1996Apr), no. 17, 3070–3075.

[55] F. Abe et al., *Measurement of Z^0 and Drell-Yan production cross section using dimuons in $\bar{p}p$ collisions at $\sqrt{s}$ = 1.8 TeV*, Phys. Rev. **D59** (1999), 052002.

[56] A. Abulencia et al., *Measurements of Inclusive W and Z Cross Sections in p-pbar Collisions at $\sqrt{s}$ =1.96 TeV*, J. Phys. **G34** (2007), 2457–2544, available at `hep-ex/0508029`.

[57] B. Abbott et al., *Extraction of the width of the W boson from measurements of $\sigma(p\bar{p} \rightarrow W + X) \times B(W \rightarrow ev)$ and $\sigma(p\bar{p} \rightarrow Z + X) \times B(Z \rightarrow ee)$ and their ratio*, Phys. Rev. **D61** (2000), 072001, available at `hep-ex/9906025`.

[58] The D0 Collaboration, D0 conference notes **4403-CONF, 4750-CONF**.

[59] A. Adare et al., *Cross Section and Parity Violating Spin Asymmetries of $W^\pm$ Boson Production in Polarized p+p Collisions at $\sqrt{s}$=500 GeV* (2010), available at `1009.0505`.

[60] M. M. Aggarwal et al., *Measurement of the parity-violating longitudinal single- spin asymmetry for $W^\pm$ boson production in polarized proton-proton collisions at $\sqrt{s}$ = 500GeV* (2010), available at `1009.0326`.

[61] Oliver Simon Brning, Paul Collier, P Lebrun, Stephen Myers, Ranko Ostojic, John Poole, and Paul Proud-lock, *LHC Design Report Vol.1*, CERN, Geneva, 2004.

[62] Oliver Simon Brning, Paul Collier, P Lebrun, Stephen Myers, Ranko Ostojic, John Poole, and Paul Proud-lock, *LHC Design Report Vol.2*, CERN, Geneva, 2004.

[63] Michael Benedikt, Paul Collier, V Mertens, John Poole, and Karlheinz Schindl, *LHC Design Report Vol.3*, CERN, Geneva, 2004.

[64] Lyndon Evans (ed.) and Philip Bryant (ed.), *LHC Machine*, JINST **3** (2008), S08001.

[65] *The Large Hadron Collider: Conceptual design.* CERN-AC-95-05-LHC.

[66] *ATLAS: technical proposal for a general-purpose pp experiment at the Large Hadron Collider at CERN*, LHC Tech. Proposal.

[67] *Technical proposal*, LHC Tech. Proposal. Cover title : CMS, the Compact Muon Solenoid : technical proposal.

[68] O Adriani, L Bonechi, M Bongi, R D'ALessandro, D A Faus, M Haguenauer, Y Itow, K Kasahara, K Masuda, Y Matsubara, H Menjo, Y Muraki, P Papini, T Sako, T Tamura, S Torii, A Tricomi, W C Turner, J Velasco, and K Yoshida, *Lhcf experiment: Technical design report*, Technical Design Report LHCf, CERN, Geneva, 2006.

[69] *LHCb : Technical Proposal*, Tech. Proposal, CERN, Geneva, 1998.

[70] *TOTEM: Total cross section, elastic scattering and diffraction dissociation at the LHC: Technical Proposal*. CERN-LHCC-99-07.

[71] *ALICE: Technical proposal for a Large Ion collider Experiment at the CERN LHC*, LHC Tech. Proposal, CERN, Geneva, 1995.

[72] G. Aad et al., *The ATLAS Experiment at the CERN Large Hadron Collider*, JINST **3** (2008), S08003.

[73] *ATLAS detector and physics performance: Technical Design Report, 1*, Technical Design Report ATLAS, CERN, Geneva, 1999. Electronic version not available.

[74] S Haywood, L Rossi, R Nickerson, and A Romaniouk, *ATLAS inner detector: Technical Design Report, 2*, Technical Design Report ATLAS, CERN, Geneva, 1997.

[75] *ATLAS calorimeter performance: Technical Design Report*, Technical Design Report ATLAS, CERN, Geneva, 1996.

[76] *ATLAS muon spectrometer: Technical Design Report*, Technical Design Report ATLAS, CERN, Geneva, 1997. distribution.

[77] H van der Graaf, H Groenstege, F Linde, and P Rewiersma, *Rasnik, an alignment system for the atlas mdt barrel muon chambers: Technical system description; revised version 2.0*, NIKHEF, Amsterdam, 2000.

[78] Hasko Stenzel, *Luminosity calibration from elastic scattering*. ATL-LUM-PUB-2007-001.

[79] Peter Jenni and Marzio Nessi, *ATLAS Forward Detectors for Luminosity Measurement and Monitoring*, Technical Report CERN-LHCC-2004-010. LHCC-I-014, CERN, Geneva, 2004. revised version number 1 submitted on 2004-03-22 14:56:11.

[80] *ATLAS first-level trigger: Technical design report*. CERN-LHCC-98-14.

[81] *ATLAS high-level trigger, data acquisition and controls: Technical design report*. CERN-LHCC-2003-022.

[82] *The ATLAS Simulation Infrastructure*, Eur. Phys. J. C (2010), available at `1005.4568`. Long author list - awaiting processing.

[83] Torbjorn Sjostrand, Stephen Mrenna, and Peter Z. Skands, *PYTHIA 6.4 Physics and Manual*, JHEP **05** (2006), 026, available at `hep-ph/0603175`.

[84] Stefano Frixione, Paolo Nason, and Carlo Oleari, *Matching NLO QCD computations with Parton Shower simulations: the POWHEG method*, JHEP **11** (2007), 070, available at `0709.2092`.

[85] D Bourilkov, R C Group, and M R Whalley, *LHAPDF: PDF use from the Tevatron to the LHC* (2006), available at `hep-ph/0605240`.

[86] Wu-Ki Tung, H. L. Lai, J. Pumplin, Pavel M. Nadolsky, and C. P. Yuan, *Global QCD Analysis and Collider Phenomenology–CTEQ* (2007), available at `0707.0275`.

[87] Matt Dobbs and Jorgen Beck Hansen, *The HepMC C++ Monte Carlo event record for High Energy Physics*, Comput. Phys. Commun. **134** (2001), 41–46.

[88] S. Agostinelli et al., *GEANT4: A simulation toolkit*, Nucl. Instrum. Meth. **A506** (2003), 250–303.

[89] Anastasiou Melnikov K Petriello F, *Electroweak gauge boson production at hadron colliders through o(alpha(s)**2)*, Phys. Rev. **D74** (2006), 114017, available at `hep-ph/0609070`.

[90] Petriello Y Gavin R Li Y, *Fewz 2.0: A code for hadronic z production at next-to-next-to-leading order* (2010), available at `hep-ph/1011.3540`.

[91] A. D. Martin, W. J. Stirling, R. S. Thorne, and G. Watt, *Parton distributions for the LHC*, Eur. Phys. J. **C63** (2009), 189–285, available at `0901.0002`.

[92] U. Langenfeld, S. Moch, and P. Uwer, *Measuring the running top-quark mass*, Phys. Rev. **D80** (2009), 054009, available at `0906.5273`.

[93] A. Sherstnev and R. S. Thorne, *Parton Distributions for LO Generators*, Eur. Phys. J. **C55** (2008), 553–575, available at `0711.2473`.

[94] S. Ask et al., *The ATLAS central level-1 trigger logic and TTC system*, JINST **3** (2008), P08002.

[95] O. Sasaki and M. Yoshida, *Asd ic for the thin gap chambers in the lhc atlas experiment*, Nuclear Science, IEEE Transactions on **46** (1999dec.), no. 6, 1871 –1875.

[96] G. Aielli et al., *The RPC first level muon trigger in the barrel of the ATLAS experiment*, Nucl. Phys. Proc. Suppl. **158** (2006), 11–15.

[97] R. Vari, F. Pastore, E. Petrolo, and S. Veneziano, *Performances of the coincidence matrix ASIC of the ATLAS barrel level-1 muon trigger*. Prepared for 11th Workshop on Electronics for LHC and Future Experiments (LECC 2005), Heidelberg, Germany, 12-16 September 2005.

[98] V. Bocci et al., *The sector logic demonstrator of the level-1 muon barrel trigger of the ATLAS experiment*. Prepared for 7th Workshop on Electronics for LHC Experiments, Stockholm, Sweden, 10-14 Sep 2001.

[99] P F Akesson, T Atkinson, M J Costa, M Elsing, S Fleischmann, A N Gaponenko, W Liebig, E Moyse, A Salzburger, and M Siebel, *ATLAS Tracking Event Data Model*, Technical Report ATL-SOFT-PUB-2006-004. ATL-COM-SOFT-2006-005. CERN-ATL-COM-SOFT-2006-005, CERN, Geneva, 2006.

[100] T G Cornelissen, N Van Eldik, M Elsing, W Liebig, E Moyse, N Piacquadio, K Prokofiev, A Salzburger, and A Wildauer, *Updates of the ATLAS Tracking Event Data Model (Release 13)*, Technical Report ATL-SOFT-PUB-2007-003. ATL-COM-SOFT-2007-008, CERN, Geneva, 2007.

[101] F Akesson, M J Costa, D Dobos, M Elsing, S Fleischmann, A Gaponenko, K Gnanvo, P T Keener, W Liebig, E Moyse, A Salzburger, M Siebel, and A Wildauer, *ATLAS Inner Detector Event Data Model*, Technical Report ATL-SOFT-PUB-2007-006. ATL-COM-SOFT-2007-015, CERN, Geneva, 2007.

[102] P. V. C. Hough, *General Purpose Visual Input for a Computer*, Annals of the New York Academy of Sciences **99** (June 1962), 323–337.

[103] P. Hough and B. Powell, *A method for faster analysis of bubble chamber photographs*, Il Nuovo Cimento (1955-1965) **18** (1960), 1184–1191. 10.1007/BF02733175.

[104] T Cornelissen, M Elsing, S Fleischmann, W Liebig, E Moyse, and A Salzburger, *Concepts, Design and Implementation of the ATLAS New Tracking (NEWT)*, Technical Report ATL-SOFT-PUB-2007-007. ATL-COM-SOFT-2007-002, CERN, Geneva, 2007.

[105] M Elsing, I Gavrilenko, G Gorfine, V Kartvelishvili, T Koffas, V Kostyukhin, J S H Lee, W Liebig, A Morley, N G Piacquadio, K Prokofiev, A Wildauer, and H Zhu, *Atlas detector paper back-up note: Electrons and photons*, Technical Report ATL-INDET-PUB-2008-013. ATL-COM-INDET-2008-010, CERN, Geneva, 2008.

[106] R. Frohwirth, *Application of kalman filtering to track and vertex fitting*, Nuclear Instruments and Methods in Physics Research Section A: Accelerators, Spectrometers, Detectors and Associated Equipment **262** (1987), no. 2-3, 444 –450.

[107] D Wicke, *A New Algorithm For Solving Track Ambiguities*, DELPHI 98-163, PROG 236 TRACK 92 (1998).

[108] R. Frohwirth, A. Strandlie, T. Todorov, and M. Winkler, *Recent results on adaptive track and multitrack fitting*, Nuclear Instruments and Methods in Physics Research Section A: Accelerators, Spectrometers, Detectors and Associated Equipment **502** (2003), no. 2-3, 702 –704. Proceedings of the VIII International Workshop on Advanced Computing and Analysis Techniques in Physics Research.

[109] S Fleischmann and P Mattig, *Track Reconstruction in the ATLAS Experiment: The Deterministic Annealing Filter*, Ph.D. Thesis, Wuppertal, 2006. Presented on 19 Oct 2006.

[110] Th Lagouri, *A Muon Identification and Combined Reconstruction Procedure for the ATLAS Detector at the LHC at CERN*. ATL-SLIDE-2003-007.

[111] Th Lagouri et al., *A muon identification and combined reconstruction procedure for the ATLAS detector at the LHC at CERN*, IEEE Trans. Nucl. Sci. **51** (2004), 3030–3033.

[112] T. Lagouri, *Muon identification and reconstruction in ATLAS*. MPI-PHE-99-18.

[113] S. Hassani et al., *A muon identification and combined reconstruction procedure for the ATLAS detector at the LHC using the (MUONBOY, STACO, MuTag) reconstruction packages*, Nucl. Instrum. Meth. **A572** (2007), 77–79.

[114] R Nicolaidou, L Chevalier, S Hassani, J F Laporte, E Le Menedeu, and A Ouraou, *Muon identification procedure for the atlas detector at the lhc using muonboy reconstruction package and tests of its performance using cosmic rays and single beam data*, Journal of Physics: Conference Series **219** (2010), no. 3, 032052.

[115] D Adams, Ketevi A Assamagan, M Biglietti, G Carlino, G Cataldi, F Conventi, A Farilla, Yu Fisyak, S Goldfarb, E Gorini, T Lagouri, K Mair, L Merola, A Nairz, A Poppleton, M Primavera, S Rosati, J T Shank, S Spagnolo, L Spogli, G D Stavropoulos, M Verducci, and T Wenaus, *Track reconstruction in the ATLAS Muon Spectrometer with MOORE*, Technical Report ATL-SOFT-2003-007, CERN, Geneva, 2003. revised version number 1 submitted on 2003-10-13 13:51:39.

[116] N Van Eldik, Frank L Linde, P M Kluit, and S C M Bentvelsen, *The atlas muon spectrometer: calibration and pattern recognition. oai:cds.cern.ch:1044839*, Ph.D. Thesis, Amsterdam, 2007. Presented on 22 Feb 2007.

[117] Jochem Snuverink, *The atlas muon spectrometer: commissioning and tracking. oai:cds.cern.ch:1232051*, Ph.D. Thesis, Twente, 2009. Presented on 16 Oct 2009.

[118] Zdenko van Kesteren, *Identification of muons in atlas. oai:cds.cern.ch:1255858*, Ph.D. Thesis, Amsterdam, 2010. Presented on 12 Mar 2010.

[119] M Baak, *Good run lists, what about them? (*`http://atlas-service-enews.web.cern.ch/atlas-service-enews/2010/features_10/features_goodrun.php`*)*.

[120] I. Aracena et al., *Overview and performance studies of jet identification in the trigger system*. ATL-PHYS-PUB-2009-032.

[121] *Luminosity Determination Using the ATLAS Detector*, Technical Report ATLAS-CONF-2010-060, CERN, Geneva, 2010.

[122] D Belohrad, JJ Gras, LK Jensen, OR Jones, M Ludwig, P Odier, JJ Savioz, and S Thoulet, *Commissioning and First Performance of the LHC Beam Current Measurement Systems*, Technical Report CERN-BE-2010-015, CERN, Geneva, 2010.

[123] W Lampl, S Laplace, D Lelas, P Loch, H Ma, S Menke, S Rajagopalan, D Rousseau, S Snyder, and G Unal, *Calorimeter Clustering Algorithms: Description and Performance*, Technical Report ATL-LARG-PUB-2008-002. ATL-COM-LARG-2008-003, CERN, Geneva, 2008.

[124] T Barillari *et al.*, *Local Hadronic Calibration*, Technical Report ATL-LARG-PUB-2009-001-2. ATL-COM-LARG-2008-006. ATL-LARG-PUB-2009-001, CERN, Geneva, 2008.

[125] *Performance of the Missing Transverse Energy Reconstruction and Calibration in Proton-Proton Collisions at a Center-of-Mass Energy of 7 TeV with the ATLAS Detector*, Technical Report ATLAS-CONF-2010-057, CERN, Geneva, 2010.

[126] G. Aad et al., *Charged-particle multiplicities in pp interactions at sqrt(s) = 900 GeV measured with the ATLAS detector at the LHC*, Phys. Lett. **B688** (2010), 21–42, available at `1003.3124`.

[127] *Performance of the ATLAS Silicon Pattern Recognition Algorithm in Data and Simulation at* $\sqrt{s}$ = 7 TeV, Technical Report ATLAS-CONF-2010-072, CERN, Geneva, 2010.

[128] *Characterization of Interaction-Point Beam Parameters Using the pp Event-Vertex Distribution Reconstructed in the ATLAS Detector at the LHC*, Technical Report ATLAS-CONF-2010-027, CERN, Geneva, 2010.

[129] *Muon Reconstruction Performance*, Technical Report ATLAS-CONF-2010-064, CERN, Geneva, 2010.

[130] M Aharrouche *et al.*, *Total inclusive W and Z boson cross-section measurements, cross-section ratios and combinations in the electron and muon decay channels at 7 TeV based on 300 nb^{-1}*, ATL-PHYS-INT-2010-125, 2010.

[131] Pavel M. Nadolsky, Hung-Liang Lai, Qing-Hong Cao, Joey Huston, Jon Pumplin, Daniel Stump, Wu-Ki Tung, and C.-P. Yuan, *Implications of cteq global analysis for collider observables*, Phys. Rev. D **78** (2008Jul), no. 1, 013004.

[132] Stefano Frixione and Bryan R. Webber, *Matching NLO QCD computations and parton shower simulations*, JHEP **06** (2002), 029, available at `hep-ph/0204244`.

[133] F. D. Aaron et al., *Combined Measurement and QCD Analysis of the Inclusive ep Scattering Cross Sections at HERA*, JHEP **01** (2010), 109, available at `0911.0884`.

[134] A Salzburger, *The ATLAS Track Extrapolation Package*, Technical Report ATL-SOFT-PUB-2007-005. ATL-COM-SOFT-2007-010, CERN, Geneva, 2007.

[135] E Lund, L Bugge, I Gavrilenko, and A Strandlie, *Track parameter propagation through the application of a new adaptive Runge-Kutta-Nystrom method in the ATLAS experiment*, J. Instrum. **4** (2008Jul), no. ATL-SOFT-PUB-2009-001. ATL-COM-SOFT-2008-006, P04001. 13 p. Approved for publication by the ATLAS Publication comitee, submitted to JINST.

[136] E Lund, L Bugge, I Gavrilenko, and A Strandlie, *Transport of covariance matrices in the inhomogeneous magnetic field of the ATLAS experiment by the application of a semi-analytical method*, J. Instrum. **4** (2008Jul), no. ATL-SOFT-PUB-2009-002. ATL-COM-SOFT-2008-007, P04016. 14 p. Approved for publication by the ATLAS Publication comitee, submitted to JINST.

[137] E Lund, L Bugge, E W Hughes, D Lopez Mateos, A Salzburger, and A Strandlie, *Treatment of energy loss and multiple scattering in the context of track parameter and covariance matrix propagation in continuous material in the ATLAS experiment*, Technical Report ATL-SOFT-PUB-2008-003. ATL-COM-SOFT-2008-008, CERN, Geneva, 2008.

[138] Wouter Verkerke and David P. Kirkby, *The RooFit toolkit for data modeling* (2003), available at `physics/0306116`.

[139] A Ahmed *et al.*, *Supporting Document: Measurement of the W cross section and asymmetry in the electron and muon decay channels at* $\sqrt{s}$*=7 TeV*, Technical Report ATL-PHYS-INT-2010-116, CERN, Geneva, 2010.

[140] Timo Antero Aaltonen et al., *Measurement of dσ/dy of Drell-Yan e$^+$e$^-$ pairs in the Z Mass Region from p$\bar{p}$ Collisions at* $\sqrt{s}$ = 1.96 TeV, Phys. Lett. **B692** (2010), 232–239, available at `0908.3914`.

[141] V. M. Abazov et al., *Measurement of the shape of the boson transverse momentum distribution in p$\bar{p}$ $\rightarrow$ Z/γ^* $\rightarrow$ e$^+$e$^-$ + X events produced at* $\sqrt{s}$*=1.96-TeV*, Phys. Rev. Lett. **100** (2008), 102002, available at `0712.0803`.